International Journal of Molecular Sciences

Monoclonal Antibodies and Their Functional Fragments in Research, Diagnosis and Therapy 2.0

Edited by
Menotti Ruvo and Annamaria Sandomenico

Printed Edition of the Special Issue Published in
International Journal of Molecular Sciences

www.mdpi.com/journal/ijms

MDPI

Monoclonal Antibodies and Their Functional Fragments in Research, Diagnosis and Therapy 2.0

Monoclonal Antibodies and Their Functional Fragments in Research, Diagnosis and Therapy 2.0

Editors

Menotti Ruvo
Annamaria Sandomenico

MDPI • Basel • Beijing • Wuhan • Barcelona • Belgrade • Manchester • Tokyo • Cluj • Tianjin

Editors

Menotti Ruvo
Chemical Biology
CNR, Institute of Biostructures and Bioimaging
Napoli
Italy

Annamaria Sandomenico
Chemical Biology
CNR, Institute of Biostructures and Bioimaging
Napoli
Italy

Editorial Office
MDPI
St. Alban-Anlage 66
4052 Basel, Switzerland

This is a reprint of articles from the Special Issue published online in the open access journal *International Journal of Molecular Sciences* (ISSN 1422-0067) (available at: www.mdpi.com/journal/ijms/special_issues/mabs2).

For citation purposes, cite each article independently as indicated on the article page online and as indicated below:

LastName, A.A.; LastName, B.B.; LastName, C.C. Article Title. *Journal Name* **Year**, *Volume Number*, Page Range.

ISBN 978-3-0365-3165-6 (Hbk)
ISBN 978-3-0365-3164-9 (PDF)

Contents

About the Editors

Menotti Ruvo

Dr. Ruvo graduated in Chemistry at the University of Naples in 1991. During the first 10 years of his career, he worked in industry, as a researcher in charge of the protein and peptide laboratory and contributing to the development of several bioactive molecules. In 2002, he joined the Institute of Biostructure and Bioimaging of the National Research Council (IBB-CNR) in Naples, Italy, leading several projects focused on the development of novel bioactive peptides and monoclonal antibodies against therapeutically relevant targets. Among others, he has developed peptides modulating the activity of PlGF, Cripto and Gadd45beta and monoclonal antibodies against Nodal, HCV E2 protein, Cripto, Ape1 and PRAME. He was one of the founders of Kesios Therapeutics Ltd (London) and Anbition (Naples). He is the author of about 170 papers and inventor of $>$30 patents.

Annamaria Sandomenico

Annamaria Sandomenico is a researcher at the Institute of Biostructure and Bioimaging (IBB) of the National Research Council (CNR), Italy. She graduated in Chemistry and Pharmaceutical Technologies (2004) and completed her PhD in Biotechnological Sciences (2008) at the University of Naples Federico II, Italy. Since 2006 she has been working with Dr. Menotti Ruvo at IBB-CNR, Naples, Italy.

Her research activities are focused on the identification and development of bioactive molecules including peptides, monoclonal antibodies and new recombinant antibody formats (Fab, scFv, ADC, humanized, bispecific antibodies) against targets of diagnostic and therapeutic interest. She is co-author of more than 70 papers and co-inventor of patents related to monoclonal antibodies. She has developed several monoclonal antibodies against novel tumour biomarkers such as Cripto-1, Nodal, Ape1 and PRAME and viral antigens such as HCV E2 protein. She also contributed to the creation of a platform to generate engineered recombinant antibody fragments with reactive sites for bioconjugation and site-specific multimerisation.

Preface to ”Monoclonal Antibodies and Their Functional Fragments in Research, Diagnosis and Therapy 2.0”

Monoclonal antibodies (mAbs) are among the most specialised molecules for the recognition and capture of specific analytes. Hundreds of thousands of mAbs have been generated for a large number of different antigens with increasing affinity and specificity and are available for the most diverse purposes. Many of them have been validated as irreplaceable agents for diagnosis and therapy or as unique reagents for research. Others have been developed using emerging technologies that avoid the need for animal immunisation. This short book strives to gather the perspective view of the various contributing authors and to survey the new strategic assets adopted to generate novel monoclonal antibodies or surrogates, such as Fab, Fab2, ScFv and nanobodies, which have an increasing impact in biomedicine as therapeutic or diagnostic assets in various diseases.

Menotti Ruvo, Annamaria Sandomenico
Editors

International Journal of
Molecular Sciences

MDPI

Article

Semi-Automated Cell Panning for Efficient Isolation of FGFR3-Targeting Antibody

Byeongkwi Min [1,2], Minyoung Yoo [2], Hyeree Kim [1,3], Minjung Cho [2], Do-Hyun Nam [1,2,4,*] and Yeup Yoon [1,2,3,5,*]

1 Department of Health Sciences and Technology, Samsung Advanced Institute for Health Sciences and Technology, Sungkyunkwan University, Seoul 06351, Korea; minbk1991@gmail.com (B.M.); unohrkim@gmail.com (H.K.)
2 Institute for Refractory Cancer Research, Research Institute for Future Medicine, Samsung Medical Center, Seoul 06351, Korea; ymy1103@gmail.com (M.Y.); wm5016@naver.com (M.C.)
3 Institute for Future Medicine, Samsung Medical Center, Seoul 06351, Korea
4 Department of Neurosurgery, Samsung Medical Center, Sungkyunkwan University School of Medicine, Seoul 06351, Korea
5 Department of Biopharmaceutical Convergence, Sungkyunkwan University, Seoul 06351, Korea
* Correspondence: nsnam@skku.edu (D.-H.N.); benedict.yoon@samsung.com (Y.Y.); Tel.: +82-(2)-3410-3497 (D.-H.N.); +82-(2)-2148-7900 (Y.Y.)

Abstract: Phage display technology is a widely used practical tool for isolating binding molecules against the desired targets in phage libraries. In the case of targeting the membrane protein with its natural conformation, conventional bio-panning has limitations on the efficient screening of the functionally relevant antibodies. To enrich the single-chain variable fragment (scFv) pools for recognizing the natural conformation of the membrane targets, the conventional bio-panning and screening process was modified to include the semi-automated cell panning protocol. Using FGFR3-overexpressing patient-derived cancer cells, biotin-X-DHPE was introduced and coupled to Streptavidin-coated magnetic beads for use in the solution-phage bio-panning procedure. The resulting clones of scFv were compared to the diversity of the binding region, especially on CDR-H3. The clones enriched further by cell-based panning procedure possessed a similar binding site and the CDR-H3 loop structure. The resulting antibodies inhibited cell growth and induced target degradation. This process may be a useful tool for screening biologically related antibodies that recognize natural conformational structure on cell membrane protein. Furthermore, cell-based panning has the potential to further expand to a high-throughput screening (HTS) system and automation process.

Keywords: phage display; cell-based panning; semi-automated cell panning; FGFR3-specific antibody

Citation: Min, B.; Yoo, M.; Kim, H.; Cho, M.; Nam, D.-H.; Yoon, Y. Semi-Automated Cell Panning for Efficient Isolation of FGFR3-Targeting Antibody. *Int. J. Mol. Sci.* **2021**, *22*, 6240. https://doi.org/10.3390/ijms22126240

Academic Editors: Annamaria Sandomenico and Menotti Ruvo

Received: 3 May 2021
Accepted: 7 June 2021
Published: 9 June 2021

1. Introduction

Phage display, first described in 1985, is a practical tool for displaying proteins or peptides of interest in bacteriophage through fusion with viral envelope proteins [1–3]. Phage libraries are used to select and isolate binding molecules with high affinity for the target antigen with applications in monoclonal antibody (mAb) discovery, affinity maturation, and humanization [4,5]. Bio-panning for affinity selection has been used to isolate target protein-binding molecules from phage libraries [1,6,7]. The bio-panning procedure includes four major steps for phage selection: (i) Incubating and binding the phage library with the desired target; (ii) washing for non-binding and non-specific phage removal; (iii) eluting the specific phage binders; (iv) amplifying for eluted phages through Escherichia coli re-infection [8–11].

Conventional bio-panning has been based on various selection methods such as solid-phase for immobilized purified antigen, solution-phase using biotinylated antigen, and whole cell panning (WCP) [2,12]. The solid-phase selection is a fairly straightforward technique; however, the antigen must be presented in the correct conformation. Otherwise,

the binders could recognize the epitopes that are naturally masked in the native form [12,13]. WCP was applied to isolated phage binders using cells intact with cell membrane proteins such as G-protein-coupled receptors, ligand-gate ion channels, receptor tyrosine kinases, and immunoglobulin-like receptors [3]. Although WCP may select non-specific phage binders to off-target cell surface protein, it could potentially enrich the phage binders recognizing the naturally exposed epitope on the cell surface [12,14,15].

We utilized the cell-based panning process in addition to the conventional bio-panning to enrich the phage binders specific for FGFR3 with the appropriate biological functions. The semi-automated cell panning method was optimized to maintain the advantages of the WCP by labeling a cell membrane-like substance (biotin-X-DHPE) and Streptavidin-coated magnetic beads without damaging the membrane proteins of intact cells [16]. Using FGFR3-overexpressing patients-derived cells (glioblastoma, GBM), biotin-X-DHPE and Streptavidin-coated magnetic beads were coupled to use in the solution-phage bio-panning procedure. It was applied to an automatic mechanical system using a magnetic particle processor (Thermo Fisher Scientific, KingFisher™ Flex, Waltham, MA, USA) to efficiently perform and reduce the screening time for WCP [17–19].

Fibroblast growth factors (FGFs) and their receptor (FGFR) signaling have functional roles in the regulation of cell proliferation, differentiation, and apoptosis. FGFR3 consists of an extracellular domain containing three immunoglobulin-like (Ig-like) domains (D1–D3), a transmembrane domain, and two intracellular tyrosine kinase domains. FGFR3 has two main splice variants FGFR3-IIIb and -IIIc. Aberrantly activated and/or overexpressed FGFR3 has been implicated in various human malignancies [20–25]. Several therapeutic antibodies targeting FGFR3 have been used in clinical development, such as monoclonal antibodies (Vofatamab, Rainier Therapeutics, San Leandro, CA, USA) or antibody-drug conjugates (LY3076226, Eil Lilly) [26–28].

In this study, we successfully selected FGFR3 antibodies with relevant biological function from a synthetic human single-chain variable fragment (scFv) phage library through the introduction of semi-automated cell panning. Sequence analysis and Fv modeling of the selected scFvs were performed, and sequence and structural similarity of CDR-H3 were analyzed using multiple alignments. In individual scFv, the respective IgG antibodies were generated based on scFvs and demonstrated the specific binding properties and biological functions such as inhibition of cell viability and target degradation. The introduction of a semi-automated cell panning process may be an efficient tool for selecting antibodies with functionality and specificity for cell membrane proteins in the generation of antibodies and antibody engineering.

2. Results

2.1. Introduction Strategy of Semi-Automated Cell Panning in Addition to Conventional Bio-Panning

We immobilized live cells using the complex of biotin-X-DHPE and Streptavidin-coated magnetic beads. This implied that the phospholipid-magnetic beads complex-labeled cells can be applied to magnetic beads-based bio-panning, as well as to the automated magnetic particle processor for semi-automated cell panning (Figure 1A). To efficiently enrich scFv binders, a semi-automated cell panning process was combined with conventional bio-panning. The scFv binders recognize the natural conformational structure expressed on the cell surface. First, 3–5 rounds of conventional bio-panning such as solid phase (e.g., immobilized antigen coating) or solution phase (e.g., magnetic beads-based with biotinylated antigen) were performed to enrich the phage pool bound to the purified protein. Next, the isolated phage pools underwent semi-automated cell panning to finally isolate scFv binders that recognize the cell surface 3D structure (Figure 1B).

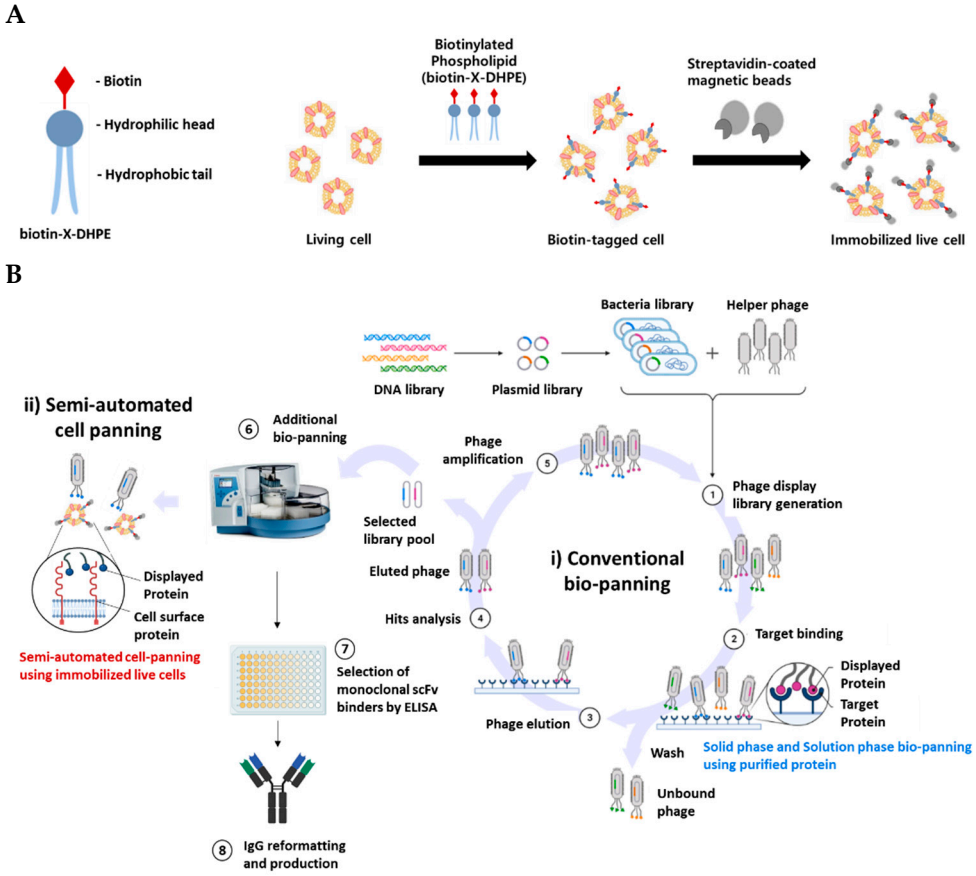

Figure 1. (**A**) Scheme for attachment of magnetic beads to live cells for applying bio-panning. Biotin-X-DHPE, a biotin tagged material, is a cell membrane-like substance composed of a hydrophilic head and a hydrophobic tail. Biotin-X-DHPE reacted with Streptavidin-coated magnetic beads to form a complex that is attached to the surface of living cells. (**B**) Bio-panning workflow combined with semi-automated cell panning. Binding to the rescued phage pool and target protein (Step 1–2). Wash to remove non-binding phage and then elute and amplify phage that binds to target protein (Step 3–5). Phage pool that recognizes naive target protein is isolated and screened by performing semi-automated cell panning on target-expressing cells (Step 6–8). Images created using BioRender.

To efficiently select clones that recognize both the purified target protein and cell surface membrane protein from a synthetic human scFv phage library, semi-automated cell panning was performed following conventional bio-panning [29]. In the case of conventional bio-panning such as bio-panning using purified protein or WCP, since clones are initially selected by a single method, it is difficult to select clones with desired binding characteristics using the bio-panning procedure (time of bio-panning: >8 weeks including repeated experiments). Conversely, in the case of semi-automated cell panning, clones that show biologically relevant properties and binding properties during the bio-panning procedure are enriched. It minimizes repetition of the bio-panning cycle in the in vitro binding test step (e.g., affinity or cell binding assay by ELISA) because unwanted clones are not selected and hence, the process is less time-consuming. Therefore, the required time and the burden of economic costs efficiently decrease because the bio-panning step is not re-performed (time of bio-panning: 3–4 weeks).

2.2. Optimal Immobilization Condition of Cell for Applying Semi-Automated Cell Panning

To confirm whether biotin-X-DHPE affects the expression level or cell viability of the target protein on the cell surface after conjugation to the cell membrane, the conjugation of biotin-X-DHPE to cell membranes and attachment into living cells were assessed by FACS analysis. Biotin-X-DHPE was detected using Streptavidin-FITC (SA-FITC), FGFR3 was

detected using anti-FGFR3-PE-conjugated control antibody, and histogram (shift, %) of FACS analysis was compared. The percent change in FITC intensity was approximately more than 80% after incubation with biotin-X-DHPE while that of PE was not changed, indicating that most of the cells were efficiently labeled with biotin-X-DHPE with no expressional change of FGFR3. Additionally, the FGFR3 expression level before and after treatment with biotin-X-DHPE remained unaltered, irrespective of the FGFR3 expression level on the cell surface (Figure 2A). On comparing the reaction time with the temperature at which biotin-X-DHPE is most effectively inserted into living cells, it was confirmed that more than 80% of biotin-X-DHPE was most attached to the cell surface under the reaction conditions of 30 min at room temperature using FACS analysis (Figure 2B). The labeling buffer was optimized by comparing various reaction buffers such as PBS (pH 7.4), 2 mM EDTA (0.1% BSA), and Pluronic F-68 buffer during cell labeling. Pluronic F-68 buffer was found to ensure more efficient cell labeling compared to other buffers under the same conditions (magnetic beads attached cells at more than 65%) (Figure 2C). Since it is a nonionic surfactant, it is considered useful for reducing the formation of bubbles that occur during agitation and incubation and for reducing the adhesion of cells to materials such as glass.

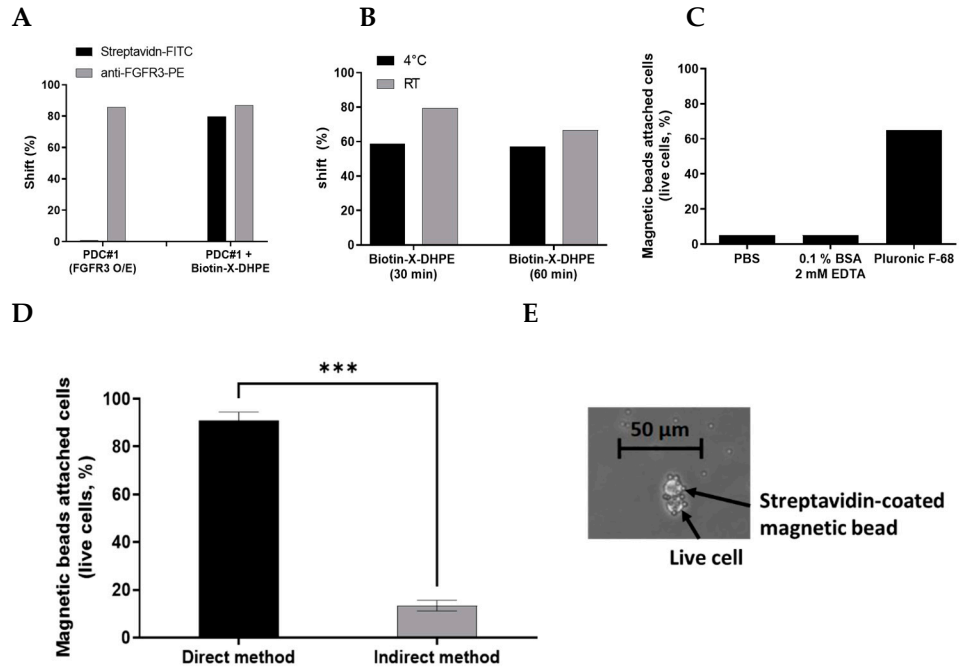

Figure 2. (**A**) Following biotin-X-DHPE labeling on FGFR3-overexpressing cells (PDC #1), FGFR3 expression levels on the cell surface were analyzed by FACS analysis. Biotin-X-DHPE was detected using Streptavidin-FITC, and FGFR3 was detected using PE-direct conjugated antibody. (**B**) The optimal reaction temperature and time for labeling the living cells with biotin-X-DHPE were analyzed by FACS analysis. (**C**) Optimal reaction buffer analysis for attaching magnetic beads on cells. (**D**) The capture yield of live cells attached with magnetic beads was compared using both direct and indirect method through cell counting and microscopic observation. *** $p < 0.001$ paired T test. (**E**) Microscopic observation of live cells attached with magnetic beads (magnification 400×).

There are direct or indirect methods for labeling cells with biotin-X-DHPE and Streptavidin-coated magnetic beads (Figure S1). In the direct method, biotin-X-DHPE and Streptavidin-coated magnetic beads are incubated prior to forming a complex, and then the complex is attached to the cell. In the indirect method, biotin-X-DHPE is first attached to the living cells and then further conjugated with the beads. When comparing the two methods, the direct method showed a significantly higher labeling efficiency than the indirect method. The direct method showed approximately 85% or more labeled yield, while the indirect method showed less than 20% yield (Figure 2D). Furthermore, it was

confirmed through microscopic observation that a complex consisting of biotin-X-DHPE and Streptavidin-coated magnetic beads was attached to the living cells (Figure 2E). The bio-panning scheme was modified from the conventional semi-automation panning to accommodate the semi-automated cell panning procedure. The dedicated software protocol for the optimal semi-automated cell panning process was modified, and the appropriate detailed scheme is included in Figure S2.

2.3. Isolation of FGFR3-Specific Clones through Introduction of Semi-Automated Cell Panning

We performed two conventional bio-panning: (1) Solution phase selection with a biotinylated antigen using semi-automated bio-panning; (2) solid phase selection with immobilization antigen coating using purified human FGFR3-IIIc. In the solution phase, semi-automated bio-panning using biotinylated human FGFR3-IIIc was performed using a magnetic particle processor. Using an automated processor and the included driving software, biotinylated FGFR3-IIIc and Streptavidin-coated magnetic beads were combined and then incubated with the rescued phage pool. Next, to collect FGFR3-IIIc-specific phage pools, the solution was washed and eluted at the designated plate. By performing five rounds of bio-panning, the scFv binders specific for human FGFR3-IIIc were amplified in the solution phase. In the solid phase, the process of amplifying the FGFR3-specific scFv binders was performed four times by immobilizing human FGFR3-IIIc to the immuno-tube and then treating the phage pool. The output to input phage titer ratio was calculated for each bio-panning round to confirm the amplification of the FGFR3-specific scFv binder pool. The ratio was improved after five rounds or four rounds of bio-panning compared to that after the first round (Table 1). Using conventional panning, 376 and 658 clones were screened and then 8 and 11 clones were isolated in the solution and solid phase, respectively, (cut-off > 2, relative O.D) with different sequences via ELISA screening analysis (Table 2).

Table 1. Phage titer following conventional bio-panning and semi-automated bio-panning.

	Round	Input Titer ($\times 10^{10}$ CFU)	Output Titer ($\times 10^{5}$ CFU)	Overall % Yield (Output/Input $\times$ 100%)
Conventional panning : Solution phase selection using semi-automated bio-panning	I	25.8	76.9	0.00298
	II	5.5	1.46	0.00027
	III	23.9	238	0.00996
	IV	27.2	906	0.03331
	V	6.5	321	0.04938
Semi-automated cell panning	VI	18.3	561	0.03066
Conventional panning : Solid phase selection using immobilization antigen coating panning	I	100	1	0.00001
	II	2.5	0.05	0.00002
	III	2.9	0.12	0.000041
	IV	3	0.1	0.000033
Semi-automated cell panning	VI	49	13	0.000265

Table 2. Summary of sequenced clones obtained from conventional bio-panning and semi-automated bio-panning.

	Clones Screened	Different Sequences
Conventional panning : Solution phase selection using semi-automated bio-panning	376	8
Semi-automated cell panning *	188	2
Conventional panning : Solid phase selection using immobilization antigen coating panning	658	11
Semi-automated cell panning **	372	4

Semi-automated cell panning *: magnetic beads-based semi-automated panning (solution phase) + semi-automated cell panning; semi-automated cell panning **: immobilized antigen panning (solid phase) + semi-automated cell panning.

To select clones, which recognize the surface FGFR3 protein of cells (PDC #1), semi-automated cell panning was performed for each phage pool that specifically binds to

FGFR3-IIIc protein purified by two conventional bio-panning method, and input and output phages were titrated (Table 1).

We compared the binding efficiency of each phage pool rescued from conventional bio-panning and additional semi-automated cell panning to FGFR3-overexpressing cells (PDC #1). Each output phage pool was collected through PEG precipitation and titration, and the same amount of phage particles was bound to FGFR3-overexpressing cells, and then the fluorescence intensity was compared using flow cytometry. The output phage pool in which semi-automated cell panning was further introduced had partially enhanced the selectivity for the FGFR3-overexpressing cells as compared with the output phage pool in which conventional bio-panning was performed (Figure 3A).

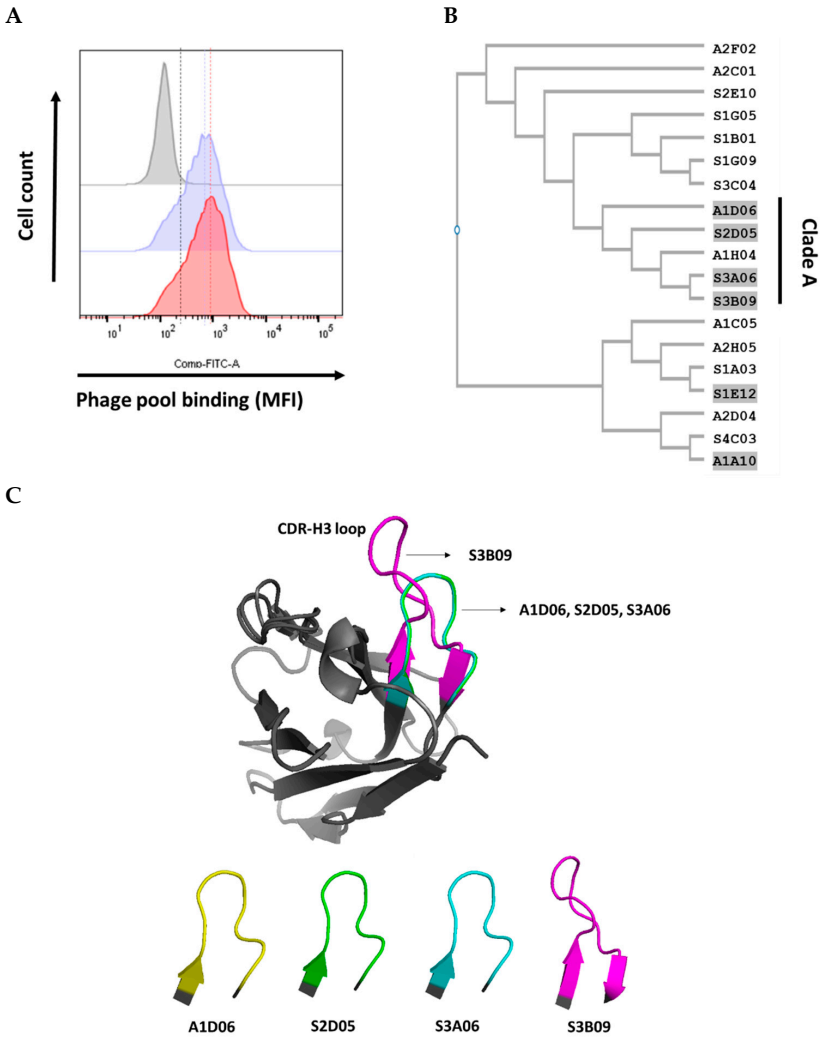

Figure 3. (**A**) Phage pool binding to FGFR3-overexpressing cells in a flow cytometer; comparison of cell surface binding between amplified phage pools obtained using conventional bio-panning (blue histogram) only or with the introduction of cell panning (red histogram). Comparison of CDR-H3 sequence similarity of isolated antibodies through cell panning introduction. (**B**) Phylogenetic tree of similar sequences built on the basis of CDR-H3 (Kabat numbering) using CLUSTAL W multiple sequence alignment programs. Each phylogenetic tree was analyzed for 13 clones selected through conventional bio-panning only and 6 clones selected through introduction of cell panning. The A1D06, S2D05, S3A06, and S3B09 clones were grouped into "Clade A". (**C**) Comparison of CDR-H3 loop structure alignment using POSA analysis (interactive multiple protein structure alignment). The CDR-H3 of the A1D06 (yellow), S2D05 (green), S3A06 (cyan), and S3B09 (magenta) clones of Clade A were aligned based on the VH region in the Fv modeling annotation. CDR-H3 loop structure and length are different for each clone (gray, framework).

After the introduction of semi-automated cell panning procedure, we screened 188 and 372 individual clones and isolated 2 and 4 clones each (cut-off > 2, relative O.D) with different sequences via ELISA screening analysis (Table 2). The sequences of the six clones selected by introduction of semi-automated cell panning are included in the 19 clones of conventional bio-panning sequences. Clones with the characteristics of binding to the surface of FGFR3-overexpressing cells were enriched in the phage pool selectively amplified for purified FGFR3-IIIc by conventional bio-panning.

2.4. Complementarity-Determining Regions of the Heavy Chain (CDR-H3) Sequence Analysis and Structure Homology Alignment Using Variable Fragment (Fv) Modeling

The sequences of CDR-H3 (Kabat numbering) were compared in the six CDR regions (CDR-L1, L2, L3, H1, H2, and H3) of the antibody [30–32]. The CDR-H3 region of an antibody has the most sequence and structural diversity and is known to play the most important role in antigen-binding specificity among the six CDRs [33–36]. Moreover, the synthetic human scFv library used in this study also has the most diverse sequence and structural features of CDR-H3 [29].

The nucleotide and amino acid sequence of phagemid vector for scFvs (VH-linker-VL) were analyzed using 19 clones of different sequences isolated by conventional bio-panning and 6 clones (included in 19 sequences) selected by semi-automated cell panning (cell panning) established in this study. The CDR-H3 sequences of 19 different clones selected by bio-panning were confirmed to have various lengths and amino acid configurations. Six clones (A1D06, S2D05, S3A06, S3B09, S1E12, and A1A10) selected by cell panning were marked with gray highlights (Figure 3B). The CDR-H3 sequences of the six clones were compared for similarity through phylogenetic tree analysis using a Clustal W (multiple sequence alignment programs) tool. Clones A1D06, S2D05, S3A06, and S3B09 (Clade A) were significantly similar in sequence and length to CDR-H3, but S1E12 and A1A10 showed differences (Figure 3B). To compare the CDR-H3 structural similarity between the selected six clones, Fv modeling was first performed using the SAbPred (a structure-based antibody prediction server) tool (Figure S3) [37]. The structure alignment of the CDR-H3 loop was performed using the POSA (partial order structure alignment) tool for the whole variable heavy chain (VH), and the structural similarity of CDR-H3 was analyzed using a flexible multiple structure alignment approach for Clade A [38,39]. The average of root-mean-square deviation (RMSD) in the VH region (tertiary structure) between each clone in Clade A was less than 1 Å, which is the general criterion considered for significant similarity (Figure 3C) [40]. Therefore, clones of Clade A with sequence and structurally similarity to CDR-H3 were considered because they have similar binding properties against FGFR3. However, the overall CDR-H3 sequence and structural similarity pattern of Clade A may not be completely identical. It has a limitation in that there may be ambiguous contradictions due to the difference between the methodology of the two alignments.

2.5. Generation of Anti-FGFR3 Antibodies (IgG) and Analysis of Physicochemical Properties

The VH and VL sequences of the anti-FGFR3 scFv binders selected using cell panning were analyzed, and each sequence was cloned into heavy (Immunoglobulin G1, IgG1) and light chain (lambda) expression vectors for reformatting IgG (Figure S4). Anti-FGFR3 antibody clones were produced by co-transfection of heavy and light chain vectors using the Expi293 expression system and highly purified clones were obtained using an affinity chromatography column. The production yield of each clone was as follows: A1D06, 20 mg/L; S2D05, 120 mg/L; S3A06, 161 mg/L; S3B09, 100 mg/L; S1E12, 180 mg/L; A1A10, 38 mg/L after 6 days of incubation.

Using sodium dodecyl sulfate polyacrylamide gel electrophoresis (SDS-PAGE) analysis, the assembly of heavy and light chains was confirmed and the molecular weight of whole IgG was analyzed. Under non-reducing conditions, all clones were observed to have a molecular weight of approximately 150 kDa, whereas under reducing conditions, heavy and light chains were observed to have molecular weights of approximately 50 kDa and 25 kDa, respectively (Figure 4A). By using size exclusion-high-performance liquid

chromatography (SEC-HPLC), all clones were analyzed to confirm their purity, and their physical properties showed to be 95% or more (Figure 4B). It indicates that there was no loss of monomer such as through fragmentation (i.e., low-molecular-weight, LMW species) or aggregation (i.e., high-molecular-weight, HMW species).

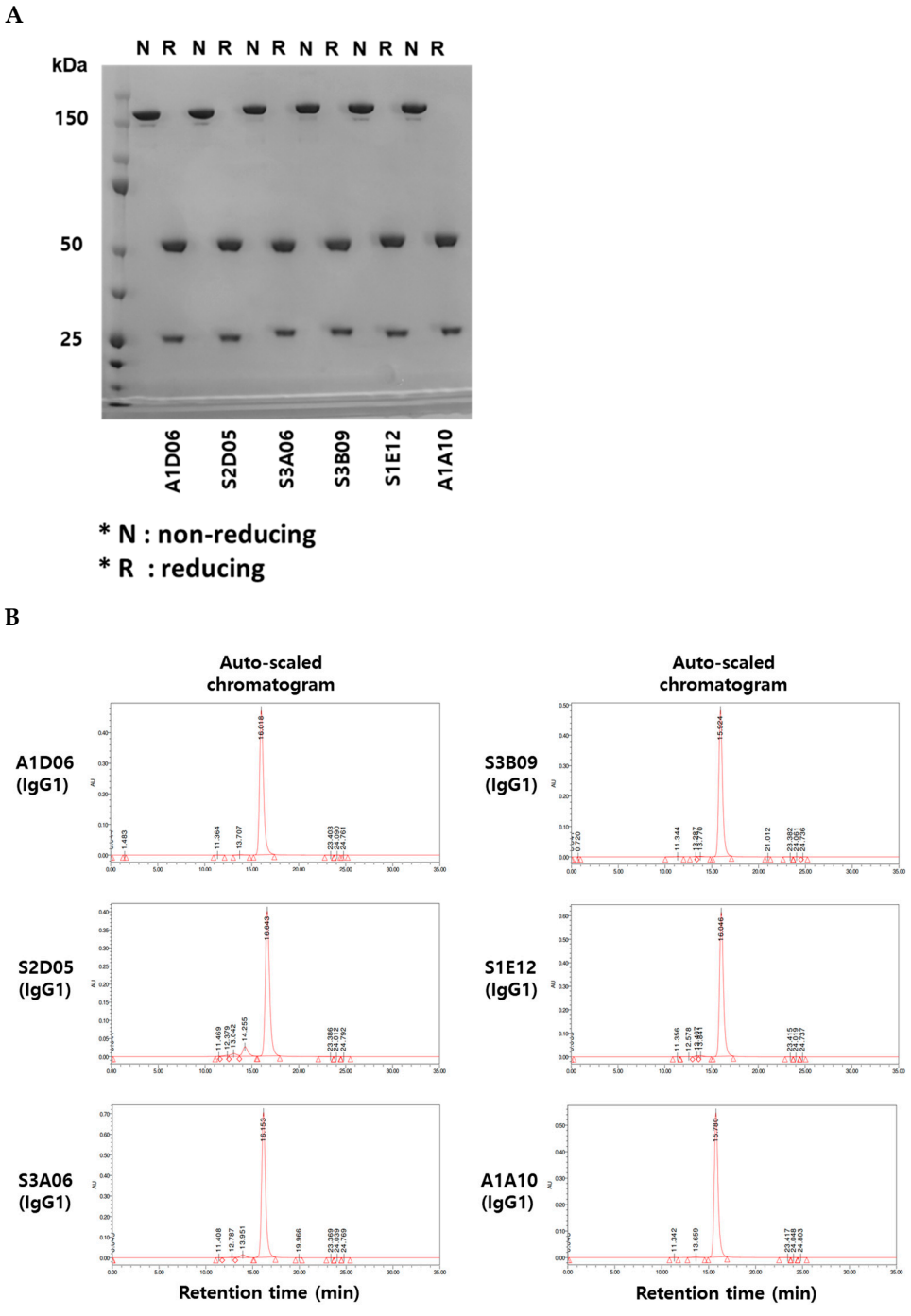

Figure 4. Physicochemical property analysis of anti-FGFR3 antibodies derived from cell panning. (**A**) Sodium dodecyl sulfate polyacrylamide gel electrophoresis (SDS-PAGE) analysis of purified antibodies in non-reducing and reducing conditions. In the non-reducing condition, 150 kDa band indicates the whole IgG, and in the reducing condition, 25 kDa and 50 kDa indicate the light chain and heavy chain of the antibody, respectively. (**B**) The purity of the anti-FGFR3 antibodies were analyzed using size exclusion-high performance liquid chromatography (SEC-HPLC). All anti-FGFR3 antibodies showed more than 95% purity of monomer.

2.6. Binding Properties of Anti-FGFR3 Antibodies

To verify the target-specific binding ability of the anti-FGFR3 antibodies, purified human FGFR3 isoform (FGFR3-IIIb, -IIIc) and several species of FGFR3 (mouse FGFR3-IIIc, cynomolgus monkey FGFR3-IIIc) were used in an ELISA assay. All clones showed specific binding for the purified human FGFR3-IIIc antigen, which were used for bio-panning, dependent on their concentration, but not to the negative protein (Fc-tagged). The six clones were considered to have apparent specificity for purified human FGFR3-IIIc (Figure 5A). Clade A (A1D06, S2D05, S3A06, and S3B09 clones), clustered based on the similarity of CDR-H3 sequences, was confirmed to have cross-reactivity between human FGFR3-IIIb and cynomolgus FGFR3-IIIc, but did not show specificity for mouse FGFR3-IIIc. The clone S1E12 was not specific to human FGFR3-IIIb, but it had apparent binding specificity for mouse FGFR3-IIIc and cynomolgus FGFR3-IIIc. It was hypothesized that this clone has a binding epitope for the IIIc region of the FGFR3 extracellular domain. The first half of the Ig III domain of FGFR3 is encoded by the invariant exon (IIIa), and the other half is the region where the variant occurs by splicing to IIIb or IIIc [24]. The clone A1A10 was estimated to have a homologous region of human (IIIb and IIIc), mouse, and cynomolgus FGFR3 as an epitope, as it binds to the other FGFR3 proteins as well as human FGFR-IIIc. Clones of Clade A were considered to have similar binding patterns to the human FGFR3 isoform or interspecies FGFR3 due to sequence and structural similarities of CDR-H3.

To accurately measure the binding kinetics (KD value) of anti-FGRF3 clones, we determined the affinity of the antibody to each purified protein based on surface plasmon resonance (SPR) analysis. Each clone showed the same binding pattern as the ELISA assay for isotype and interspecies of FGFR3 proteins (Figure S5). Clade A bound to hFGFR3-IIIc, hFGFR3-IIIb, and cynoFGFR3-IIIc, but did not bind to mFGFR3-IIIc. Clone S1E12 showed specific affinity for FGFR3-IIIc regardless of species and did not bind to FGFR3-IIIb. Clone A1A10 showed specificity for all types of FGFR3 proteins. The affinity of each clone for the FGFR3-purified protein is distributed from about ten nanomolar to sub-nanomolar, and it is considered that could be applied as a therapeutics (Table 3).

We verified that the selected clones bind to the FGFR3 expressed on cell surface using FACS analysis. All clones showed specific binding to FGFR3-overexpressing cell (PDC #1) and did not bind to FGFR3-negative cell (PDC #2) (Figure 5B). Thus, the clones selected through the introduction of cell panning were proved to have specific binding affinity for the purified FGFR3 protein as well as the natural FGFR3 tertiary structure on the cell surface membrane.

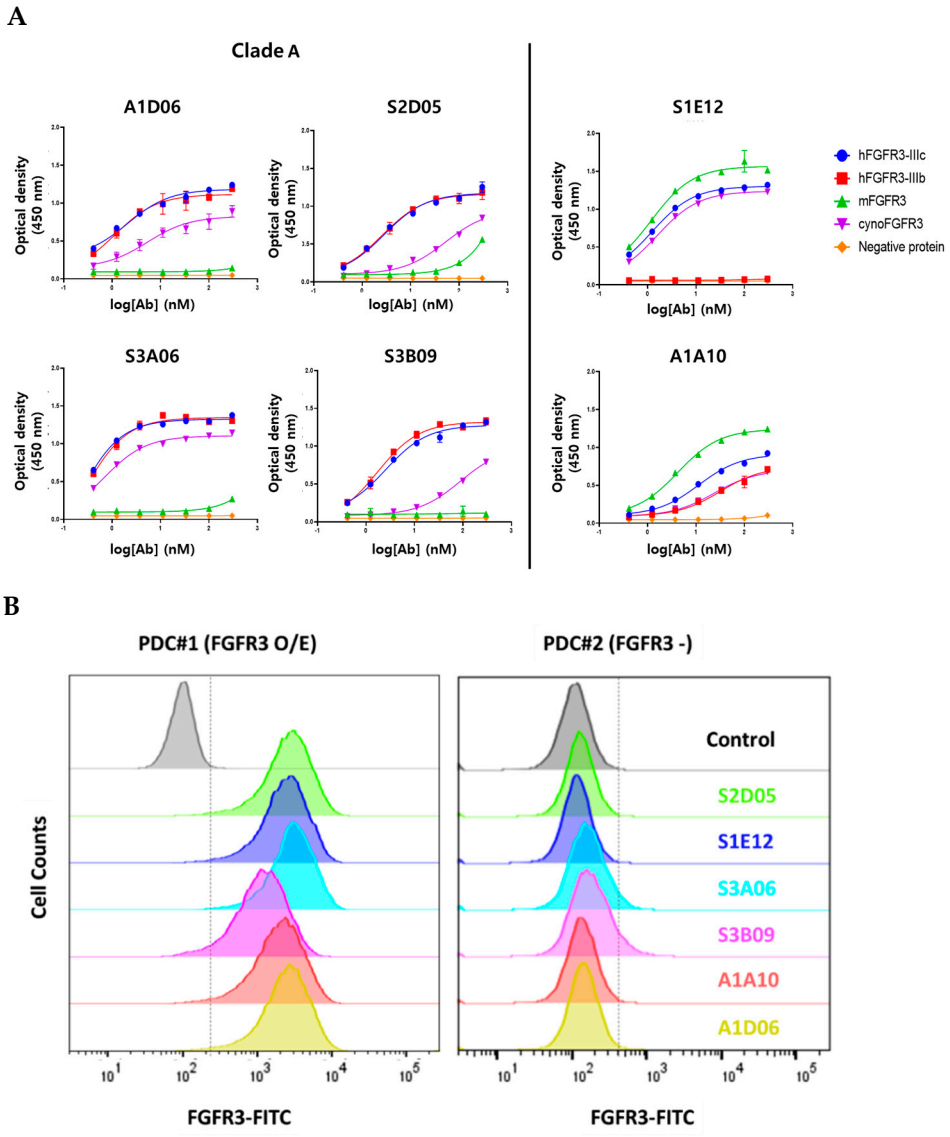

Figure 5. Binding characterization analysis of anti-FGFR3 antibody derived following the introduction of semi-automated bio-panning. (**A**) The binding specificity of selected FGFR3 antibodies to FGFR3 isoforms and interspecies was evaluated using ELISA. (**B**) The binding ability of FGFR3 antibodies to FGFR3-overexpressing cells (PDC#1) and FGFR3 negative cells (PDC#2) was determined using flow cytometry.

Table 3. Binding affinities (KD) of selected clones to human FGFR3 isotypes and interspecies FGFR3.

Antigen	Species	KD, nmol/L					
		Clade A					
		A1D06	S2D05	S3A06	S3B09	S1E12	A1A10
FGFR3-IIIc	Human	2.78	4.54	0.63	21.2	1.39	6.37
FGFR3-IIIb	Human	3.52	5.43	1.66	23.5	n.b.	15.8
FGFR3(IIIc)	Cynomolgus monkey	2.1	5.62	1.02	32.8	2.36	7.77
FGFR3 (IIIc)	Mouse	n.b.	n.b.	n.b.	n.b.	1.93	7.49

n.b.: non-binding.

2.7. Biological Function Analysis of Anti-FGFR3 Antibodies to FGFR3-Overexpressing Cells

To compare biological functions, in vitro functional assays for S3B09 of Clade A, which is the representative clone selected by cell panning, and S3C04 selected by conventional bio-panning were performed on FGFR3-overexpressing PDCs. The cell growth inhibition of anti-FGFR3 antibodies (S3B09, S3C04) was evaluated for FGFR3-overexpressing cells incubated with FGF1 ligand. To accurately analyze the anti-proliferation effect of the antibody, cell viability was assessed. After 96 h of antibody treatment, it was confirmed that the S3B09 selected by cell panning inhibited the tumor growth by approximately 30% (Figure 6A). The S3C04 selected by conventional bio-panning inhibited the tumor growth by less than 10%. It means that S3B09 antibody significantly inhibits the cell growth compared to control IgG and S3C04 against FGFR3-overexpressing PDCs.

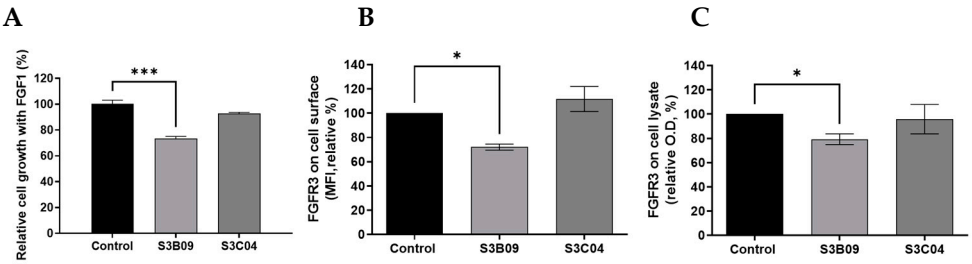

Figure 6. Biological functional assay of anti-FGFR3 antibodies. Inhibitory effect of clone S3B09 (Clade A) and S3C04 selected from conventional bio-panning on proliferation of FGFR3-overexpressing cells (PDC #1) was evaluated. Cells were cultured in the presence of 10 ng/mL FGF1 plus 10 μg/mL heparin sulfate or with S3B09 or S3C04 antibodies. Relative cell growth was evaluated through (**A**) cell viability after 96 h incubation with antibodies. Data represent mean ± SD; ***, $p < 0.001$ using one-way ANOVA. (**B**) Cell surface FGFR3 degradation assay. Individual antibodies were treated on FGFR3-overexpressing cells (PDC #1) and incubated for 1 h at 37 °C, and FGFR3 expression on the cell surface was detected through FACS analysis. (**C**) Total FGFR3 degradation assay. After the FGFR3-overexpressing cells (PDC #1) were treated with the antibody, total FGFR3 contained in the cell lysate was detected through sandwich ELISA. Data represent mean ± SD; *, $p < 0.03$ using one-way ANOVA.

To confirm the mechanism of inhibition of S3B09 on FGFR3-overexpressing cells, the induction of FGFR3 degradation by the antibody was verified. Changes in FGFR3 expression level on the cell surface was analyzed using flow cytometry and the change in total FGFR3 protein level was analyzed using sandwich ELISA. After incubating the S3B09 or S3C04 with the FGFR3-overexpressing cell line for 1 h, changes in the FGFR3 expression level on the surface of living cells were confirmed. S3B09 decreased the FGFR3 expression level by 28% compared to control IgG; however, S3C04 did not affect the FGFR3 expression level (Figure 6B). Additionally, after treatment with S3B09 or S3C04, the total FGFR3 protein level was evaluated using the lysate of the FGFR3-overexpressing cells, and the total FGFR3 protein level decreased by approximately 20% when treated with S3B09 (Figure 6C). These results suggest that S3B09 antibody selected by the introduction of cell panning effectively inhibits the growth of FGFR3-overexpressing cells through FGFR3 degradation.

3. Discussion

In phage display with WCP, the binders are separated in a state where the membrane protein is expressed in a natural tertiary structure to recognize the epitope of the naturally exposed region [3,10,13]. Therefore, WCP could represent a suitable strategy to obtain antibodies that are conformational-specific for membrane protein such as G protein-coupled receptors, ligand-gate ion channels, receptor tyrosine kinases, and immunoglobulin-like receptors, etc. [3,41–44]. Various cell-based panning strategies have been studied and optimized over a long period of time such as shadow-stick selection technique, FACS

sorting technique, and bio-panning and rapid analysis of selective interactive ligands (BRASIL) [3,45–48]. However, technical optimization is required to reduce the non-specific binders to the common cell surface proteins or the irrelevant proteins and to improve the time-consuming process using the intact cells [12,14].

To efficiently separate the phage binder that binds to the cell surface membrane protein, we designed a screening process that enriches the binder using conventional bio-panning along with a semi-automated cell panning process. We optimized a method of labeling cells with biotin-X-DHPE (biotinylated phospholipid), the substance with a biotin tag on a cell membrane-like structure, to apply living cells to magnetic beads-based panning. Since this substance has a hydrophilic head and a hydrophobic tail similar to the structure of cell membrane phospholipids, it can be easily immobilized to the cell membrane while minimizing cell damage. Since the biotin tag has a strong affinity for Streptavidin, Streptavidin-coated magnetic beads can be efficiently used with cells during the bio-panning procedure. The PDCs were conjugated with biotin-X-DHPE and attached to the Streptavidin-coated magnetic beads under optimized conditions to maintain viable cells with the natural conformation of the membrane protein [16]. Additionally, we implemented this method using an automatic instrument as the magnetic particle processor owing to its advantages in terms of time and labor required to efficiently isolate binders [17–19]. Furthermore, it may be applicable for high-throughput screening using multiple libraries, and binders can be selected simultaneously using various cells such as PDCs and cancer cell lines.

Abnormal FGFR3 signaling due to overexpression and/or mutation induces tumor proliferation and metastasis in multiple tumors [20–25]. Several antibody therapeutics targeting FGFR3 have been developed such as mAb, Vofatamab (Rainier Therapeutics) currently undergoing phase 1/2(b) clinical trial and Antibody-drug conjugate, LY3076226 (Eli Lilly) currently undergoing phase 1 clinical trials [49–51]. In our laboratory, we tried to screen the specific and functional antibody targeting FGFR3; however, it was difficult to isolate the binders with degradation and/or internalization properties (data not shown).

In this study, we enriched the functional antibodies through the additional semi-automated cell panning process using PDCs (glioblastoma, GBM) with a high level of FGFR3 expression. The 19 individual clones were isolated using the 1034 clones obtained from four or five rounds of the conventional bio-panning, and the 6 individual clones using 560 clones obtained from the additional semi-automated cell panning. The IgGs reformatting and production were performed on isolated clones, and target specificity was confirmed through affinity ELISA analysis and SPR analysis for the purified FGFR3 protein. Through the evaluation of the functional analysis, the final 4 candidates were selected. The semi-automated cell panning showed the enrichment of the desired 4 candidates from the 6 clones in comparison to the 4 of 19 clones obtained from conventional bio-panning. All of the 4 clones showed binding specificity for FGFR3-overexpressing cells, and non-specific binding or unwanted binding patterns were not observed. We performed cell proliferation and target degradation assays to analyze the biological function against FGFR3-overexpressing cells. The candidate clone obtained through the introduction of semi-automated cell panning was shown to inhibit tumor growth and degrade FGFR3 on the cell surface; however, the remaining clones (15 clones of 19 clones) obtained through conventional bio-panning alone showed poor biological-related function against the FGFR3-overexpressing cells.

In summary, we optimized the semi-automated cell panning method and then introduced an additional process to enrich binders that have specific binding properties with natural conformation of cell surface protein. It was applied to efficiently select FGFR3-specific antibodies that have binding specificity and biologically relevant function. Finally, we selected a clone that showed anti-tumor effects and FGFR3 degradation against FGFR3-overexpressing cells. This method may be an efficient screening tool for isolating clones that recognize membrane protein structure and have biological functions in antibody discovery

through phage display. Furthermore, it has the potential to extend cell panning procedure to HTS systems and fully automated systems.

4. Materials and Methods

4.1. Immobilization of Cells Using Biotin-X-DHPE and Coated Magnetic Beads

PDCs (Glioblastoma, GBM) were dispensed into the tubes at a density of 5.0×10^5 cells/mL. The cells were centrifuged at 1500 rpm for 3 min with 1% FBS (in PBS, pH 7.4, Thermo Fisher Scientific, Waltham, MA, USA) and washed twice to remove the supernatant. Fluorescein DHPE (N-(Fluorescein-5-Thiocarbamoyl)-1,2-Dihexadecanoyl-sn-Glycero-3-Phosphoethanolamine, Triethylammonium Salt, Invitrogen, F362, Carlsbad, CA, USA) or biotin-X-DHPE (1,2-dihexadecanoyl-sn-glycero-3-phosphoethanolamine, Invitrogen, B1550, Carlsbad, CA, USA), a cell membrane-like substance, was incubated with the cells to attach magnetic beads to the surface of living cells in a rotator at room temperature or 37 °C for 30 or 60 min. Cells labeled with biotin-X-DHPE were further incubated with Streptavidin-FITC (Invitrogen, SA1001, Carlsbad, CA, USA), which has biotin-specific binding force, at 4 °C for 1 h and washed twice with 1% FBS wash buffer. Flow cytometry (BD FACSAria™ III Cell Sorter) was used to analyze whether biotin-X-DHPE was fused to the cell surface. To attach magnetic beads to cells labeled with biotin-X-DHPE, 2 mg of Dynabeads™ M-280 Streptavidin (Invitrogen, 11206D, Carlsbad, CA, USA) was washed twice in PBS using a magnetic separation rack and incubated with the cells at room temperature for 1 h. After the reaction, the cells were washed through a magnetic separation rack and observed using a microscope to confirm whether the cells were attached to the biotin-X-DHPE and the magnetic beads complex.

4.2. Optimization of Cell Immobilization Conditions

The direct beads mounting method is as follows: 3 μg of biotin-X-DHPE and 200 μg of Dynabeads™ M-280 Streptavidin were first incubated at room temperature for 30 min and then isolated using a magnetic separation rack to form biotin-X-DHPE-magnetic beads complex. Then, the complex was incubated with 1.0×10^6 to 5.0×10^6 living cells in a rotor at room temperature for 1 h and then the washing was performed to isolate the immobilized cells.

The indirect beads mounting method is as follows: 3 μg of biotin-X-DHPE was incubated with living cells using a rotor at room temperature for 30 min and then washed. The pre-washed Dynabeads™ M-280 Streptavidin was then incubated with cells labeled with biotin-X-DHPE to attach the beads to the cell surface.

To increase the efficiency of attachment between cells and magnetic beads, reaction conditions were optimized using PBS (pH 7.4), 2 mM EDTA/0.1% BSA, and 0.1% Pluronic F-68 (Gibco, 24040032, Carlsbad, CA, USA).

4.3. Bio-Panning Using Phage Display

Bio-panning for FGFR3-specific antibody screening was performed using the synthetic human scFv library [29]. Conventional bio-panning using the recombinant FGFR3-Fc tagged protein was performed using two methods: magnetic beads-based semi-automated bio-panning (solution phase) and immobilized antigen coating bio-panning (solid phase). In the case of the magnetic beads-based semi-automated bio-panning method, the recombinant FGFR3-Fc protein (R&D systems, 766-FR-050, Minneapolis, MN, USA) was biotinylated using Biotinylation kit (Abcam, ab201796, Cambridge, UK) and then a magnetic particle processor (Thermo Fisher Scientific, KingFisher™ Flex, Waltham, MA, USA) was used to perform semi-automated bio-panning. This automatic process was performed according to the protocol pre-designed through BindIt Software 3.3 and repeated five times to amplify the FGFR3-specific scFv binder pool. For the immobilized antigen coating method, the immuno-tube was coated with 3 μg each of recombinant FGFR3-Fc tagged protein and recombinant negative-Fc tagged protein. To remove the scFv binder that binds to the Fc tag through negative selection, the phage library pool was first incubated on an immuno-tube coated with a negative-Fc tagged protein. The supernatant was further

incubated on the immuno-tube coated with the FGFR3-Fc tagged protein to obtain scFv binders specifically binding to FGFR3. The scFv binder pool that specifically binds to FGFR3 was amplified by performing four rounds of bio-panning.

4.4. Semi-Automated Cell Panning Using Immobilized Cells

Semi-automated cell panning was performed using beads-attached cells to rapidly isolate clones that bind to the surface of FGFR3-overexpressing cells from output of the previous two conventional bio-panning methods. First, the rescued phage pool was incubated with the FGFR3-negative cells and Streptavidin-coated magnetic beads for negative selection and only the supernatant was collected using a centrifuge. The recovered phage pool was placed in a 24-deep-well plate of KingFisher™ Flex, and approximately 1.0×10^6 to 2.0×10^6 of FGFR3-overexpressing cells labeled by biotin-X-DHPE and Streptavidin-coated magnetic beads were added into a dedicated plate (24-deep well) of an automated magnetic particle processor. Wash buffer (0.1% PBST), followed by elution buffer, was also added to the plates, and semi-automated cell panning was then performed using the pre-designed BindIt Software 3.3 protocol. From the phage pool recovered by semi-automated cell panning, clones which specifically bind to the FGFR3 protein but not the negative protein were isolated via affinity ELISA analysis for scFv screening.

4.5. 3D-Structure Modeling and Alignment Analysis of Anti-FGFR3 Antibodies

Structure-based prediction and design for antibody engineering were performed using a web-server called SAbPred [37]. This tool annotates antibody sequences, which are required for both heavy and light chains for modeling paired antibody, and automatically generates a homology model of the antibody Fv region. Six antibody sequences were selected for this study. The putative Fv model was annotated and refined into the region of CDR-H3 or not by using PyMOL.

Structural alignment was performed using a multi-protein structure alignment server called POSA, which uses multiple flexible structural alignment [38,39]. Fv models (PBD IDs) of six clones were submitted, and RMSD values and visualization modeling were verified based on the alignment results. Finally, annotation and refinement were performed using PyMoL.

4.6. IgG Reformatting and Production of Anti-FGFR3 Antibodies

The antibody variable region of isolated FGFR3-specific scFv was analyzed using phagemid vectors. The variable region sequences of heavy chain (IgG1) or light chain isolated from phagemid vectors were inserted into each mammalian expression vectors, respectively. Anti-FGFR3 antibodies were produced using the Expi293 transient mammalian expression system (Gibco, A14635, Carlsbad, CA, USA) through co-transfection of the above-mentioned vectors. Following transfection, the culture supernatant was purified using the ÄKTA protein purification system (GE Healthcare Life Sciences, Uppsala, Sweden) with HiTrap Mabselect SuRe (GE Healthcare Life Sciences, 11-0034-93, Uppsala, Sweden). After purification, enrichment was performed with Amicon® Ultra Centrifugal Filter (Merck Millipore, MA, USA). The characteristics of the highly purified antibodies were analyzed using SDS-PAGE and SEC-HPLC.

4.7. ELISA Binding Assay

One microgram per milliliter of each human (FGFR3-IIIb and -IIIc) (R&D systems, 1264-FR-050, Minneapolis, MN, USA), mouse (R&D systems, 710-MF-050, Minneapolis, MN, USA), and cynomolgus FGFR3 (Sino Biological, 90313-C02H, Beijing, China) protein was coated on 96-well EIA/RIA plates (Costar, #3590, Corning, NY, USA) at 4 °C for over-night, respectively. The plates were blocked with 3% skim milk containing anti-FGFR3-antibodies and incubated for 1 h at room temperature. After washing with PBST (0.1%), the anti-human Fab antibody-conjugated horseradish peroxidase (HRP) (Thermo Scientific, 31482, Waltham, MA, USA) was added at a ratio of 1:3000 in 3% skim milk. Following the wash,

the plate was treated with TMB solution (Thermo Scientific, N301, Waltham, MA, USA) as an HRP substrate, and the reaction was stopped with STOP solution (Cell Signaling Technology, #7002, Danvers, MA, USA). The absorbance for each well was detected at 450 nm wavelength with an Infinite® M200 pro (Tecan, Männedorf, Switzerland).

4.8. Surface Plasmon Resonance Analysis

The binding affinity (KD values) of anti-FGFR3 antibodies was measured using Biacore 3000 (GE Healthcare Life Sciences, Uppsala, Sweden). The human (FGFR3-IIIb and -IIIc), mice, and cynomolgus FGFR3 proteins were immobilized on a Sensor Chip CM5 (GE Healthcare Life Sciences, 29149604, Uppsala, Sweden) with Amine coupling kit (GE Healthcare Life Sciences, BR100050, Uppsala, Sweden). The KD (Ka and Kd) value was assessed according to the concentration gradient of antibodies.

4.9. Cell Binding Analysis Using Flow Cytometry

Binding efficiency of phage pools to FGFR3-overexpressing cells was determined using flow cytometry (BD Biosciences, FACSAria III, Mountainview, CA, USA). The phage pools (approximately 5.0×10^{12} phage particles) precipitated with PEG were titrated in advance and blocked using 1% BSA at room temperature for 1 h. FGFR3-overexpressing cells at a density of approximately 3.0×10^5 to 5.0×10^5 cells/mL were washed in eBioscience™ Flow Cytometry Staining Buffer (Invitrogen, 00-4222-57, Carlsbad, CA, USA) and then incubated with pre-blocked phage pool at 4 °C for 1 h. After washing twice with a staining buffer, anti-HA tag antibody (Cell signaling technology, # 3724S, Danvers, MA, USA) was diluted 1:800 in a staining buffer and incubated at 4 °C for 1 h. After washing, goat anti-Rabbit IgG (H+L) cross-adsorbed secondary antibody conjugated with Alexa Fluor 488 (Invitrogen, A-11008, Carlsbad, CA, USA) was diluted 1:200 in a staining buffer and incubated for 30 min at 4 °C. The binding pattern of phage pools was analyzed using flow cytometry.

The cell-surface-binding efficiency of anti-FGFR3 antibodies was analyzed using flow cytometry. About 3.0×10^5 to 5.0×10^5 FGFR3-overexpressing or FGFR3 negative cells were incubated with anti-FGFR3 antibodies with 200 nM at 4 °C for 1 h. After washing twice with eBioscience™ Flow Cytometry Staining Buffer, the cells were stained with the goat anti-human IgG (H+L) cross-adsorbed secondary antibody conjugated with Alexa Fluor 488 (Invitrogen, A-11013, Carlsbad, CA, USA) diluted 1:200 in staining buffer at 4 °C for 30 min. Mean fluorescence intensity was analyzed by flow cytometry.

4.10. Assessment of Cell Growth

FGFR3-overexpressing cell were seeded with FGF1 ligand (10 ng/mL) plus heparin sulfate (10 μg/mL) in a 96-well plate at a density of 20,000 cells/well and incubated with 500 nM anti-FGFR3 antibodies for 96 h. The cell growth was assessed using an Ez-Cytox cell viability assay kit (DAEIL Lab, EZ-1000, Seoul, Korea) at an optical density of 450 nm using a microplate reader.

4.11. Target Degradation Assay

FGFR3 degradation of the selected antibody was confirmed by analyzing the FGFR3 on the cell surface following antibody treatment. FGFR3-overexpressing cells (3.0×10^5) were incubated with 100 nM of anti-FGFR3-antibodies for 2 h at 37 °C. After washing with 1% FBS (pH 7.4, PBS), the cells were stained with human FGFR3 PE-conjugated antibody (R&D systems, FAB766P, Minneapolis, MN, USA) and the FGFR3 expression level on the cell surface was analyzed by FACS analysis.

FGFR3 degradation through total FGFR3 comparison of cells was determined using solid phase sandwich ELISA. Approximately 5000 to 10,000 FGFR3-overexpressing cells were cultivated on a 96-well plate, treated with 200 nM of anti-FGFR3 antibodies, and then incubated at 37 °C for 1 h. The cells were centrifuged to remove the supernatant and lysed with cOmplete™ Lysis-M buffer (Roche Diagnostics, 04719956001, Mannheim,

Germany). The lysate was quantified and analyzed using sandwich ELISA at an optical density of 450 nm using human total FGFR3 DuoSet IC ELISA (R&D systems, DYC766-2, Minneapolis, MN, USA).

4.12. Statistical Data Analysis

All statistical analysis were performed using Graph Pad Prism software (GraphPad Software, Inc., La Jolla, CA, USA). One-way ANOVA using paired t-test was used to compare two or more data sets and the statistical significance was set at p-value < 0.03.

4.13. Ethical Statement

GBM specimens were obtained from patients undergoing surgery based on consent in accordance with the appropriate Institutional Review Boards. The study was approved by the Institutional Review Board of Samsung Medical Center (IRB No. 2010-04-004) and performed in accordance with the principles of the Declaration of Helsinki. Written informed consents were obtained.

5. Patent

A patent application has been filed in South Korea (application number: 10-2019-0125222).

Supplementary Materials: The following are available online at https://www.mdpi.com/article/10.3390/ijms22126240/s1.

Author Contributions: Conceptualization, B.M., D.-H.N. and Y.Y.; methodology, B.M. and M.Y.; software, B.M.; validation, B.M., M.Y. and M.C.; formal analysis, B.M. and H.K.; investigation, B.M., M.Y. and M.C.; resources, D.-H.N. and Y.Y.; data curation, D.-H.N. and Y.Y.; writing—original draft preparation, B.M., Y.Y.; writing—review and editing, B.M., H.K. and Y.Y.; visualization, B.M.; supervision, D.-H.N. and Y.Y.; project administration, D.-H.N. and Y.Y.; funding acquisition, D.-H.N. and Y.Y. All authors have read and agreed to the published version of the manuscript.

Funding: This research was supported by a grant from the Korea Health Technology R&D through the Korea Health Industry Development Institute, funded by the Ministry of Health & Welfare, Republic of Korea (HI14C3418). This research was supported by the Bio & Medical Technology Development Program of the National Research Foundation (NRF) funded by the Korean government (MSIT) (No. 2017M3A9C8064720).

Institutional Review Board Statement: The study was conducted according to the guidelines of the Declaration of Helsinki, and approved by the Institutional Review Board (or Ethics Committee) of the Institutional Review Board of Samsung Medical Center (IRB No. 2010-04-004).

Informed Consent Statement: Informed consent was obtained from all subjects involved in the study.

Data Availability Statement: Not applicable.

Acknowledgments: This research was partly supported by Basic Science Research Program through the National Research Foundation of Korea (NRF) funded by the Ministry of Education (2020R1I1A1A01075559).

Conflicts of Interest: D.-H.N. and B.M. are the inventors of IP for "Method of Biopanning Using Magnetic Bead attached cell". D.-H.N. is the CTO of AimedBio Inc. and owns shares of AimedBio Inc. which owns IP. B.M., M.Y. and M.C. are under paid employment by AimedBio Inc. and owns shares of AimedBio Inc. which owns IP. The other authors declare that they have no competing interests.

References

1. Smith, G.P. Filamentous fusion phage: Novel expression vectors that display cloned antigens on the virion surface. *Science* **1985**, *228*, 1315. [CrossRef]
2. Bradbury, A.R.; Sidhu, S.; Dubel, S.; McCafferty, J. Beyond natural antibodies: The power of in vitro display technologies. *Nat. Biotechnol.* **2011**, *29*, 245–254. [CrossRef]
3. Alfaleh, M.A.; Jones, M.L.; Howard, C.B.; Mahler, S.M. Strategies for Selecting Membrane Protein-Specific Antibodies Using Phage Display with Cell-Based Panning. *Antibodies* **2017**, *6*, 10. [CrossRef]

4. Solemani Zadeh, A.; Grasser, A.; Dinter, H.; Hermes, M.; Schindowski, K. Efficient Construction and Effective Screening of Synthetic Domain Antibody Libraries. *Methods Protoc.* **2019**, *2*, 17. [CrossRef]
5. Wilson, H.D.; Li, X.; Peng, H.; Rader, C. A Sortase A Programmable Phage Display Format for Improved Panning of Fab Antibody Libraries. *J. Mol. Biol.* **2018**, *430*, 4387–4400. [CrossRef] [PubMed]
6. Parmley, S.F.; Smith, G.P. Antibody-selectable filamentous fd phage vectors: Affinity purification of target genes. *Gene* **1988**, *73*, 305–318. [CrossRef]
7. Zhao, A.; Tohidkia, M.R.; Siegel, D.L.; Coukos, G.; Omidi, Y. Phage antibody display libraries: A powerful antibody discovery platform for immunotherapy. *Crit. Rev. Biotechnol.* **2016**, *36*, 276–289. [CrossRef] [PubMed]
8. Lerner, R.A. Combinatorial antibody libraries: New advances, new immunological insights. *Nat. Rev. Immunol.* **2016**, *16*, 498–508. [CrossRef] [PubMed]
9. Bazan, J.; Calkosinski, I.; Gamian, A. Phage display—A powerful technique for immunotherapy: 1. Introduction and potential of therapeutic applications. *Hum. Vaccin. Immunother.* **2012**, *8*, 1817–1828. [CrossRef]
10. Griffiths, A.D.; Duncan, A.R. Strategies for selection of antibodies by phage display. *Curr. Opin. Biotechnol.* **1998**, *9*, 102–108. [CrossRef]
11. Pacheco, S.; Soberón, M. Phage display: Fundamentals and applications. *Transw. Res. Netw.* **2012**, *9*, 143–161.
12. Nikfarjam, S.; Tohidkia, M.R.; Mehdipour, T.; Soleimani, R.; Rahimi, A.A.R.; Nouri, M. Successful Application of Whole Cell Panning for Isolation of Phage Antibody Fragments Specific to Differentiated Gastric Cancer Cells. *Adv. Pharm. Bull.* **2019**, *9*, 624–631. [CrossRef]
13. Hoogenboom, H.R. Selecting and screening recombinant antibody libraries. *Nat. Biotechnol.* **2005**, *23*, 1105–1116. [CrossRef] [PubMed]
14. Heitner, T.; Moor, A.; Garrison, J.L.; Marks, C.; Hasan, T.; Marks, J.D. Selection of cell binding and internalizing epidermal growth factor receptor antibodies from a phage display library. *J. Immunol. Methods* **2001**, *248*, 17–30. [CrossRef]
15. Lipes, B.D.; Chen, Y.-H.; Ma, H.; Staats, H.F.; Kenan, D.J.; Gunn, M.D. An Entirely Cell-Based System to Generate Single-Chain Antibodies against Cell Surface Receptors. *J. Mol. Biol.* **2008**, *379*, 261–272. [CrossRef]
16. Ishizuka-Katsura, Y.; Wazawa, T.; Ban, T.; Morigaki, K.; Aoyama, S. Biotin-containing phospholipid vesicle layer formed on self-assembled monolayer of a saccharide-terminated alkyl disulfide for surface plasmon resonance biosensing. *J. Biosci. Bioeng.* **2008**, *105*, 527–535. [CrossRef]
17. Turunen, L.; Takkinen, K.; Soderlund, H.; Pulli, T. Automated panning and screening procedure on microplates for antibody generation from phage display libraries. *J. Biomol. Screen.* **2009**, *14*, 282–293. [CrossRef]
18. Hornsby, M.; Paduch, M.; Miersch, S.; Sääf, A.; Matsuguchi, T.; Lee, B.; Wypisniak, K.; Doak, A.; King, D.; Usatyuk, S.; et al. A High Through-put Platform for Recombinant Antibodies to Folded Proteins. *Mol. Cell Proteom.* **2015**, *14*, 2833–2847. [CrossRef] [PubMed]
19. Dominik, P.K.; Kossiakoff, A.A. Phage display selections for affinity reagents to membrane proteins in nanodiscs. *Methods Enzymol.* **2015**, *557*, 219–245.
20. Cappellen, D.; De Oliveira, C.; Ricol, D.; de Medina, S.; Bourdin, J.; Sastre-Garau, X.; Chopin, D.; Thiery, J.P.; Radvanyi, F. Frequent activating mutations of FGFR3 in human bladder and cervix carcinomas. *Nat. Genet.* **1999**, *23*, 18–20. [CrossRef]
21. Chesi, M.; Brents, L.A.; Ely, S.A.; Bais, C.; Robbiani, D.F.; Mesri, E.A.; Kuehl, W.M.; Bergsagel, P.L. Activated fibroblast growth factor receptor 3 is an oncogene that contributes to tumor progression in multiple myeloma. *Blood* **2001**, *97*, 729–736. [CrossRef]
22. Hernández, S.; de Muga, S.; Agell, L.; Juanpere, N.; Esgueva, R.; Lorente, J.A.; Mojal, S.; Serrano, S.; Lloreta, J. FGFR3 mutations in prostate cancer: Association with low-grade tumors. *Mod. Pathol.* **2009**, *22*, 848–856. [CrossRef]
23. di Martino, E.; L'Hôte, C.G.; Kennedy, W.; Tomlinson, D.C.; Knowles, M.A. Mutant fibroblast growth factor receptor 3 induces intracellular signaling and cellular transformation in a cell type- and mutation-specific manner. *Oncogene* **2009**, *28*, 4306–4316. [CrossRef]
24. Turner, N.; Grose, R. Fibroblast growth factor signalling: From development to cancer. *Nat. Rev. Cancer* **2010**, *10*, 116–129. [CrossRef]
25. Kalff, A.; Spencer, A. The t(4;14) translocation and FGFR3 overexpression in multiple myeloma: Prognostic implications and current clinical strategies. *Blood Cancer J.* **2012**, *2*, e89. [CrossRef]
26. Qing, J.; Du, X.; Chen, Y.; Chan, P.; Li, H.; Wu, P.; Marsters, S.; Stawicki, S.; Tien, J.; Totpal, K.; et al. Antibody-based targeting of FGFR3 in bladder carcinoma and t(4;14)-positive multiple myeloma in mice. *J. Clin. Investig.* **2009**, *119*, 1216–1229. [CrossRef] [PubMed]
27. Gust, K.M.; McConkey, D.J.; Awrey, S.; Hegarty, P.K.; Qing, J.; Bondaruk, J.; Ashkenazi, A.; Czerniak, B.; Dinney, C.P.; Black, P.C. Fibroblast growth factor receptor 3 is a rational therapeutic target in bladder cancer. *Mol. Cancer Ther.* **2013**, *12*, 1245–1254. [CrossRef] [PubMed]
28. Yin, Y.; Ren, X.; Smith, C.; Guo, Q.; Malabunga, M.; Guernah, I.; Zhang, Y.; Shen, J.; Sun, H.; Chehab, N.; et al. Inhibition of fibroblast growth factor receptor 3-dependent lung adenocarcinoma with a human monoclonal antibody. *Dis. Models Mech.* **2016**, *9*, 563–571. [CrossRef] [PubMed]
29. Yang, H.; Kang, K.; Tcw, J.; Shim, H. Construction of a large synthetic human scFv library with six diversified CDRs and high functional diversity. *Mol. Cells* **2009**, *27*, 225–235. [CrossRef] [PubMed]

30. Kabat, E.A.; Wu, T.T. Attempts to Locate complementarity-determining residues in the variable positions of light and heavy chains. *Ann. N. Y. Acad. Sci.* **1971**, *190*, 382–393. [CrossRef]
31. Kabat, E.A.; Wu, T.T.; Bilofsky, H. Unusual distributions of amino acids in complementarity-determining (hypervariable) segments of heavy and light chains of immunoglobulins and their possible roles in specificity of antibody-combining sites. *J. Biol. Chem.* **1977**, *252*, 6609–6616. [CrossRef]
32. Kabat, E.A.; Te Wu, T.; Bilofsky, H. *Sequences of Immunoglobulin Chains: Tabulation and Analysis of Amino Acid Sequences of Precursors, V-Regions, C-Regions, J-Chain and BP-Microglobulins*; National Institute of Health: Bethesda, MD, USA, 1979.
33. Shirai, H.; Kidera, A.; Nakamura, H. H3-rules: Identification of CDR-H3 structures in antibodies. *FEBS Lett.* **1999**, *455*, 188–197. [CrossRef]
34. Shirai, H.; Kidera, A.; Nakamura, H. Structural classification of CDR-H3 in antibodies. *FEBS Lett.* **1996**, *399*, 1–8. [CrossRef]
35. Weitzner, B.D.; Dunbrack, R.L.; Gray, J.J. The Origin of CDR H3 Structural Diversity. *Structure* **2015**, *23*, 302–311. [CrossRef]
36. Tsuchiya, Y.; Mizuguchi, K. The diversity of H3 loops determines the antigen-binding tendencies of antibody CDR loops. *Protein Sci.* **2016**, *25*, 815–825. [CrossRef]
37. Dunbar, J.; Krawczyk, K.; Leem, J.; Marks, C.; Nowak, J.; Regep, C.; Georges, G.; Kelm, S.; Popovic, B.; Deane, C.M. SAbPred: A structure-based antibody prediction server. *Nucleic Acids Res.* **2016**, *44*, W474–W478. [CrossRef]
38. Li, Z.; Natarajan, P.; Ye, Y.; Hrabe, T.; Godzik, A. POSA: A user-driven, interactive multiple protein structure alignment server. *Nucleic Acids Res.* **2014**, *42*, W240–W245. [CrossRef] [PubMed]
39. Ye, Y.; Godzik, A. Multiple flexible structure alignment using partial order graphs. *Bioinformatics* **2005**, *21*, 2362–2369. [CrossRef] [PubMed]
40. Carugo, O. How root-mean-square distance (r.m.s.d.) values depend on the resolution of protein structures that are compared. *J. Appl. Crystallogr.* **2003**, *36*, 125–128. [CrossRef]
41. Huang, R.; Kiss, M.M.; Batonick, M.; Weiner, M.P.; Kay, B.K. Generating Recombinant Antibodies to Membrane Proteins through Phage Display. *Antibodies* **2016**, *5*, 11. [CrossRef]
42. Eisenhardt, S.U.; Schwarz, M.; Bassler, N.; Peter, K. Subtractive single-chain antibody (scFv) phage-display: Tailoring phage-display for high specificity against function-specific conformations of cell membrane molecules. *Nat. Protoc.* **2007**, *2*, 3063–3073. [CrossRef] [PubMed]
43. Popkov, M.; Rader, C.; Barbas, C.F., 3rd. Isolation of human prostate cancer cell reactive antibodies using phage display technology. *J. Immunol. Methods* **2004**, *291*, 137–151. [CrossRef]
44. Siva, A.C.; Kirkland, R.E.; Lin, B.; Maruyama, T.; McWhirter, J.; Yantiri-Wernimont, F.; Bowdish, K.S.; Xin, H. Selection of anti-cancer antibodies from combinatorial libraries by whole-cell panning and stringent subtraction with human blood cells. *J. Immunol. Methods* **2008**, *330*, 109–119. [CrossRef]
45. Giordano, R.J.; Cardo-Vila, M.; Lahdenranta, J.; Pasqualini, R.; Arap, W. Biopanning and rapid analysis of selective interactive ligands. *Nat. Med.* **2001**, *7*, 1249–1253. [CrossRef] [PubMed]
46. Fitting, J.; Blume, T.; Ten Haaf, A.; Blau, W.; Gattenlohner, S.; Tur, M.K.; Barth, S. Phage display-based generation of novel internalizing antibody fragments for immunotoxin-based treatment of acute myeloid leukemia. *MAbs* **2015**, *7*, 390–402. [CrossRef] [PubMed]
47. Sorensen, M.D.; Kristensen, P. Selection of antibodies against a single rare cell present in a heterogeneous population using phage display. *Nat. Protoc.* **2011**, *6*, 509–522. [CrossRef] [PubMed]
48. Jones, M.L.; Alfaleh, M.A.; Kumble, S.; Zhang, S.; Osborne, G.W.; Yeh, M.; Arora, N.; Hou, J.J.; Howard, C.B.; Chin, D.Y.; et al. Targeting membrane proteins for antibody discovery using phage display. *Sci. Rep.* **2016**, *6*, 26240. [CrossRef]
49. A Study of LY3076226 in Participants with Advanced or Metastatic Cancer. Clinical Trial Identification Number: NCT02529553. Available online: https://clinicaltrials.gov/ct2/show/NCT02529553 (accessed on 1 February 2021).
50. Dose Escalation, Expansion Study of Vofatamab (B-701) in Treatment of Locally Advanced or Metastatic Urothelial Cell Carcinoma (FIERCE-21). Clinical Trial Identification Number: NCT02401542. Available online: https://clinicaltrials.gov/ct2/show/NCT02401542 (accessed on 1 February 2021).
51. A Study of B-701 in Combination with Pembrolizumab in Treatment of Locally Advanced or Metastatic Urothelial Cell Carcinoma (FIERCE-22). Clinical Trial Identification Number: NCT03123055. Available online: https://clinicaltrials.gov/ct2/show/NCT03123055 (accessed on 1 February 2021).

International Journal of
Molecular Sciences

MDPI

Article

Candida Cell-Surface-Specific Monoclonal Antibodies Protect Mice against *Candida auris* Invasive Infection

Jonothan Rosario-Colon, Karen Eberle, Abby Adams, Evan Courville and Hong Xin *

Department of Microbiology, Immunology, and Parasitology, Louisiana State University—Health Sciences Center, New Orleans, LA 70112, USA; jcolo1@lsuhsc.edu (J.R.-C.); keberl@lsuhsc.edu (K.E.); abbya@lsu.edu (A.A.); ecour2@lsuhsc.edu (E.C.)
* Correspondence: hxin@lsuhsc.edu; Tel.: +1-504-568-8121

Abstract: *Candida auris* is a multidrug-resistant fungal pathogen that can cause disseminated bloodstream infections with up to 60% mortality in susceptible populations. Of the three major classes of antifungal drugs, most *C. auris* isolates show high resistance to azoles and polyenes, with some clinical isolates showing resistance to all three drug classes. We reported in this study a novel approach to treating *C. auris* disseminated infections through passive transfer of monoclonal antibodies (mAbs) targeting cell surface antigens with high homology in medically important *Candida* species. Using an established A/J mouse model of disseminated infection that mimics human candidiasis, we showed that C3.1, a mAb that targets β-1,2-mannotriose (β-Man_3), significantly extended survival and reduced fungal burdens in target organs, compared to control mice. We also demonstrated that two peptide-specific mAbs, 6H1 and 9F2, which target hyphal wall protein 1 (Hwp1) and phosphoglycerate kinase 1 (Pgk1), respectively, also provided significantly enhanced survival and reduction of fungal burdens. Finally, we showed that passive transfer of a 6H1+9F2 cocktail induced significantly enhanced protection, compared to treatment with either mAb individually. Our data demonstrate the utility of β-Man_3- and peptide-specific mAbs as an effective alternative to antifungals against medically important *Candida* species including multidrug-resistant *C. auris*.

Keywords: *C. auris*; candidiasis; multidrug resistance; monoclonal antibodies; universal antibodies; cell wall; passive immunization

Citation: Rosario-Colon, J.; Eberle, K.; Adams, A.; Courville, E.; Xin, H. *Candida* Cell-Surface-Specific Monoclonal Antibodies Protect Mice against *Candida auris* Invasive Infection. *Int. J. Mol. Sci.* **2021**, *22*, 6162. https://doi.org/10.3390/ijms22116162

Academic Editors: Annamaria Sandomenico and Menotti Ruvo

Received: 11 May 2021
Accepted: 3 June 2021
Published: 7 June 2021

1. Introduction

Candida auris is an emerging fungal pathogen first identified in Tokyo, Japan in 2009 [1]. It has since emerged throughout much of the world, with many countries reporting multiple clinical cases [2]. Unlike other pathogenic *Candida* species, *C. auris* has a propensity to colonize abiotic surfaces as well as the human skin [3]. This makes the nosocomial spread of the pathogen especially prevalent and contributes to a higher potential to disseminate into bloodstream infections compared to other *Candida* species. Consequently, ICU patients and nursing home residents are highly vulnerable to nosocomial infections with *C. auris*, and migration from the skin to a disseminated bloodstream infection is especially common in patients with underlying comorbidities, those under immunosuppressed conditions, or those who have undergone invasive surgical interventions [4,5]. This ease of spread has contributed to a slew of healthcare-associated outbreaks, with contamination of ICUs persisting for several weeks [2,6]. Furthermore, with the ongoing COVID-19 pandemic caused by the novel coronavirus, SARS-CoV-2, the rate of hospitalizations is currently extremely high. With many ICU units being filled to capacity, this creates the perfect environment for further *C. auris* ICU outbreaks [7–9]. Once systemic, *C. auris* infection is often fatal, having a case mortality rate of 33–60% [4,10–12], which is much higher than that of other pathogenic *Candida* species. Mortality is most often attributed to multiorgan failure, with the kidney and heart being most susceptible [13–15].

A defining feature of *C. auris*, among other *Candida* species, is its multidrug resistance. Although antifungal resistance has been reported in other *Candida* species, most notably with *Candida glabrata*, the degree of antifungal resistance observed in *C. auris* is unprecedented [2]. In a study that looked at antifungal resistance in 99 clinical isolates of *C. auris* from the United States, 89% of isolates were resistant to fluconazole, 30% were resistant to amphotericin B, and 6% were resistant to echinocandin drugs [16]. In another study of 1385 United States clinical isolates of *C. glabrata*, 9.6% of isolates were resistant to fluconazole and 6% were resistant to echinocandin drugs [17]. Similarly, *C. auris* clinical isolates from across the globe have consistently shown high resistance to antifungals within the azole and polyene drug classes [4,18]. Being so, the typical course of treatment for *C. auris* bloodstream infections is the daily administration of echinocandin drugs, such as micafungin, caspofungin, or anidulafungin. A major limitation of antifungals, however, is their associated drug toxicities. Immunocompromised patients, who are most susceptible to disseminated infection, are in a fragile state and often unable to tolerate additional organ toxicity caused by commonly prescribed antifungal drugs, therefore rending these drugs ineffective [19]. Furthermore, there have been several reports of *C. auris* isolates that are pan-resistant to all three major antifungal drug classes, which greatly limits treatment options [4]. Due to its high degree of antifungal resistance, the potential to spread throughout the hospital environment, and its associated high mortality rate, *C. auris* is the first fungal pathogen to be labeled a serious global public health threat, and new treatments are urgently needed [20].

To overcome the problems of *C. auris* antifungal resistance and drug toxicity, we sought to investigate if prophylactic treatment using *Candida*-specific monoclonal antibodies (mAbs) could induce protection against *C. auris* bloodstream infections in A/J mice, as an alternative to conventional antifungal drug treatment. Protective mAb therapy is an emerging, yet highly promising strategy for the treatment of microbial diseases [21,22]. Antibodies are known to confer protection to various pathogens via several mechanisms, including neutralization, opsonization, and complement activation [23]. As of today, the United States Food and Drug Administration (FDA) has approved five different synthetic mAb for the treatment of various viral and bacterial diseases, including human immunodeficiency virus (HIV) and *Clostridioides difficile* infections [24]. Additionally, two new synthetic mAb-based treatments, Eli Lilly's Bamlanivimab and Regeneron's REGN-COV2 cocktail, are currently in clinical trials and have shown promising efficacy against COVID-19 [25], and the FDA has approved both drugs for emergency use authorization (EUA) [26,27]. Presently, there are no mAb-derived drugs for the treatment of fungal diseases, even within clinical trials. Particularly with pathogens such as *C. auris*, which have developed high levels of drug resistance and cause high mortality in immunocompromised patients, mAb therapy is an attractive treatment option.

Since the cell wall is the first point of contact between *Candida* and the host's immune system, we developed "universal mAbs" that target various *Candida* cell wall epitopes that share high homology among various *Candida* species. A major benefit of universal mAbs is that they could potentially be applied for the treatment of candidemia caused by multiple pathogenic species of *Candida*, such as *Candida albicans*, *Candida glabrata*, *Candida tropicalis*, *Candida krusei*, and *C. auris*. This is especially important because infected individuals often do not receive a timely diagnosis due to unspecific symptoms of invasive candidiasis.

Overall, we hypothesized that prophylactic treatment with universal mAbs would induce extended survival and enhanced fungal clearance within an A/J mouse model of *C. auris* disseminated infection. A/J mice are deficient in complement protein C5 and its cleaved product C5a, a pro-inflammatory chemoattractant important for anti-*Candida* protection [28–30]. This renders A/J mice highly susceptible to *C. auris* disseminated infection without the need for immunosuppressive drugs [31]. Using this model, we identified three mAbs that provided significant protection, as evidenced by extended survival and lower fungal burdens in the kidney, brain, and heart, compared to control mice. In addition, our results showed that two of our mAbs could be administered as a cocktail to further

enhance their effectiveness. Overall, our results demonstrate the efficacy of passive transfer with universal mAbs as a novel treatment against multidrug-resistant *C. auris*.

2. Results

2.1. In Vitro and In Vivo Efficacy of Antifungals against Multidrug-Resistant C. auris

C. auris isolates can be grouped into five clades (I-V) originating from different geographic regions [4]. Within each clade, isolates may have differences in morphology, levels of virulence, growth rates, and antifungal-resistance profiles [4,32]. Being so, in preparation for our animal studies, we first investigated the antifungal susceptibility of two clinical isolates of *C. auris* belonging to distinct clades: AR-0386 (CAU-06) of Clade IV and AR-0389 (CAU-09) of Clade I. AR-0386 is a highly aggregative South American isolate that has been shown to be less virulent than *C. albicans* in mouse models [33], while AR-0389 is a nonaggregative South Asian isolate that is highly virulent in mouse models [31,34]. It has been reported that nonaggregating *C. auris* isolates such as AR-0389 are among the most virulent clinical isolates, with virulence comparable to that of *C. albicans* in the invertebrate *Galleria mellonella* model [35].

We first performed an in vitro minimum inhibitory concentration (MIC) assay using two commonly administered antifungal drugs, micafungin, and itraconazole. These two antifungals belong to the echinocandin and azole drug classes, respectively, and isolates AR-0386 and AR-0389 have been reported to be susceptible to both drugs in vitro [34,36]. As a comparison, we also tested the MICs for *C. albicans* reference strain SC5314. After 48-h of drug exposure, the micafungin MIC50 was determined to be 0.063 μg/mL for AR-0386, 0.125 μg/mL for AR-0389, and 0.031 μg/mL for *C. albicans* (Table 1). For itraconazole, the 48 h MIC50 was 2.0 μg/mL for AR-0386, 0.25 μg/mL for AR-0389, and 0.031 μg/mL for *C. albicans*. These results showed that AR-0386 and AR-0389 were susceptible to micafungin and itraconazole in vitro, although both isolates were much more resistant to itraconazole than was *C. albicans*.

Table 1. Micafungin and itraconazole MIC50 for *C. auris* isolates AR-0386 and AR-0389 and *C. albicans* isolate SC5314 at 24 and 48 h.

Drug	AR-0386 MIC50 (μg/mL)		AR-0389 MIC50 (μg/mL)		SC5314 MIC50 (μg/mL)	
	24 h	48 h	24 h	48 h	24 h	48 h
Micafungin	0.031	0.063	0.063	0.125	0.031	0.031
Itraconazole	2.0	2.0	2.0	0.25	0.031	0.031

A limitation of in vitro assays is that they reflect the limited environment within the test tube, which is considerably different from the environmental conditions encountered in vivo. Being that MIC data cannot always reliably predict in vivo drug susceptibility [37], we next tested the micafungin and itraconazole susceptibility of *C. auris* using a complement C5-deficient A/J mouse model of disseminated infection [33]. To begin, we established an appropriate sublethal challenge dose that would result in 80–100% survival within 10 days post challenge using the highly virulent AR-0389 strain (Figure 1A). Our results showed that doses below 8×10^7 CFUs resulted in 100% survival by day 10. Accordingly, we decided to use a dose of 4×10^7 CFUs for our in vivo antifungal susceptibility study. After the challenge, mice were treated daily with a minimum protective dose of micafungin (0.25 mg/kg/day) or itraconazole (1.67 mg/kg/day), which were determined via an antifungal pilot study (data not shown). Upon termination on Day 6, micafungin-treated mice showed no reduction in fungal burdens in the kidney, brain, or heart compared to control mice (Figure 1B). Similarly, itraconazole provided no significant reduction in organ burdens using the minimum dose.

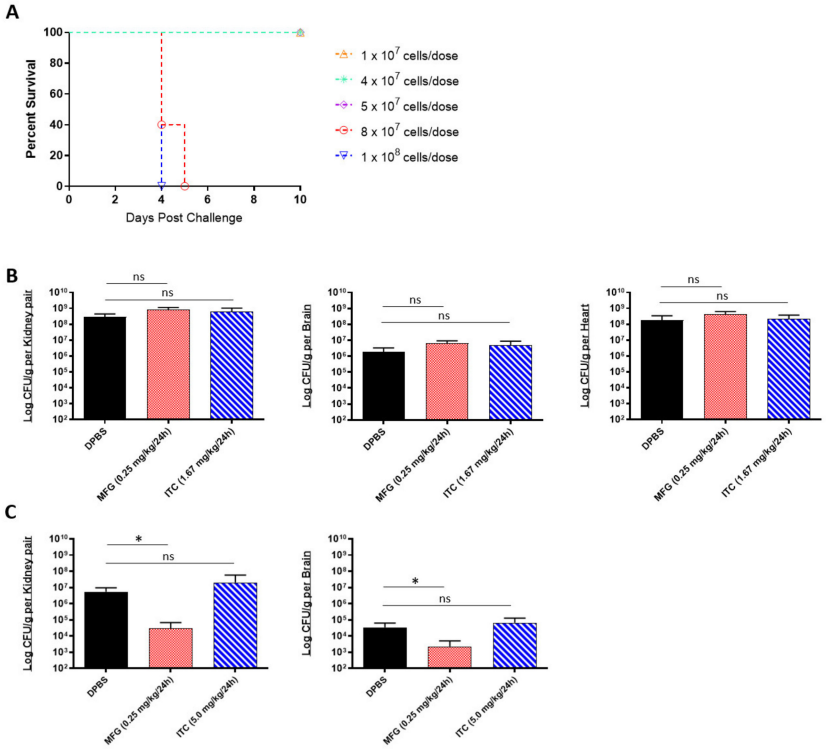

Figure 1. In vivo efficacy of antifungals against multidrug-resistant *C. auris*: (**A**) the 10-day survival curve of 7-week-old female A/J mice challenged with *C. auris* AR-0389 doses ranging from 1×10^7 to 1×10^8 CFUs; (**B**) quantification of kidney, brain, and heart fungal burdens from 7-week-old female A/J treated daily for 5 days with a minimum protective dose of micafungin or itraconazole. Mice were challenged with a sub-lethal dose of 4×10^7 CFUs of *C. auris* isolate AR-0389. Starting 24 h later, mice received daily administration of 200 µL of DPBS, micafungin (0.25 mg/kg body weight), or itraconazole (1.67 mg/kg body weight). Mice were sacrificed on day 6 post challenge; (**C**) quantification of kidney and brain fungal burdens from 16- to 17-week-old male and female neutropenic C57BL/6 mice treated daily for 14 days with a minimum protective dose of micafungin or itraconazole. To induce neutropenia, mice were administered cyclophosphamide (200 mg/kg body weight) on day 3 and every 7 days after (150-mg/kg body weight). On day 0, mice were challenged with a sublethal dose of 4×10^7 CFUs of *C. auris* isolate AR-0389. Starting 24 h later, mice received daily administration of 200 µL of DPBS, micafungin (0.25 mg/kg body weight), or itraconazole (5.0 mg/kg body weight). Mice were sacrificed on day 15 post challenge. MFG = micafungin, ITC = itraconazole. Data are mean + SD (**B**,**C**). $n = 4$ (**B**) $n = 5$ (**A**,**C**). Log-rank (Mantel–Cox) test (**A**) or two-tailed *t*-test (**B**,**C**) were used to identify significant differences. * $p < 0.05$; *ns* = not significant.

Different inbred mouse strains have differences in MHC haplotypes, immunophenotype features, and isoforms of metabolic enzymes which can contribute to varying rates of drug metabolism [38,39]. Being so, we repeated our in vivo micafungin and itraconazole susceptibility assay using an immunosuppressed C57BL/6 mouse model of disseminated infection to compare *C. auris* susceptibility to that of A/J mice. C57BL/6 mice were immunosuppressed with cyclophosphamide prior to challenge with a sub-lethal dose of *C. auris* AR-0389. Beginning 18 h post challenge, mice were administered micafungin or itraconazole daily for 14 days and then sacrificed on day 15. As with our A/J mouse model, we saw no protective effect using itraconazole, even with a higher dose (5.0 mg/kg/day) (Figure 1C). Interestingly, with the minimum dose of micafungin, we observed a significant reduction in fungal burdens in the kidney and brain (2.9×10^4 and 2.2×10^3 CFUs/g, respectively) by day 15 as compared to DPBS mice kidney and brain burdens (5.5×10^6 and 3.4×10^4 CFUs/g, respectively). Comparing these results to our MIC data showed that although *C. auris* AR-0389 is susceptible to both micafungin and itraconazole in vitro,

only low-dose micafungin was effective at significantly reducing fungal burdens in immunosuppressed C57BL/6 mice. The data showed that *C. auris* is susceptible to minimum doses of micafungin in vivo, but this could vary with mouse strain and cannot be predicted solely using in vitro MIC data.

2.2. Candida Cell Surface Binding of Universal Candida-Specific Monoclonal Antibodies

Considering that antifungals have limited efficacy against multidrug-resistant *C. auris*, we next investigated the protective efficacy of a panel of universal monoclonal antibodies (mAbs) that target different *Candida* cell surface epitopes, which share high homology among various *Candida* species (Table 2). First, we validated antibody binding to cell surface epitopes by flow cytometric analysis using *C. auris* AR-0386 and AR-0389 and *C. albicans* SC5314. We focused on three mAbs that were shown to be protective in our preliminary studies: C3.1, which targets β-1,2-mannotriose (β-Man_3, IgG3), a mannose sugar that is abundantly expressed and distributed on the outer cell wall of most *Candida* species [40,41]; 6H1, which targets hyphal wall protein 1 (Hwp1, IgG2a), a cell wall mannoprotein that is involved in adhesion, biofilm formation, and hyphal development in several *Candida* species [42]; 9F2, which targets phosphoglycerate kinase 1 (Pgk1, IgG1), a metabolic enzyme that is primarily involved in glycolysis and gluconeogenesis within the cytoplasm [43,44].

Table 2. Universal *Candida* monoclonal antibodies and their cell surface targets.

Universal Antibody	Isotype	Cell Surface Target
C3.1 (anti-β-Man_3)	IgG3	β-1,2-mannotriose
6H1 (anti-Hwp1)	IgG2b	Hyphal wall protein 1
9F2 (anti-Pgk1)	IgG2a	Phosphoglycerate kinase 1
10E7 (anti-GPV-P3)	IgG1	Phosphoglycerate kinase 1 [1]

[1] The 9F2 and 10E7 antibodies target two different epitopes on Pgk1.

Isolates were incubated with each primary mAb, washed, and then incubated with goat anti-mouse secondary antibody conjugated to Alexa Fluor 488. Antibody binding was then detected using flow cytometry (Figure 2A–C). C3.1 (anti-β-Man_3, IgG3) showed 56.6% binding to AR-0386, 98.4% binding to AR-0389, and 86.5% to *C. albicans*, while 6H1 (anti-Hwp1, IgG2b) showed binding of 38.1% to AR-0386, 2.6% to AR-0389, and 21.2% to *C. albicans*. Finally, binding of 9F2 (anti-Pgk 1, IgG2a) was at 33.0% for AR-0386, 3.4% for AR-0389, and 38.6% for *C. albicans*. Additionally, fluorescent microscopy imaging of cells stained with each antibody (Figure 2D–F) depicted levels of fluorescence that corresponded with our flow cytometry data. Since mannose sugars are abundantly expressed on the outer cell wall [40,41], a high level of C3.1 binding in all isolates was expected. Pgk1 and Hwp1, on the other hand, are not major components of the *Candida* cell wall and not as abundantly expressed as β-Man_3, which was reflected in our mAb-binding data. It was, however, surprising to see modest Hwp1 binding, since *C. auris* has not been demonstrated to express Hwp1, and its genome has not been shown to contain an ortholog of the *Hwp1* gene. This pointed to the possibility that our anti-Hwp1 mAb could be cross-reactive with another *C. auris* cell wall protein, in which further investigation is required to identify the target as well as confirm its sequence. It was also surprising to see such disparate levels of 6H1 or 9F2 binding between the two *C. auris* isolates. The lower levels of 9F2 and 6H1 binding to AR-0389 could be an indication of epitope masking, which could explain the higher level of virulence of this isolate, compared to AR-0386. Overall, the data showed that the universal mAbs bind to *C. auris* in an isolate-specific manner.

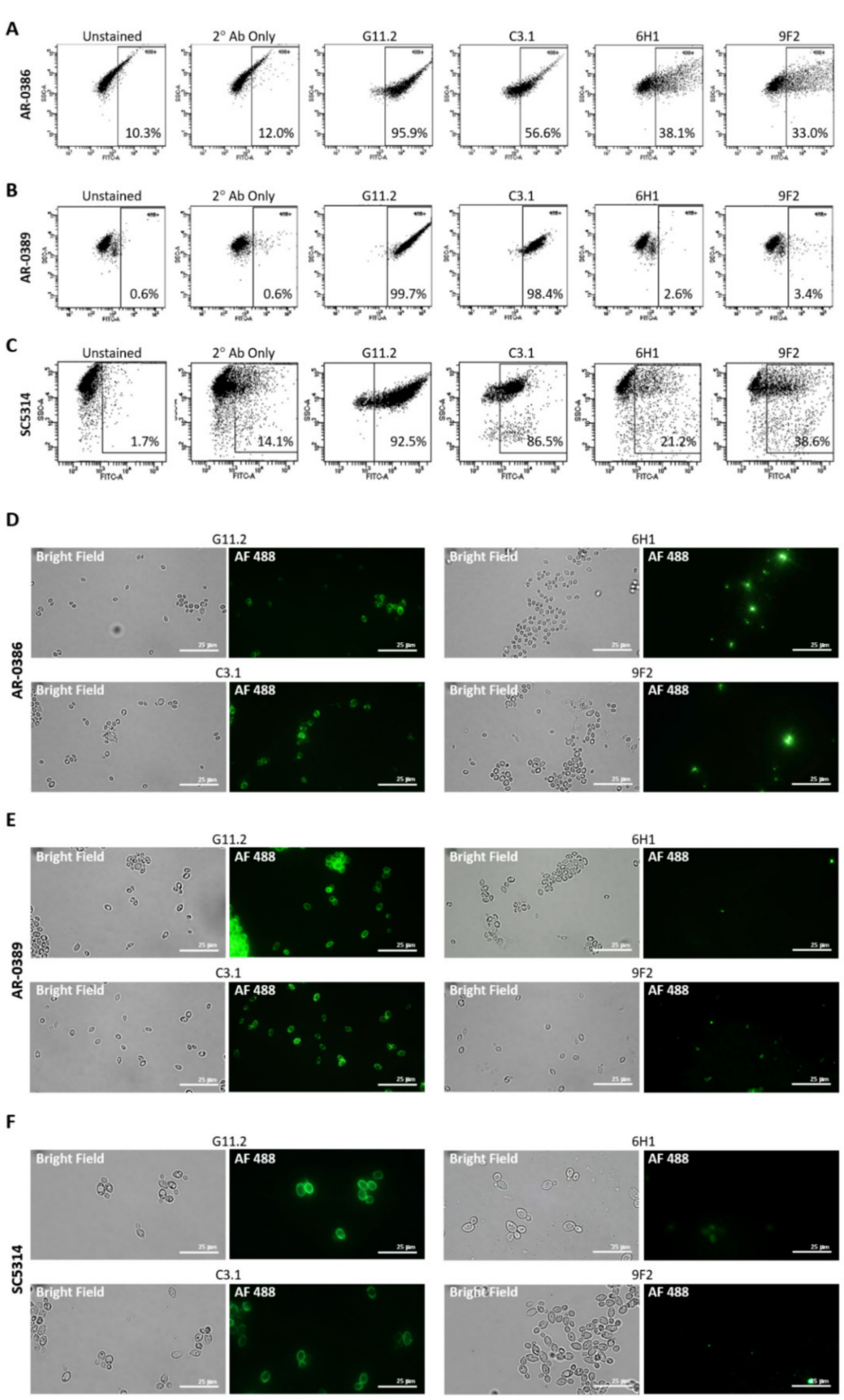

Figure 2. Cell surface binding of universal *Candida*-specific monoclonal antibodies: (**A**–**C**) flow cytometry scatter plots depicting levels of cell surface binding of monoclonal antibodies as a measure of Alexa Fluor 488 expression in (**A**) *C. auris* isolate AR-0386, (**B**) *C. auris* isolate AR-0389, and (**C**) *C. albicans* isolate SC5314; (**D**–**F**) confocal microscopy analysis (1000X) showing antibody cell surface staining of (**D**) *C. auris* isolate AR-0386, (**E**) *C. auris* isolate AR-0389, and (**F**) *C. albicans* isolate SC5314 using mAbs C3.1, 6H1, and 9F2. G11.2 = β-1,2-mannotriose (IgG1), C3.1 = β-1,2-mannotriose (IgG3), Hwp1 = hyphal wall protein 1, Pgk1 = phosphoglycerate kinase 1. Bar = 25 μm.

2.3. In Vivo Protective Efficacy of Universal Candida β-1,2-Mannotriose- and Peptide-Specific Monoclonal Antibodies

We next evaluated if the prophylactic passive transfer of our universal mAbs would protect mice against *C. auris* disseminated infection. We began with C3.1 (anti-β-Man_3, IgG3), a mAb that has previously been shown to be highly protective against *C. albicans* disseminated bloodstream infections in mice [45]. Since the *C. auris* cell wall has a high composition of β-1-2-mannans—reportedly even higher than in *C. albicans* [46], we hypothesized that mAb C3.1 would also protect against disseminated infection caused by *C. auris*. To compare the efficacy of C3.1 to that of micafungin, A/J mice were treated one time with C3.1 or DPBS or treated daily for 7 days with micafungin. 24 h after C3.1 treatment, mice were challenged with a sublethal dose of *C. auris* AR-0386. By day 35 post infection, there was a significant increase in survival of C3.1-treated mice (100% survival), compared to DPBS control mice (40% survival) (Figure 3A). Micafungin-treated mice survival (60% survival) was not significantly extended, compared to the DPBS group. When quantifying fungal burdens, C3.1-treated mice had a significant reduction in kidney and brain burdens (1.2×10^4 and 5.0×10^1 CFUs/g, respectively), compared to control mice (6.6×10^8 and 6.2×10^6 CFUs/g, respectively) (Figure 3B). Remarkably, all C3.1-treated mice had undetectable brain burdens by day 35. While there was also a reduction in heart burdens in C3.1-treated mice (8.2×10^2 CFUs/g), compared to DPBS control (4.4×10^6 CFUs/g), this change was not statistically significant. Consistent with survival data, there was no significant reduction in the kidney, brain, or heart burdens in micafungin-treated mice (2.8×10^8, 4.9×10^4, and 4.4×10^6 CFUs/g, respectively), as compared to DPBS mice. The data showed that mAb C3.1 treatment outperformed low-dose micafungin, a gold-standard drug for the treatment of invasive *C. auris* infection in an A/J mouse model.

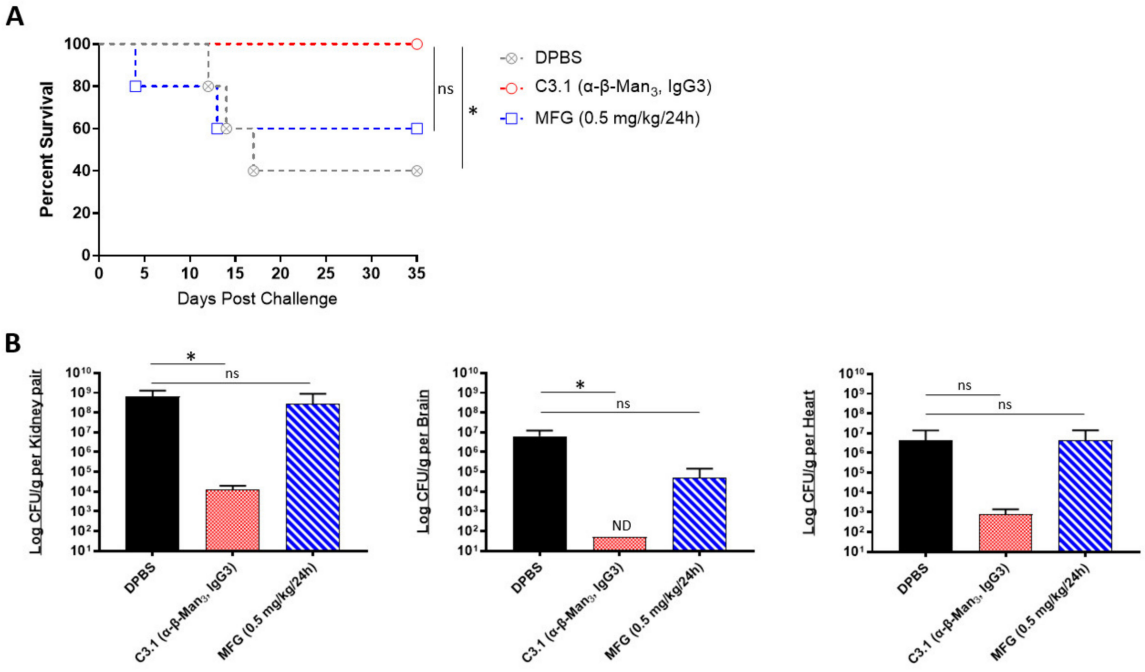

Figure 3. In vivo protective efficacy of universal *Candida* β-1,2-mannotriose-specific monoclonal antibody: (**A**) the 35-day survival curve and (**B**) quantification of kidney, brain, and heart fungal burdens from 7-week-old female A/J mice treated with mAb C3.1 or micafungin. Mice were treated with 200 µL DPBS, mAb C3.1 (0.24 mg/200 µL DPBS), or micafungin (0.5 mg/kg body weight daily for 7 days) then challenged 18 h later with a sub-lethal dose of 4×10^7 CFUs of *C. auris* AR-0386. β-Man_3 = β-1,2-mannotriose. Data are mean + SD (**B**). $n = 5$. Log-rank (Mantel–Cox) test (**A**) or two-tailed *t*-test (**B**) were used to identify significant differences. * $p < 0.05$; *ns* = not significant. ND = not detectable.

We then evaluated the prophylactic efficacy of our peptide-specific mAbs. In addition to the mAbs 6H1 and 9F2, we also screened one additional universal mAb, 10E7, which targets a different epitope on Pgk1 (GPV-P3, IgG1). A/J mice were treated with each mAb, followed by a lethal dose challenge with *C. auris* AR-0386 18 h later. Survival was observed for 40 days, and fungal burdens were quantified in the kidney, brain, and heart. With this lethal challenge dose, all control mice died on day 5 post challenge (Figure 4A). On the other hand, 9F2 and 10E7 mice had prolonged survival (50% and 25% survival, respectively) by day 40, with 9F2 inducing significantly higher survival, compared to control mice. Although not statistically significant, both mAb-treated groups had slightly reduced fungal burdens in the kidneys, with 9F2 also inducing significantly lower heart burdens (2.5×10^7 CFUs/g), compared to DPBS mice (2.1×10^8 CFUs/g) (Figure 4B). This reduction in heart burdens is host significant, because A/J mice ultimately succumb to cardiac failure, therefore making the heart the best indicator for evaluating disease progress and protection [33,47]. There was no difference in brain burdens among mAb-treated and control groups.

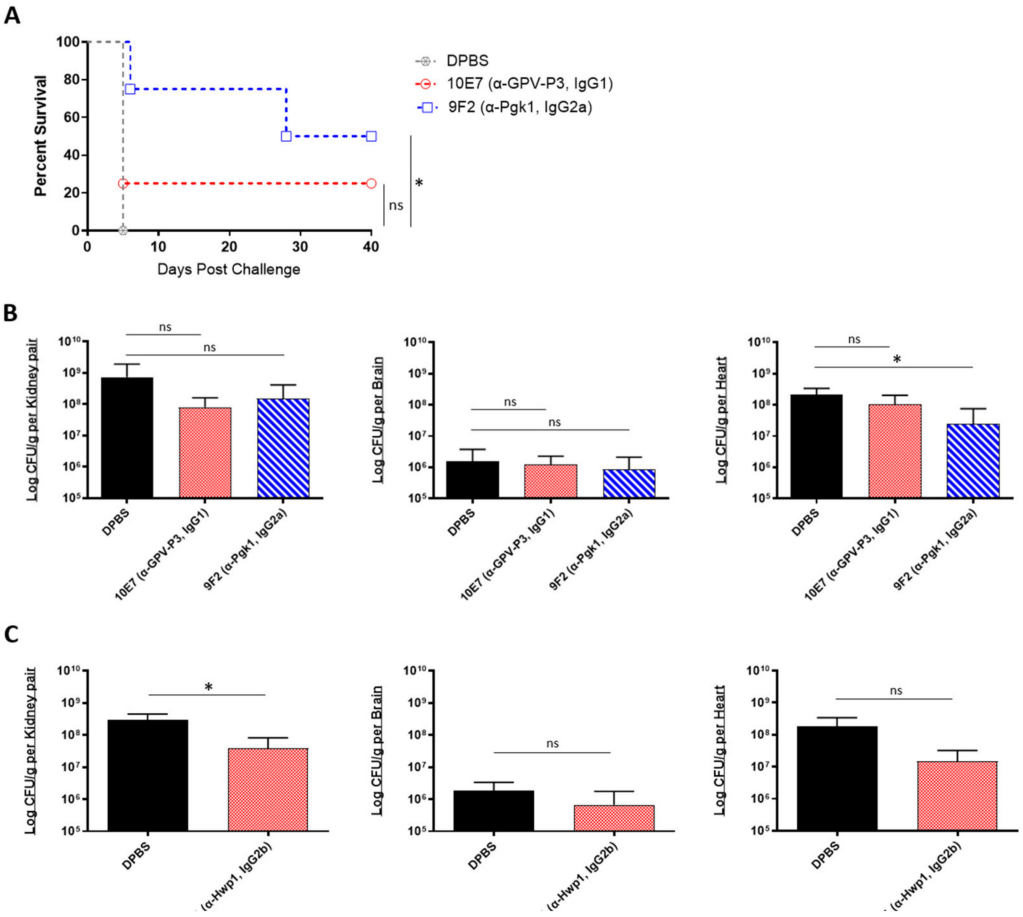

Figure 4. In vivo protective efficacy of universal *Candida* peptide-specific monoclonal antibodies: (**A**) the 40-day survival curve and (**B**) quantification of kidney, brain, and heart fungal burdens from 7-week-old male A/J mice treated with two Pgk1-specific mAbs; (**A**,**B**) mice were treated with 200 µL DPBS or antibody (0.285 mg/200 µL DPBS), then challenged 18 h later with a lethal dose of 1×10^8 CFUs of *C. auris* AR-0386; (**C**) quantification of kidney, brain, and heart fungal burdens from 7-week-old female A/J mice treated with mAb 6H1 or micafungin. Mice were treated with 100 µL DPBS or mAb (0.135 mg/100 µL DPBS), then challenged 18 h later with a sublethal dose of 4×10^7 CFUs of *C. auris* AR-0389. GPV-P3 = phosphoglycerate kinase 1 (IgG1), Pgk1 = phosphoglycerate kinase 1 (IgG2a). Data are mean + SD (**B**,**C**). $n = 4$. Log-rank (Mantel–Cox) test (**A**) or two-tailed *t*-test (**B**,**C**) were used to identify significant differences. * $p < 0.05$; *ns* = not significant.

In a separate experiment, we also tested the prophylactic protective efficacy of 6H1 (anti-Hwp1, IgG2b) in A/J mice using a sublethal challenge dose of *C. auris* AR-0389. Mice were sacrificed on day 6, and fungal burdens were quantified as previously (Figure 4C). Based on the data, 6H1-treated mice had lower fungal burdens in the kidney, brain, and heart (3.8×10^7, 6.7×10^5, and 1.5×10^7 CFUs/g, respectively), compared to DPBS mice kidney, brain, and heart burdens (2.9×10^8, 1.8×10^6, and 1.8×10^8 CFUs/g, respectively). Of these, only the kidneys had a statistically significant reduction in fungal burdens, while the reduction in heart burdens was nearly significant ($p = 0.0798$). Collectively, the data showed that passive transfer of universal *Candida* peptide-specific mAbs, 9F2 and 6H1 provided significantly extended survival (9F2) and significantly reduced fungal burdens in the kidney (6H1) and heart (9F2), compared to control mice in an A/J mouse model of *C. auris* disseminated infection.

2.4. In Vivo Protective Efficacy of Monoclonal Antibody Cocktails

Being that several of our antibodies were able to induce protection in mice when administered individually, we further tested if combining two different mAbs would induce enhanced or even synergistic protection in mice. Since our mAbs are specific to different cell surface antigens, we hypothesized that using a cocktail of two mAbs could result in a more effective "double hit" protection against *C. auris*. The selected two-mAb cocktail consisted of 6H1, which performed best in the kidney (Figure 4C), and 9F2, which performed best in the heart (Figure 4B). A/J mice were treated with 6H1, 9F2, or both, followed by a sublethal dose challenge of AR-0386 24 h later. Survival was observed for 35 days. Mice that received the 6H1+9F2 cocktail had significantly higher survival (100% survival) by day 35, compared to mice that received only 6H1 (20% survival) or 9F2 (0% survival) (Figure 5A). Regarding fungal burdens (Figure 5B), mice that received the cocktail had significantly lower burdens in the kidney (1.5×10^8 CFUs/g), compared to mice that received only 9F2 (1.0×10^9 CFUs/g). Kidney burdens in the cocktail group were also lower than in the 6H1 group (6.7×10^8 CFUs/g), although this was not statistically significant. Similarly, fungal burdens in the brain were significantly lower in mice that received the cocktail (5.8×10^3 CFUs/g), compared to mice that received only 9F2 (9.3×10^6 CFUs/g). The cocktail group brain burdens were also lower than the 6H1 group (3.4×10^4 CFUs/g), although this was not statistically significant. We also observed a consistent trend of lower heart burdens for the mAb cocktail treated group (1.1×10^4 CFUs/g), compared to 6H1 mice (3.3×10^6 CFUs/g) or 9F2 (8.3×10^6 CFUs/g), although not statistically significant. Overall, the data showed that protective mAbs, such as 6H1 and 9F2, can be combined into cocktails to provide enhanced protection against *C. auris* disseminated infection compared to treatment with either mAb individually.

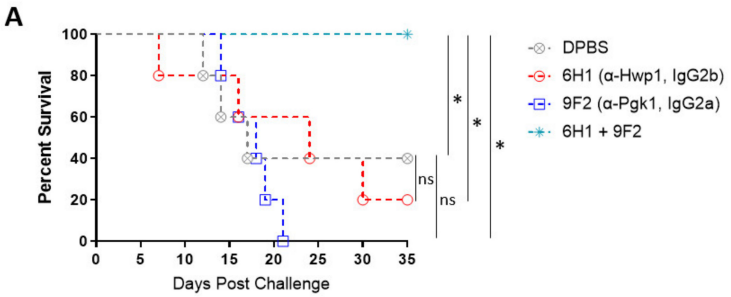

Figure 5. *Cont.*

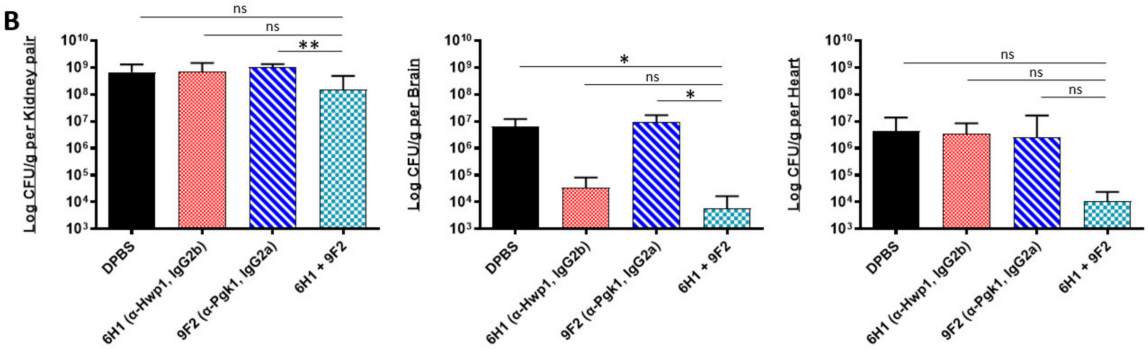

Figure 5. In vivo protective efficacy of monoclonal antibody cocktails: (**A**) the 35-day survival curve and (**B**) quantification of kidney, brain, and heart fungal burdens from 7-week-old female A/J mice treated with mAbs 6H1, 9F2, or a cocktail of 6H1 + 9F2. Mice were treated with two 400-µL-doses of mAb 6H1 given 18 h apart, one 200-µL-dose of mAb 9F2, or a combination of both mAbs consisting of one dose of 9F2 and two doses of 6H1 given 18 h apart. Then, 18 h after first dose of mAb, mice were challenged with a sublethal dose of 4×10^7 CFUs of *C. auris* AR-0386. Hwp1 = hyphal wall protein 1, Pgk1 = phosphoglycerate kinase 1. Data are mean + SD (B). $n = 5$. Log-rank (Mantel–Cox) test (**A**) or two-tailed *t*-test (**B**) were used to identify significant differences. * $p < 0.05$; ** $p < 0.01$; *ns* = not significant.

3. Discussion

C. auris is the first fungal pathogen to cause a serious global public health threat [20]. In vitro and in vivo studies of drug efficacy against this MDR pathogen have shown that most isolates are highly resistant to azoles and polyenes, which severely limits effective drug treatments. As this pathogen easily spreads throughout hospital ICUs and assisted living facilities, *C. auris* seriously threatens the lives of patients living with comorbidities. In those who are most at risk, such as the immunocompromised, antifungal drugs are often not effective and cause additional organ toxicity, which can further exacerbate the conditions of these highly susceptible patients [19].

In this study, we demonstrated for the first time that passive transfer of *Candida* peptide- and glycan-specific universal mAbs is an effective means of immunotherapy for protecting against *C. auris* invasive infections in an established A/J mouse model. During systemic infection, *Candida spp.* disseminates through the bloodstream and enters target organs within hours of infection [48]. During early infection, *Candida* cells are rapidly eliminated from circulation, and the pathogen is often undetectable in the blood [49]. Consequently, our study evaluated antibody efficacy by quantifying fungal burdens in the kidney, brain, and heart, as well as overall survival. A key characteristic of our mAbs is that they target epitopes that share high homology among various clinically significant *Candida* species. This "universal" targeting allows for their potential application in preventing candidemia caused by different *Candida* species and isolates regardless of isolate-specific antifungal-resistance profiles.

The two *C. auris* isolates analyzed, AR-0386 (CAU-06) and AR-0389 (CAU-09), come from different clades and have unique genetic variations resulting in isolate-specific morphologies, rates of proliferation, virulence, and antifungal resistance [32]. These genetic differences may also affect cell wall composition. The lower level of antibody binding observed with isolate AR-0389 could be due to epitope masking by cell wall polysaccharides, which could account for evasion of immune responses and higher levels of virulence observed with isolate AR-0389, compared to AR-0386. This hypothesis is supported by evidence showing that the unmasking of cell wall components, such as β-(1,3)-glucan, can lead to attenuated *C. albicans* virulence in mouse models of systemic infection [50,51]. More work is required to determine why the same mAb has different binding patterns to the cell surface epitopes of *C. auris* isolates, and how this is related to isolate virulence, host–pathogen interaction, and immune escape.

Of our mAb panel, C3.1 (anti-β-Man_3) had the highest level of cell surface binding, provided the best overall protection, and significantly outperformed micafungin as a

treatment for invasive *C. auris* infection. β-mannose is a major glycan component of the outer cell wall of many *Candida spp*., and it is abundantly expressed on the surface of *C. auris* [46]. Our previous data with *C. albicans* has shown that C3.1-mediated protection depends on its ability to rapidly and efficiently fix complement to the fungal surface, which is associated with enhanced phagocytosis and killing of the fungus [40,45]. Being that A/J mice are C3-competent, C3.1 likely protects against *C. auris* via the same mechanism. Furthermore, it has been shown that immune complexes of IgG3 can bind to FcγRI receptors on phagocytic cells [52]. Thus, C3.1 opsonization of *C. auris* may lead to additional FcγRI binding, increased adherence and internalization, and enhanced phagocytosis; however, quantitation of these values will be the subject of a later study.

In contrast to C3.1, 6H1 (anti-Hwp1) and 9F2 (anti-Pgk1) mAbs target epitopes that are not abundantly expressed in the *Candida* cell wall, which was reflected in our flow cytometry data. Although Pgk1 is primarily a glycolytic enzyme localized in the cytoplasm, it is also exposed on the *Candida* surface and has been identified as a cell-wall-associated moonlight protein that is immunoreactive during invasive fungal infections in humans [43,44,53]. Hwp1, on the other hand, is expressed on the cell surface during hyphal morphology [54]; however, some evidence does suggest that it may also be expressed during pseudohyphal morphology [55], which has been induced in *C. auris* in vitro [56]. Interestingly, the *C. auris* genome does not appear to contain an ortholog of the Hwp1 gene [54,56], which points to the possibility of cross reaction of the anti-Hwp1 mAb with another cell wall protein. Nonetheless, both mAbs were able to induce significant protection in our mouse model.

Our animal model also showed the enhanced efficacy of two-mAb cocktails as a prophylactic treatment against *C. auris* disseminated infection. A benefit of mAb cocktails is that each antibody can individually induce a different effector mechanism, which can work in concert to inhibit the growth and dissemination of the pathogen [57]. This is a strategy that has been highly effective in treating other infectious diseases, such as HIV infection using highly active antiretroviral therapy (HAART), which uses a cocktail of three or more drugs that inhibit different steps of the virus's replication cycle [58]. In the case of the 6H1+9F2 cocktail, the enhanced protection could be due to improved access of phagocytic cells to *C. auris* yeast, leading to increased oxidative damage. Research conducted by other groups has shown that Pgk1 confers protection to *C. albicans* against reactive oxygen species (ROS) [59] and that immunization with recombinant Pgk1 protein leads to a significant reduction in kidney burdens in mice infected with *C. albicans* or with *C. glabrata* [60]. Additionally, in an in vivo rat venous catheter model of infection, *C. albicans* Hwp1 mutants were shown to display severe biofilm defects with few hyphae [61]. This may indicate that 6H1 and 9F2 mAbs could function together to disrupt biofilm formation and increase susceptibility to respiratory burst by phagocytic cells, although this mechanism would need to be further investigated. Alternatively, the binding of one mAb could induce a conformational change that results in the unmasking of the second mAb's target epitope, leading to functional cooperativity between mAbs targeting different epitopes. Further investigation may also show that these different mechanisms are not mutually exclusive and may both contribute to the observed enhanced efficacy.

In recent years, several novel antifungal compounds have been developed that have proven effective against MDR *Candida* species. One such compound, carvacrol, was shown to have antifungal activity against clinical isolates of *C. auris* while also inducing synergistic antifungal activity when combined with fluconazole, amphotericin B, caspofungin, and micafungin [62]. As with these compounds, mAbs have the potential to be combined with antifungals to induce synergistic protection while also significantly reducing drug MICs and associated toxicity. Future experiments will evaluate the enhanced protection of combining our mAbs with conventional antifungals as well as the therapeutic efficacy of these mAbs.

Finally, it is important to note that similar to most pathogenic *Candida* species, *C. auris* has the propensity to form biofilms within its host. It is well established that within biofilms, *Candida spp.* exhibit higher resistance to antifungal drugs. This is largely due

to the upregulation of efflux pumps [63] and the production of extracellular polymeric substances (EPS), which can interfere with drug diffusion [64]. Although we observed that micafungin was effective at reducing fungal burdens within our immunosuppressed C57BL/6 model, this efficacy would likely be reduced against biofilm-derived *C. auris* cells. In one mouse study of disseminated candidiasis using biofilm-derived *C. glabrata* cells, micafungin treatment was ineffective at reducing liver and kidney burdens [65]. MAbs could be effective here as well. In one study, after incubating *C. albicans* and *Candida dubliniensis* with antibodies targeting the surface antigen, complement receptor 3-related protein (CR3-RP), both species had a reduction in surface adherence and in biofilm thickness in vitro [66]. Using a combination therapy, the binding of mAbs to the surface of the pathogen could interfere with biofilm formation, leading to increased diffusion of antifungals.

In summary, the potential for mAb therapy against microbial pathogens is vast since mAbs inherently have high specificity for their targets without selecting for resistance. The application of protective mAbs against *C. auris* disseminated infection represents a highly promising alternative to the often-ineffective use of antifungal drugs against this MDR pathogen. Not only can effective mAbs protect against severe infection more rapidly than antifungal drugs [67–69], but specific antibodies may also be synergistic with conventional antimicrobials. The data presented here have significant implications for both immunotherapy and vaccine development in the future, and the demonstration of preclinical efficacy of the immunoprotective mAbs in this study will provide compelling data that can be advanced into the clinical setting.

4. Materials and Methods

4.1. Candida Isolates and Culture Conditions

Two antifungal-resistant isolates of *C. auris*, AR-0386 (CAU-06) and AR-0389 (CAU-09), were supplied by the United States Centers for Disease Control and Prevention (CDC, Atlanta, GA, USA). *C. albicans* reference strain SC5314 was supplied by the American Type Culture Collection (MYA-2876, ATCC, Manassas, VA, USA). For passive transfer of mAb experiments, the inoculum was serially passaged daily for three days in 25 mL glucose yeast peptide broth at 37 °C and then washed three times in Dulbecco's phosphate-buffered saline (DPBS). Cell density was measured using a hemocytometer and adjusted to the desired density in DPBS. For MIC assays, culture was plated onto Sabouraud Dextrose Broth (SDB) agar plates and incubated at 35 °C for 24 h. Five colonies were selected and suspended in 1 mL of sterile deionized H_2O, and cell density was measured using a hemocytometer. The density was then adjusted to desired concentration in RPMI 1640 + 0.165 M MOPS medium (with L-glutamine and phenol red, without bicarbonate).

4.2. Mice

Male and female A/J mice were purchased from the Jackson Laboratory (JAX, Bar Harbor, ME, USA) and Envigo (Indianapolis, IN, USA). Male and female C57BL/6 mice were purchased from the Jackson Laboratory (JAX, Bar Harbor, ME, USA). At the time of studies, A/J mice were 7 weeks old, and C57BL/6 mice were 16–17 weeks old. Mice were maintained in the Louisiana State University Health Sciences Center's AAALAC-accredited animal facility (#000037, LSUHSC-NO, New Orleans, LA, USA), and all animal experiments were performed using a protocol approved by the Louisiana State University Health Sciences Center's Institutional Animal Care and Use Committee (#3559, 1/18/2019, LSUHSC-NO IACUC, New Orleans, LA, USA).

4.3. Immunosuppression

16–17-week-old male and female C57BL/6 mice were immunosuppressed using cyclophosphamide monohydrate (#C0768, Sigma-Aldrich, St. Louis, MO, USA) three days prior to challenge by intraperitoneal (i.p.) injection using a dose of 200 mg/kg of body weight. Immunosuppression was maintained with additional i.p. injections of a 150 mg/kg dose of cyclophosphamide every 7 days.

4.4. Antifungals

Micafungin (≥97% HPLC) was purchased from Sigma-Aldrich (#SML2268, Sigma-Aldrich, St. Louis, MO, USA), and itraconazole (≥98% TLC) was purchased from Sigma-Aldrich (#I6657, Sigma-Aldrich, St. Louis, MO, USA). For MIC assay, micafungin and itraconazole were dissolved in RPMI 1640 + 0.165 M MOPS medium (with L-glutamine and phenol red, without bicarbonate) + 1% DMSO to the desired concentrations. For animal experiments, micafungin was dissolved in DPBS to the desired concentration, and itraconazole was dissolved in sterile deionized H_2O + 10% DMSO to the desired concentration.

4.5. Antifungal Susceptibility

C. auris and *C. albicans* micafungin and itraconazole minimum inhibitory concentrations (MICs) were determined using the broth microdilution method (BMD) according to the guidelines of the Clinical and Laboratory Standards Institute (CLSI) Reference Method for Broth Dilution Antifungal Susceptibility Testing of Yeasts; Approved Standard (CLSI M27-A3, 3rd Ed. 2008. Vol 28, No 14).

4.6. Antibodies

All monoclonal antibodies were isolated from hybridoma cells, purified, and sterile filtered in phosphate-buffered saline (PBS) by GenScript Biotech Corporation (GenScript, Piscataway, NJ, USA) and by Autoimmune Technologies (AiT, New Orleans, LA, USA). Antibody concentrations were determined using a Pierce BCA Protein Assay Kit (#23227, Thermo Scientific, Waltham, MA, USA), according to the manufacturer's directions. A standard curve was constructed using bovine gamma globulin standard (BGG) (#23212, Thermo Scientific, Waltham, MA, USA). Absorbance was read on a plate reader at 562 nm, and sample absorbances were compared to the BGG standard curve to determine antibody concentration.

4.7. Antibody Titers

Titers of mAbs were determined via enzyme-linked immunosorbent assay (ELISA). A 96-well polystyrene plate was coated with whole synthetic protein (Pgk1, Hwp1) (GenScript, Piscataway, NJ, USA) or mannan extract at 4 μg/mL in bicarbonate coating buffer and incubated overnight at 4 °C. The following day, the wells were blocked using 1% BSA blocking buffer for 1 h at room temperature. Monoclonal antibodies were then added in duplicate to respective wells using twofold serial dilutions from 1:500 to 1:256,000 and incubated for 2 h at room temperature. Horseradish peroxidase (HRP)-conjugated goat anti-mouse polyvalent IgG, IgA, IgM secondary antibody (#A0412, Sigma-Aldrich, St. Louis, MO, USA) was then added (1:3000) and incubated in the dark for 1 h at room temperature. Tetramethyl benzidine (TMB) (#34022, Thermo Scientific, Waltham, MA, USA) was then added to each well and incubated in the dark for 30 min at room temperature. HCl was added to stop the reaction, and the optical density was measured at 450 nm using a spectrophotometer. As a negative control, wells were incubated with secondary antibody alone. Titers were given as the dilution whose OD reading was greater than two times that of the negative control.

4.8. Antibody Cell Surface Staining

Overnight cultures of *C. auris* AR-0386, AR-0389, and *C. albicans* SC5314 were washed three times with DPBS. Pellets were resuspended in 100 μL of C3.1 (anti-β-Man_3), 9F2 (anti-Pgk1), or 6H1 (anti-Hwp1) antibodies in 1X PBS + 1% BSA and incubated for 1 h at room temperature. Cells were washed three additional times, and pellets were resuspended in Alexa Fluor 488-conjugated goat anti-mouse IgG, IgM secondary antibody (#A10680, Invitrogen, Carlsbad, CA, USA) (1:100) in 1X PBS + 1% BSA and incubated for 1 h at room temperature. Cells were washed three additional times and resuspended in 500 μL DPBS and acquired by flow cytometry at 488 nm (FACSDiva 8.0.3, FACSCanto II, BD Biosciences, San Jose, CA, USA), As a positive control, an additional high-binding

anti-β-Man_3 mAb, G11.2 (IgG1), was used. As a negative control, cells were stained with secondary antibody alone. Gating was set on the secondary antibody (Alexa Fluor 488 only) control. A portion of the stained cells was spread on slides for fluorescent imaging.

4.9. In Vivo Model of Disseminated Infection

For this, 7-week-old A/J mice or 16–17-week-old immunosuppressed C57BL/6 mice were treated via intraperitoneal (i.p.) injection with 200 µL of monoclonal antibody or DPBS. Then, 18 h later, mice were challenged via intravenous (i.v.) injection in the tail vein with *C. auris* AR-0386 at a sublethal dose of 4×10^7 CFUs in 100 µL DPBS or a lethal dose of 1×10^8 CFUs in 100 µL DPBS or with *C. auris* AR-0389 at a sublethal dose of 4×10^7 in 100 µL DPBS, depending on the experiment. For experiments that measured antifungal efficacy, mice received daily i.p. administration of micafungin or itraconazole starting 24 h post challenge. All mice were monitored daily for death or the development of a moribund state, at which point they were sacrificed via CO_2 inhalation. All surviving mice were sacrificed at the conclusion of each study.

4.10. Quantification of Fungal Burdens

Upon death, the kidney, brain, and heart were extracted from mice, and each organ was homogenized in DPBS. The homogenate was then serial diluted and plated onto GYEP agar plates containing chloramphenicol. The plates were incubated for 48 h at 37 °C at which time CFUs were quantified. The limit of detection was 50 CFUs/g for each organ.

4.11. Statistical Analysis

Plots and statistical comparisons were performed using Prism Software (Version 9, GraphPad Software, San Diego, CA, USA). Survival data was evaluated by Kaplan–Meier analysis, and statistical significance was calculated using a log-rank (Mantel–Cox) test. For fungal burden data, results were expressed as mean ± SD, and statistical significance was calculated using a two-tailed *t*-test to compare mAb-treated groups to the control group. Each study contained five mice per group unless otherwise stated. Significant *p* values were defined as follows: * $p < 0.05$; ** $p < 0.01$.

Author Contributions: Conceptualization and methodology, H.X.; investigation, J.R.-C., K.E., A.A., and E.C.; data curation, J.R.-C. and K.E.; writing—original draft preparation, J.R.-C.; writing—review and editing, H.X.; supervision, H.X.; funding acquisition, H.X. All authors have read and agreed to the published version of the manuscript.

Funding: This research was funded by the Department of Defense CDMRP, Award PR171482.

Institutional Review Board Statement: The study was approved by and conducted according to the guidelines of the Louisiana State University Health Sciences Center's Institutional Animal Care and Use Committee (#3559, 1/18/2019, LSUHSC-NO IACUC, New Orleans, LA, USA). Mice were maintained in the Louisiana State University Health Sciences Center's AAALAC-accredited animal facility (#000037, LSUHSC-NO, New Orleans, LA, USA).

Data Availability Statement: Data supporting reported results are available upon request (jcolo1@lsuhsc.edu).

Acknowledgments: We thank Constance Porretta for technical assistance with flow cytometry acquisition and analysis, Louisiana State University Health Sciences Center (LSUHSC) for the support of our research, and the National Institutes of Health (NIH) for funding support.

Conflicts of Interest: The authors declare no conflict of interest. The funders had no role in the design of the study; in the collection, analyses, or interpretation of data; in the writing of the manuscript, or in the decision to publish the results.

References

1. Satoh, K.; Makimura, K.; Hasumi, Y.; Nishiyama, Y.; Uchida, K.; Yamaguchi, H. *Candida auris* sp. nov., a novel ascomycetous yeast isolated from the external ear canal of an inpatient in a Japanese hospital. *Microbiol. Immunol.* **2009**, *53*, 41–44. [CrossRef] [PubMed]
2. Forsberg, K.; Woodworth, K.; Walters, M.; Berkow, E.L.; Jackson, B.; Chiller, T.; Vallabhaneni, S. *Candida auris*: The recent emergence of a multidrug-resistant fungal pathogen. *Med. Mycol.* **2018**, *57*, 1–12. [CrossRef]
3. Schelenz, S.; Hagen, F.; Rhodes, J.L.; Abdolrasouli, A.; Chowdhary, A.; Hall, A.; Ryan, L.; Shackleton, J.; Trimlett, R.; Meis, J.F.; et al. First hospital outbreak of the globally emerging *Candida auris* in a European hospital. *Antimicrob. Resist. Infect. Control.* **2016**, *5*, 35. [CrossRef]
4. Lockhart, S.R.; Etienne, K.A.; Vallabhaneni, S.; Farooqi, J.; Chowdhary, A.; Govender, N.P.; Colombo, A.L.; Calvo, B.; Cuomo, C.A.; Desjardins, C.A.; et al. Simultaneous Emergence of Multidrug-Resistant *Candida auris* on 3 Continents Confirmed by Whole-Genome Sequencing and Epidemiological Analyses. *Clin. Infect. Dis.* **2017**, *64*, 134–140. [CrossRef]
5. Chowdhary, A.; Kumar, V.A.; Sharma, C.; Prakash, A.; Agarwal, K.; Babu, R.; Dinesh, K.R.; Karim, S.; Singh, S.K.; Hagen, F.; et al. Multidrug-resistant endemic clonal strain of *Candida auris* in India. *Eur. J. Clin. Microbiol. Infect. Dis.* **2014**, *33*, 919–926. [CrossRef]
6. Zhu, Y.; O'Brien, B.; Leach, L.; Clarke, A.; Bates, M.; Adams, E.; Ostrowsky, B.; Quinn, M.; Dufort, E.; Southwick, K.; et al. Laboratory Analysis of an Outbreak of *Candida auris* in New York from 2016 to 2018: Impact and Lessons Learned. *J. Clin. Microbiol.* **2019**, *58*, e01503–e01519. [CrossRef] [PubMed]
7. Prestel, C.; Anderson, E.; Forsberg, K.; Lyman, M.; De Perio, M.A.; Kuhar, D.; Edwards, K.; Rivera, M.; Shugart, A.; Walters, M.; et al. *Candida auris* Outbreak in a COVID-19 Specialty Care Unit—Florida, July–August 2020. *MMWR Morb. Mortal. Wkly. Rep.* **2021**, *70*, 56–57. [CrossRef] [PubMed]
8. Di Pilato, V.; Codda, G.; Ball, L.; Giacobbe, D.; Willison, E.; Mikulska, M.; Magnasco, L.; Crea, F.; Vena, A.; Pelosi, P.; et al. Molecular Epidemiological Investigation of a Nosocomial Cluster of *C. auris*: Evidence of Recent Emergence in Italy and Ease of Transmission during the COVID-19 Pandemic. *J. Fungi* **2021**, *7*, 140. [CrossRef] [PubMed]
9. de Almeida, J.; Francisco, E.; Hagen, F.; Brandão, I.; Pereira, F.; Dias, P.P.; Costa, M.D.M.; Jordão, R.D.S.; de Groot, T.; Colombo, A. Emergence of *Candida auris* in Brazil in a COVID-19 Intensive Care Unit. *J. Fungi* **2021**, *7*, 220. [CrossRef]
10. Chowdhary, A.; Sharma, C.; Duggal, S.; Agarwal, K.; Prakash, A.; Singh, P.K.; Jain, S.; Kathuria, S.; Randhawa, H.S.; Hagen, F.; et al. New Clonal Strain of *Candida auris*, Delhi, India. *Emerg. Infect. Dis.* **2013**, *19*, 1670–1673. [CrossRef]
11. Morales, S.; Parra-Giraldo, C.M.; Garzón, A.C.; Martínez, H.P.; Rodríguez, G.J.; Álvarez-Moreno, C.A.; Rodriguez, J.Y. Invasive Infections with Multidrug-Resistant Yeast *Candida auris*, Colombia. *Emerg. Infect. Dis.* **2017**, *23*, 162–164. [CrossRef]
12. Armstrong, P.A.; Rivera, S.M.; Escandon, P.; Caceres, D.H.; Chow, N.; Stuckey, M.J.; Díaz, J.; Gomez, A.; Vélez, N.; Espinosa-Bode, A.; et al. Hospital-Associated Multicenter Outbreak of Emerging Fungus *Candida auris*, Colombia, 2016. *Emerg. Infect. Dis.* **2019**, *25*, 1339–1346. [CrossRef]
13. Parra-Giraldo, C.M.; Valderrama, S.L.; Cortes-Fraile, G.; Garzón, J.R.; Ariza, B.E.; Morio, F.; Linares-Linares, M.Y.; Ceballos-Garzón, A.; De la Hoz, A.; Hernandez, C.; et al. First report of sporadic cases of *Candida auris* in Colombia. *Int. J. Infect. Dis.* **2018**, *69*, 63–67. [CrossRef] [PubMed]
14. Ruiz-Gaitán, A.; Moret, A.M.; Tasias-Pitarch, M.; Aleixandre-López, A.I.; Martínez-Morel, H.; Calabuig, E.; Salavert-Lletí, M.; Ramírez, P.; López-Hontangas, J.L.; Hagen, F.; et al. An outbreak due to *Candida auris* with prolonged colonisation and candidaemia in a tertiary care European hospital. *Mycoses* **2018**, *61*, 498–505. [CrossRef]
15. Alatoom, A.; Sartawi, M.; Lawlor, K.; AbdelWareth, L.; Thomsen, J.; Nusair, A.; Mirza, I. Persistent candidemia despite appropriate fungal therapy: First case of *Candida auris* from the United Arab Emirates. *Int. J. Infect. Dis.* **2018**, *70*, 36–37. [CrossRef]
16. Chow, N.A.; Gade, L.; Tsay, S.V.; Forsberg, K.; Greenko, J.A.; Southwick, K.L.; Barrett, P.M.; Kerins, J.L.; Lockhart, S.R.; Chiller, T.M.; et al. Multiple introductions and subsequent transmission of multidrug-resistant *Candida auris* in the USA: A molecular epidemiological survey. *Lancet Infect. Dis.* **2018**, *18*, 1377–1384. [CrossRef]
17. Vallabhaneni, S.; Cleveland, A.A.; Farley, M.M.; Harrison, L.H.; Schaffner, W.; Beldavs, Z.G.; Derado, G.; Pham, C.D.; Lockhart, S.R.; Smith, R.M. Epidemiology and Risk Factors for Echinocandin Nonsusceptible *Candida glabrata* Bloodstream Infections: Data From a Large Multisite Population-Based Candidemia Surveillance Program, 2008–2014. *Open Forum Infect. Dis.* **2015**, *2*, ofv163. [CrossRef]
18. Lone, S.A.; Ahmad, A. *Candida auris*—The growing menace to global health. *Mycoses* **2019**, *62*, 620–637. [CrossRef] [PubMed]
19. Perfect, J.R. The antifungal pipeline: A reality check. *Nat. Rev. Drug Discov.* **2017**, *16*, 603–616. [CrossRef]
20. Kean, R.; Ramage, G. Combined Antifungal Resistance and Biofilm Tolerance: The Global Threat of *Candida auris*. *mSphere* **2019**, *4*, e00458-19. [CrossRef]
21. Motley, M.P.; Banerjee, K.; Fries, B.C. Monoclonal antibody-based therapies for bacterial infections. *Curr. Opin. Infect. Dis.* **2019**, *32*, 210–216. [CrossRef]
22. Salazar, G.; Zhang, N.; Fu, T.-M.; An, Z. Antibody therapies for the prevention and treatment of viral infections. *npj Vaccines* **2017**, *2*, 19. [CrossRef] [PubMed]
23. Elluru, S.R.; Kaveri, S.; Bayry, J. The protective role of immunoglobulins in fungal infections and inflammation. *Semin. Immunopathol.* **2015**, *37*, 187–197. [CrossRef] [PubMed]
24. Lu, R.-M.; Hwang, Y.-C.; Liu, I.-J.; Lee, C.-C.; Tsai, H.-Z.; Li, H.-J.; Wu, H.-C. Development of therapeutic antibodies for the treatment of diseases. *J. Biomed. Sci.* **2020**, *27*, 1. [CrossRef]

25. Tuccori, M.; Ferraro, S.; Convertino, I.; Cappello, E.; Valdiserra, G.; Blandizzi, C.; Maggi, F.; Focosi, D. Anti-SARS-CoV-2 neutralizing monoclonal antibodies: Clinical pipeline. *mAbs* **2020**, *12*, 1854149. [CrossRef] [PubMed]
26. FDA Press Announcements. Coronavirus (COVID-19) Update: FDA Authorizes Monoclonal Antibody for Treatment of COVID-19. 2020. Available online: https://www.fda.gov/news-events/press-announcements/coronavirus-covid-19-update-fda-authorizes-monoclonal-antibody-treatment-covid-19 (accessed on 12 January 2021).
27. FDA Press Announcements. Coronavirus (COVID-19) Update: FDA Authorizes Monoclonal Antibodies for Treatment of COVID-19. 2020. Available online: https://www.fda.gov/news-events/press-announcements/coronavirus-covid-19-update-fda-authorizes-monoclonal-antibodies-treatment-covid-19 (accessed on 12 January 2021).
28. Clarke, E.V.; Tenner, A.J. Complement modulation of T cell immune responses during homeostasis and disease. *J. Leukoc. Biol.* **2014**, *96*, 745–756. [CrossRef]
29. Cheng, S.-C.; Sprong, T.; Joosten, L.A.; Van Der Meer, J.W.M.; Kullberg, B.-J.; Hube, B.; Schejbel, L.; Garred, P.; Van Deuren, M.; Netea, M.G. Complement plays a central role in *Candida albicans*-induced cytokine production by human PBMCs. *Eur. J. Immunol.* **2012**, *42*, 993–1004. [CrossRef] [PubMed]
30. Mullick, A.; Elias, M.; Picard, S.; Bourget, L.; Jovcevski, O.; Gauthier, S.; Tuite, A.; Harakidas, P.; Bihun, C.; Massie, B.; et al. Dysregulated Inflammatory Response to Candida albicans in a C5-Deficient Mouse Strain. *Infect. Immun.* **2004**, *72*, 5868–5876. [CrossRef]
31. Torres, S.R.; Pichowicz, A.; Torres-Velez, F.; Song, R.; Singh, N.; Lasek-Nesselquist, E.; De Jesus, M. Impact of *Candida auris* Infection in a Neutropenic Murine Model. *Antimicrob. Agents Chemother.* **2019**, *64*, e01625-19. [CrossRef]
32. Wurster, S.; Bandi, A.; Beyda, N.D.; Albert, N.D.; Raman, N.M.; Raad, I.I.; Kontoyiannis, D.P. *Drosophila melanogaster* as a model to study virulence and azole treatment of the emerging pathogen *Candida auris*. *J. Antimicrob. Chemother.* **2019**, *74*, 1904–1910. [CrossRef]
33. Xin, H.; Mohiuddin, F.; Tran, J.; Adams, A.; Eberle, K. Experimental Mouse Models of Disseminated *Candida auris* Infection. *mSphere* **2019**, *4*, e00339-19. [CrossRef]
34. Singh, S.; Uppuluri, P.; Mamouei, Z.; Alqarihi, A.; Elhassan, H.; French, S.; Lockhart, S.R.; Chiller, T.; Edwards, J.E., Jr.; Ibra-him, A.S. The NDV-3A vaccine protects mice from multidrug resistant *Candida auris* infection. *PLoS Pathog.* **2019**, *15*, e1007460. [CrossRef] [PubMed]
35. Borman, A.M.; Szekely, A.; Johnson, E.M. Comparative Pathogenicity of United Kingdom Isolates of the Emerging Pathogen *Candida auris* and Other Key Pathogenic *Candida* Species. *mSphere* **2016**, *1*, e00189-16. [CrossRef]
36. AR Isolate Bank. Candida auris. 2021. Available online: https://wwwn.cdc.gov/ARIsolateBank/Panel/PanelDetail?ID=2 (accessed on 27 May 2021).
37. Mouton, J.W.; Muller, A.; Canton, R.; Giske, C.G.; Kahlmeter, G.; Turnidge, J. MIC-based dose adjustment: Facts and fables. *J. Antimicrob. Chemother.* **2018**, *73*, 564–568. [CrossRef]
38. Enríquez, J.A. Mind your mouse strain. *Nat. Metab.* **2019**, *1*, 5–7. [CrossRef]
39. Barr, J.T.; Tran, T.B.; Rock, B.M.; Wahlstrom, J.L.; Dahal, U.P. Strain-Dependent Variability of Early Discovery Small Molecule Pharmacokinetics in Mice: Does Strain Matter? *Drug Metab. Dispos.* **2020**, *48*, 613–621. [CrossRef]
40. Faille, C.; Michalski, J.C.; Strecker, G.; MacKenzie, D.W.; Camus, D.; Poulain, D. Immunoreactivity of neoglycolipids constructed from oligomannosidic residues of the *Candida albicans* cell wall. *Infect. Immun.* **1990**, *58*, 3537–3544. [CrossRef]
41. Navarro-Arias, M.J.; Hernández-Chávez, M.J.; Garcia-Carnero, L.C.; Amezcua-Hernández, D.G.; Lozoya-Pérez, N.E.; Estrada-Mata, E.; Martínez-Duncker, I.; Franco, B.; Mora-Montes, H.M. Differential recognition of *Candida tropicalis*, *Candida guilliermondii*, *Candida krusei*, and *Candida auris* by human innate immune cells. *Infect. Drug Resist.* **2019**, *12*, 783–794. [CrossRef] [PubMed]
42. Modrzewska, B.; Kurnatowski, P. Adherence of *Candida* sp. to host tissues and cells as one of its pathogenicity features. *Ann. Parasitol.* **2015**, *61*, 3–9.
43. Alloush, H.M.; Lopez-Ribot, J.; Masten, B.J.; Chaffin, W.L. 3-Phosphoglycerate kinase: A glycolytic enzyme protein present in the cell wall of *Candida albicans*. *Microbiology* **1997**, *143*, 321–330. [CrossRef] [PubMed]
44. Serrano-Fujarte, I.; López-Romero, E.; Cuéllar-Cruz, M. Moonlight-like proteins of the cell wall protect sessile cells of *Candida* from oxidative stress. *Microb. Pathog.* **2016**, *90*, 22–33. [CrossRef]
45. Han, Y.; Riesselman, M.H.; Cutler, J.E. Protection against Candidiasis by an Immunoglobulin G3 (IgG3) Monoclonal Antibody Specific for the Same Mannotriose as an IgM Protective Antibody. *Infect. Immun.* **2000**, *68*, 1649–1654. [CrossRef]
46. Yan, L.; Xia, K.; Yu, Y.; Miliakos, A.; Chaturvedi, S.; Zhang, F.; Chen, S.; Chaturvedi, V.; Linhardt, R.J. Unique Cell Surface Mannan of Yeast Pathogen *Candida auris* with Selective Binding to IgG. *ACS Infect. Dis.* **2020**, *6*, 1018–1031. [CrossRef] [PubMed]
47. Mullick, A.; Leon, Z.; Min-Oo, G.; Berghout, J.; Lo, R.; Daniels, E.; Gros, P. Cardiac Failure in C5-Deficient A/J Mice after *Candida albicans* Infection. *Infect. Immun.* **2006**, *74*, 4439–4451. [CrossRef] [PubMed]
48. Conti, H.R.; Huppler, A.R.; Whibley, N.; Gaffen, S.L. Animal Models for Candidiasis. *Curr. Protoc. Immunol.* **2014**, *105*, 19.6.1–19.6.17. [CrossRef]
49. Clancy, C.J.; Nguyen, M.H. Finding the "Missing 50%" of Invasive Candidiasis: How Nonculture Diagnostics Will Improve Understanding of Disease Spectrum and Transform Patient Care. *Clin. Infect. Dis.* **2013**, *56*, 1284–1292. [CrossRef]
50. Chen, T.; Wagner, A.S.; Tams, R.N.; Eyer, J.E.; Kauffman, S.J.; Gann, E.R.; Fernandez, E.J.; Reynolds, T.B. Lrg1 Regulates β (1,3)-Glucan Masking in *Candida albicans* through the Cek1 MAP Kinase Pathway. *mBio* **2019**, *10*, e01767-19. [CrossRef] [PubMed]

51. Wheeler, R.T.; Kombe, D.; Agarwala, S.D.; Fink, G.R. Dynamic, Morphotype-Specific *Candida albicans* β-Glucan Exposure during Infection and Drug Treatment. *PLoS Pathog.* **2008**, *4*, e1000227. [CrossRef] [PubMed]
52. Gavin, A.L.; Barnes, N.; Dijstelbloem, H.M.; Hogarth, P.M. Identification of the mouse IgG3 receptor: Implications for antibody effector function at the interface between innate and adaptive immunity. *J. Immunol.* **1998**, *160*, 20–23. [PubMed]
53. Satala, D.; Karkowska-Kuleta, J.; Zelazna, A.; Rapala-Kozik, M.; Kozik, A. Moonlighting Proteins at the Candidal Cell Surface. *Microorganisms* **2020**, *8*, 1046. [CrossRef]
54. Muñoz, J.F.; Gade, L.; Chow, N.A.; Loparev, V.N.; Juieng, P.; Berkow, E.L.; Farrer, R.A.; Litvintseva, A.P.; Cuomo, C.A. Genomic insights into multidrug-resistance, mating and virulence in *Candida auris* and related emerging species. *Nat. Commun.* **2018**, *9*, 5346. [CrossRef]
55. Naglik, J.R.; Fostira, F.; Ruprai, J.; Staab, J.F.; Challacombe, S.J.; Sundstrom, P. *Candida albicans* HWP1 gene expression and host antibody responses in colonization and disease. *J. Med. Microbiol.* **2006**, *55*, 1323–1327. [CrossRef] [PubMed]
56. Ruiz, G.B.; Ross, Z.K.; Gow, N.A.R.; Lorenz, A. Pseudohyphal Growth of the Emerging Pathogen *Candida auris* Is Triggered by Genotoxic Stress through the S Phase Checkpoint. *mSphere* **2020**, *5*, e00151-00120. [CrossRef]
57. Logtenberg, T. Antibody cocktails: Next-generation biopharmaceuticals with improved potency. *Trends Biotechnol.* **2007**, *25*, 390–394. [CrossRef]
58. Kumar, A.; Coquard, L.; Herbein, G. Targeting TNF-Alpha in HIV-1 Infection. *Curr. Drug Targets* **2015**, *17*, 15–22. [CrossRef]
59. Ramírez-Quijas, M.D.; López-Romero, E.; Cuéllar-Cruz, M. Proteomic analysis of cell wall in four pathogenic species of *Candida* exposed to oxidative stress. *Microb. Pathog.* **2015**, *87*, 1–12. [CrossRef]
60. Medrano-Díaz, C.L.; Vega-González, A.; Ruiz-Baca, E.; Moreno, A.; Cuéllar-Cruz, M. Moonlighting proteins induce protection in a mouse model against *Candida* species. *Microb. Pathog.* **2018**, *124*, 21–29. [CrossRef]
61. Nobile, C.J.; Nett, J.E.; Andes, D.R.; Mitchell, A.P. Function of *Candida albicans* Adhesin Hwp1 in Biofilm Formation. *Eukaryot. Cell* **2006**, *5*, 1604–1610. [CrossRef] [PubMed]
62. Černáková, L.; Roudbary, M.; Brás, S.; Tafaj, S.; Rodrigues, C. *Candida auris*: A Quick Review on Identification, Current Treatments, and Challenges. *Int. J. Mol. Sci.* **2021**, *22*, 4470. [CrossRef] [PubMed]
63. Nobile, C.J.; Johnson, A.D. *Candida albicans* Biofilms and Human Disease. *Annu. Rev. Microbiol.* **2015**, *69*, 71–92. [CrossRef]
64. Cavalheiro, M.; Teixeira, M.C. *Candida* Biofilms: Threats, Challenges, and Promising Strategies. *Front. Med.* **2018**, *5*, 28. [CrossRef] [PubMed]
65. Rodrigues, C.F.; Correia, A.; Vilanova, M.; Henriques, M. Inflammatory Cell Recruitment in *Candida glabrata* Biofilm Cell-Infected Mice Receiving Antifungal Chemotherapy. *J. Clin. Med.* **2019**, *8*, 142. [CrossRef] [PubMed]
66. Chupáčová, J.; Borghi, E.; Morace, G.; Los, A.; Bujdáková, H. Anti-biofilm activity of antibody directed against surface antigen complement receptor 3-related protein—Comparison of *Candida albicans* and *Candida dubliniensis*. *Pathog. Dis.* **2018**, *76*, ftx127. [CrossRef]
67. Saylor, C.; Dadachova, E.; Casadevall, A. Monoclonal antibody-based therapies for microbial diseases. *Vaccine* **2009**, *27*, G38–G46. [CrossRef] [PubMed]
68. Pachl, J.; Svoboda, P.; Jacobs, F.; Vandewoude, K.; Van Der Hoven, B.; Spronk, P.; Masterson, G.; Malbrain, M.; Aoun, M.; Garbino, J.; et al. A Randomized, Blinded, Multicenter Trial of Lipid-Associated Amphotericin B Alone versus in Combination with an Antibody-Based Inhibitor of Heat Shock Protein 90 in Patients with Invasive Candidiasis. *Clin. Infect. Dis.* **2006**, *42*, 1404–1413. [CrossRef] [PubMed]
69. Akiyama, M.; Oishi, K.; Tao, M.; Matsumoto, K.; Pollack, M. Antibacterial Properties of *Pseudomonas aeruginosa* Immunotype 1 Lipopolysaccharide-Specific Monoclonal Antibody (MAb) in a Murine Thigh Infection Model: Combined Effects of MAb and Ceftazidime. *Microbiol. Immunol.* **2000**, *44*, 629–635. [CrossRef] [PubMed]

International Journal of
Molecular Sciences

MDPI

Article

A Nano-Emulsion Platform Functionalized with a Fully Human scFv-Fc Antibody for Atheroma Targeting: Towards a Theranostic Approach to Atherosclerosis

Samuel Bonnet [1,2,*,†], Geoffrey Prévot [3,†], Stéphane Mornet [2], Marie-Josée Jacobin-Valat [1], Yannick Mousli [3], Audrey Hemadou [1], Mathieu Duttine [2], Aurélien Trotier [1], Stéphane Sanchez [1], Martine Duonor-Cérutti [4], Sylvie Crauste-Manciet [3,†] and Gisèle Clofent-Sanchez [1,†]

1 Centre de Résonance Magnétique des Systèmes Biologiques, CNRS UMR 5536, Université de Bordeaux, CRMSB, 33076 Bordeaux, France; marie-josee.jacobin-valat@rmsb.u-bordeaux.fr (M.-J.J.-V.); audrey.hemadou@orange.fr (A.H.); aurelien.trotier@rmsb.u-bordeaux.fr (A.T.); stephane.sanchez@rmsb.u-bordeaux.fr (S.S.); gisele.clofent-sanchez@rmsb.u-bordeaux.fr (G.C.-S.)
2 Institut de Chimie de la Matière Condensée, CNRS UMR 5026, Université de Bordeaux, Bordeaux INP, ICMCB, 33600 Pessac, France; Stephane.Mornet@icmcb.cnrs.fr (S.M.); Mathieu.Duttine@icmcb.cnrs.fr (M.D.)
3 ARNA, ARN, Régulations Naturelle et Artificielle, ChemBioPharm, INSERM U1212, CNRS UMR 5320, Université de Bordeaux, 33076 Bordeaux, France; geoffrey.prevot@gmail.com (G.P.); ymousli33@gmail.com (Y.M.); sylvie.crauste-manciet@u-bordeaux.fr (S.C.-M.)
4 CNRS UPS 3044, Baculovirus et Thérapie, 30380 Saint-Christol-lès-Alès, France; Martine.CERUTTI@cnrs.fr
* Correspondence: samuel.bonnet@univ-angers.fr
† These authors contributed equally.

Abstract: Atherosclerosis is at the onset of the cardiovascular diseases that are among the leading causes of death worldwide. Currently, high-risk plaques, also called vulnerable atheromatous plaques, remain often undiagnosed until the occurrence of severe complications, such as stroke or myocardial infarction. Molecular imaging agents that target high-risk atheromatous lesions could greatly improve the diagnosis of atherosclerosis by identifying sites of high disease activity. Moreover, a "theranostic approach" that combines molecular imaging agents (for diagnosis) and therapeutic molecules would be of great value for the local management of atheromatous plaques. The aim of this study was to develop and characterize an innovative theranostic tool for atherosclerosis. We engineered oil-in-water nano-emulsions (NEs) loaded with superparamagnetic iron oxide (SPIO) nanoparticles for magnetic resonance imaging (MRI) purposes. Dynamic MRI showed that NE-SPIO nanoparticles decorated with a polyethylene glycol (PEG) layer reduced their liver uptake and extended their half-life. Next, the NE-SPIO-PEG formulation was functionalized with a fully human scFv-Fc antibody (P3) recognizing galectin 3, an atherosclerosis biomarker. The P3-functionalized formulation targeted atheromatous plaques, as demonstrated in an immunohistochemistry analyses of mouse aorta and human artery sections and in an *Apoe*$^{-/-}$ mouse model of atherosclerosis. Moreover, the formulation was loaded with SPIO nanoparticles and/or alpha-tocopherol to be used as a theranostic tool for atherosclerosis imaging (SPIO) and for delivery of drugs that reduce oxidation (here, alpha-tocopherol) in atheromatous plaques. This study paves the way to non-invasive targeted imaging of atherosclerosis and synergistic therapeutic applications.

Keywords: atherosclerosis; nano-emulsion; magnetic resonance imaging; stealth; human antibody

Citation: Bonnet, S.; Prévot, G.; Mornet, S.; Jacobin-Valat, M.-J.; Mousli, Y.; Hemadou, A.; Duttine, M.; Trotier, A.; Sanchez, S.; Duonor-Cérutti, M.; et al. A Nano-Emulsion Platform Functionalized with a Fully Human scFv-Fc Antibody for Atheroma Targeting: Towards a Theranostic Approach to Atherosclerosis. *Int. J. Mol. Sci.* **2021**, *22*, 5188. https://doi.org/10.3390/ijms22105188

Academic Editors: Annamaria Sandomenico and Menotti Ruvo

Received: 25 March 2021
Accepted: 9 May 2021
Published: 14 May 2021

1. Introduction

Atherosclerosis is characterized by the development of lipid-rich plaques, called atheromatous plaques, in the artery wall [1]. Atheromatous plaques can be classified into two types: stable plaques and vulnerable plaques [2]. Stable plaques are usually rich in extracellular matrix and smooth muscle cells that maintain the integrity of these fibrous

plaques for years. Conversely, vulnerable plaques are rich in macrophages and inflammatory cells that make them prone to rupture, leading to cardiovascular complications [3–5].

Currently, angiography is normally used for imaging peripheral arterial disease [6]. However, it gives information only on vessel lumen reduction (stenosis) but not on the plaque morphology and risk of rupture [7]. Moreover, in two-thirds of ruptured plaques, stenosis is insignificant on angiograms [8,9]. Recently, other imaging modalities have emerged. For instance, intravascular ultrasound and optical coherence tomography [10–13] provide information on plaque morphology but are invasive procedures. Other non-invasive imaging strategies might offer new opportunities for atheroma diagnosis [14,15], particularly magnetic resonance imaging (MRI), which combines excellent soft-tissue contrast, good resolution, and absence of exposure to ionizing radiation [16–19].

MRI with highly specific targeting probes, in which contrast agents are conjugated to antibodies against molecular components of the atheromatous plaque, might allow the contrast agents to be directed specifically to the lesions. Molecular imaging of vulnerable plaques is of utmost interest because plaque composition might contribute to plaque rupture more than artery narrowing. The aim of this study was to develop an improved targeted contrast agent using nano-emulsions (NE) and the first human antibody (HuAb) against galectin-3 (HuAb P3, WO2019068863A1). Indeed, previous work demonstrated that oil-in-water NEs loaded with superparamagnetic iron oxide (SPIO) nanoparticles generated an accurate MRI signal, making them highly suitable as imaging agents [20,21]. The P3 antibody was chosen because galectin-3 is strongly expressed by the TREM2-positive foamy macrophage subset [22], which has been recently identified by single-cell RNA sequencing as the main immune cell subset in atherosclerosis. Importantly, the TREM2-positive subset endowed with specialized functions in lipid metabolism and catabolism was almost exclusively detectable in atherosclerotic aortas and present at different time points of lesion formation [23]. Moreover, using a HuAb decreases the potential immunogenicity in clinical settings. Before conjugation to the P3 HuAb, the NE surface was decorated with polyethylene glycol (PEG), the most common method to reduce clearance from the blood circulation [24]. PEG macromolecules create a protective hydrophilic layer around nanoparticles that can repel binding by opsonin proteins (i.e., opsonization) [25] and increase their half-life in the blood [26]. PEGylation of liposomes [27], micelles [28], and nanoparticles [29] has been widely investigated, but only a few works have focused on NE surface modification with PEG. Hak et al. [30] studied the impact of PEG surface density on NE half-life by blood sampling at different time points after administration in mice. Here, the effect of NE surface modification by PEG layers of different molecular weights (PEG_{2000} and/or PEG_{3400}) on liver uptake was studied by dynamic MRI. The HuAb P3 engineered via the single chain fragment variable (scFv)-Fc format was conjugated to the formulation with the lowest liver uptake and a longer half-life according to previous procedures [31].

Finally, theranostic PEGylated NEs loaded with SPIO nanoparticles and alpha-tocopherol were developed. Oral supplementation with alpha-tocopherol failed to show a clear benefit on the reduction of cardiovascular events in clinical trials [32]. Indeed, systemic administration does not allow one to reach the critical active concentration of the specific antioxidant at key sites [33]. In this study, we aimed to tackle this issue by proposing a targeted drug delivery strategy that could overcome the failure of specific tissue concentration of orally administered antioxidants. The antioxidant properties of PEGylated NEs loaded with SPIO nanoparticles and alpha-tocopherol were assessed as a multi-modal tool for atherosclerosis imaging and treatment.

2. Results

2.1. PEGylated NE Formulations and Characterization

Formulations were prepared using Miglyol 840, a neutral pharmaceutical oil based on propylene glycol diether of C8 and C10 saturated plant fatty acids. Two surfactants were used to stabilize the oily droplets, Tween 80 and Lipoid E80. The NE formulations were loaded with maghemite-based SPIO nanoparticles to develop T_2*-shortening MR contrast agents with relaxivity values close to the gold standard, as previously described [20]

(r_2^* = 42 to 45 $mM^{-1} \cdot s^{-1}$ and r_1 < 0.1 $mM^{-1} \cdot s^{-1}$). To produce stealth NEs with limited liver uptake and, consequently, a longer half-life in the blood circulation, the droplet surface was PEGylated. PEG creates a hydrophilic and biocompatible layer that limits opsonin adsorption [34,35] and non-specific cellular uptake compared with unmodified carriers. Several therapeutic strategies using PEG have been approved by the Food and Drug Administration (FDA) [25]. In this study, two lipid–PEG combinations with different molecular weight and functionalization were used: DSPE–PEG_{2000} and DSPE–PEG_{3400}–maleimide. The maleimide linker allows the conjugation of the HuAb P3. The two lipid–PEG combinations were added at the same molar concentration (5 μmol/mL) to the oily phase before the phase inversion step. Some formulations included only lipid–PEG_{2000} (#2), only lipid–PEG_{3400}–maleimide (#3), or a mixture of both (#4). Non-PEGylated NEs (#1) were used as controls.

Decoration of the droplet surface with PEG increased the hydrodynamic diameter from 175.8 nm for NE (#1) to 190.9 nm, 197.2 nm, and 191.0 nm, for NE–PEG_{2000} (#2), NE–PEG_{3400}–maleimide (#3), and NE–$PEG_{2000/3400}$–maleimide (#4), respectively. The size of all NE formulations remained in the submicronic range and their polydispersity index (PdI) was <0.2 (monodisperse samples) (Table 1). Thus, the formulation diameter remained smaller than the tiniest blood vessel, preventing their occlusion [36]. Moreover, the nature of the lipids associated with NE plasticity might favor deeper tissue penetration and biological barrier crossing [37].

Table 1. NEs' physicochemical data.

	NE	**NE–PEG_{2000}**	**NE–PEG_{3400}–Maleimide**	**NE–$PEG_{2000/3400}$–Maleimide**
Formulation Number	**(#1)**	**(#2)**	**(#3)**	**(#4)**
Mean diameter (nm) ± SD (n = 3)	175.8 ± 1.0	190.9 ± 2.2	197.2 ± 4.6	191.0 ± 2.4
Polydispersity index	0.108	0.134	0.115	0.097

NE: nano-emulsion; PEG: polyethylene glycol; SD: standard deviation.

SPIO nanoparticle inclusion in the oily droplets was confirmed by transmission electron microscopy (TEM) analysis (Figure S1). Nanoparticle tracking analysis (NTA) was used to determine the size and number of submicron particles. The size distribution was consistent with the dynamic light scattering (DLS) analysis results and the droplet number was $5.75 \times 10^{13} \pm 3.66 \times 10^{12}$ droplets per mL. To our knowledge, this is the first time oily droplet number has been determined to control the theoretical antibody:PEGylated NE ratio.

2.2. Stealthy Features of PEGylated NEs

Among the several promising new drug delivery systems, NEs are an advanced technology used to carry molecules to a specific site, and several NE formulations are already used in clinics [38–40]. Before improving NE targeting thanks to an antibody conjugated to its surface, it was important to characterize the in vivo stealthy feature of each NE formulation. Stealth is a parameter directly related to the half-life in the bloodstream. Here, the stealthy behavior of three PEGylated NE formulations ((#2), (#3), and (#4)) and of non-PEGylated NE ((#1); control) was studied by dynamic MRI after NE injection at the same iron concentration (3 mg/kg bodyweight) in the tail vein of C57BL/6 mice. The iron concentration of 3 mg/kg was chosen based on guidelines and doses used in the literature for ferumoxytol, approved by the FDA for anemia treatment. The dose of 3 mg/kg of ferumoxytol seems to be well tolerated for MRI-based diagnostic imaging without serious adverse events, according to a recent multi-centric study that underlined the positive safety profile [41]. Liver uptake was monitored continuously by MRI for about 10 min before and up to 50 min after injection (Figure 1).

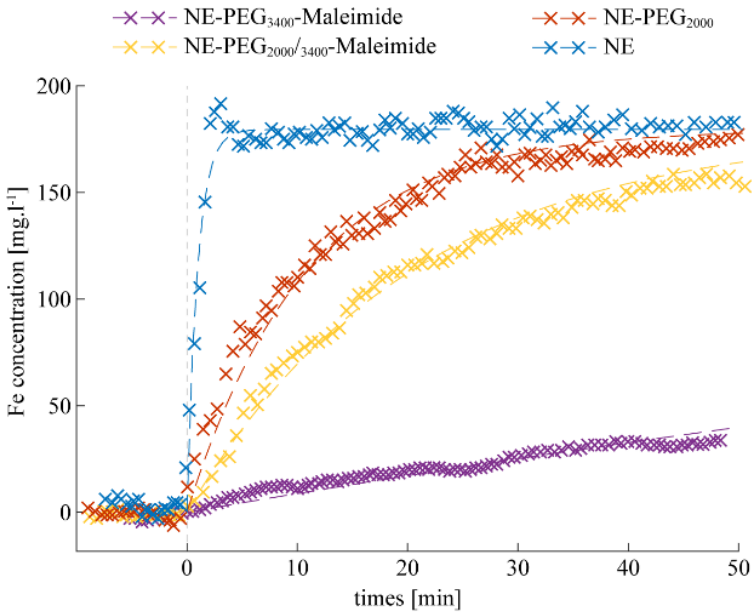

Figure 1. Estimation of the in vivo liver iron (Fe) uptake in mice by dynamic MRI after injection of the different NE formulations. Non-PEGylated NEs (#1) are rapidly cleared from the blood. NE-PEG_{3400}-maleimide (#3) displays the best stealth properties with very low liver accumulation at 50 min. NEs decorated with PEG_{2000} (#2) or PEG_{2000}/PEG_{3400}–maleimide (#4) displayed a similar profile, with a relatively rapid clearance. Each NE half-life was estimated from the corresponding graph (dashed lines in Figure 1; Table 2).

Table 2. Half-life of the tested NE formulations in the bloodstream.

	NE	NE–PEG_{2000}	NE–PEG_{3400}–Maleimide	NE–$PEG_{2000/3400}$–Maleimide	NE–PEG_{3400}–Maleimide-P3
Formulation Number	**(#1)**	**(#2)**	**(#3)**	**(#4)**	**(#5)**
Blood half-life (min) ± SD (n = 3) * (n = 1)	<1	7.2 ± 3.4	14.1 ± 2.5	138.7 ± 11.2	103 *

Depending on the lipid–PEG molecular weight, the formulations displayed different liver uptake patterns. After injection, the non-PEGylated formulation (#1) rapidly accumulated in the liver and the signal was saturated at 2 min after injection, confirming its less stealthy properties. Such rapid NE clearance is consistent with literature data showing that typically up to 90% of the formulation is taken up by the liver within 5 min [36]. NEs decorated with lipid–PEG_{2000} (#2) or the mixture of two PEGs (#4) showed similar clearance profiles, with a rapid liver uptake after injection, although it was slower compared with (#1). NEs functionalized with lipid–PEG_{3400}–maleimide (#3) showed the lowest liver uptake at 50 min post-injection, and therefore the best stealth profile. The MR signal in the kidneys remained stable throughout the in vivo experiments, with all tested formulations.

On the basis of these in vivo results, the NE–PEG_{3400}–maleimide (#3) formulation was chosen, due to its having the lowest liver uptake, for conjugation with scFv-Fc-2Cys P3 HuAb to obtain NE-P3 (#5). The next experiments focused on the characterization of NE-P3 (#5).

2.3. Bio-Conjugation with P3 HuAb and In Vivo Clearance of NE-P3

Conjugation of HuAb P3 to the NE–PEG_{3400}–maleimide surface (NE-P3, (#5)) induced an increase in NE diameter, assessed by DLS (199.5 ± 2.3), as previously reported [20]. The formulation of NE-P3 (#5) was monodisperse (PdI = 0.167) and its size was still in the submicronic range, with a diameter similar to that of commercial NEs used for human

parenteral nutrition [36]. To determine whether the addition of antibody affected the formulation's stealthy properties, the in vivo clearance of the NE-P3 (#5) formulation was evaluated by dynamic MRI monitoring of liver uptake for 24 h after injection in the tail vein of one *Apoe*$^{-/-}$ mouse (Figure 2). This experiment allowed calculation of the NE-P3 (#5) half-life (103 min) in blood (Table 2).

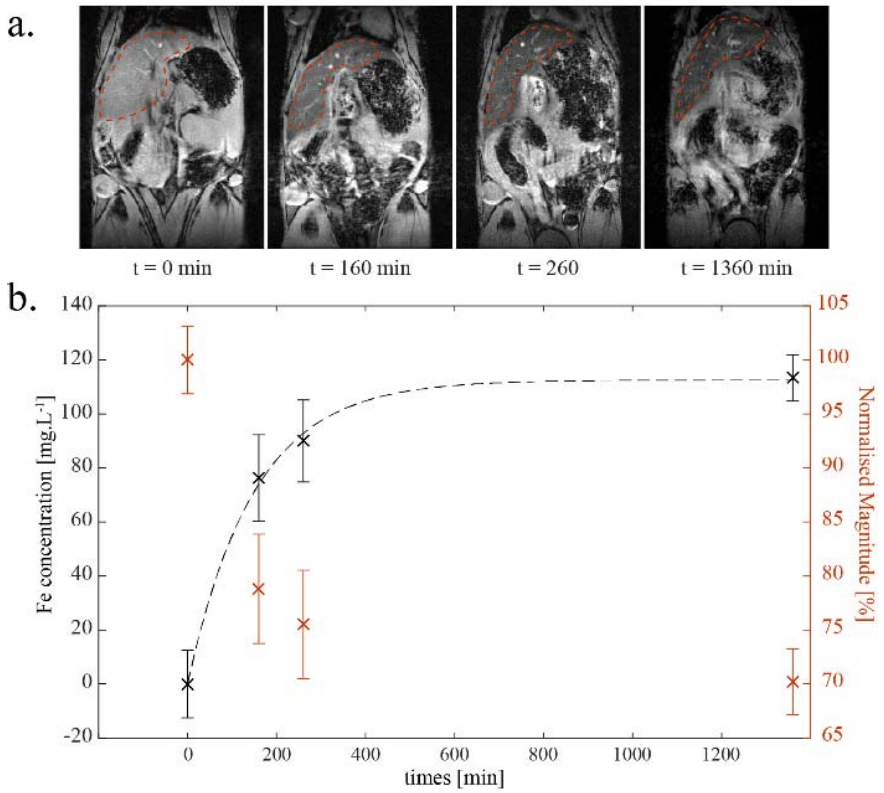

Figure 2. NE-P3 (#5) half-life in the bloodstream was determined by dynamic MRI. (**a**): MR images at different time points showing the regions of interest (ROI, inside the red dashed lines) that encompass the liver and were used to measure the mean magnitude of the signal. (**b**): Mean normalized magnitude of the signal (red) and the corresponding iron concentration (black) estimated from the transverse relaxivity r_2^* of NE- P3 (#5). Error bars come from the normalized magnitude's standard deviation of the voxels included in each ROI. The conjugation of biological moieties (scFv-Fc-2Cys P3 HuAb) to the PEGylated NE surface decreased the NE's half-life in the blood from 139 min to 103 min (calculated from the graph of the iron concentration, dashed line).

After calculation of NE-P3's (#5) half-life in the bloodstream, its targeting efficiency was assessed in vitro, in vivo, and ex vivo (see below).

2.4. In Vitro Atheroma Targeting

First, NE-P3's (#5) ability to specifically target atheromatous plaques was tested by immunohistochemistry (IHC) using aorta tissue sections from hypercholesterolemic *Apoe*$^{-/-}$ mice. A strong positive signal was observed only in aorta sections incubated with NE-P3 (#5) (Figure 3(Ab)), but not with NE–PEG_{3400}–maleimide (#3) (without antibody) (Figure 3(Ad)). The uniform intense signal obtained with NE-P3 (#5) compared with the free P3 antibody, used at the same concentration, (compare Figure 3(Aa,Ab)) is certainly due to the ratio of 14 antibody molecules per PEGylated NE droplet used for the bio-conjugation that contributed to increase P3's binding avidity.

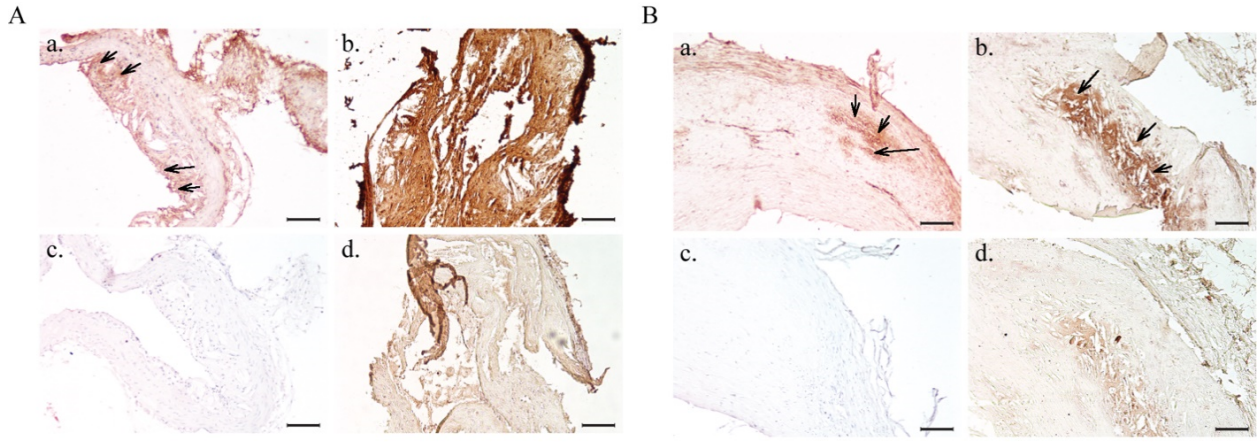

Figure 3. IHC analysis of aorta sections from hypercholesterolemic *Apoe*$^{-/-}$ mice (**A**) and human endarterectomy samples (**B**). NE-P3 (#5) can recognize galectin-3 in mouse aorta sections (**Ab**) and in human samples (**Bb**). No signal was observed with NE–PEG_{3400}–maleimide (#3) (without antibody) (**Ad**,**Bd**) and in the negative control (secondary antibody only: **Ac**,**Bc**). Unconjugated scFv-Fc-2Cys P3 (**Aa**,**Ba**) was used as a positive control. Black arrows highlight specific binding by P3 or NE-P3 (#5). Scale bar: 250 µm (upper panels) and 100 µm (lower panels). Two tissue blocks were used for mouse aorta sections labeling in Panel A (one for a and c, and another for b and d). The same tissue block from the same patient was used in Panel B. The mouse aorta and endarterectomy sections shown are representative images taken from successive stained sections. Three independent experiments were performed with these formulations (a section per formulation).

Next, NE-P3 (#5) and PEG_{3400}-maleimide (#3) were tested on human endarterectomy samples (Figure 3B). As before, a strong signal was observed only in atheromatous plaques incubated with NE-P3 (#5) (Figure 3(Bb)) but not with NE-PEG_{3400}-maleimide (#3) (Figure 3(Bd)). The faint signal observed with NE–PEG_{3400}–maleimide (#3) was mostly due to human immunoglobulins in atheromatous plaques. Moreover, the NE-P3 (#5) signal was stronger than that of the unconjugated P3 antibody (positive control) (Figure 3(Ba)), as observed in the mouse sections. These findings indicate that NE-P3 (#5) efficiently targets atheromatous lesions in mouse aortas (pre-clinical model) and also in human endarterectomy samples (for future translational assays). These results underline NE-P3's (#5) potential as a new molecular contrast agent to target atherosclerosis by binding to galectin-3.

2.5. Preliminary Data on In Vivo Atheroma Targeting by NE-P3

To determine whether NE-P3 (#5) can also target atheromatous plaques in vivo, this formulation was injected in the tail vein of one *Apoe*$^{-/-}$ mouse and atheroma targeting was monitored by MRI. The T_2* relaxation maps of atheromatous plaques were then computed from a multi-slice (RF)-spoiled gradient echo sequence (multi-echo GRE) obtained at 4.7 T at different time points: before (baseline), 7 h, and 24 h after NE-P3 (#5) injection. Aorta segmentation and T_2* mapping were performed concomitantly by two skilled experimenters. The slice-by-slice diagrams representing the T_2* mean values (in ms) at baseline, 7 h and 24 h post-injection calculated by the two experimenters (Figure 4A) showed a slice-by-slice decrease in the T_2* mean values, with differences between slices particularly at 7 h after injection. As the plaque characteristics (e.g., size, permeability, components) can change along the aorta, it is not surprising to observe differences in T_2* decrease from one slice to another. Figure 4B–D shows the segmented T_2* maps of the abdominal atheromatous plaque for the same five adjacent slices before, at 7 h, and at 24 h after injection, respectively. For each slice, the T_2* map was overlaid on its corresponding magnitude image (i.e., the last panel, in the lower right corner, for each time point in Figure 4B–D). Comparisons of the data at the three time points (Figure 4B–D) highlighted the decrease in T_2* values at 7 h post-injection and their increase again (but still lower than at baseline) at 24 h post-injection. These first results showed that NE-P3 (#5) could be used for in vivo targeting

of atheromatous plaques and indicated that the in vivo behavior of NE-P3 (#5) must be accurately monitored over time to determine the optimal imaging window.

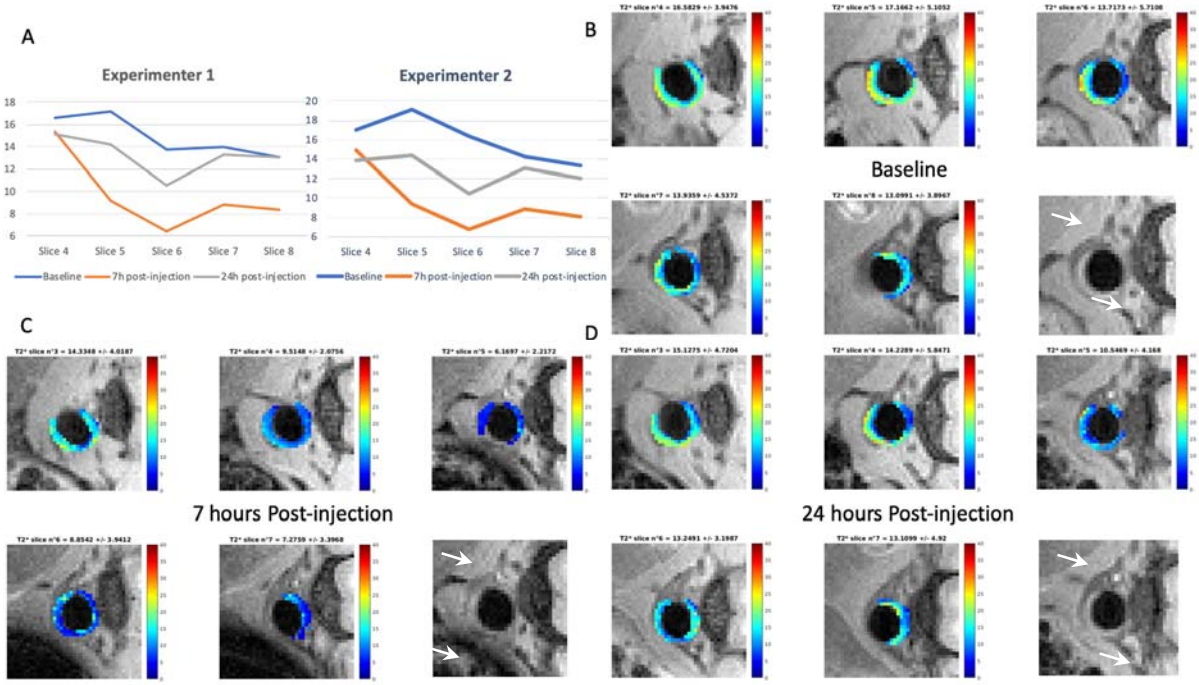

Figure 4. In vivo atheroma T_2* variations after injection of NE-P3 (#5). (**A**): Diagrams made by two experimenters representing the T_2* mean values (in ms) for each slice of the abdominal aorta of one *Apoe*$^{-/-}$ mouse at baseline, 7 h, and 24 h after NE-P3 (#5) injection. Typical segmented T_2* maps of five slices before (**B**), 7 h (**C**), and 24 h (**D**) after NE-P3 (#5) injection, shown with the color scale. Slices 4, 5, 6, 7, and 8 before injection correspond to Slices 3, 4, 5, 6, and 7 after injection. After injection, great care was taken to reposition the mouse in exactly the same way as before injection; however, sections before and after injection could be shifted by one or two slices. The corresponding magnitude image (first echo) of the third slice in each dataset (i.e., Slice 6 at baseline and Slice 5 post-injection) is shown in the rightmost lower panel at each time point. In this image, the atheromatous plaque is clearly visible in white (arrow). Slice-by-slice T_2* maps were obtained using a homemade MATLAB-based tool.

2.6. Ex Vivo Analyses of Isolated Aorta Samples

Ex vivo studies were then carried out after in vivo MRI imaging to confirm the presence of the targeted contrast agent in the aorta using two methods: MRI (to visualize the areas with a decreased T_2* signal) and Electron Spin Resonance (ESR, to quantify the iron present in the aorta).

2.6.1. Ex Vivo MRI

Ex vivo MRI scans of the aorta embedded in agarose gel after isolation from one *Apoe*$^{-/-}$ mouse following in vivo injection of NE-P3 (#5) in the tail vein highlighted the intimal thickening characteristic of an atherosclerotic plaque. A drop in the MR signal due to the T_2* effect characterized the accumulation of the iron oxide-based targeted contrast agent in the atherosclerotic lesions (black arrows in Figure 5).

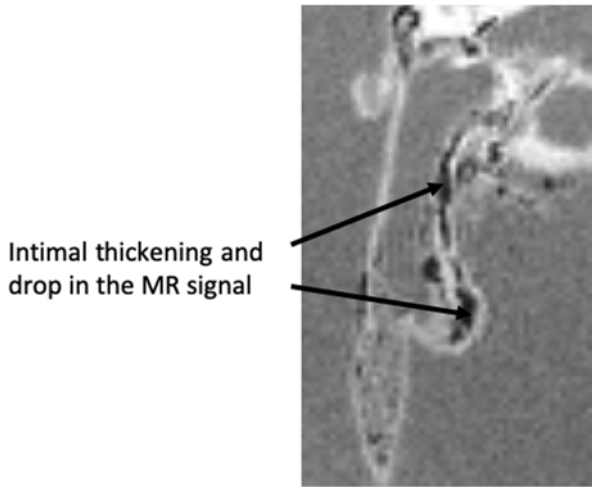

Figure 5. MRI magnitude image of the agarose-embedded aorta after isolation from one *Apoe*$^{-/-}$ mouse following in vivo injection of NE-P3 (#5) in the tail vein. Black arrows highlight the decrease in the MR signal.

2.6.2. Iron Oxide Accumulation Assessment by ESR

Iron quantification by ESR in the same isolated aorta corroborated the detection of iron accumulation in the atheromatous plaque due to NE-P3 (#5) targeting. After injection, the broad and intense ESR signal detected at about 320 mT (g = 2.12) with a peak-to-peak line width of about 80 mT (Figure 6) was due to the presence of Fe_2O_3 nanoparticles at an estimated concentration of $1.7 \pm 0.4 \times 10^{-8}$ mol/g in the analyzed tissue.

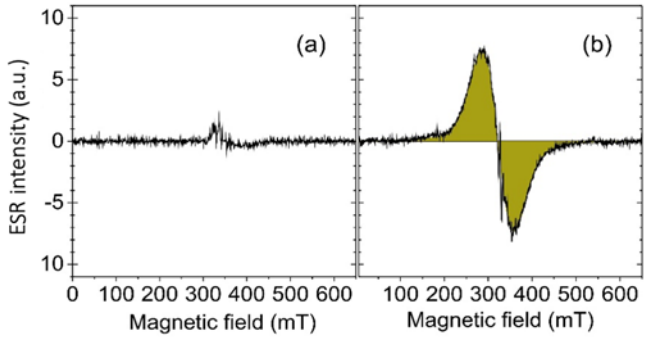

Figure 6. Room temperature X-band (9.54 GHz) Electron Spin Resonance (ESR) spectra of (**a**) an aorta isolated from a *Apoe*$^{-/-}$ mouse untreated (control) and (**b**) from a *Apoe*$^{-/-}$ mouse after NE-P3 (#5) injection.

2.7. Antioxidant Alpha-Tocopherol-Containing NEs for a Theranostic Approach: Formulation, Characterization, and Activity

For this theranostic approach, NE samples decorated with PEG_{3400}–maleimide (4.4 μmol·mL^{-1}) were combined with alpha-tocopherol and SPIO (12.5 μmol·mL^{-1}) in the oily phase (NE–PEG_{3400}–maleimide–SPIO–tocopherol, (#10)) (Table 3). To determine the antioxidant or prooxidant contribution of each component of this formulation, four other formulations were assessed as controls (Table 3). All formulations were in the submicronic size range and monodisperse (PdI < 0.3) (Table 4).

Table 3. NE composition for the antioxidant assessment.

	NE	NE–Tocopherol	NE–PEG_{3400}–Maleimide–SPIO	NE–PEG_{3400}–Maleimide–Tocopherol	NE–PEG_{3400}–Maleimide–SPIO–Tocopherol
Formulation Number	**(#6)**	**(#7)**	**(#8)**	**(#9)**	**(#10)**
Miglyol 840 (%)	20	15	20	15	15
Alpha-tocopherol (%)	-	5	-	5	5
Tween 80 (%)	2.5	2.5	2.5	2.5	2.5
Lipoid 80 (%)	1.2	1.2	1.2	1.2	1.2
Milli-Q water (%)	qs 100	qs 100	qs 100	qs 100	qs 100
SPIO (µmol/mL)	-	-	12.5	-	12.5
Lipid–PEG_{3400}–maleimide (µmol/mL)	-	-	4.4	4.4	4.4

SPIO: superparamagnetic iron oxide nanoparticles; qs: quantum satis.

Table 4. NE characterization.

	NE	NE–Tocopherol	NE–PEG_{3400}–Maleimide–SPIO	NE–PEG_{3400}–Maleimide–Tocopherol	NE–PEG_{3400}–Maleimide–SPIO–Tocopherol
Formulation Number	**(#6)**	**(#7)**	**(#8)**	**(#9)**	**(#10)**
Mean diameter (nm) ± SD (n = 3)	173.5 ± 0.8	171.7 ± 0.5	162.6 ± 2	181.3 ± 1.8	213.7 ± 1.2
Polydispersity index	0.140	0.152	0.123	0.163	0.255

First, the antioxidant properties of these NE formulations were assessed by comparing their ability to increase the time to produce the hemolysis of 50% of red blood cells (T50% hemolysis, in minutes) after the initiation of free radical attack (Figure 7).

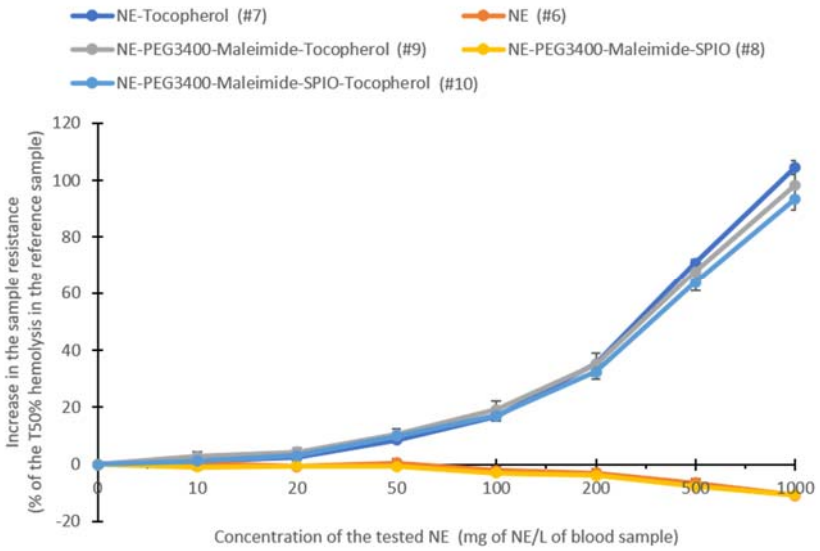

Figure 7. "Kit Radicaux Libres" test (KRL test) to determine the antioxidant properties of the tested NE formulations (Table 3). The graph shows the change (in percent) of the time in which 50% of red blood cells were lysed (T50% hemolysis in minutes) after the initiation of free radical attack relative to the control sample (n = 3).

The results indicated that NEs without alpha-tocopherol (#6) and NE–PEG_{3400}–maleimide–SPIO (#8)) had a slight prooxidant effect. When used at the concentration of 1000 mg/L, they reduced the T50% hemolysis by 10.95% and 10.66%, respectively, compared with the reference sample. Conversely, alpha-tocopherol-containing formulations ((#7), (#9), and (#10)) at the concentration of 1000 mg/L) significantly and similarly

increased the T50% hemolysis by up to 104.63%. However, the presence of iron oxide nanoparticles (#10) slightly hindered alpha-tocopherol's antioxidant activity. Furthermore, when the results were expressed as Trolox equivalents (Figure 8), which is a water-soluble analog of Vitamin E commonly used in biological and biochemical applications as an antioxidant reference, the Trolox equivalent of 1 g of alpha-tocopherol-containing NEs ranged from 39.88 mg to 44.62 mg. These values were close to the amount of alpha-tocopherol loaded in the NEs (50 mg), thus proving that the formulation does not impair or hinder alpha-tocopherol's antioxidant activity.

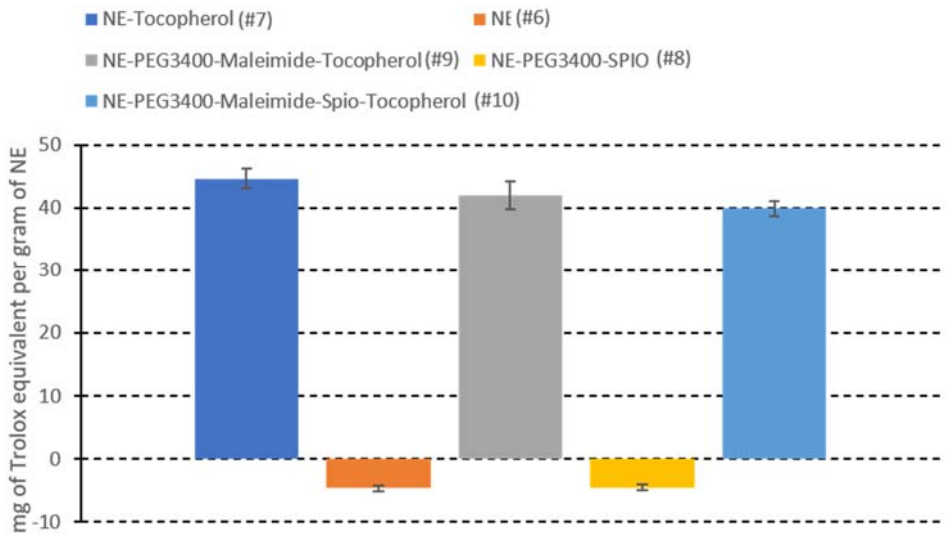

Figure 8. Antioxidant properties of the tested NE formulations expressed as mg of Trolox equivalent per gram of NE (n = 3).

3. Discussion

As cardiovascular complications caused by atherosclerosis are the leading cause of death in Western countries, it is crucial to develop tools for the early detection of vulnerable atheromatous plaques. In this context, the combination of nanotechnology and molecular imaging is a promising non-invasive strategy for detecting unstable plaques. Providing multi-territorial imaging of the atherosclerotic disease burden is now seen as necessary for a comprehensive patient assessment. Indeed, the mechanism of "vulnerable" plaque rupture is clearly more complex than initially assumed, and focusing only on the treatment of a single atherosclerotic plaque may not necessarily lead to a survival advantage. Proof of this is a recent systematic review and meta-analysis showing that there is no survival benefit of revascularization among patients with stable ischemic heart disease [42]. Numerous clinical investigations have demonstrated that many plaques rupture without clinical symptoms [43]. Moreover, plaque morphology changes over a few months, highlighting the necessity of longitudinal imaging studies. Our strategy is in keeping with new concepts indicating that risk would be more strongly predicted by detecting the total atheromatous burden of the arterial tree in the whole body [44]. The development of non-invasive molecular MRI imaging modality using contrast agents functionalized with antibodies capable of detecting high-risk plaques would allow longitudinal studies and assess the dynamic nature of atherosclerotic disease for a comprehensive approach to the atheroma burden in the "vulnerable" patient.

Due to their high magnetic susceptibility and nanometric size, SPIO nanoparticles have been extensively investigated as MRI contrast agents [5]. However, they must be loaded into a nanocarrier to improve their biocompatibility and half-life. In this work, SPIO nanoparticles made hydrophobic by an oleic acid coating were loaded inside the oily core of PEGylated NEs functionalized with the first anti-galectin-3 human antibody for specific atheroma targeting. When classical iron oxide-based contrast agents are used,

the MR signal changes observed during their accumulation in tissues are weighted both by the R_2^* and R_1 effects. In the environment of oily droplets, SPIO nanoparticles do not have any access to water and, therefore, their tissue accumulation mainly affects the local R_2^* relaxation rate (and not the R_1). We took advantage of the "pure" R_2^*-increasing effect obtained in oily droplets to estimate the blood half-life of each tested NE formulation.

NEs have been in medical use for more than five decades as a parenteral nutrition system for patients who cannot be fed orally (e.g., Intralipid, approved in Europe in 1962) [36]. The huge potential of NEs as drug delivery systems is currently unexploited despite the advantages compared with other nanocarriers [45,46]. To target atheroma with NEs, their half-life must be increased. This is commonly achieved by decorating the droplet surface with PEG chains (i.e., PEGylation) to delay opsonization. PEG has the advantages of being FDA-approved, soluble in hydrophilic and hydrophobic phases, non-toxic, and non-immunogenic [47]. PEG is also available in different molecular weights. For long-term circulation, PEG chains with a molecular weight of at least 2000 must be used [45,48–50].

To our knowledge, only a few studies have investigated how to prolong the half-life of PEGylated NEs [30,51,52]. Cheng et al. studied how different molecular weights and different concentrations of lipid–PEG affected NE size but did not analyze their pharmacokinetic profiles [52]. Hak et al. studied the influence of lipid–PEG_{2000} density on NE pharmacokinetics by fluorescence analysis of animal serum samples [53]. In all these studies, NE pharmacokinetics were assessed by blood sampling, while our approach relies on the in vivo determination of NE uptake by the liver using MRI. In our study, the kinetics of four NE formulations were compared. The mean NE diameters tended to increase with the increase in PEG molecular weight, confirming PEG's brush-like conformation, whereas a mushroom-like conformation would result in a decrease in NE diameter [51–54]. Dynamic MRI is a powerful tool to rapidly follow, in a longitudinal manner, the stealth properties of nanocarriers over time, in contrast to classical methodologies that rely on blood sampling at defined time points.

The dynamic MRI approach showed that the half-life of NE–PEG_{3400}–maleimide (#3) was significantly increased compared with the other formulations. Stealth properties are important for extending the half-life and consequently improving the targeting efficacy. To develop an optimized tool for molecular imaging of atherosclerosis, an atheroma-specific HuAb, P3, was chosen for conjugation to the NE–PEG formulation with the longest half-life (NE–PEG_{3400}–maleimide (#3)). P3 specifically targets galectin-3, a protein that has been highlighted in recent studies as a new atherosclerosis biomarker [55]. P3 was discovered by in vivo phage-display selection in an animal model of atherosclerosis using a human scFv library [56,57]. Its ability to target galectin-3 within atherosclerotic lesions has been demonstrated in vitro and ex vivo (patent WO2019068863A1). P3 variable domains were engineered in the scFv-Fc format with a 2Cys tag for site-specific conjugation to NE–PEG_{3400}–maleimide (#3) using thiol–maleimide "click" chemistry. Site-specific conjugation has many advantages; particularly, it maintains bioreactivity and can be achieved on the Fc fragment. A theoretical ratio of 14 antibodies per droplet was chosen for efficient molecular targeting, without denaturing the system. Indeed, previous work on SPIO nanoparticles showed that too high a ratio causes object flocculation. Compared with other synthetic nanocarriers, such as SPIO and ultrasmall paramagnetic iron oxide (USPIO) nanoparticles, which are rigid objects, oily droplets have a soft consistency and can efficiently cross the vascular fenestrae of the impaired endothelium and penetrate into the targeted lesions, even if their size is >25 nm. Other groups have demonstrated that lipid-based formulations up to 200 nm in diameter can enter a plaque [58–60]. The preliminary results of the assay testing whether in vivo NE–PEG_{3400}–maleimide-P3 (#5) can target the atheromatous plaques located in the abdominal aorta of one $Apoe^{-/-}$ atherosclerotic mouse are sufficiently encouraging to justify additional in vivo MRI studies to determine the best imaging window. To this end, the contrast agent's accumulation must be accurately monitored at different time points: directly after injection and up to 48 h post-injection.

In this work, IHC experiments showed that the P3 HuAb can recognize galectin-3 in the *Apoe*$^{-/-}$ mouse aorta and also in human atheroma samples. It should be noted that the ligands used in the more recent studies for functionalizing nanoparticles, micelles, or liposomes tend to be non-immunogenic molecules that cross-react with different species, including humans [61–63]. This could facilitate the translation from pre-clinical to clinical studies. Additionally, if the developed diagnostic agents reach the clinics, the use of human antibodies will limit the risk of immunogenicity, thus saving the time required for the humanization of murine antibodies.

Finally, the use of such NEs as a potential theranostic tool was demonstrated using alpha-tocopherol as an antioxidant agent that could reduce the proliferation of radical species inside the atheromatous plaque, thus potentially decreasing the risk of rupture. The "Kit Radicaux Libre" test (KRL test) clearly showed that alpha-tocopherol-containing NEs display antioxidant properties (not observed with NEs without alpha-tocopherol), and also that the full potential of the encapsulated antioxidant agent is available to counteract a free radical attack. Indeed, the antioxidant activity expressed in Trolox equivalents was close to the amount of antioxidant agent loaded inside the NEs, demonstrating that all the alpha-tocopherol contained in the formulation was used in the test. However, it is worth noting that adding SPIO nanoparticles may have a slight prooxidant effect. Moreover, a limitation of this study is the lack of a toxicity assessment. If we want to further develop this theranostic approach using NE formulations that include SPIO nanoparticles, this point should be addressed in priority, although, here, NE-P3 was injected at 3 mg/kg, which was lower than the dose of ferumoxytol, an intravenous iron preparation, used in clinics to treat iron deficiencies. Overall, these results encourage us to develop a complex multi-modal theranostic approach for the diagnosis and treatment of atherosclerosis that could be tested longitudinally in small animal models of this disease in pre-clinical studies. The full potential of the theranostic approach would need to be tested in future in vivo studies using the NE–PEG_{3400}–maleimide formulation loaded with SPIO and tocopherol, and functionalized with the scFv-Fc P3 human antibody.

More generally, this work shows the development of a nanomedicine platform that could be advantageously used with stronger reductant molecules chemically derived from tocopherol [33] or other payloads such as prostacycline for its anti-aggregant properties, which are of high value in atherothrombosis [64]. It could also be used with alternative HuAbs. An anti-platelet HuAb under the same format including cysteines for site-specific functionalization has been successfully grafted on the same platform [20]. The SPIO-loaded NE–PEG_{3400}–maleimide formulation could thus be adapted to other pathologies, just by changing the active principle and the targeting HuAb.

4. Materials and Methods

4.1. Materials

Purified Miglyol 840 (oil phase) was kindly provided by IOI OLEO GmbH (Hamburg, Germany). Egg lecithin containing 82.3% phosphatidylcholine (Lipoid E80) and N-(carbonyl-methoxypolyethylenglycol-2000)-1,2-distearoyl-sn-glycero-3-phosphoethanolamine (DSPE–PEG_{2000}) were provided by Lipoid GmbH (Ludwigshafen, Germany); polysorbate 80 (Tween 80) was purchased from SEPPIC (Paris, France). The hetero-bifunctional linker 1,2-distearoyl-sn-glycero-3-phosphoethanolamine-N-poly(ethylene glycol)-maleimide (DSPE–PEG_{3400}–maleimide) was purchased from Laysan Bio, Inc. (Arab, AL 35016, USA). SPIO nanoparticles were synthesized and made hydrophobic by following previously described procedures [65–67]. Tris(2-carboxyethyl)phosphine hydrochloride (TCEP; $\geq$98%), hydrochloric acid, formic acid, the PBS buffer, sodium hydroxide, and IgG were bought from Sigma-Aldrich (St. Louis, MO 63178, USA). The PBS–heparin solution was from Sanofi Aventis (Vitry-sur-Seine, France). Glycerol was purchased from Cooperation Pharmaceutique Française (Melun, France). MACS Cell Separation Columns were from Miltenyi Biotec (Bergisch Gladbach, Germany).

4.2. NE Formulations

NEs were formulated as previously described [20]. Briefly, 12 mg of Lipoid E80 was dispersed in 200 mg of Miglyol 840 (IOI Oleo GmbH, Hamburg, Germany) by heating, followed by addition of 12.5 µmol/mL SPIO nanoparticles. The aqueous phase was a dispersion of 25 mg Tween 80 in 800 mg Milli-Q water. For NE PEGylation, lipid–PEG at different molecular weights (DSPE–PEG_{2000} and/or DSPE–PEG_{3400}-maleimide) was added at 5 µmol/mL. A molar ratio of 3:1 was used for the PEG_{2000}/PEG_{3400}–maleimide mixture. The composition of the different NE formulations is described in Table 5. NE-P3 was obtained after bio-conjugation with HuAb P3, as described in Section 4.4.

Table 5. NE composition.

	NE	**NE–PEG_{2000}**	**NE–PEG_{3400}–Maleimide**	**NE–$PEG_{2000/3400}$–Maleimide**	**NE–PEG_{3400}–Maleimide–P3**
Formulation Number	**(#1)**	**(#2)**	**(#3)**	**(#4)**	**(#5: NE-P3)**
Miglyol 840 (%)	20	20	20	20	20
Tween 80 (%)	2.5	2.5	2.5	2.5	2.5
Lipoid 80 (%)	1.2	1.2	1.2	1.2	1.2
Milli-Q water (%)	qs 100	qs 100	qs 100	qs 100	qs 100
SPIO (µmol/mL)	12.5	12.5	12.5	12.5	12.5
Lipid–PEG_{2000} (µmol/mL)	-	5	-	3.8	-
Lipid–PEG_{3400}–maleimide (µmol/mL)	-	-	5	1.2	5
P3 antibody (nmol/mL)	-	-	-	-	1.9

Alpha-tocopherol-containing NEs were obtained as before, except that the oily phase included 50 mg of alpha-tocopherol and 150 mg of Miglyol 840. The compositions of the different theranostic NE formulations are described in Table 3.

All mixtures were emulsified by phase inversion and homogenized by sonication (Sonic Vibra Cell–VC 250 set at 70% and output 7; Sonics & Materials Inc, Newtown, CT 06470, USA) to obtain oil droplets in the submicron size range. Before the in vitro and in vivo experiments, the pH of the different formulations was adjusted to the physiological value using 0.1 N sodium hydroxide, and 2% glycerol was added to adjust osmolality.

4.3. NE Characterization

The physical characteristics of the NE formulations were assessed by DLS, Zeta potential measurement, and TEM. The hydrodynamic size was determined using a DLS device (Zetasizer Nano ZS; Malvern Instruments, Malvern, UK) and with the NEs diluted to 1:1000 (v/v) (mean of 3 independent measurements performed at 25 °C). The Zeta potential was measured using a Zetasizer Nano ZS device coupled to a Folded Capillary Cell (DTS1060) from Malvern Instruments. Oily droplets were quantified by NTA using a NanoSight NS300 instrument (Malvern Instruments). A Hitachi H7650 transmission electron microscope linked to an ORIUS SC1000 11MPX (Gatan Inc., Pleasanton, CA, USA) camera run by Digital Micrograph (Gatan Inc.) was used to study the NE samples (1:50 dilution, v/v) transferred to a carbon-coated copper grid. Iron concentration was quantified by UV spectrometry as previously described [66].

4.4. P3 Antibody Bio-Conjugation to NEs

To achieve optimal targeting of atheromatous plaques, the HuAb P3 was engineered in the single chain fragment variable (scFv)-Fc format with a 2-cysteine tag (ScFv-Fc-2Cys) for site-specific conjugation to the NE's surface. The production of antibodies with this cysteine tag has been described previously for the TEG4 antibody [31]. Before bio-conjugation to NE–PEG_{3400}–maleimide (#3), the thiol groups on the cysteine tag of ScFv-Fc-2Cys P3 were activated using TCEP (20 mol per mol of P3). Antibody conjugation to the thiol-reactive maleimide of NE–PEG_{3400}–maleimide (#3) to obtain NE-P3 (#5) was performed overnight

with a theoretical ratio of 14 antibody molecules per NE droplet. Unconjugated antibodies were removed using a magnetic sorting column (MACS Cell Separation Columns), as previously described [31].

4.5. In Vitro Immunoreactivity Analysis by IHC

NE-P3 immunoreactivity was assessed by IHC using paraffin-embedded tissue sections of mouse and human atheromatous plaques. Human biopsies were provided by the vascular and general surgery service of the Pellegrin academic hospital, Bordeaux, France. Samples were from patients who underwent endarterectomy after an acute vascular event. All clinical interventions were carried out at Pellegrin hospital and the use of human samples for research was approved by the Bordeaux CPP ethics committee (Comité de Protection des Personnes Sud-Ouest et Outre Mer) and by the French Research Ministry (Authorization number DC-2016-2724). The CPP committee waived the need for the patients' written consent because surgical waste no longer attached to the person is considered res nullius. Nevertheless, the patients were informed by the clinicians; if they did not express their opposition to research, de-identified samples were immediately processed and embedded in paraffin. IHC experiments were performed as previously described [31]. Briefly, after deparaffinization, heat-induced epitope retrieval and non-specific interaction blocking, as described in [56], aorta sections were incubated with NE-P3 ((#5), 53 μg/mL of P3 antibody, 158 mg/L of Fe), unconjugated NE–PEG_{3400}–maleimide ((#3), 158 mg/L of Fe), ScFv-Fc-2Cys P3 HuAb (53 μg/L) (positive control), or the diluent alone (negative control) overnight. This was followed by incubation with the secondary HRP-conjugated goat anti-human antibody (Fcγ-specific; 1:1000 (*v*/*v*) (Jackson ImmunoResearch; West Grove, PA, USA), and antibody binding was revealed using the Dako Liquid DAB+ Substrate Chromogen System (Agilent Technologies Inc, Santa Clara, CA, USA).

4.6. In Vivo Experimental Animal Model

Six-week-old female C57BL/6 mice (weighing 17 to 18 g) and 8- to 12-month-old JAX *Apoe*$^{-/-}$ mice (28 to 32 g) were purchased from Charles River Laboratories (Saint Germain Nuelles, France) and housed under a 12 h light/dark cycle with food and water provided ad libitum. *Apoe*$^{-/-}$ mice were fed a high-cholesterol diet (0.15% cholesterol) for 21 weeks to allow the development of atherosclerotic lesions. Experimental animals were cared for in accordance with institutional guidelines, and they were acclimatized for at least 7 days before the initiation of any experiment. All preclinical experiments described in this publication were approved by the Animal Care and Use Committee of Bordeaux, France (N°50120192-A).

4.7. Magnetic Resonance Imaging

All MR experiments and relaxometry measurements were performed at 37 °C using a 4.7-Tesla Bruker Biospec System (Ettlingen, Germany) equipped with a gradient system with a maximum strength of 660 mT/m and a 110 μs rise time.

4.7.1. In Vivo Assessment of Stealthy Features by Dynamic MRI

Dynamic MRI was performed using a radiofrequency (RF)-spoiled echo gradient sequence (FLASH) with the following parameters: flip angle = 30°; echo time = 3.4 ms; TR ≈ 30 ms; resolution = 0.16 × 0.16; number of slices = 3; FOV = 40 × 30 mm; slice thickness = 1 mm; Nex = 10; dynamic scan time ≈ 60 s.

Mice (12 C57BL/6 females; n = 3 per condition) were anesthetized by inhalation of isoflurane (1.5%). Each animal then underwent imaging (50 s for each dynamic image) for 8 to 10 min (depending on the variation of the respiration rate). Imaging was stopped and 1 NE formulation (#1 to #4) (see Table 5) was injected intravenously in the tail vein at 53.7 μmol (Fe) kg^{-1} bodyweight. Straight after injection completion, MR image acquisition was restarted and the interval between the injection and the acquisition of the first dynamic image was measured. This interval varied from 1 to 3 min. Finally, the 2 dynamic sessions

were fused, considering the injection delay. The time between 2 MR dynamic images for each dynamic session was estimated as the total scan time (which depended on the respiration rate) divided by the number of dynamic images obtained.

For this study, only the signals of the liver and kidneys (renal cortex and renal pyramids) were quantified. To restrict the motion analysis to these organs, a segmentation procedure was performed before analysis. Briefly, on each slice acquired before injection, an initial region of interest (ROI) was defined and subsequently refined by manual correction. Dynamic motion fields were then estimated for each dynamic MR image using the RealTITracker method described by Zachiu et al. [68,69]. These motion (vector) fields were used to update the ROI position in an elastic manner to each dynamic image to follow the organ's motion throughout the MRI session. The mean MR signals of the liver and one kidney were then extracted from these dynamic ROIs and used to estimate iron accumulation in these organs, as described in the next section. An example of the results of this correction can be found in the Supplementary Materials (Video S1).

4.7.2. Estimation of the NE Half-Life in the Blood

As the NEs used in this study displayed a longitudinal relaxivity (r_1) of almost zero [20], the MR signal changes in the liver and kidney over time were estimated to be caused only by R_2^* changes and not by R_1 changes. Therefore, the signal equation of the gradient echo sequence (1) was simplified to Equation (2):

$$S(TE, TR, \alpha)_t = M_0 \sin(\alpha) e^{-TE \cdot R_2^*} \times \frac{1 - e^{-TR \cdot R_1}}{1 - \cos(\alpha) e^{-TR \cdot R_1}} \quad (1)$$

$$S\,(t) = M_0 \sin(\alpha) e^{-TE \cdot (R_2^* + r_2^* C(t))} \quad (2)$$

where α is the flip angle, M_0 is the MR signal when the echo time (TE) tends to zero, r_2^* is the transversal relaxivity of the tested NE, and C(t) is the iron concentration originating from the NE sample.

To estimate iron accumulation, the MR signal over time ($S_{(t)}$) was first normalized to the signal measured at the first dynamic acquisition, before NE injection. Because at t = 0, the iron concentration (C(t)) is equal to 0, Equation (2) can be rewritten as:

$$S_0 = M_0 \sin(\alpha) e^{-TE \cdot R_{2(0)}^*} \quad (3)$$

where $R_{2(0)}^*$ is the original relaxation rate. Therefore, the normalized signal of each new dynamic image (S_{norm}) is equal to:

$$S_{norm}(t) = \frac{S(t)}{S(0)} = e^{-TE \cdot r_2^* C(t)} \quad (4)$$

and the iron concentration can be estimated over time as:

$$C(t) = \frac{-\ln(S_{norm}(t))}{TE \cdot r_2^*} \quad (5)$$

In vivo, most injected nanoparticles (and also NEs) are cleared from the bloodstream by different organs (liver, spleen, and bone marrow). In this study, the liver was considered to be the main organ of NE clearance and, therefore, iron accumulation in this organ directly reflected blood clearance of NEs. To estimate the apparent NE half-life in the blood, the iron concentration was assumed to change over time as:

$$\frac{dC(t)}{dt} = \tau \left(C_{max} - C(t)\right) \quad (6)$$

where C_{max} is the maximum iron concentration estimated from the time of NE injection with no surface functionalization and τ is the accumulation rate. Therefore, the clearance

rate, τ, was estimated from a Marquardt–Levenberg fit of C(t) using a first-order differential equation (Equation (7)):

$$C(t) = C_{max}\left(1 - e^{-t\tau}\right) \quad (7)$$

Finally, the apparent NE half-life in the blood was defined as:

$$t_{1/2} = \ln(2)/\tau \quad (8)$$

4.7.3. In Vivo Dynamic MRI and T_2* Mapping of Atheromatous Plaques in *Apoe*$^{-/-}$ Mice

Tail vein injections of NE-P3 (#5) were performed at 53.7 μmol(Fe)·kg^{-1} bodyweight. In one *Apoe*$^{-/-}$ female, the NE half-life in the blood was estimated, based on the FLASH sequence obtained in the dynamic study. Atheromatous plaque labeling by NE-P3 (#5) was monitored in another *Apoe*$^{-/-}$ female by MRI before and at 7 h and 24 h after injection. Isoflurane concentrations were adjusted over time to maintain the respiration rate between 40 and 60 bpm. For in vivo T_2* mapping of atheromatous plaques, 10 transversal slices passing through the aorta in the thoraco-abdominal region were acquired using a multi-slice RF-spoiled echo gradient sequence: TR/TE1/ΔTE = 1300/2.8/3.6 ms; α = 60°; 15 echoes; NEx = 8; BW = 89.2 MHz; voxel size = 0.1 × 0.1 × 1 mm^3; FOV = 2.56 × 1.6 cm. Manual segmentation at the aorta level was performed to include only voxels that corresponded to the plaque using the first echo image. The mean T_2* values were computed for each slice. All calculations were performed using custom scripts written in MATLAB (MathWorks, Natick, MA, USA) and in C++ for the Levenberg–Marquardt algorithm. For each dataset, T_2* maps were estimated after correction of the macroscopic susceptibilities (e.g., arising from air/tissue interfaces, ΔB0z), as proposed by Dahnke et al. [70]. The limit of acceptability for the signal-to-noise ratio in the T_2* calculations was fixed to 4. The optical flow algorithm RealTITracker method described by Zachiu et al. [68,69] was used to avoid any image shifts during the echo times that could hamper the correct T_2* estimate. T_2* values of >30 ms were not considered to be representative of atheromatous plaques at 4.7 T. These few outliers were excluded from the analysis.

4.8. Ex Vivo Analyses of Isolated Aorta Samples

4.8.1. MRI Analyses

Aorta samples embedded in agarose gel (1%) were analyzed ex vivo by MRI using multiple gradient echoes with positive readouts and number of echoes = 20; delta TE = 3 ms; max TE = 59.48 ms; TE/TR = 2.48/100 ms; acquisition bandwidth = 125 kHz; matrix = 256 × 128 × 128; FOV = 20 × 10 × 10; isotropic resolution = 78 μm; number of repetitions = 16; total acquisition time = 7 h 30 min.

4.8.2. Iron Quantification by ESR

ESR experiments were performed at room temperature with a Bruker ESP300E spectrometer operating at X-band frequency (9.54 GHz). The microwave power was set to 20 mW and the magnetic field modulation frequency and amplitude to 100 kHz and 1 mT, respectively. The spectral resolution was 0.7 mT/pt and the acquisition time was 30 min for each sample. After weighing, each aorta sample was carefully digested in HNO_3 (65%) under a flame. Digestion was repeated 3 times to ensure the sample's complete mineralization. After the last addition of HNO_3, 100 mg of $NaNO_3$ salt was added to obtain a homogeneous solid powder for the ESR analysis. The recorded ESR spectra were normalized to the aorta mass (expressed in g), and their intensity (obtained by double-integration of the first derivative absorption curve) was compared with that of reference samples with a known concentration of Fe_2O_3 nanoparticles (ranging from 5 × 10^{-10} to 1 × 10^{-7} mol/g).

4.9. In Vitro Antioxidant Measurement

The antioxidant properties of alpha-tocopherol-containing NEs were assessed by Kirial International/Laboratoires Spiral (Couternon, France) using the KRL test according to Caspar-Bauguil et al. [71]. The antioxidant or prooxidant activity was evaluated in whole

blood samples mixed with the different NE formulations and exposed to a controlled free radical attack. The overall resistance of the blood samples against the free radical attack was assessed by calculating the time to produce the hemolysis of 50% of red blood cells (T50% hemolysis, in minutes) after the initiation of the attack. The antioxidant/prooxidant effect of the different NE formulations was then expressed as the percentage of increase/decrease in the T50% hemolysis relative to the control sample (without NE formulation). The results were also expressed in Trolox equivalents (used as a reference).

5. Conclusions

HuAbs represent a class of ligands that are theoretically safer for clinical translation. The same is true for NE formulations due to their proven biocompatibility and their easy dissemination through biological barriers. The results of this study pave the way to future non-invasive targeted imaging of atherosclerosis (by combining safe magnetic nanoparticles as a contrast agent and a new anti-galectin-3 HuAb as a targeting agent) and synergistic therapeutic applications using active pharmaceutical ingredients (e.g., alpha-tocopherol, an antioxidant, anti-inflammatory, and cardioprotective vitamin) to induce the regression of the vulnerable plaque. Moreover, a more personalized approach to therapies against atherosclerosis could be guided by molecular imaging. Advances in the in vivo targeting efficiency of agents against proteins overexpressed in the plaque, such as galectin-3, could also improve the assessment and monitoring of atherosclerosis.

Supplementary Materials: The following are available online at https://www.mdpi.com/article/10.3390/ijms22105188/s1. Figure S1: Transmission electron microscopy (TEM) picture without negative staining of the nanoemulsions loaded with magnetic particles. Video S1: Example of dynamic correction.

Author Contributions: Conceptualization, G.C.-S., S.C.-M., M.D.-C., and S.M.; methodology, S.B., G.P., Y.M., A.H., M.-J.J.-V., M.D., A.T., M.D.-C., and S.S.; software, S.B.; validation, S.B., G.P., and A.H.; formal analysis, S.B.; resources, G.C.-S., S.C.-M., M.D.-C., and S.M.; data curation, S.B.; writing—original draft preparation, G.P., S.B., Y.M., M.-J.J.-V., M.D., and M.D.-C.; writing—review and editing, G.C.-S., S.C.-M., S.B., S.M., G.P., and M.-J.J.-V.; visualization, G.C.-S., S.B., G.P., and M.D.; supervision, G.C.-S., S.C.-M., and M.D.-C.; project administration, G.C.-S., S.C.-M., and S.M.; funding acquisition, G.C.-S. and S.C.-M. All authors have contributed substantially to the work reported and have read and agreed to the published version of the manuscript.

Funding: This study was achieved within the context of the Laboratory of Excellence TRAIL ANR-10-LABX-57 and LabEx MAbImprove: ANR-10-LABX-53. A public grant from the SVSE5 program, named ATHERANOS, supported this work. Geoffrey Prévot was a recipient of a PhD scholarship from the French Ministry of Education, Research and Technology. Samuel Bonnet was supported by TRAIL ANR-10-LABX-57.

Institutional Review Board Statement: Experimental animals were cared for in accordance with the institutional guidelines, and they were acclimatized for at least 7 days before the initiation of any experiment. All preclinical experiments described in this publication were approved by the Animal Care and Use Committee of Bordeaux, France (No. 50120192-A).

Informed Consent Statement: Human biopsies were provided by the vascular and general surgery service of the Pellegrin academic hospital, Bordeaux, France. Samples were from patients who underwent endarterectomy after an acute vascular event. All clinical interventions were carried out at Pellegrin hospital and the use of human samples for research was approved by the Bordeaux CPP ethics committee (Comité de Protection des Personnes Sud-Ouest et Outre Mer) and by the French Research Ministry (Authorization Number DC-2016-2724). The CPP committee waived the need for patient written consent because surgical waste no longer attached to the person is considered res nullius. Nevertheless, the patients were informed by the clinicians; if they did not express their opposition to research, de-identified samples were immediately processed and embedded in paraffin.

Data Availability Statement: The data presented in this study are available on request from the corresponding author.

Acknowledgments: We thank Cyril Lorenzato for his help in designing the dynamic MRI experiments.

Conflicts of Interest: The authors Marie-Josée Jacobin-Valat, Martine Duonor-Cérutti, Gisèle Clofent-Sanchez, and Audrey Hémadou are listed as inventors on the patent for the human anti-galectin-3 antibody (WO2019068863A1, https://patents.google.com/patent/WO2019068863A1/en, accessed on 18 March 2021). All authors have approved the final article.

References

1. Lusis, A.J. Atherosclerosis. *Nature* **2000**, *407*, 233–241. [CrossRef]
2. Rudd, J.H.F.; Davies, J.R.; Weissberg, P.L. Imaging of atherosclerosis—Can we predict plaque rupture? *Trends Cardiovasc. Med.* **2005**, *15*, 17–24. [CrossRef] [PubMed]
3. Virmani, R.; Burke, A.P.; Kolodgie, F.D.; Farb, A. Vulnerable plaque: The pathology of unstable coronary lesions. *J. Interv. Cardiol.* **2002**, *15*, 439–446. [CrossRef] [PubMed]
4. Cuadrado, I.; Saura, M.; Castejón, B.; Martin, A.M.; Herruzo, I.; Balatsos, N.; Zamorano, J.L.; Zaragoza, C. Preclinical models of atherosclerosis. The future of Hybrid PET/MR technology for the early detection of vulnerable plaque. *Expert Rev. Mol. Med.* **2016**, *18*, e6. [CrossRef] [PubMed]
5. Montiel Schneider, M.G.; Lassalle, V.L. Magnetic iron oxide nanoparticles as novel and efficient tools for atherosclerosis diagnosis. *Biomed. Pharmacother. Biomed. Pharmacother.* **2017**, *93*, 1098–1115. [CrossRef]
6. Mehta, A.; Shah, S. Unstable or High Risk Plaque: How Do We Approach It? *Med. J. Armed Forces India* **2006**, *62*, 2–7. [CrossRef]
7. Kashyap, V.S.; Pavkov, M.L.; Bishop, P.D.; Nassoiy, S.P.; Eagleton, M.J.; Clair, D.G.; Ouriel, K. Angiography Underestimates Peripheral Atherosclerosis: Lumenography Revisited. *J. Endovasc. Ther.* **2008**, *15*, 117–125. [CrossRef]
8. Little, W.C.; Constantinescu, M.; Applegate, R.J.; Kutcher, M.A.; Burrows, M.T.; Kahl, F.R.; Santamore, W.P. Can coronary angiography predict the site of a subsequent myocardial infarction in patients with mild-to-moderate coronary artery disease? *Circulation* **1988**, *78*, 1157–1166. [CrossRef] [PubMed]
9. Mann, J.M.; Davies, M.J. Vulnerable plaque. Relation of characteristics to degree of stenosis in human coronary arteries. *Circulation* **1996**, *94*, 928–931. [CrossRef]
10. Osborn, E.A.; Jaffer, F.A. Imaging atherosclerosis and risk of plaque rupture. *Curr. Atheroscler. Rep.* **2013**, *15*, 359. [CrossRef]
11. Rathod, K.S.; Hamshere, S.M.; Jones, D.A.; Mathur, A. Intravascular ultrasound versus optical coherence tomography for Coronary artery imaging—Apples and oranges? *Interv. Cardiol. Lond. Engl.* **2015**, *10*, 8–15. [CrossRef]
12. Tarkin, J.M.; Dweck, M.R.; Evans, N.R.; Takx, R.A.P.; Brown, A.J.; Tawakol, A.; Fayad, Z.A.; Rudd, J.H.F. Imaging Atherosclerosis. *Circ. Res.* **2016**, *118*, 750–769. [CrossRef]
13. Tearney, G.J.; Yabushita, H.; Houser, S.L.; Aretz, H.T.; Jang, I.-K.; Schlendorf, K.H.; Kauffman, C.R.; Shishkov, M.; Halpern, E.F.; Bouma, B.E. Quantification of macrophage content in atherosclerotic plaques by optical coherence tomography. *Circulation* **2003**, *107*, 113–119. [CrossRef] [PubMed]
14. Mulder, W.J.M.; Jaffer, F.A.; Fayad, Z.A.; Nahrendorf, M. Imaging and nanomedicine in inflammatory atherosclerosis. *Sci. Transl. Med.* **2014**, *6*, 239sr1. [CrossRef] [PubMed]
15. Li, Y.; Liu, J.; Huang, J.-W.; Song, J.-C.; Ma, Z.-L.; Shi, H.-B. In vivo MRI detection of atherosclerosis in ApoE-deficient mice by using tenascin-C-targeted USPIO. *Acta Radiol. Stockh. Swed. 1987* **2018**, *59*, 1431–1437. [CrossRef] [PubMed]
16. Corti, R.; Fuster, V. Imaging of atherosclerosis: Magnetic resonance imaging. *Eur. Heart J.* **2011**, *32*, 1709–1719. [CrossRef]
17. Poon, C.; Gallo, J.; Joo, J.; Chang, T.; Bañobre-López, M.; Chung, E.J. Hybrid, metal oxide-peptide amphiphile micelles for molecular magnetic resonance imaging of atherosclerosis. *J. Nanobiotechnol.* **2018**, *16*, 92. [CrossRef]
18. Pellico, J.; Ruiz-Cabello, J.; Herranz, F. Microwave-driven Synthesis of Iron Oxide Nanoparticles for Fast Detection of Atherosclerosis. *J. Vis. Exp. JoVE* **2016**. [CrossRef]
19. Herranz, F.; Salinas, B.; Groult, H.; Pellico, J.; Lechuga-Vieco, A.; Bhavesh, R.; Ruiz-Cabello, J. Superparamagnetic Nanoparticles for Atherosclerosis Imaging. *Nanomaterials* **2014**, *4*, 408–438. [CrossRef] [PubMed]
20. Prévot, G.; Kauss, T.; Lorenzato, C.; Gaubert, A.; Larivière, M.; Baillet, J.; Laroche-Traineau, J.; Jacobin-Valat, M.J.; Adumeau, L.; Mornet, S.; et al. Iron oxide core oil-in-water nanoemulsion as tracer for atherosclerosis MPI and MRI imaging. *Int. J. Pharm.* **2017**, *532*, 669–676. [CrossRef]
21. Wallyn, J.; Anton, N.; Mertz, D.; Begin-Colin, S.; Perton, F.; Serra, C.A.; Franconi, F.; Lemaire, L.; Chiper, M.; Libouban, H.; et al. Magnetite- and Iodine-Containing Nanoemulsion as a Dual Modal Contrast Agent for X-ray/Magnetic Resonance Imaging. *ACS Appl. Mater. Interfaces* **2019**, *11*, 403–416. [CrossRef]
22. Zernecke, A.; Winkels, H.; Cochain, C.; Williams, J.W.; Wolf, D.; Soehnlein, O.; Robbins, C.S.; Monaco, C.; Park, I.; McNamara, C.A.; et al. Meta-analysis of leukocyte diversity in atherosclerotic mouse aortas. *Circ. Res.* **2020**, *127*, 402–426. [CrossRef]
23. Cochain, C.; Vafadarnejad, E.; Arampatzi, P.; Pelisek, J.; Winkels, H.; Ley, K.; Wolf, D.; Saliba, A.-E.; Zernecke, A. Single-Cell RNA-Seq Reveals the Transcriptional Landscape and Heterogeneity of Aortic Macrophages in Murine Atherosclerosis. *Circ. Res.* **2018**, *122*, 1661–1674. [CrossRef] [PubMed]
24. Amoozgar, Z.; Yeo, Y. Recent advances in stealth coating of nanoparticle drug delivery systems. *Wiley Interdiscip. Rev. Nanomed. Nanobiotechnol.* **2012**, *4*, 219–233. [CrossRef]
25. Ryan, S.M.; Mantovani, G.; Wang, X.; Haddleton, D.M.; Brayden, D.J. Advances in PEGylation of important biotech molecules: Delivery aspects. *Expert Opin. Drug Deliv.* **2008**, *5*, 371–383. [CrossRef]

26. Owens, D.E.; Peppas, N.A. Opsonization, biodistribution, and pharmacokinetics of polymeric nanoparticles. *Int. J. Pharm.* **2006**, *307*, 93–102. [CrossRef] [PubMed]
27. Suk, J.S.; Xu, Q.; Kim, N.; Hanes, J.; Ensign, L.M. PEGylation as a strategy for improving nanoparticle-based drug and gene delivery. *Adv. Drug Deliv. Rev.* **2016**, *99*, 28–51. [CrossRef] [PubMed]
28. Torchilin, V.P. PEG-based micelles as carriers of contrast agents for different imaging modalities. *Adv. Drug Deliv. Rev.* **2002**, *54*, 235–252. [CrossRef]
29. Jokerst, J.V.; Lobovkina, T.; Zare, R.N.; Gambhir, S.S. Nanoparticle PEGylation for imaging and therapy. *Nanomedicine* **2011**, *6*, 715–728. [CrossRef] [PubMed]
30. Hak, S.; Garaiova, Z.; Olsen, L.T.; Nilsen, A.M.; de Lange Davies, C. The effects of oil-in-water nanoemulsion polyethylene glycol surface density on intracellular stability, pharmacokinetics, and biodistribution in tumor bearing mice. *Pharm. Res.* **2015**, *32*, 1475–1485. [CrossRef]
31. Prévot, G.; Duonor-Cérutti, M.; Larivière, M.; Laroche-Traineau, J.; Jacobin-Valat, M.J.; Barthélémy, P.; Clofent-Sanchez, G.; Crauste-Manciet, S. Data on atherosclerosis specific antibody conjugation to nanoemulsions. *Data Brief* **2017**, *15*, 824–827. [CrossRef] [PubMed]
32. Ziegler, M.; Wallert, M.; Lorkowski, S.; Peter, K. Cardiovascular and Metabolic Protection by Vitamin E: A Matter of Treatment Strategy? *Antioxidants* **2020**, *9*, 935. [CrossRef] [PubMed]
33. Toledo-Ibelles, P.; Mas-Oliva, J. Antioxidants in the Fight Against Atherosclerosis: Is This a Dead End? *Curr. Atheroscler. Rep.* **2018**, *20*, 36. [CrossRef]
34. Abbina, S.; Parambath, A. 14—PEGylation and its alternatives: A summary. In *Engineering of Biomaterials for Drug Delivery Systems*; Parambath, A., Ed.; Woodhead Publishing Series in Biomaterials; Woodhead Publishing: Cambridge, UK, 2018; pp. 363–376. ISBN 978-0-08-101750-0.
35. Schöttler, S.; Becker, G.; Winzen, S.; Steinbach, T.; Mohr, K.; Landfester, K.; Mailänder, V.; Wurm, F.R. Protein adsorption is required for stealth effect of poly(ethylene glycol)- and poly(phosphoester)-coated nanocarriers. *Nat. Nanotechnol.* **2016**, *11*, 372–377. [CrossRef] [PubMed]
36. Hörmann, K.; Zimmer, A. Drug delivery and drug targeting with parenteral lipid nanoemulsions—A review. *J. Control. Release Off. J. Control. Release Soc.* **2016**, *223*, 85–98. [CrossRef]
37. Prévot, G.; Soria, F.N.; Thiolat, M.-L.; Daniel, J.; Verlhac, J.B.; Blanchard-Desce, M.; Bezard, E.; Barthélémy, P.; Crauste-Manciet, S.; Dehay, B. Harnessing Lysosomal pH through PLGA Nanoemulsion as a Treatment of Lysosomal-Related Neurodegenerative Diseases. *Bioconjug. Chem.* **2018**, *29*, 4083–4089. [CrossRef] [PubMed]
38. Lovelyn, C.; Attama, A.A. Current State of Nanoemulsions in Drug Delivery. *J. Biomater. Nanobiotechnol.* **2011**, *2*, 626–639. [CrossRef]
39. Jarzyna, P.A.; Skajaa, T.; Gianella, A.; Cormode, D.P.; Samber, D.D.; Dickson, S.D.; Chen, W.; Griffioen, A.W.; Fayad, Z.A.; Mulder, W.J.M. Iron oxide core oil-in-water emulsions as a multifunctional nanoparticle platform for tumor targeting and imaging. *Biomaterials* **2009**, *30*, 6947–6954. [CrossRef]
40. Gianella, A.; Jarzyna, P.A.; Mani, V.; Ramachandran, S.; Calcagno, C.; Tang, J.; Kann, B.; Dijk, W.J.R.; Thijssen, V.L.; Griffioen, A.W.; et al. Multifunctional Nanoemulsion Platform for Imaging Guided Therapy Evaluated in Experimental Cancer. *ACS Nano* **2011**, *5*, 4422–4433. [CrossRef] [PubMed]
41. Nguyen, K.-L.; Yoshida, T.; Kathuria-Prakash, N.; Zaki, I.H.; Varallyay, C.G.; Semple, S.I.; Saouaf, R.; Rigsby, C.K.; Stoumpos, S.; Whitehead, K.K.; et al. Multicenter Safety and Practice for Off-Label Diagnostic Use of Ferumoxytol in MRI. *Radiology* **2019**, *293*, 554–564. [CrossRef]
42. Bangalore, S.; Maron David, J.; Stone Gregg, W.; Hochman Judith, S. Routine Revascularization Versus Initial Medical Therapy for Stable Ischemic Heart Disease. *Circulation* **2020**, *142*, 841–857. [CrossRef] [PubMed]
43. Arbab-Zadeh, A.; Fuster, V. The Myth of "The Vulnerable Plaque": Transitioning from a Focus on Individual Lesions to Atherosclerotic Disease Burden for Coronary Artery Disease Risk Assessment. *J. Am. Coll. Cardiol.* **2015**, *65*, 846–855. [CrossRef] [PubMed]
44. Arbab-Zadeh, A.; Fuster, V. From Detecting the Vulnerable Plaque to Managing the Vulnerable Patient: JACC State-of-the-Art Review. *J. Am. Coll. Cardiol.* **2019**, *74*, 1582–1593. [CrossRef]
45. Gonzales, J.; Kossatz, S.; Roberts, S.; Pirovano, G.; Brand, C.; Pérez-Medina, C.; Donabedian, P.; de la Cruz, M.J.; Mulder, W.J.M.; Reiner, T. Nanoemulsion-Based Delivery of Fluorescent PARP Inhibitors in Mouse Models of Small Cell Lung Cancer. *Bioconjug. Chem.* **2018**, *29*, 3776–3782. [CrossRef]
46. Calcagno, V.; Vecchione, R.; Quagliariello, V.; Marzola, P.; Busato, A.; Giustetto, P.; Profeta, M.; Gargiulo, S.; Cicco, C.D.; Yu, H.; et al. Oil Core–PEG Shell Nanocarriers for In Vivo MRI Imaging. *Adv. Healthc. Mater.* **2019**, 1801313. [CrossRef]
47. Veronese, F.M.; Mero, A. The impact of PEGylation on biological therapies. *BioDrugs Clin. Immunother. Biopharm. Gene Ther.* **2008**, *22*, 315–329. [CrossRef]
48. Liu, F.; Liu, D. Long-circulating emulsions (oil-in-water) as carriers for lipophilic drugs. *Pharm. Res.* **1995**, *12*, 1060–1064. [CrossRef] [PubMed]
49. Alayoubi, A.; Alqahtani, S.; Kaddoumi, A.; Nazzal, S. Effect of PEG surface conformation on anticancer activity and blood circulation of nanoemulsions loaded with tocotrienol-rich fraction of palm oil. *AAPS J.* **2013**, *15*, 1168–1179. [CrossRef]

50. Ganta, S.; Sharma, P.; Paxton, J.W.; Baguley, B.C.; Garg, S. Pharmacokinetics and pharmacodynamics of chlorambucil delivered in long-circulating nanoemulsion. *J. Drug Target.* **2010**, *18*, 125–133. [CrossRef]
51. Devalapally, H.; Silchenko, S.; Zhou, F.; McDade, J.; Goloverda, G.; Owen, A.; Hidalgo, I.J. Evaluation of a nanoemulsion formulation strategy for oral bioavailability enhancement of danazol in rats and dogs. *J. Pharm. Sci.* **2013**, *102*, 3808–3815. [CrossRef]
52. Cheng, Y.; Liu, M.; Hu, H.; Liu, D.; Zhou, S. Development, Optimization, and Characterization of PEGylated Nanoemulsion of Prostaglandin E1 for Long Circulation. *AAPS PharmSciTech* **2015**, *17*, 409–417. [CrossRef]
53. Hak, S.; Helgesen, E.; Hektoen, H.H.; Huuse, E.M.; Jarzyna, P.A.; Mulder, W.J.M.; Haraldseth, O.; de Lange Davies, C. The effect of nanoparticle polyethylene glycol surface density on ligand-directed tumor targeting studied in vivo by dual modality imaging. *ACS Nano* **2012**, *6*, 5648–5658. [CrossRef]
54. Li, S.-D.; Huang, L. Stealth nanoparticles: High density but sheddable PEG is a key for tumor targeting. *J. Control. Release Off. J. Control. Release Soc.* **2010**, *145*, 178–181. [CrossRef]
55. Falcone, C.; Lucibello, S.; Mazzucchelli, I.; Bozzini, S.; D'Angelo, A.; Schirinzi, S.; Totaro, R.; Falcone, R.; Bondesan, M.; Pelissero, G. Galectin-3 plasma levels and coronary artery disease: A new possible biomarker of acute coronary syndrome. *Int. J. Immunopathol. Pharmacol.* **2011**, *24*, 905–913. [CrossRef]
56. Hemadou, A.; Laroche-Traineau, J.; Antoine, S.; Mondon, P.; Fontayne, A.; Le Priol, Y.; Claverol, S.; Sanchez, S.; Cerutti, M.; Ottones, F.; et al. An innovative flow cytometry method to screen human scFv-phages selected by in vivo phage-display in an animal model of atherosclerosis. *Sci. Rep.* **2018**, *8*. [CrossRef]
57. Hemadou, A.; Giudicelli, V.; Smith, M.L.; Lefranc, M.-P.; Duroux, P.; Kossida, S.; Heiner, C.; Hepler, N.L.; Kuijpers, J.; Groppi, A.; et al. Pacific Biosciences Sequencing and IMGT/HighV-QUEST Analysis of Full-Length Single Chain Fragment Variable from an In Vivo Selected Phage-Display Combinatorial Library. *Front. Immunol.* **2017**, *8*. [CrossRef]
58. Ding, J.; Wang, Y.; Ma, M.; Zhang, Y.; Lu, S.; Jiang, Y.; Qi, C.; Luo, S.; Dong, G.; Wen, S.; et al. CT/fluorescence dual-modal nanoemulsion platform for investigating atherosclerotic plaques. *Biomaterials* **2013**, *34*, 209–216. [CrossRef]
59. Hyafil, F.; Cornily, J.-C.; Feig, J.E.; Gordon, R.; Vucic, E.; Amirbekian, V.; Fisher, E.A.; Fuster, V.; Feldman, L.J.; Fayad, Z.A. Noninvasive detection of macrophages using a nanoparticulate contrast agent for computed tomography. *Nat. Med.* **2007**, *13*, 636–641. [CrossRef]
60. Briley-Saebo, K.C.; Amirbekian, V.; Mani, V.; Aguinaldo, J.G.S.; Vucic, E.; Carpenter, D.; Amirbekian, S.; Fayad, Z.A. Gadolinium mixed-micelles: Effect of the amphiphile on in vitro and in vivo efficacy in apolipoprotein E knockout mouse models of atherosclerosis. *Magn. Reson. Med.* **2006**, *56*, 1336–1346. [CrossRef]
61. Senders, M.L.; Hernot, S.; Carlucci, G.; van de Voort, J.C.; Fay, F.; Calcagno, C.; Tang, J.; Alaarg, A.; Zhao, Y.; Ishino, S.; et al. Nanobody-Facilitated Multiparametric PET/MRI Phenotyping of Atherosclerosis. *JACC Cardiovasc. Imaging* **2019**, *12*, 2015–2026. [CrossRef]
62. Broisat, A.; Hernot, S.; Toczek, J.; De Vos, J.; Riou, L.M.; Martin, S.; Ahmadi, M.; Thielens, N.; Wernery, U.; Caveliers, V.; et al. Nanobodies targeting mouse/human VCAM1 for the nuclear imaging of atherosclerotic lesions. *Circ. Res.* **2012**, *110*, 927–937. [CrossRef]
63. Jacobin-Valat, M.-J.; Laroche-Traineau, J.; Larivière, M.; Mornet, S.; Sanchez, S.; Biran, M.; Lebaron, C.; Boudon, J.; Lacomme, S.; Cérutti, M.; et al. Nanoparticles functionalised with an anti-platelet human antibody for in vivo detection of atherosclerotic plaque by magnetic resonance imaging. *Nanomed. Nanotechnol. Biol. Med.* **2015**, *11*, 927–937. [CrossRef]
64. Oumzil, K.; Ramin, M.A.; Lorenzato, C.; Hémadou, A.; Laroche, J.; Jacobin-Valat, M.J.; Mornet, S.; Roy, C.-E.; Kauss, T.; Gaudin, K.; et al. Solid Lipid Nanoparticles for Image-Guided Therapy of Atherosclerosis. *Bioconjug. Chem.* **2016**, *27*, 569–575. [CrossRef]
65. Massart, R. Preparation of aqueous magnetic liquids in alkaline and acidic media. *IEEE Trans. Magn.* **1981**, *17*, 1247–1248. [CrossRef]
66. Prévot, G.; Mornet, S.; Lorenzato, C.; Kauss, T.; Adumeau, L.; Gaubert, A.; Baillet, J.; Barthélémy, P.; Clofent-Sanchez, G.; Crauste-Manciet, S. Data on iron oxide core oil-in-water nanoemulsions for atherosclerosis imaging. *Data Brief* **2017**, *15*, 876–881. [CrossRef]
67. van Ewijk, G.A.; Vroege, G.J.; Philipse, A.P. Convenient preparation methods for magnetic colloids. *J. Magn. Magn. Mater.* **1999**, *201*, 31–33. [CrossRef]
68. Zachiu, C.; Denis de Senneville, B.; Moonen, C.; Ries, M. A framework for the correction of slow physiological drifts during MR-guided HIFU therapies: Proof of concept. *Med. Phys.* **2015**, *42*, 4137–4148. [CrossRef]
69. Zachiu, C.; Papadakis, N.; Ries, M.; Moonen, C.; Denis De Senneville, B. An improved optical flow tracking technique for real-time MR-guided beam therapies in moving organs. *Phys. Med. Biol.* **2015**, *60*, 9003. [CrossRef]
70. Dahnke, H.; Schaeffter, T. Limits of detection of SPIO at 3.0 T using T2 relaxometry. *Magn. Reson. Med.* **2005**, *53*, 1202–1206. [CrossRef]
71. Caspar-Bauguil, S.; Maestre, N.; Segafredo, C.; Galinier, A.; Garcia, J.; Prost, M.; Périquet, B.; Pénicaud, L.; Salvayre, R.; Casteilla, L. Evaluation of whole antioxidant defenses of human mononuclear cells by a new in vitro biological test: Lack of correlation between erythrocyte and mononuclear cell resistance to oxidative stress. *Clin. Biochem.* **2009**, *42*, 510–514. [CrossRef]

International Journal of
Molecular Sciences

MDPI

Article

Phage Display Screening of Bovine Antibodies to Foot-and-Mouth Disease Virus and Their Application in a Competitive ELISA for Serodiagnosis

Sukyo Jeong [1], Hyun Joo Ahn [1], Kyung Jin Min [1], Jae Won Byun [2], Hyun Mi Pyo [2], Mi Young Park [2], Bok Kyung Ku [2], Jinju Nah [2], Soyoon Ryoo [2], Sung Hwan Wee [2] and Sang Jick Kim [1,*]

[1] Synthetic Biology and Bioengineering Research Center, Korea Research Institute of Bioscience and Biotechnology, Daejeon 34141, Korea; pearl2926@kribb.re.kr (S.J.); neolub99@naver.com (H.J.A.); 1206rudwls@kribb.re.kr (K.J.M.)
[2] Foot-and-Mouth Disease Division, Animal and Plant Quarantine Agency, Gimcheon 39660, Korea; jaewon8911@korea.kr (J.W.B.); hmpyo@korea.kr (H.M.P.); parkmy71@korea.kr (M.Y.P.); kubk@korea.kr (B.K.K.); nahjj75@korea.kr (J.N.); soyooni@korea.kr (S.R.); wsh2010@korea.kr (S.H.W.)
* Correspondence: sjick@kribb.re.kr; Tel.: +82-42-860-4229

Abstract: For serodiagnosis of foot-and-mouth disease virus (FMDV), monoclonal antibody (MAb)-based competitive ELISA (cELISA) is commonly used since it allows simple and reproducible detection of antibody response to FMDV. However, the use of mouse-origin MAb as a detection reagent is questionable, as antibody responses to FMDV in mice may differ in epitope structure and preference from those in natural hosts such as cattle and pigs. To take advantage of natural host-derived antibodies, a phage-displayed scFv library was constructed from FMDV-immune cattle and subjected to two separate pannings against inactivated FMDV type O and A. Subsequent ELISA screening revealed high-affinity scFv antibodies specific to a serotype (O or A) as well as those with pan-serotype specificity. When BvO17, an scFv antibody specific to FMDV type O, was tested as a detection reagent in cELISA, it successfully detected FMDV type O antibodies for both serum samples from vaccinated cattle and virus-challenged pigs with even higher sensitivity than a mouse MAb-based commercial FMDV type O antibody detection kit. These results demonstrate the feasibility of using natural host-derived antibodies such as bovine scFv instead of mouse MAb in cELISA for serological detection of antibody response to FMDV in the susceptible animals.

Keywords: foot-and-mouth disease virus; type O; type A; phage display; antibody; competitive ELISA

Citation: Jeong, S.; Ahn, H.J.; Min, K.J.; Byun, J.W.; Pyo, H.M.; Park, M.Y.; Ku, B.K.; Nah, J.; Ryoo, S.; Wee, S.H.; et al. Phage Display Screening of Bovine Antibodies to Foot-and-Mouth Disease Virus and Their Application in a Competitive ELISA for Serodiagnosis. *Int. J. Mol. Sci.* **2021**, *22*, 4328. https://doi.org/10.3390/ijms22094328

Academic Editors: Menotti Ruvo and Annamaria Sandomenico

Received: 10 March 2021
Accepted: 19 April 2021
Published: 21 April 2021

1. Introduction

Foot-and-mouth disease virus (FMDV) causes significant foot-and-mouth disease for cloven-hoofed animals [1]. The FMDV is one of the contagious animal disease resulting in social and economic problem due to its rapid spread in countries across the world [2]. The genome of FMDV is a single-stranded RNA (approximately 8.5 kb) that is surrounded by a protein coat consisting of four capsid proteins, namely, VP1, VP2, VP3, and VP4 [3,4]. FMDV occurs in seven major immunologically distinct serotypes: A, O, C, Asia I, and South African Territories (SAT1, SAT2, and SAT3). Of the serotypes, FMDV type O and A have widely spread around the world. Rapid and accurate diagnosis is paramount to limit their distribution and eradiate the diseases.

One of the effective approaches for FMDV diagnosis is to serologically detect FMDV-specific antibodies, which are generated by host immune response against either the viral non-structural proteins (NSPs) or capsid structural proteins (SPs). Unlike NSP antibodies of which presence are used to differentiate infected from vaccinated animals, SP antibodies are detected in both infected and vaccinated animals. Hence, the SP antibody test has been used for FMD surveillance as well as for post-vaccination monitoring. Virus neutralization

test (VNT) is a gold standard for detecting SP antibodies, which measures the neutralizing activity of SP antibodies that block virus infection in susceptible cell lines [5]. However, the VNT suffers from such drawbacks as unavoidable use of a live virus, poor reproducibility, and difficulty in large-scale testing. As an alternative, competitive ELISA (cELISA)-based methods have been developed using serotype-specific monoclonal antibodies (MAbs) [6,7]. For example, a commercial kit for FMDV type O antibody includes type O-specific MAb as a key reagent and measures the percent of inhibition (PI) of the MAb binding to antigen by a serum tested. When the PI value is greater than 50%, the serum turns out to be FMDV type O antibody positive. Accordingly, kit performance such as sensitivity and specificity is very dependent on the choice of MAb. The concern about using MAb reagent in cELISA is how well the antibody recognizing a single epitope can represent overall antibody response against diverse epitopes on FMDV capsid. Hence the epitope of antibody reagent in cELISA should be immunodominant and overlap with those of the majority of antibodies produced by an anti-FMDV immune response in host animals.

Diverse sets of MAbs against FMDV have been generated by murine hybridoma technology [7–10]. Extensive studies on antigenic features of FMDV, especially type O, have identified major neutralizing epitopes recognized by the mouse MAbs [11–13]. Even though these epitope regions are suggested to be also recognized by bovine antibodies [14,15], the relative preference of each epitope region and fine epitope structure may be different in cattle. In fact, investigations of antibody response in natural host animals such as cattle, pigs, and sheep have revealed that antibody response does not dominantly direct to the G-H loop of VP1, the historically considered immunodominant epitope of FMDV type O in mice [14,16]. The mouse MAb currently used for cELISA targets the linear epitope on the G-H loop [6] and has such an epitope matching issue that improved performance can be expected from cELISA development using antibody reagent derived from a natural FMDV host animal such as cattle. In addition, the bovine antibody gene repertoire has distinct features when compared with that of a mouse. Mouse germline heavy chain variable (VH) gene segments are diverse in sequence and classified into 16 families, while bovine germline VH gene segments have similar sequences and belong to a single family [17]. Instead, the bovine antibody has extraordinary long heavy-chain complementarity-determining region 3 (HCDR3), which is believed to be the way to achieve high antibody diversity even using the limited source of VH frameworks [18].

Bovine anti-FMDV MAbs can be generated using hetero-hybridoma as well as phage display technology, as reported before [15,19]. Phage display is now considered a better option than hybridoma technology because it erases the instability issue of hybridoma cells, gives more flexibility in antibody selection strategy, and allows higher throughput screening. Recent accumulation of sequence information for bovine germline antibody genes enables the construction of a more reliable antibody library when compared with the first bovine Fab library, which was constructed using limited primer sets [20–22]. In this study, we constructed a phage-displayed bovine scFv library from peripheral blood lymphocytes (PBL) of FMDV-vaccinated cattle. Bovine scFv clones with specificity for type O or A as well as pan-serotype could be isolated by panning and screening from the library. Their binding activity and epitope were precisely characterized after the expression and purification of scFv-Fc proteins. Furthermore, the feasibility of their use in cELISA-based serodiagnosis of FMDV was tested using standard FMDV positive sera purchased from Pirbright and serum samples obtained from vaccinated cattle and virus-challenged pigs. Details are reported herein.

2. Results

2.1. Selection of FMDV-Specific Bovine Antibodies

A bovine scFv library was constructed from PBLs of FMDV-immunized cattle as described in Materials and Methods, and its diversity was estimated 2×10^8 cfu (colony forming unit). To select FMDV-specific antibodies from the library, a library phage was

prepared and subjected to panning against both type O (O1 Manisa) and type A (A22 Iraq) of inactivated virus antigens.

After three rounds of panning, the successful enrichment of FMDV binding phage was confirmed by monitoring the phage recovery rate (output/input phage ratio). For both pannings against type O and A, a more than 100-fold increase in the rate was observed after the third round when compared with that after the first round. Most of the scFv phage clones selected randomly after the third round of panning showed FMDV-binding activity in phage ELISA (data not shown), and analysis of their scFv sequences revealed six unique HCDR3 sequences (Table 1). For each HCDR3, a representative scFv phage clone was chosen and tested for its binding activity to type O and A antigens. Three clones with comparable binding activity to both type O and A antigens were named BvOA1, BvOA7, and BvOA18. They could be found from both pannings against type O and A. Two clones (BvO17, BvO22) with type O-specific binding activity were derived from the panning against type O, whereas BvA3, the only clone with preferential binding activity to type A antigen, was selected from the panning against type A.

Table 1. Analysis of VH and VL gene usage in the selected scFv clones. The nucleotide sequences were analyzed using IMGT/V-QUEST (http://www.imgt.org/IMGT_vquest/input, last accessed December 2, 2020).

Clone	Bovine Germline VH Segment	Differences from Germline (nt, aa)	HCDR3 (IMGT)	Bovine Germline VL Segment	Differences from Germline (nt, aa)	LCDR3 (IMGT)
BvO17	IGHV1-17*01	(21, 13)	AKCSHEYANYACYDFEDESYFDA	IGLV1-47*01	(14, 9)	AAHDSSINNGV
BvO22	IGHV1-10*01	(17, 9)	AKEADDDADHCADLDI	IGLV1-67*02	(16, 8)	VTYDSTSSTDL
BvOA1	IGHV1-10*01	(20, 8)	AKYAGDHGISGDGCYAFAVGYVDA	IGLV1-67*02	(40, 22)	VVYDSAKDTAI
BvOA7	IGHV1-10*01	(22, 12)	AKNMGDMGSCYAWANGYVDA	IGLV1-67*02	(25, 13)	AAYDSSSNAV
BvOA18	IGHV1-21*01	(16, 7)	AKGYDAGYTADCIYDYGYGRERYVDA	IGLV1-47*01	(16, 9)	ASPGGSSTNAV
BvA3	IGHV1-10*01 F or IGHV1-10*02 F	(15, 8)	TKDVNLYNLWSGGGYGCFGDGRGID YNYVDT	IGLV1-67*01 F	(24, 11)	ATGDYSSSTSI

2.2. Characterization of Antibody Specificity

For precise characterization of the selected clones, scFv-Fc expression construct was made for each clone by simple cut-and-paste cloning of scFv insert into the cassette mammalian expression vector pDR-OriP-Fc1 [23]. After transfection of the construct, transient expression in 293E cells resulted in an scFv-Fc molecule of 55 kDa secreted as dimers of 110 kDa, which was purified from the culture supernatant by affinity chromatography on a protein G column. The purity and integrity of the purified scFv-Fcs were confirmed by SDS-PAGE analysis, which showed more than 95% purity of scFv-Fcs (Figure S1).

The binding affinity of the purified scFv-Fcs for either type O or A antigen was measured by an indirect ELISA (Figure 1). As in Table 2, the apparent dissociation constant (K_D) for each binding interaction was determined by binding curve fitting as described previously [24]. As expected, BvOA1, BvOA7, and BvOA18 bound to both O1 Manisa and A22 Iraq antigens in a concentration-dependent manner. Their affinities appeared to be very high for both strains of FMDV, with K_D values ranging from 18.5 to 93.3 pM. BvO17 and BvO22 also showed very high affinity for O1 Manisa with K_D values of about 20 pM but negligible binding activity for A22 Iraq. BvA3 showed preferential binding to A22 Iraq, and its affinity was relatively low when compared with those of the other clones.

Table 2. Binding affinity of selected scFv clones. Asterisks (*) are not detected.

	Binding Affinity (K_D, pM)	
	O1 Manisa	A22 Iraq
BvO17	25.9 ± 1.9	* N.D.
BvO22	21.8 ± 1.4	* N.D.
BvOA1	93.3 ± 9.0	91.8 ± 9.0
BvOA7	27.9 ± 1.2	18.5 ± 1.3
BvOA18	46.1 ± 3.9	50.5 ± 5.3
BvA3	* N.D.	2179.9 ± 322.0

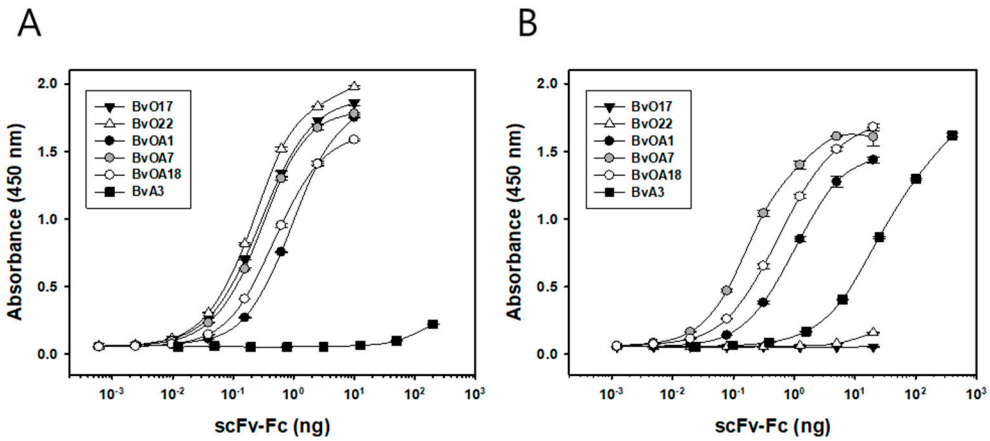

Figure 1. Binding activities of selected bovine scFvs toward (**A**) FMDV type O (O1 Manisa) and (**B**) FMDV type A (A22 Iraq) antigens. scFv sequences selected by phage library screening of FMDV-immunized cattle were cloned into a pDR-OriP-Fc1 vector, which allowed scFv-Fc expression in mammalian cells. Serial dilutions of purified scFv-Fc were applied onto FMDV antigen-coated 96-well Maxisorp plate. Bound scFv-Fc proteins were detected using HRP-conjugated anti-human IgG (Fc-specific). Data are shown as mean ± SD of triplicate samples.

Next, we further tested the cross-reactivity of scFv-Fcs for the other serotypes (Figure 2). As expected, BvOA1, BvOA7, and BvOA18 were reactive to all the tested serotypes of FMDV serotypes. They may recognize common epitopes of FMDV regardless of serotype and can be used for pan-serotype diagnosis of FMDV. As clearly shown in Figure 2, BvO17 and BvO22 specifically bound to O1 Manisa and were not cross-reactive with the other serotypes of FMDV strains tested. It is likely that they recognize type O-specific epitope and can be used for the detection of type O-specific antibody response. Unlike the type O-specific clones, BvA3 was not perfectly specific to type A. Even though BvA3 bound to A22 Iraq preferentially, it seemed to be still reactive to other serotypes of strains, especially O1 Manisa.

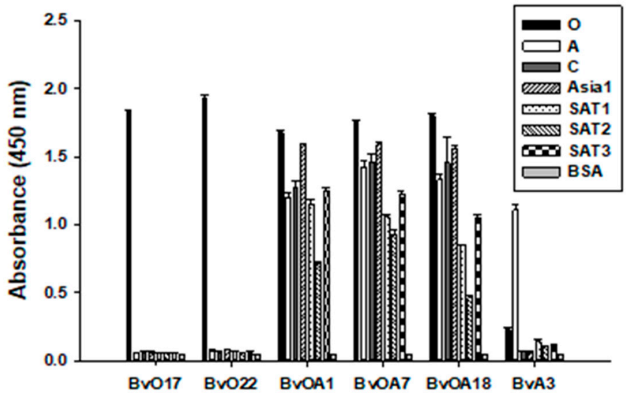

Figure 2. Cross-reactivities of bovine scFvs to seven serotypes of FMDV. Inactivated FMDV antigens for seven serotypes purchased from Pirbright Institute and BSA (negative control) were coated onto a 96-well Maxisorp plate. A total of 0.1 μg/mL of purified scFv-Fc was applied onto the wells for most clones except BvA3, of which 2 μg/mL was applied. Bound scFv-Fc proteins were detected using HRP-conjugated anti-human IgG (Fc-specific). Data are shown as mean ± SD of triplicate samples.

2.3. Characterization of the Antibody Binding Epitopes

To investigate whether the selected clones recognize overlapping epitopes or not, cross-competition binding experiments for both O1 Manisa and A22 Iraq antigens were carried out using scFv phage and scFv-Fcs. Figure 3 shows antibody epitope binning data, and the value in each cell represents relative absorbance for the binding of scFv phage shown on the upper side in the presence of competitor scFv-Fc shown on the left side. The

degree of binding inhibition was also expressed as the darkness of the cell background, which allowed easy grouping of antibodies according to their epitopes. Pan-serotype antibodies, BvOA1, BvOA7, and BvOA18, competed with each other for binding to both types of antigens suggesting their recognition of overlapping epitopes common to all serotypes. Type O-specific antibodies, BvO17 and BvO22, also competed with each other for binding to type O antigen, which indicated a shared epitope region on type O antigen recognized by both. Since BvA3 did not compete with the other antibodies, three different groups could be finally defined in terms of epitope specificity.

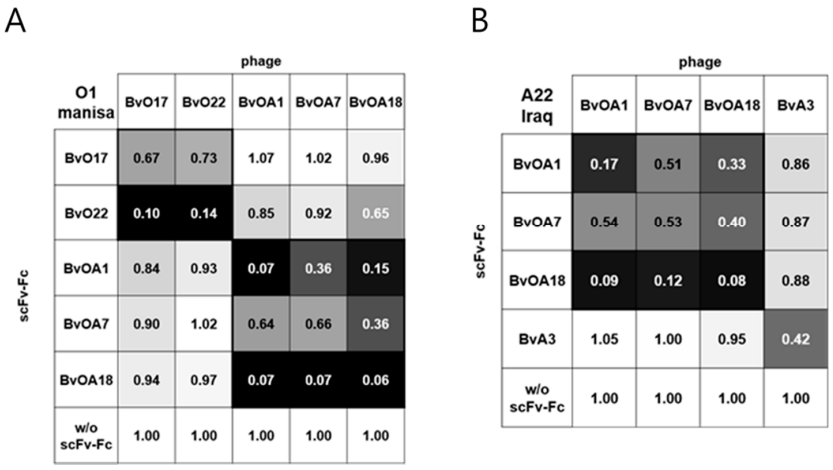

Figure 3. Epitope binning of bovine scFvs by cross-competition ELISA. Inactivated FMDV type O (O1 Manisa) (**A**) or type A (A22 Iraq) (**B**) antigens were coated onto a 96-well Maxisorp plate. A total of 10 μg/mL of purified scFv-Fc was added as a competitor, followed by incubation with scFv phage. Bound scFv phages were detected using HRP-conjugated anti-M13 antibody. The data represents normalized values obtained by dividing the absorbance values by that of scFv phage binding in the absence of competitor scFv-Fc. Strong binding inhibition is also represented by the darker background in the cell.

2.4. Detection of FMDV Antibody in Serum by cELISA Using Bovine Antibodies

To test whether the selected bovine antibodies can be used for the detection of serum antibodies against SP of FMDV, a solid-phase competitive ELISA (SPCE) was developed using biotinylated scFv-Fcs as described in Materials and Methods. In the SPCE, binding of biotinylated scFv-Fcs to FMDV antigen is detected by premixed to NeutrAvidin-HRP (NA-HRP) and can be inhibited by the presence of anti-SP antibodies in test sera. Because BvA3 lost its binding activity after biotinylation, intact scFv-Fcs was instead used together with anti-human IgG (Fc-specific)-HRP. After a preliminary test using a small size of serum samples from vaccinated cattle and virus-challenged pigs (Figure S2), BvO17 and BvOA7 were selected as representative clones for the respective groups since they showed slightly better response than the other clones in the same group. The final three clones, BvO17, BvA3, and BvOA7, were further tested for the SPCE to detect antibodies against FMDV type O and A. PrioCHECK Kits for type O and A were used for comparison in this study since PrioCHECK family of type-specific FMDV antibody tests are widely used as commercial SPCE kits for primary screening.

First, strong positive control sera for each serotype of FMDV and a negative control serum purchased from Pirbright Institute were tested in SPCE (Figure S3). When BvO17 was used as a reagent, its binding was significantly reduced by type O serum (Figure S3B). Except for type Asia1 serum, it showed very weak or negligible cross-reactivity for non-type O control sera. In all the tested SPCE, type Asia1 serum was reactive regardless of serotype specificity of antibody reagent used. The pattern of binding inhibition by the control sera in BvO17-based SPCE was very similar to that in PrioCHECK type O Kit (Figure S3A,B). BvA3-based SPCE showed significant binding inhibition by type A serum

and weak or negligible cross-reactivity for non-type A control sera except type Asia1 serum (Figure S3E). Unlike BvA3-based SPCE, PrioCHECK type A Kit did not show comparable binding inhibition by type A serum (Figure S3D,E). When excluding the cross-reactive type Asia1 serum, these results indicate BvO17 and BvA3 can be used for serotype-specific detection of FMDV antibodies. In the case of the pan-serotype antibody, BvOA7, its binding inhibition was observed for most of the sera tested. However, the degree of inhibition was dependent on the serotype as well as the FMDV antigen used (Figure S3C,F).

Next, serum samples from vaccinated cattle and virus-challenged pigs were tested in SPCE. The bovine sera were collected from a local slaughterhouse and were supposed to be both positive for type O and A FMDV antibodies due to national vaccination programs in South Korea. The porcine sera expected to be positive for FMDV type O or A antibodies were collected from pigs exposed to infection with Korean isolates, either FMDV (O/Anseong/SKR/2002) or FMDV (A/Yeoncheon/SKR/2017). In BvO17-based SPCE (Figure 4A), the bovine sera were strongly positive, exhibiting PI values near 100%. The values were comparable with those obtained by PrioCHECK type O Kit. The porcine sera derived from FMDV (O/Anseong/SKR/2002)-challenged pigs provided relatively lower PI values than the bovine sera but still had a high average PI value, 94%. When compared with the PrioCHECK type O Kit, which showed a low average PI value (only 59%) with large variance, BvO17-based SPCE seemed to be much better in the sensitive detection of the porcine FMDV antibodies. In BvA3-based SPCE (Figure 4B), the average PI value was 74% for bovine sera, which was comparable with the PrioCHECK type A Kit. However, the variance was huge, unlike the PrioCHECK type A Kit, and even one sample showed a PI value far below 50%. The PI values for the porcine sera derived from FMDV (A/Yeoncheon/SKR/2017)-challenged pigs were relatively low with an average of 60% and showed wide fluctuations. PrioCHECK type A Kit provided even worse data for the porcine sera exhibiting the average PI value less than 50%, also with huge variance. In the case of BvOA7-based SPCE (Figure 4A,B), the PI values were sufficiently high for both type O and A formats, indicating that they can be generally used for detection of the FMDV antibody, regardless of serotype.

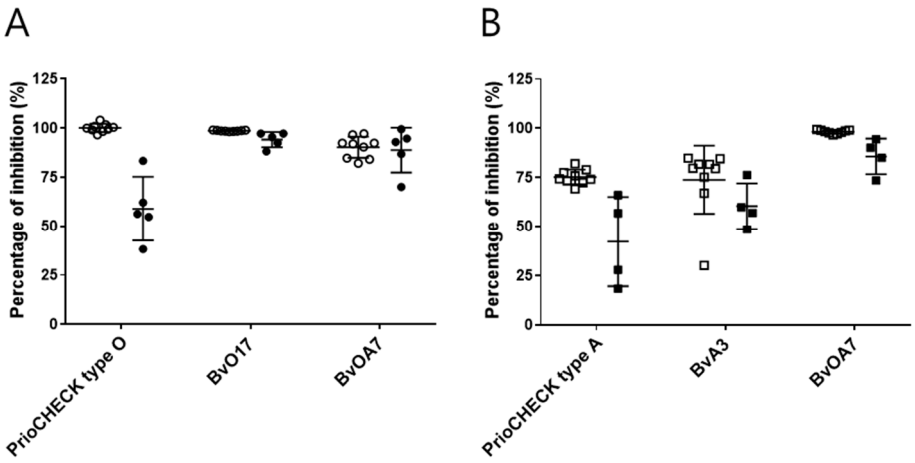

Figure 4. Detection of FMDV antibodies in the serum samples from vaccinated and virus-challenged animals using bovine scFv antibody-based SPCE. (**A**) For type O antibody detection in the serum samples from vaccinated cattle (n = 9, ○) and FMDV (O/Anseong/SKR/2002)-challenged pigs (n = 5, ●), BvO17 and BvOA7-based SPCEs were carried out as described in Figure S3, and their performance was compared with a parallel experiment using PrioCHECK type O antibody ELISA Kit. The results were expressed as a percentage of inhibition as described in Materials and Methods. (**B**) For type A antibody detection in the serum samples from vaccinated cattle (n = 9, □) and FMDV (A/Yeoncheon/SKR/2017)-challenged pigs (n = 4, ■), BvA3 and BvOA7-based SPCEs were carried out as described in Figure S3, and their performance was compared with a parallel experiment using PrioCHECK type A antibody ELISA Kit.

3. Discussion

In this study, we successfully isolated bovine anti-FMDV antibodies by phage display using scFv library generated from PBLs of cattle in a local slaughterhouse. The cattle were considered to be adequate for the FMDV-immune antibody library construction because they were supposed to be immune to both FMDV type O and A due to a vaccine policy in South Korea. In fact, they were seropositive for FMDV type O and A when checked with PrioCHECK FMDV antibody detection kits. The bovine scFv library constructed was hence presumed to contain antibodies against FMDV type O and A. Through two separate pannings against type O and A antigens, we could obtain serotype (O or A)-specific scFvs that distinguish other serotypes. In addition, scFv clones reactive to both type O and A antigens could be isolated and further characterized to be cross-reactive to all seven serotypes.

It is well known that the bovine antibody repertoire is derived from a highly limited diversity of germline immunoglobulin variable region genes [17,20,21,25]. For germline VH genes, there are 12 functional VH gene segments, all of which belong to one subgroup, VH1. For germline VL genes, the Vλ1 subfamily dominantly participated in the bovine light chain repertoire that consists of 95% of lambda (λ) and 5% of kappa (κ) light chains expressed. The sequence analysis of our bovine scFvs revealed VH1 and Vλ1 as the only germline VH and VL gene subfamily, respectively (Table 1). For the six selected bovine scFvs, the germline VH1-10 gene segment was most frequently used in our study. It was also one of the two most frequently used germline VH genes in the recent report on analysis of germline gene use of 55 plasmablast-derived MAbs from FMDV-infected cattle [26]. This high frequency of VH1-10 can be simply attributed to its abundance in bovine antibody repertoire rather than FMDV-specific selection. In fact, VH1-10 has been found in about 70% of sequences in a recent analysis of deep sequencing of bovine VH repertoire [27]

Another feature in the bovine antibody sequence is the long length of HCDR3, which is believed to compensate for the limited diversity of V-D-J recombination. The average length is well over 20 a.a. residues and about 10% of the antibodies have extremely long HCDR3 of between 40 and 70 a.a. [18,28,29]. This ultra-long HCDR3 could be also identified by sequence analysis of the plasmablast-derived anti-FMDV MAbs in the previous study. However, all the selected HCDR3s in our study were normal (from 14 to 29 a.a.) in length. Our scFvs went through repetitive panning rounds, which might enrich binders that have advantages in affinity and expression. Hence, we can assume that they may have such advantages over antibodies with ultra-long HCDR3 and become final survivors after in vitro selection procedure.

Studies on the antigenic profile of FMDV type O using mouse MAbs have revealed five neutralizing epitope sites [11–13]. Site 1 is well known as an immunodominant and linear epitope that includes the G-H loop in VP1, whereas the other sites are all conformational epitopes [30,31]. When the bovine MAbs developed by heterohybridoma technology were tested for epitope specificity [15], none of them recognized site 1. Instead, they all recognized the other conformational epitope sites. Similarly, most bovine plasmablast-derived MAbs were found to be specific to conformational epitopes outside of site 1 [26]. Thus, unlike in mice, immunodominant epitopes for FMDV type O in cattle seemed to be conformational rather than linear. BvO17 and BvO22 were selected as type O-specific clones with high affinity in this study. Despite no sequence homology in the HCDR3 region, they showed similar epitope specificity in cross-competition ELISA (Figure 3). When they were tested for western blotting of capsid protein, none could succeed (data not shown). This result indicates that they recognize conformational epitopes but not site 1 at least and may reflect the previous suggestion that antibody response against FMDV type O in cattle differs from that in mice and does not interact dominantly with the linear epitope in the G-H loop of VP1. In this study, we did not further characterize the epitopes recognized by the bovine scFv antibodies. Since they are conformational, it may be difficult to fully characterize the epitope structure. The clues for the structure can be given by several experimental tools such as binding test with recombinant viral capsid proteins, viral epitope library scan, and

selection and identification of the antibody-resistant mutant virus. Such endeavors are very important and will contribute to the understanding of the performance of bovine scFv in cELISA and the further development of improved antibody reagent.

This difference in epitope specificity affected the performance of SPCE for the detection of FMDV type O antibodies. PrioCHECK kit includes HRP-labeled mouse MAb as a key reagent. Like the previous report on solid-phase blocking ELISA for detection of FMDV type O antibody [6], the MAb also targeted the linear epitope in the G-H loop when we checked specificity using synthetic peptide (Data not shown). Compared with the mouse MAb-based PrioCHECK kit, BvO17-based SPCE showed a similar competition pattern for controlling bovine anti-FMDV sera for seven serotypes (Figure S3). However, it was better in the sensitive detection of FMDV type O antibody, especially for serum samples from virus-challenged pigs (Figure 4). This result may indicate that more antibodies are developed against the conformational epitope region recognized by BvO17 than the linear epitope in the G-H loop when cattle and pigs are exposed to FMDV serotype O. It seems to be promising to develop BvO17-based SPCE for sensitive detection of FMDV type O antibody in both bovine and porcine serum samples.

Unlike BvO17, BvA3 did not provide good performance in SPCE. Though BvA3-based SPCE showed better serotype A-specific competition than the PrioCHECK type A kit in a test using control bovine anti-FMDV sera for seven serotypes, its sensitivity turned out to be low in tests using the serum samples from vaccinated cattle and virus-challenged pigs. PrioCHECK type A kit also showed low sensitivity, especially for the porcine samples. More sensitive detection of FMDV type A antibody in serum samples may require further screening of natural host-derived antibodies recognizing immunodominant epitope that is unique to type A. For such purpose, screening of antibody repertoire from host animals immunized with type A only can be considered as an alternative option since it is reasonable to speculate that our approach using both type O- and A-vaccinated cattle provided rare type A-specific antibody clones due to biased enrichment of antibody clones recognizing both serotypes during in vitro selection procedure.

BvOA7-based SPCE could be used successfully to detect both FMDV type O and A antibodies. When it comes to the detection of type A antibodies, it showed even better sensitivity than the BvA3-based SPCE and PrioCHECK type A kit (Figure 4B). Due to pan-serotype specificity, BvOA7 cannot be used to differentiate serotypes but can be developed as a general detection reagent for FMDV antibodies regardless of serotypes. Other than type-specific assay, there is also a need for a universal serological test as simplified frontline diagnostics as described recently [32].

It looks like some data in Figure S3 seem to be inconsistent with the data in Figure 4. For example, BvOA7-based SPCE and PrioCHECK type A kit did not respond effectively to type A reference serum sample (Figure S3) while both responded very well to vaccinated bovine serum samples (Figure 4B). Since Figure S3 is derived from a single serum sample for each serotype, it has a limitation of data interpretation even though each sample is purchased as a reference control serum for each subtype. When considering sample to sample variation, one should not interpret the data in Figure S3 as a representation for a specific serotype. Each bar in Figure S3 can be just one of the dots in the plot of Figure 4. Hence we relied on Figure 4, representing data collection for diverse test serum samples, to judge the feasibility of using our antibodies in cELISA. There may still remain concerns about a limited number of serum samples tested. As this was a preliminary feasibility study for the bovine scFvs selected, the serum samples were not broadly representative, and the sample size was not big enough. For further validation study, we will expand sample size and diversity by adding positive and negative samples from a broad range of host animals and virus isolates, which can meet the requirement for commercial development.

In conclusion, we herein demonstrate the isolation of anti-FMDV bovine scFv clones specific to a serotype (O or A) as well as those with pan-serotype specificity by phage library screening of antibody repertoire from FMDV-vaccinated cattle. Their performance in SPCE showing better sensitivity than conventional mouse MAbs suggests the feasibility of their

application in serodiagnosis of FMDV. The benefit of using the bovine scFvs for FMDV serodiagnosis will be further proved by a validation study using a large number of diverse field serum samples, including negative serum samples. In parallel, further engineering of them as antibody reagents can also be considered for optimization of performance through direct genetic fusion with detection modules such as HRP and fluorescent proteins. Such endeavors will allow commercial development of a novel bovine scFv-based cELISA as a more reliable tool for FMDV surveillance and ultimately contribute to control FMDV spread in the world.

4. Materials and Methods

4.1. Construction of Bovine scFv Library

Blood samples of ten Hanwoo (*Bos Taurus coreanae*) cows were collected from a local slaughterhouse. Peripheral blood lymphocytes (PBLs) were isolated using Histopaque-1077 (Sigma-Aldrich, St. Louis, MO, USA) and subjected to total RNA extraction with Trizol (Thermo Fisher Scientific, Waltham, MA, USA) to obtain a high percentage of inhibition (PI) values when tested by PrioCHECK FMDV type O Antibody ELISA Kit (Thermo Fisher Scientific, Waltham, MA, USA). cDNA was synthesized using Superscript IV (Thermo Fisher Scientific, Waltham, MA, USA) and used for PCR amplification of bovine antibody variable regions, VH and VL (Vκ and Vλ). The PCR primer set used for each variable region (Table S1) was designed by considering the sequences of bovine germline antibody gene segments as described previously [33]. The amplified VH and VL sequences were combined by assembly and extension PCR using extension primers (Table S1), and the resulting scFv sequences with $(G_4S)_3$ linker between VH and VL were cloned into phagemid vector, pDR-D1 as described before [23]. Bacteriophages displaying the scFv repertoire were prepared from the transformed *E.coli* ER2738 cells using VCSM13 helper phage (Stratagen, La Jolla, CA, USA) as described previously [23].

4.2. Bio-Panning and Screening

Immunotubes (Nunc, Maxisorp, Thermo Fisher Scientific, Waltham, MA, USA) were coated with either inactivated FMDV type O (O1 Manisa) or type A (A22 Iraq) antigen (Pirbright Institute, Pirbright, U.K.) for panning. The tubes were washed twice with PBS and blocked with 2% skim milk in 1X PBS supplemented with final 0.05% Tween-20 (PBST). The library phages were added to the antigen-coated tube and incubated at room temperature for 2 h. Then, unbound phages were removed by PBST washing five times. A total of 0.2 M Glycine-HCl (pH 2.7) was used to elute bound phage, and 1 M Tris-HCl (pH 8.0) was added for neutralization. The eluted phages were infected with *E.coli* ER2738 cells, followed by their superinfection with VCSM13 helper phage for amplification. The amplified phages were used for the next round of panning with an increased number of times of PBST washing.

To screen individual scFv phage clones, forty-eight colonies were randomly selected from the output plates after the third round of panning for each panning procedure. After growing them until OD_{600} = 0.5, scFv phages were rescued by superinfection with helper phage. The rescued phages were applied onto the FMDV-coated 96-well Maxisorp plate (Nunc, Maxisorp). The phage binding was detected by phage ELISA using horseradish peroxidase (HRP)-conjugated anti-M13 antibody (Sino Biological, Beijing, China). The clones showing specific binding activity were subjected to DNA sequencing, and the nucleotide sequences determined were submitted to IMGT/V-QUEST (http://imgt.org/IMGT_vquest/input, last accessed December 2, 2020) for sequence analysis.

4.3. Expression and Purification of scFv-Fc Proteins in 293E Cells

The genes encoding the selected scFv clones were cloned into the pDR-OriP-Fc vector, which allows genetic fusion of scFv sequences to human gamma-1 Fc and hinges domain sequences for transient expression of scFv-Fc as described previously [23]. The constructed expression plasmid was transfected using polyethyleneimine (PEI, Polysciences, Warring-

ton, PA, USA) into 293E (CRL-10852, ATCC) cells cultivated in suspension with Ex-Cell 293 serum-free medium (Sigma-Aldrich, St. Louis, MO, USA) at 37 °C in 8% CO_2. The transfected cells were cultured for seven days at 32 °C in 8% CO_2 while being fed with 15% glucose (Thermo Fisher Scientific, Waltham, MA, USA) and 200× Glutamax (Thermo Fisher Scientific, Waltham, MA, USA) twice. For purification of scFv-Fc, the supernatant was subjected to affinity chromatography based on a protein G-agarose column (Merck Millipore, Darmstadt, Germany).

4.4. ELISA

96-well Maxisorp plate (Nunc, Maxisorp, Thermo Fisher Scientific, Waltham, MA, USA) were coated with FMDV antigens (O1 Manisa or A22 Iraq) (Pirbright Institute, Pirbright, U.K.) diluted in PBS (pH 7.4) overnight at 4 °C, and blocked with 2% skim milk or 1% BSA in PBST. The plates were washed four times with PBST between steps. All incubations were carried out at RT for 1-2 h. The color was developed with tetramethylbenzidine (TMB) substrate reagents (BD Biosciences, San Diego, CA, USA), and the reaction was stopped with 50 µL of 2.5 M H_2SO_4. The absorbance was measured at 450 nm (A_{450}) using a microtiter reader (Emax, Molecular Devices, Sunnyvale, CA, USA).

The binding activities of the purified scFv-Fc were measured by an indirect ELISA. Serial dilutions of scFv-Fc were applied to FMDV antigen-coated wells and bound scFv-Fc was detected by HRP-conjugated anti-human IgG antibody produced in goat (Jackson ImmunoResearch, West Grove, PA, USA). From the binding data, equilibrium dissociation constant, K_D was estimated as described previously [24]. By plotting absorbance as y and antibody concentration applied as x, K_D can be calculated by nonlinear regression using hyperbola model equation, $y = A_{max} * x/(K_D + x)$.

For antibody cross-competition binding experiment, 10 µg/mL of purified scFv-Fc was added as a competitor into each well and incubated for 1 h at RT. After washing, an scFv phage diluted with 2% skim milk in PBST was added into each well and incubated for 45 min at RT. After washing, HRP-conjugated anti-M13 monoclonal antibody (1:5000 dilution) was used to detect bound phage.

4.5. Biotinylation of scFv-Fc

The scFv-Fc proteins were conjugated with Biotin using a Sulfo-NHS-LC-Biotin (sulfosuccinimidyl-6-(biotinamido) hexanoate; Thermo Fisher Scientific, Waltham, MA, USA) according to the manufacturer's instructions. A total of 10 mM of Sulfo-NHS-LC-Biotin reagent was added to 1 mg of scFv-Fc proteins and incubated at 4 °C for 2 h. The mixture was then washed using amicon ultra centrifugal tube (10 K) several times and stored at 4 °C until further use.

4.6. Serum Samples

As reference sera, bovine control sera strongly positive for seven serotypes (O/UKG, A/A22, C/Oberbayern, SAT1/RHO, SAT2, SAT3/ZIM, and Asia1/Shamir) as well as negative control serum were purchased from Pirbright Institute. Bovine test sera were prepared from blood samples collected from cattle at a local slaughterhouse that were supposed to be immunized by both FMDV type O and A vaccines. Porcine test sera were collected from pigs challenged either by FMDV (O/Anseong/SKR/2002) or by FMDV (A/Yeoncheon/SKR/2017) with support from the Animal and Plant Quarantine Agency (Gimcheon, South Korea).

4.7. Solid-Phase Competitive ELISA (SPCE)

The biotinylated scFv-Fc together with NeutrAvidin-HRP (NA-HRP, Thermo Fisher Scientific, Waltham, MA, USA) was used to develop bovine scFv-based SPCE. In the case of BvA3, unlabeled scFv-Fc together with HRP-conjugated anti-human IgG (Fc-specific) was used since it lost binding activity after biotinylation. For detection of FMDV type O or A antibodies, a 96-well Maxisorp plate was coated overnight at 4 °C with FMDV type

O (O1 Manisa) or type A (A22 Iraq) antigens, respectively. The wells were blocked with 1% BSA in PBST at RT for 1 h. A total of 1:10 dilutions of serum samples were added to the wells and incubated at RT for 1 h. After washing with PBST, either a premix of biotinylated scFv-Fcs and NA-HRP or a premix of unlabeled scFv-Fc and HRP-conjugated anti-human IgG (Fc-specific) was added and incubated for 45 min at RT. The wells were washed four times with PBST, followed by incubation with 100 µL of TMB substrate for 10 min and subsequent addition of 2.5 M H_2SO_4. A_{450} was measured for each serum sample. Percentage of inhibition (PI) was calculated using the following formula Equation (1):

$$\mathrm{PI}(\%) = \left\{1 - \left(\frac{A_{450}test\ serum}{A_{450}negative\ reference\ serum}\right)\right\} \times 100 \quad (1)$$

For comparison, commercial SPCE (PrioCHECK FMDV type O or A antibody ELISA Kit; Prionics AG, Schlieren-Zurich, Switzerland) was also carried out in parallel according to the manufacturer's instructions. Briefly, 1:10 (type O kit) or 1:5 (type A kit) dilution of serum was incubated in the respective FMDV antigen-coated wells. After washing, dilution of HRP-conjugate provided by the kit was added to the wells and incubated for 1 h at RT. After removing unbound conjugate by repeated washes, color was developed by adding 100 µL of TMB substrate solution and incubating for 15 min. Then the reaction was stopped by adding 100 µL of stop solution. PI value was calculated according to the manufacturer's instructions.

Supplementary Materials: The following are available online at https://www.mdpi.com/article/10.3390/ijms22094328/s1.

Author Contributions: Conceptualization, S.J.K.; methodology, S.J., H.J.A., J.W.B., H.M.P., M.Y.P., J.N., and S.R.; validation, J.W.B., H.M.P., M.Y.P., B.K.K., and S.H.W.; investigation, S.J., H.J.A., and K.J.M.; writing—original draft preparation, S.J. and S.J.K.; writing—review and editing, S.J. and S.J.K.; supervision, S.J.K.; project administration, S.J.K.; funding acquisition, S.J.K. All authors have read and agreed to the published version of the manuscript.

Funding: This research was supported by grants from the R&D Convergence Program of the National Research Council of Science & Technology of the Republic of Korea (Grant No. CAP-16-02-KIST) and the KRIBB Research Initiative Program (KGM9942112), Republic of Korea.

Conflicts of Interest: The authors declare no conflict of interest

References

1. Samuel, A.R.; Knowles, N.J. Foot-and-mouth disease type O viruses exhibit genetically and geographically distinct evolutionary lineages (topotypes). *J. Gen. Virol.* **2001**, *82*, 609–621. [CrossRef] [PubMed]
2. Donaldson, A.I.; Alexandersen, S. Predicting the spread of foot and mouth disease by airborne virus. *Rev. Sci. Tech.* **2002**, *21*, 569–575. [CrossRef] [PubMed]
3. Belsham, G.J. Translation and replication of FMDV RNA. *Curr. Top. Microbiol. Immunol.* **2005**, *288*, 43–70. [PubMed]
4. Acharya, R.; Fry, E.; Stuart, D.; Fox, G.; Rowlands, D.; Brown, F. The three-dimensional structure of foot-and-mouth disease virus at 2.9 a resolution. *Nature* **1989**, *337*, 709–716. [CrossRef] [PubMed]
5. Golding, S.M.; Hedger, R.S.; Talbot, P. Radial immuno-diffusion and serum-neutralisation techniques for the assay of antibodies to swine vesicular disease. *Res. Vet. Sci.* **1976**, *20*, 142–147. [CrossRef]
6. Chenard, G.; Miedema, K.; Moonen, P.; Schrijver, R.S.; Dekker, A. A solid-phase blocking ELISA for detection of type O foot-and-mouth disease virus antibodies suitable for mass serology. *J. Virol. Methods* **2003**, *107*, 89–98. [CrossRef]
7. Yang, M.; Xu, W.; Bittner, H.; Horsington, J.; Vosloo, W.; Goolia, M.; Lusansky, D.; Nfon, C. Generation of mAbs to foot-and-mouth disease virus serotype A and application in a competitive ELISA for serodiagnosis. *Virol. J.* **2016**, *13*, 195. [CrossRef]
8. Nguyen, Q.T.; Yang, J.; Byun, J.W.; Pyo, H.M.; Park, M.Y.; Ku, B.K.; Nah, J.; Ryoo, S.; Wee, S.H.; Choi, K.S.; et al. Development of Monoclonal Antibody Specific to Foot-and-Mouth Disease Virus Type A for Serodiagnosis. *Pathogens* **2019**, *8*, 301. [CrossRef]
9. Pfaff, E.; Thiel, H.J.; Beck, E.; Strohmaier, K.; Schaller, H. Analysis of neutralizing epitopes on foot-and-mouth disease virus. *J. Virol.* **1988**, *62*, 2033–2040. [CrossRef]
10. Yang, M.; Mudabuka, B.; Quizon, K.; Nfon, C. Generation of monoclonal antibodies against foot-and-mouth disease virus SAT 2 and the development of a lateral flow strip test for virus detection. *Transbound. Emerg. Dis.* **2019**, *66*, 1158–1166. [CrossRef]

11. McCahon, D.; Crowther, J.R.; Belsham, G.J.; Kitson, J.D.A.; Duchesne, M.; Have, P.; Meloen, R.H.; Morgan, D.O.; De Simone, F. Evidence for At Least Four Antigenic Sites on Type O Foot-and-Mouth Disease Virus Involved in Neutralization; Identification by Single and Multiple Site Monoclonal Antibody-resistant Mutants. *J. Gen. Virol.* **1989**, *70*, 639–645. [CrossRef] [PubMed]
12. Xie, Q.C.; McCahon, D.; Crowther, J.R.; Belsham, G.J.; McCullough, K.C. Neutralization of Foot-and-Mouth Disease Virus Can Be Mediated Through Any of at least Three Separate Antigenic Sites. *J. Gen. Virol.* **1987**, *68*, 1637–1647. [CrossRef] [PubMed]
13. Crowther, J.R.; Farias, S.; Carpenter, W.C.; Samuel, A.R. Identification of a fifth neutralizable site on type O foot-and-mouth disease virus following characterization of single and quintuple monoclonal antibody escape mutants. *J. Gen. Virol.* **1993**, *74 (Pt 8)*, 1547–1553. [CrossRef]
14. Aggarwal, N.; Barnett, P.V. Antigenic sites of foot-and-mouth disease virus (FMDV): An analysis of the specificities of anti-FMDV antibodies after vaccination of naturally susceptible host species. *J. Gen. Virol.* **2002**, *83*, 775–782. [CrossRef]
15. Barnett, P.V.; Samuel, A.R.; Pullen, L.; Ansell, D.; Butcher, R.N.; Parkhouse, R.M. Monoclonal antibodies, against O1 serotype foot-and-mouth disease virus, from a natural bovine host, recognize similar antigenic features to those defined by the mouse. *J. Gen. Virol.* **1998**, *79 (Pt 7)*, 1687–1697. [CrossRef]
16. Mahapatra, M.; Hamblin, P.; Paton, D.J. Foot-and-mouth disease virus epitope dominance in the antibody response of vaccinated animals. *J. Gen. Virol.* **2012**, *93*, 488–493. [CrossRef] [PubMed]
17. Berens, S. Use of a single VH family and long CDR3s in the variable region of cattle Ig heavy chains. *Int. Immunol.* **1997**, *9*, 189–199. [CrossRef]
18. Wang, F.; Ekiert, D.C.; Ahmad, I.; Yu, W.; Zhang, Y.; Bazirgan, O.; Torkamani, A.; Raudsepp, T.; Mwangi, W.; Criscitiello, M.F.; et al. Reshaping antibody diversity. *Cell* **2013**, *153*, 1379–1393. [CrossRef]
19. Kim, Y.J.; Lebreton, F.; Kaiser, C.; Cruciere, C.; Remond, M. Isolation of foot-and-mouth disease virus specific bovine antibody fragments from phage display libraries. *J. Immunol. Methods* **2004**, *286*, 155–166. [CrossRef]
20. Ekman, A.; Niku, M.; Liljavirta, J.; Iivanainen, A. *Bos taurus* genome sequence reveals the assortment of immunoglobulin and surrogate light chain genes in domestic cattle. *BMC Immunol.* **2009**, *10*, 22. [CrossRef]
21. Zhao, Y.; Jackson, S.M.; Aitken, R. The bovine antibody repertoire. *Dev. Comp. Immunol.* **2006**, *30*, 175–186. [CrossRef]
22. O'Brien, P.M.; Aitken, R.; O'Neil, B.W.; Campo, M.S. Generation of native bovine mAbs by phage display. *Proc. Natl. Acad. Sci. USA* **1999**, *96*, 640–645. [CrossRef]
23. Yoon, H.; Song, J.M.; Ryu, C.J.; Kim, Y.G.; Lee, E.K.; Kang, S.; Kim, S.J. An efficient strategy for cell-based antibody library selection using an integrated vector system. *BMC Biotechnol.* **2012**, *12*, 62. [CrossRef]
24. Barinka, C.; Ptacek, J.; Richter, A.; Novakova, Z.; Morath, V.; Skerra, A. Selection and characterization of Anticalins targeting human prostate-specific membrane antigen (PSMA). *Protein Eng. Des. Sel.* **2016**, *29*, 105–115. [CrossRef]
25. Stanfield, R.L.; Haakenson, J.; Deiss, T.C.; Criscitiello, M.F.; Wilson, I.A.; Smider, V.V. The Unusual Genetics and Biochemistry of Bovine Immunoglobulins. *Adv. Immunol.* **2018**, *137*, 135–164. [PubMed]
26. Li, K.; Wang, S.; Cao, Y.; Bao, H.; Li, P.; Sun, P.; Bai, X.; Fu, Y.; Ma, X.; Zhang, J.; et al. Development of Foot-and-Mouth Disease Virus-Neutralizing Monoclonal Antibodies Derived From Plasmablasts of Infected Cattle and Their Germline Gene Usage. *Front. Immunol.* **2019**, *10*, 2870. [CrossRef]
27. Deiss, T.C.; Vadnais, M.; Wang, F.; Chen, P.L.; Torkamani, A.; Mwangi, W.; Lefranc, M.P.; Criscitiello, M.F.; Smider, V.V. Immunogenetic factors driving formation of ultralong VH CDR3 in *Bos taurus* antibodies. *Cell Mol. Immunol.* **2019**, *16*, 53–64. [CrossRef] [PubMed]
28. Haakenson, J.K.; Deiss, T.C.; Warner, G.F.; Mwangi, W.; Criscitiello, M.F.; Smider, V.V. A Broad Role for Cysteines in Bovine Antibody Diversity. *Immunohorizons* **2019**, *3*, 478–487. [CrossRef] [PubMed]
29. Saini, S.S.; Allore, B.; Jacobs, R.M.; Kaushik, A. Exceptionally long CDR3H region with multiple cysteine residues in functional bovine IgM antibodies. *Eur. J. Immunol.* **1999**, *29*, 2420–2426. [CrossRef]
30. Aktas, S.; Samuel, A.R. Identification of antigenic epitopes on the foot and mouth disease virus isolate O1/Manisa/Turkey/69 using monoclonal antibodies. *Rev. Sci. Tech.* **2000**, *19*, 744–753. [CrossRef] [PubMed]
31. Asfor, A.S.; Upadhyaya, S.; Knowles, N.J.; King, D.P.; Paton, D.J.; Mahapatra, M. Novel antibody binding determinants on the capsid surface of serotype O foot-and-mouth disease virus. *J. Gen. Virol.* **2014**, *95*, 1104–1116. [CrossRef] [PubMed]
32. Asfor, A.S.; Howe, N.; Grazioli, S.; Berryman, S.; Parekh, K.; Wilsden, G.; Ludi, A.; King, D.P.; Parida, S.; Brocchi, E.; et al. Detection of Bovine Antibodies against a Conserved Capsid Epitope as the Basis of a Novel Universal Serological Test for Foot-and-Mouth Disease. *J. Clin. Microbiol.* **2020**, *58*. [CrossRef] [PubMed]
33. Diesterbeck, U.S. Construction of Bovine Immunoglobulin Libraries in the Single-Chain Fragment Variable (scFv) Format. *Methods Mol. Biol.* **2018**, *1701*, 113–131. [PubMed]

International Journal of
Molecular Sciences

MDPI

Article

Monoclonal Antibody Aggregation Associated with Free Radical Induced Oxidation

Kai Zheng [1,*], Diya Ren [2], Y. John Wang [1], Wayne Lilyestrom [1], Thomas Scherer [1], Justin K. Y. Hong [3] and Junyan A. Ji [1]

[1] Pharmaceutical Development, Genentech, South San Francisco, CA 94080, USA; pharmulator@yahoo.com (Y.J.W.); wayne.lilyestrom@gmail.com (W.L.); tms_508@yahoo.com (T.S.); jji@gene.com (J.A.J.)
[2] Oceanside Pharmaceutical Technical Development, Genentech, Oceanside, CA 92056, USA; diya.ren@gmail.com
[3] Department of Pharmaceutical Sciences, University of Michigan, Ann Arbor, MI 48109, USA; hkyjustin@gmail.com
* Correspondence: zheng.kai@gene.com

Abstract: Oxidation is an important degradation pathway of protein drugs. The susceptibility to oxidation is a common concern for therapeutic proteins as it may impact product efficacy and patient safety. In this work, we used 2,2′-azobis (2-amidinopropane) dihydrochloride (AAPH) as an oxidative stress reagent to evaluate the oxidation of therapeutic antibodies. In addition to the oxidation of methionine (Met) and tryptophan (Trp) residues, we also observed an increase of protein aggregation. Size-exclusion chromatography and multi-angle light scattering showed that the soluble aggregates induced by AAPH consist of dimer, tetramer, and higher-order aggregate species. Sodium dodecyl sulfate polyacrylamide gel electrophoresis indicated that inter-molecular disulfide bonds contributed to the protein aggregation. Furthermore, intrinsic fluorescence spectra suggested that dimerization of tyrosine (Tyr) residues could account for the non-reducible cross-links. An excipient screening study demonstrated that Trp, pyridoxine, or Tyr could effectively reduce protein aggregation due to oxidative stress. This work provides valuable insight into the mechanisms of oxidative-stress induced protein aggregation, as well as strategies to minimize such aggregate formation during the development and storage of therapeutic proteins.

Keywords: monoclonal antibody; free radical; protein aggregation; oxidation; excipient

Citation: Zheng, K.; Ren, D.; Wang, Y.J.; Lilyestrom, W.; Scherer, T.; Hong, J.K.Y.; Ji, J.A. Monoclonal Antibody Aggregation Associated with Free Radical Induced Oxidation. *Int. J. Mol. Sci.* **2021**, *22*, 3952. https://doi.org/10.3390/ijms22083952

Academic Editor: Menotti Ruvo

Received: 26 February 2021
Accepted: 2 April 2021
Published: 12 April 2021

1. Introduction

Oxidation-induced degradation of therapeutic proteins is commonly observed during pharmaceutical manufacturing, handling, and storage [1–3]. These oxidation reactions occur when there are activated oxygen species including singlet oxygen ($^1O_2$), superoxide radical ($O_2\bullet^-$), hydroxyl radical (•OH), and peroxide (-OO-) in the environment. Reactive oxygen species can be created through light, heat, free radicals, or transition metals [4,5]. These species can oxidize methionine (Met), tryptophan (Trp), histidine (His), tyrosine (Tyr), and cysteine (Cys) residues in proteins [6]. For example, it has been reported that ultraviolet (UV) irradiation induced oxidation of Met and Trp residues in a monoclonal antibody (mAb) [7], thermal or chemical stresses caused Met oxidation in proteins [8–10], and free radicals promoted Tyr oxidation in ATPase [11].

Oxidative modifications can alter protein's secondary and tertiary structures [12], hydrophobicity [13], stability [14], biological activity [14], and plasma circulation half-life [15]. Owing to these potential impacts, oxidation is typically an important quality attribute to be closely monitored during the development of therapeutic proteins. Various stress models including light and chemical stresses are often used to identify potential oxidation hot spots in therapeutic proteins and to characterize the vulnerability of labile

residues to oxidation. *Tert*-butyl hydroperoxide (*t*-BHP), hydrogen peroxide (H_2O_2), or 2,2′-azobis (2-amidinopropane) dihydrochloride (AAPH) are often used as chemical stress reagents to evaluate protein oxidation [6,8–10,12,16–18]. In general, *t*-BHP and H_2O_2 primarily oxidize Met residues via nucleophilic substitution reactions. In contrast, AAPH (a water-soluble radical initiator) oxidizes both Met and Trp residues [8,19] through free radical reactions. The azo compound, AAPH, is thermally unstable and can generate alkyl radicals at elevated temperatures. In the presence of oxygen, alkyl radicals can form peroxyl radicals [20], which can further form alkoxyl radicals [11]. These radical species can effectively oxidize Met, Trp, and other oxidation-labile residues in proteins. One advantage of using an azo-radical initiator, such as AAPH or azobisisobutyronitrile, as an oxidative reagent is that it can produce a controllable and reproducible amount of oxidizing species [19,21,22].

In previous work conducted by Ji et al. [9], researchers used oxidative reagents of *t*-BHP, H_2O_2, and AAPH to study the mechanism of Met, Trp, and His oxidation in parathyroid hormone. Although Ji et al.'s work provided valuable insights into the oxidation mechanisms and the corresponding stabilization strategy, the model protein, parathyroid hormone, used in the study is a small protein with minimal tertiary structure. On the other hand, oxidation in large proteins, such as mAbs, may not only cause oxidation of Met, Trp, His, or other labile residues, but also induce additional physicochemical degradations. For example, the previous work did not assess aggregation that can be observed during protein oxidation. Therefore, in this work, we evaluated the oxidative degradation of therapeutic mAbs under the AAPH stress, where we observed both mAb oxidation and aggregation. Protein aggregation is often induced by physical stresses, such as agitation [23], freeze/thawing, and freeze/drying processes [24]. The AAPH-induced aggregation observed here is likely formed through covalent bonds as a result of free radical reactions. Protein aggregates can potentially trigger immune responses and are considered as a critical quality attribute for therapeutic proteins [25]. Thus, it is important to have a good understanding of the formation and the nature of protein aggregates associated with protein oxidation. In addition, this study also provides insight to reduce protein aggregation when exposing to oxidative reagents during therapeutic protein production and storage.

2. Results

2.1. Aggregate Formation under the AAPH Stress

AAPH was used to assess the oxidative degradation of mAbs during the formulation development. Size exclusion chromatography (SEC) of the oxidized mAb1 revealed a substantial increase of protein aggregates (SEC; Figure 1). The percentages of aggregates, monomer, and fragments were calculated based on SEC peak areas and are summarized in Table 1. Increasing AAPH concentrations results in a quantitative loss of monomer with corresponding increases of aggregates (SEC peaks A-C between 11 and 15 min in Figure 1). The impact on mAb1 fragmentation under the oxidative stress is relatively subtle. SEC coupled with multi-angle light scattering (SEC-MALS) was used to further characterize the aggregates in the mAb1 sample stressed with 5 mM AAPH. SEC-MALS data indicated that the aggregates upon the oxidative stress contained dimer (peak C, 3.0×10^5 Da) and higher-order aggregates (peaks A/B 5.2×10^5–1.4×10^6 Da) (Figure 1).

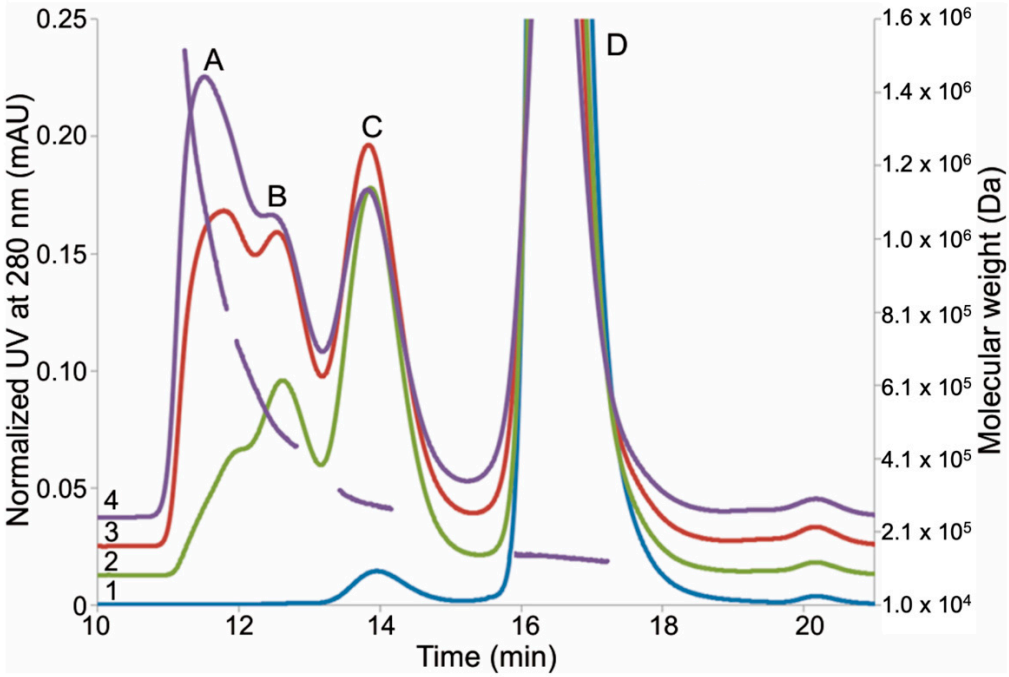

Figure 1. Expanded view of mAb1 size exclusion chromatography (SEC) profiles after 2,2′-azobis (2-amidinopropane) dihydrochloride (AAPH) stress. Chromatogram 1: control sample (mAb1 without the AAPH stress); chromatogram 2: mAb1 oxidized by 1 mM AAPH; chromatogram 3: mAb1 oxidized by 3 mM AAPH; 4: mAb1 oxidized by 5 mM AAPH. Molecular weights of peaks (A–D) for mAb1 oxidized by 5 mM AAPH are calculated and overlaid in the figure as the dashed line.

Table 1. Size distribution of 2,2′-azobis (2-amidinopropane) dihydrochloride (AAPH)-stressed mAb1.

Sample	Aggregates (%)	Monomer (%)	Fragments (%)
AAPH Control	1.0	98.8	0.2
1 mM AAPH	33.7	65.9	0.4
3 mM AAPH	50.5	48.9	0.6
5 mM AAPH	55.8	43.5	0.7

MAb1 was incubated with AAPH for 24 h at 40 °C. Percentages were calculated from size exclusion chromatography (SEC) data.

2.2. Fraction Collection from SEC

Given that mAb1 stressed by 5 mM AAPH showed the most pronounced changes, we henceforth collected fractions of 5 mM AAPH stressed mAb1 using SEC for further characterization. Higher-order aggregates (peaks A and B in Figure 1), dimer (peak C in Figure 1), and monomer (peak D in Figure 1) peaks were collected and buffer exchanged to 20 mM sodium acetate buffer at pH 5.5. The sizes and purity of the enriched species were further confirmed by the SEC analysis. Each sample eluted as a single peak in SEC (Figure 2). The purity of higher-order aggregates, dimer, and monomer was estimated to be 99.1%, 93.2%, and 98.4%, respectively, based on SEC peak areas.

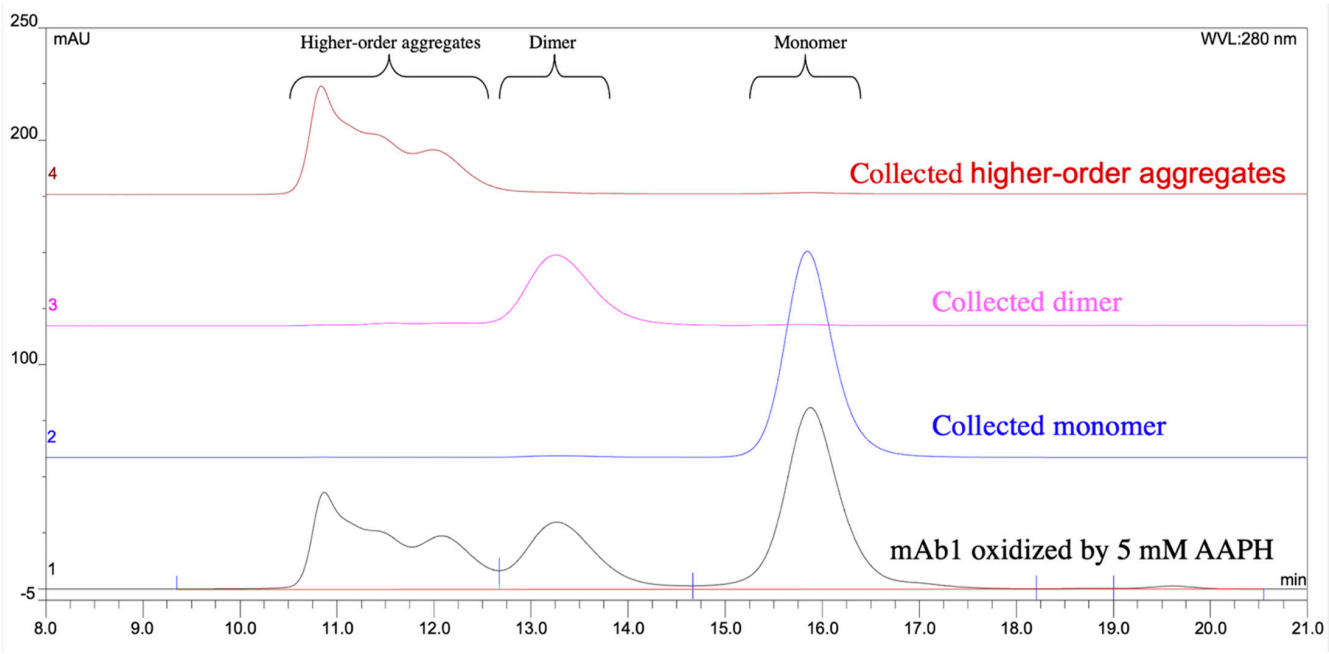

Figure 2. SEC of the collected fractions of mAb1 oxidized by 5 mM AAPH. Chromatogram 1: before fraction collection; chromatogram 2: re-injected monomer fraction; chromatogram 3: re-injected dimer fraction; chromatogram 4: re-injected higher-order aggregates fraction.

2.3. Aggregate Characterization

Sodium dodecyl sulfate polyacrylamide gel electrophoresis (SDS-PAGE) analysis with Coomassie blue staining was used to characterize properties of the fractions collected from SEC. Both reduced and non-reduced samples were analyzed by SDS-PAGE (Figure 3). Under the non-reduced condition, the un-oxidized control (lane 2 in the SDS-PAGE gel) runs with a molecular weight (MW) of ~150 kDa, as expected. Higher-order aggregates (lane 3 in the gel) showed multiple bands with MWs higher than the 188 kDa standard, indicating that higher-order aggregates consist of covalently linked multimers that do not dissociate under the denaturing condition. The dimer species (lane 4 in the gel) showed a single band with a MW higher than 188 kDa, indicating that the dimer is also covalently linked. The monomer peak (lane 5 in the gel) has a MW similar to the un-oxidized control sample in lane 2. Under the reduced condition, both the un-oxidized control sample and the monomer fraction (lanes 7 and 10 in the gel, respectively) dissociated into light chains (~25 kDa) and heavy chains (~50 kDa). Reduced higher-order aggregates (lane 8 in the gel) dissociated to light chains, heavy chains, and a few faint bands with MWs of 100 kDa or higher. These results indicate that inter-molecular disulfide cross-links contribute to the formation of higher-order aggregates. The aggregates with MWs of 100 kDa or higher suggest that the aggregates also contain non-reducible inter-molecular cross-links. The mass of 100 kDa suggests that the cross-links may be formed between two heavy chains. The dimer species (lane 9 in the gel) dissociated mainly to light chains and heavy chains upon reduction, indicating that inter-molecular disulfide bonds played a major role in mAb1 dimerization. In addition, a few faint bands with MWs of 100 kDa or higher were observed as well, suggesting other inter-molecular cross-links also contributed to dimerization.

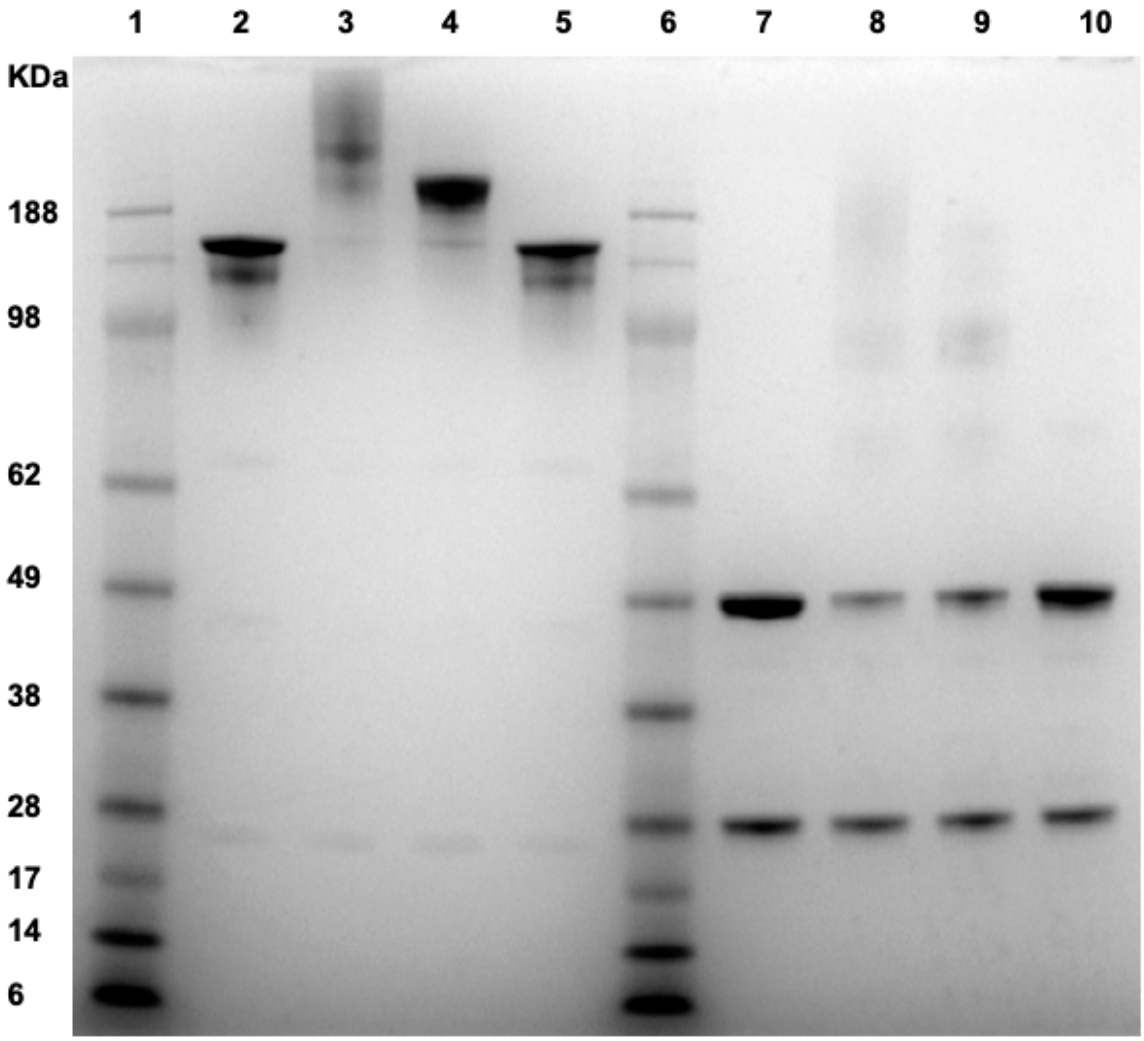

Figure 3. Sodium dodecyl sulfate polyacrylamide gel electrophoresis (SDS-PAGE) of the collected fractions from SEC. Lane 1: protein standards; lane 2: non-reduced control sample (no AAPH stressed mAb1); lane 3: non-reduced higher-order aggregates; lane 4: non-reduced dimer; lane 5: non-reduced monomer; lane 6: protein standards; lane 7: reduced control sample (no AAPH stressed mAb1); lane 8: reduced higher-order aggregates; lane 9: reduced dimer; lane 10: reduced monomer.

2.4. Mass Spectrometry with Trypsin Digestion

Because the aggregates contain non-reducible cross-links, we used the tryptic peptide maps to characterize chemical modifications of mAb1 after the AAPH stress (Figure 4). MAb1 contains Trp-33 in the CDR and Met-256 and Met-432 in the Fc region. Oxidation of these residues in higher-order aggregates, dimer, and monomer samples was observed as expected (indicated by arrows in Figure 4). Upon oxidation, the hydrophobicity of oxidized Met and Trp residues decreased and, therefore, eluted early on the reverse phase high-performance liquid chromatography (HPLC). Oxidation of Met-256 and Met-432 resulted in a single peak of MetOx-256 and MetOx-432 on the chromatograms, respectively. On the other hand, oxidation of Trp is more complicated than oxidation of Met because the indole side-chain of Trp could undergo various reactions during oxidation and lead to products with mass increases of +4, +16, +20, and +32 [26]; indeed, multiple peaks representing various oxidation products of Trp-33 were observed (Figure 4). These Trp-33 oxidation products eluted at 116–122 min. Some Trp oxidation products were visible as new peaks in the chromatograms and others co-eluted with other peptides. The mass increase of each Trp oxidation product is labeled in Figure 4. Except Met and Trp oxidation, we did not

observe any other new peaks in the chromatogram of the higher-order aggregate or dimer fraction that indicated non-reducible cross-links, as suggested by the data of SDS-PAGE. A reasonable explanation could be that the tryptic peptide containing cross-linking sites is very large, which has low ionization efficiency and is difficult to be detected by mass spectrometry. Another possible reason is that there are multiple cross-linking sites with low abundance, which can be detected by SDS-PAGE as broad faint bands, but not by mass spectrometry once eluted at different regions on the chromatogram.

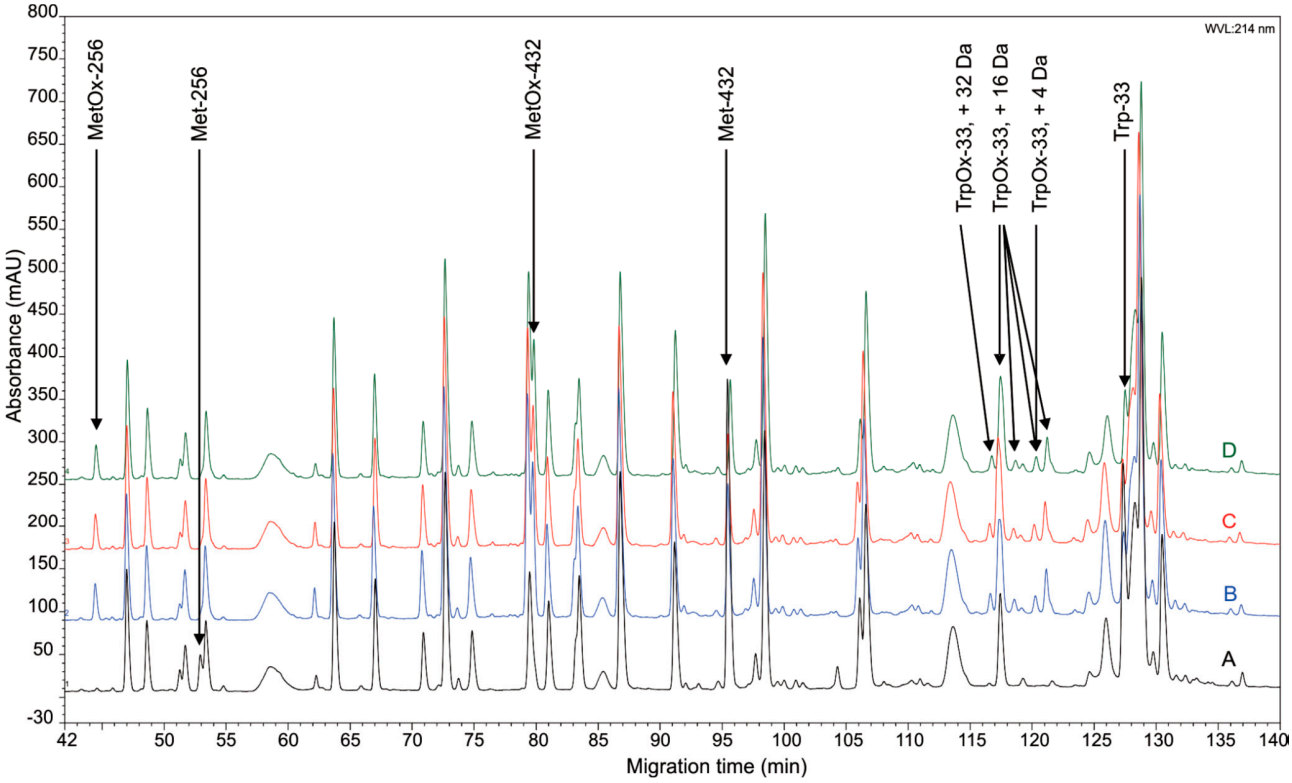

Figure 4. Expanded view of tryptic maps of collected SEC fractions of mAb1. Chromatogram A: control sample (no AAPH stressed mAb1); chromatogram B: collected monomer fraction from SEC; chromatogram C: collected dimer fraction from SEC; chromatogram D: collected higher-order aggregate fraction from SEC. Oxidized Met and Trp products and their parent peaks are labeled in the figure.

2.5. Intrinsic Fluorescence

Given that mass spectrometry cannot identify non-reducible cross-linking sites, we used intrinsic fluorescence spectroscopy for further characterization. Fluorescence emission spectra of AAPH-oxidized samples under the excitation wavelength of 325 nm are shown in Figure 5A. The broad emission peak between 400 and 430 nm suggests the existence of bityrosine cross-links after AAPH oxidation, as described in a previous report [11]. This result indicated that cross-links between Tyr residues could account for the non-reducible bands in SDS-PAGE (lanes 8 and 9 in Figure 3). In addition, we collected emission spectra of bityrosine standard to further support this hypothesis (Figure 5B). Spectra of the standard and oxidized mAb1 exhibited similar fluorescent peaks between 400 and 430 nm. Furthermore, a higher intensity of fluorescent emission was observed with increased AAPH concentration (Figure 5A), indicating an increasing trend of bityrosine cross-links with higher levels of AAPH.

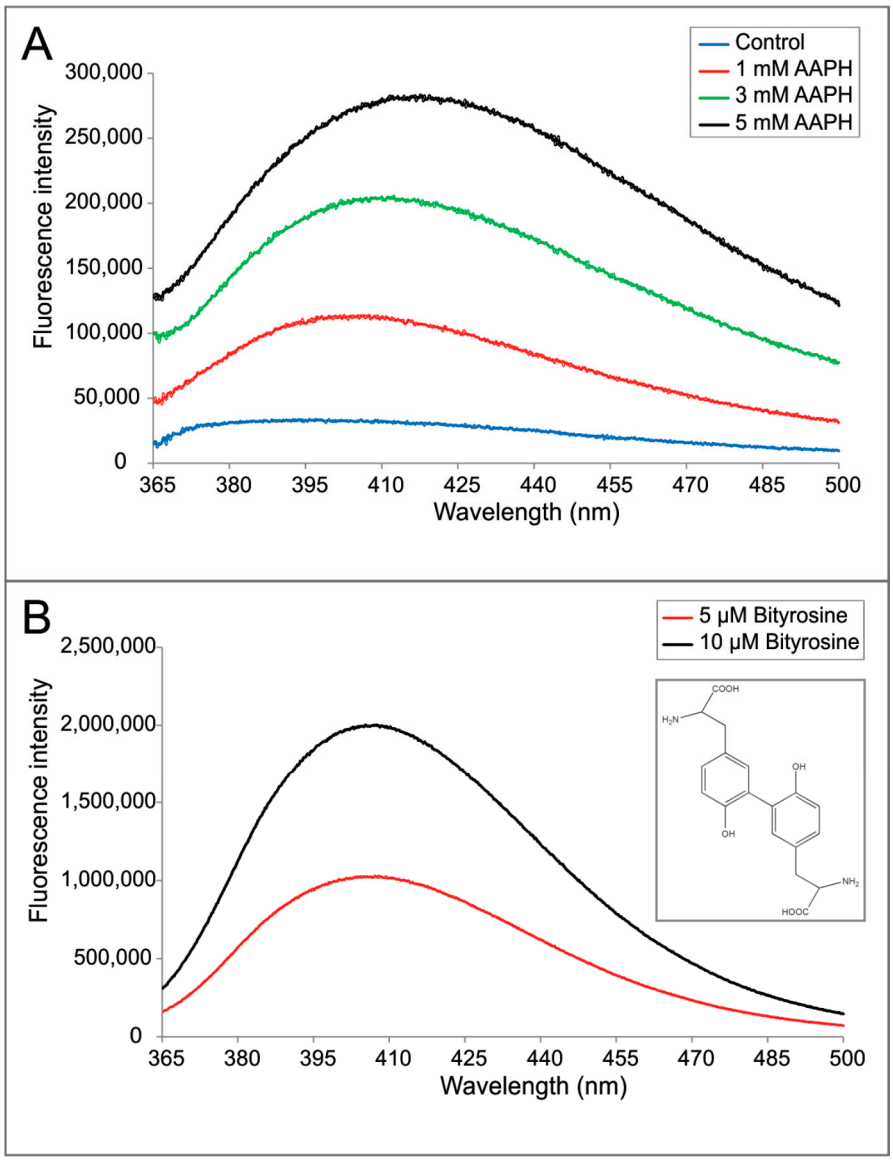

Figure 5. (**A**) Intrinsic fluorescence spectra of the control sample (no AAPH stressed mAb1) and mAb1 after stressing by 1, 3, and 5 mM AAPH. (**B**) Intrinsic fluorescence spectra of bityrosine standard at 5 μM and 10 μM. Inset: chemical structure of bityrosine.

2.6. Aggregation Inhibition

Because protein aggregates could induce immune responses and impact patient safety, it is important to protect therapeutic proteins from aggregation, especially when free radicals may be present in the protein solution [27]. In this study, we first screened Met, Trp, Tyr, His, and pyridoxine as aggregation inhibitors for the following reasons: free Met or Trp was added because Met and Trp oxidation was observed in mAb1 under the AAPH stress; free Tyr was evaluated as the fluorescence data suggest the formation of bityrosine cross-links; free His was selected because His oxidation has been reported in other studies [9,28]; and pyridoxine was included as a free radical scavenger [29]. We did not include ascorbic acid and N-acetyl cysteine (NAC), which are typical anti-oxidants, in the screening study as they will not be suitable excipients for therapeutic proteins: ascorbic acid has been shown to cause undesirable reactions with proteins and NAC may cause disulfide exchange [9]. The structures of the screened inhibitors are shown in Figure 6A. After incubation at 40 °C for 72 h, the aggregate levels were evaluated using SEC. The chromatograms shown in Figure 6B indicated that Trp, pyridoxine, and Tyr can effectively

protect protein from oxidation-induced aggregation under the AAPH stress. His and Met also decreased protein aggregation, but not to the same extent as Trp, pyridoxine, and Tyr.

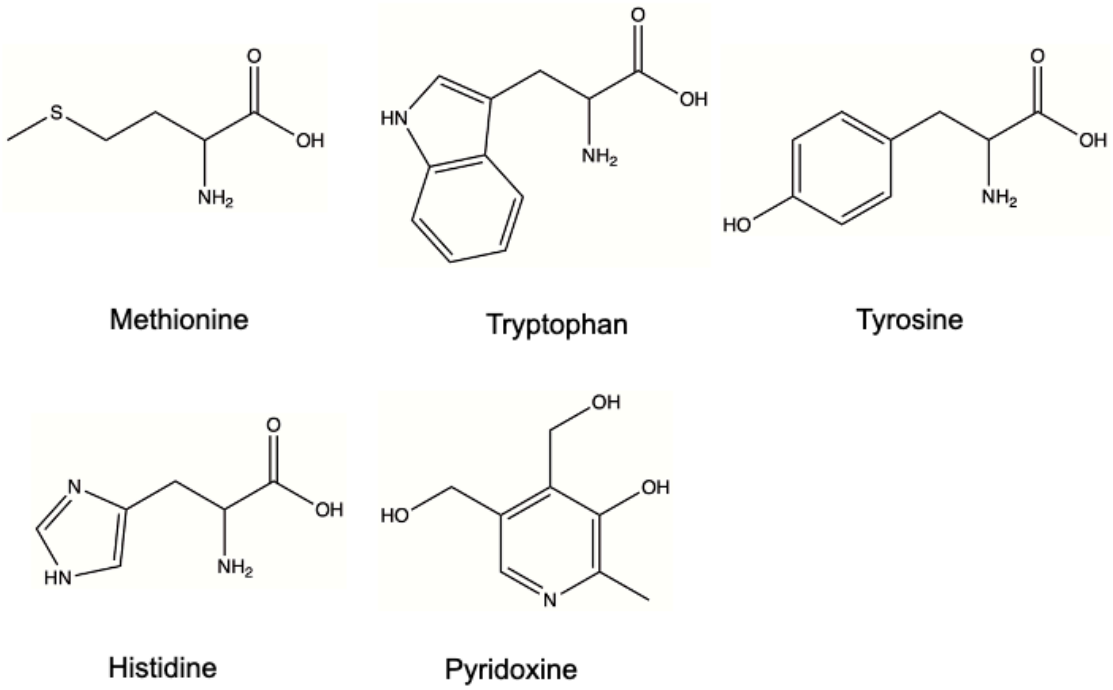

(**A**)

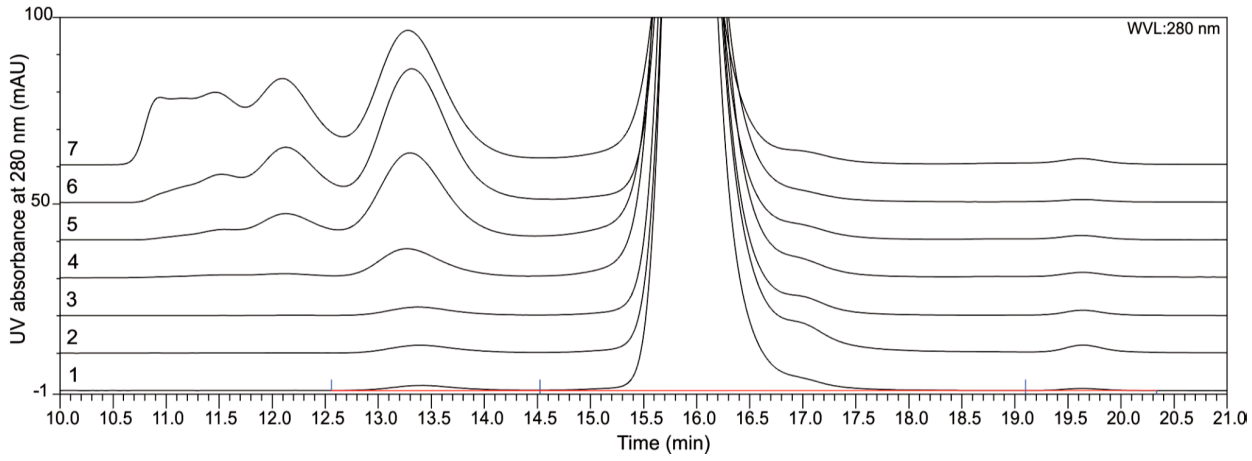

(**B**)

Figure 6. (**A**) Structure of tested aggregation inhibitors. (**B**) Expanded view of mAb1 SEC profiles for excipient screening (except the negative control, all samples contained 1 mM AAPH). Chromatogram 1: negative control sample (no AAPH stressed mAb1); chromatogram 2: sample contained 2 mM Trp; chromatogram 3: sample contained 2 mM pyridoxine; chromatogram 4: sample contained 2 mM Tyr; chromatogram 5: sample contained 2 mM His; chromatogram 6: sample contained 2 mM Met; chromatogram 7: positive control sample (AAPH stressed mAb1). All samples contained 10 mg/mL mAb1 and were incubated at 40 °C for 72 h prior to SEC analysis.

With this observation, we further expanded the assessment of the aggregation inhibition effect of Trp, pyridoxine, and Tyr on other types of mAbs, including another IgG1 mAb (mAb2), an IgG2 mAb (mAb3), and an IgG4 mAb (mAb4). Under the AAPH stress, all three mAbs showed substantial increases of aggregates (~12–18%) after 72 h of storage

at 40 °C (Figure 7), while the addition of Trp, pyridoxine, or Tyr can significantly reduce the aggregation, with the order of pyridoxine ≥ Trp > Tyr.

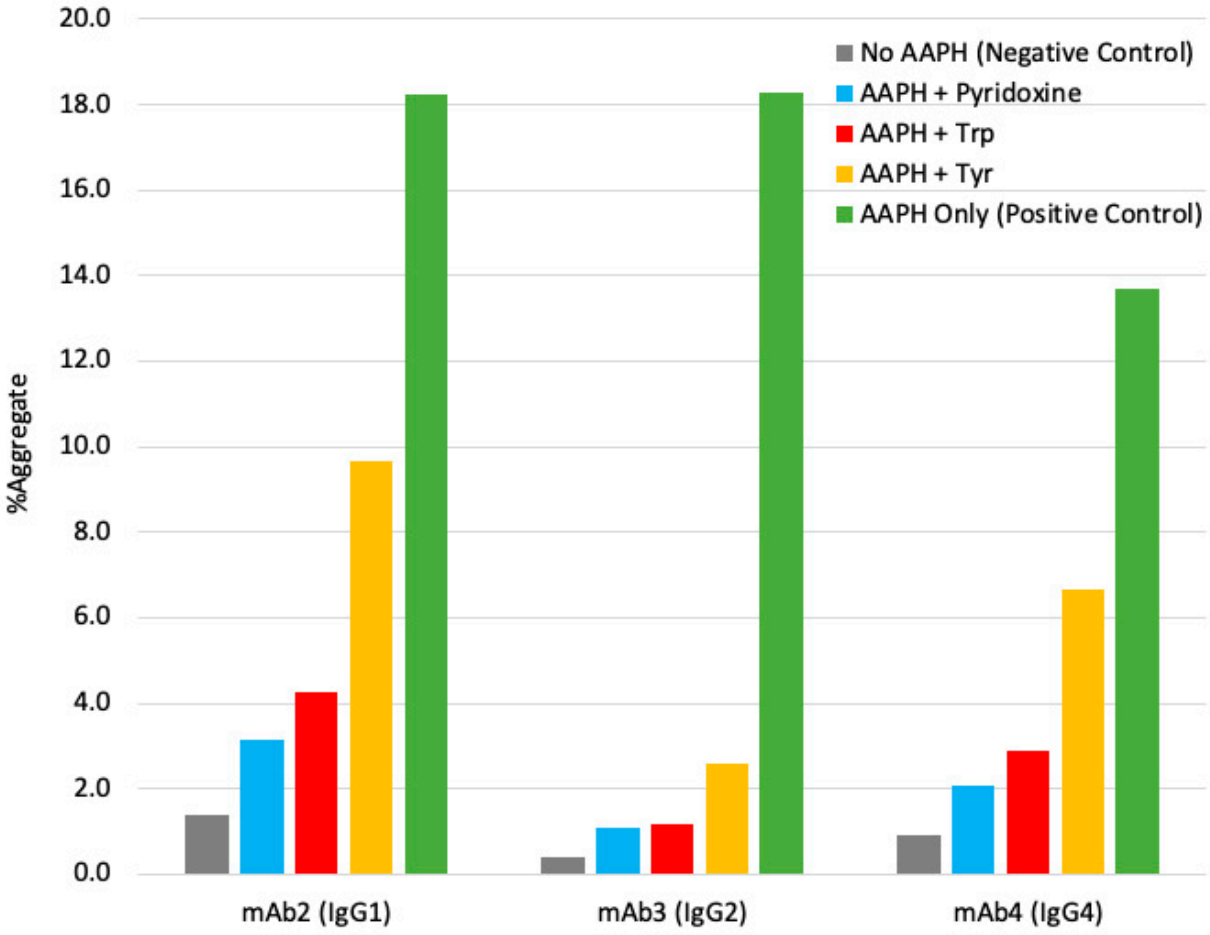

Figure 7. Aggregation of various mAbs under 1 mM AAPH stress after 72 h at 40 °C. Grey bar: no AAPH stressed mAb (negative control); light blue bar: AAPH stressed mAb containing pyridoxine; red bar: AAPH stressed mAb containing Trp; yellow bar: AAPH stressed mAb containing Tyr; green bar: AAPH stressed mAb without aggregation inhibitors (positive control).

3. Discussion

Protein oxidation is a very complicated process that could be triggered by chemical [4,6,30–33] or light [34–36] stresses and produces a diverse collection of oxidation products. In this study, we used AAPH as a chemical stress reagent to characterize oxidation of therapeutic mAbs. In addition to expected Met and Trp oxidation, we observed substantial protein aggregation. Although aggregated species of therapeutic proteins could cause immunogenicity risks and impact patient safety, there are few reports having a thorough investigation on oxidative-stress induced protein aggregation. Our work revealed that the newly formed aggregates are primarily covalently linked. Our results also differ from some previous reports. One report described a study that used *t*-BHP to assess Trp oxidation in a recombinant IgG1 mAb [17]. In that study, only a small increase in aggregation was observed by SEC, while our data showed a remarkable increase in aggregation. In another study [11], AAPH was used to oxidize Ca^{2+}-ATPase. There, protein aggregation was observed, but the contribution from disulfide cross-links was ruled out, whereas the data in our study suggested that a majority of aggregates in mAbs were covalently linked through inter-molecular disulfide bonds under the AAPH stress. Because an mAb contains a large number of disulfide bridges, inter-molecular disulfide cross-links could begin with the reduction of a disulfide bridge by free radicals and then the formation of a cysteine

thiyl radical intermediate, which is not stable and can react with another disulfide bridge in an adjacent molecule to form an inter-molecular disulfide cross-link [37].

In addition to disulfide cross-links, bityrosine cross-links can also contribute to the covalent aggregates in mAbs. Based on a number of previous reports [11,38,39], bityrosine cross-links may be formed through a phenoxyl radical intermediate, which is the product of the reaction between free radicals and tyrosine side-chains. Two phenoxyl radicals then recombine to form an inter-molecular or intra-molecular cross-link between two benzyl-ring side chains of Tyr residues. In this work, we observed fluorescence emission spectra that are characteristic of bityrosine, which suggests the formation of bityrosine cross-links under the AAPH stress (Figure 5A). As mAbs possess complex structures and numerous Tyr residues, it increases the challenge to identify the specific bityrosine cross-linking site compared with small proteins. For mAb1, in this study, there are eighteen Tyr residues in the heavy chain and ten Tyr residues in the light chain. The observed fluorescent peak in oxidized samples can be contributed from a single bityrosine cross-linking site or multiple cross-linking sites. To further characterize bityrosine cross-links, we generated homology models of heavy chain Fab, heavy chain Fc, and light chain regions (Figure 8A–C). In the heavy chain Fab region, only the side chain of Tyr-57 is fully exposed to solvent (the green color residue in Figure 8A). In heavy chain Fc and light chain regions (Figure 8B,C), all Tyr residues are buried inside. Thus, it is likely that the non-reducible inter-molecular cross-links are formed through heavy chain Fab regions. If that is the case, the $G^{41} \ldots \ldots DY^{57}A \ldots K^{62}$ peptide that dimerized through Tyr-57 should be observed in tryptic peptide mapping analysis (Figure 4). However, after careful analysis of mass spectroscopy data, such dimer peptide was not identified. This result may be because the dimer peptide is too hydrophobic to elute. In addition, as mentioned previously, the dimer peptide may lack sufficient ionization efficiency. Furthermore, during the AAPH stress, the mAb tertiary structure could be altered, and other Tyr residues may be exposed and cross-linked. In that case, protein aggregates contain heterogeneous bityrosine cross-links and the abundance of tryptic digested peptides that contain a specific cross-link would be too low to be detected by mass spectroscopy. A possible approach to identify cross-linking sites is to synthesize some peptides containing bityrosine cross-links and use them as standard compounds for peptide mapping analysis. Another strategy is to use site-specific mutations to investigate whether specific residues, such as Tyr-57 in the heavy chain, are responsible for the formation of inter-molecular cross-links. In addition, in-gel digestion may be another approach to identify cross-linking sites by combining SDS-PAGE and mass spectroscopy analysis. These alternative approaches are worthy of further investigation and can be explored in a separate study.

In this work, we assessed Trp, pyridoxine, and Tyr as aggregation inhibitors for IgG1, IgG2, and IgG4 types of mAbs, which covers a good range of antibody platforms as potential therapeutic proteins. To our knowledge, this is the first report to assess IgG1, IgG2, and IgG4 mAbs side-by-side for these inhibitors. Our results showed that these inhibitors can effectively reduce protein aggregation induced by free radicals for the tested mAbs. In general, these inhibitors protect proteins by consuming free radicals in the solution. Therefore, they can also provide a certain level of protection to oxidation labile residues in proteins, which was demonstrated in the previous report [9]. Ji et al.'s work showed that free Trp or pyridoxine in the formulation can effectively protect Trp oxidation in parathyroid hormone under the AAPH stress, while Tyr exhibited only slight protection of the Trp residue. Thus, to protect against both aggregation and oxidation of therapeutic proteins, we can consider combining the inhibitors tested in this work, or their homologs [40], with other anti-oxidant excipients in protein formulations. This strategy can be an effective approach, especially for large proteins that can have complex degradation mechanisms under oxidative stresses. Lastly, besides protection effectiveness, researchers also need to assess whether these excipients form adducts to therapeutic proteins and the impact of the oxidative end-products of these excipients. Though these experiments had

not been done in this work because they were outside the scope of the intended study, they should be considered during formulation development when using these excipients.

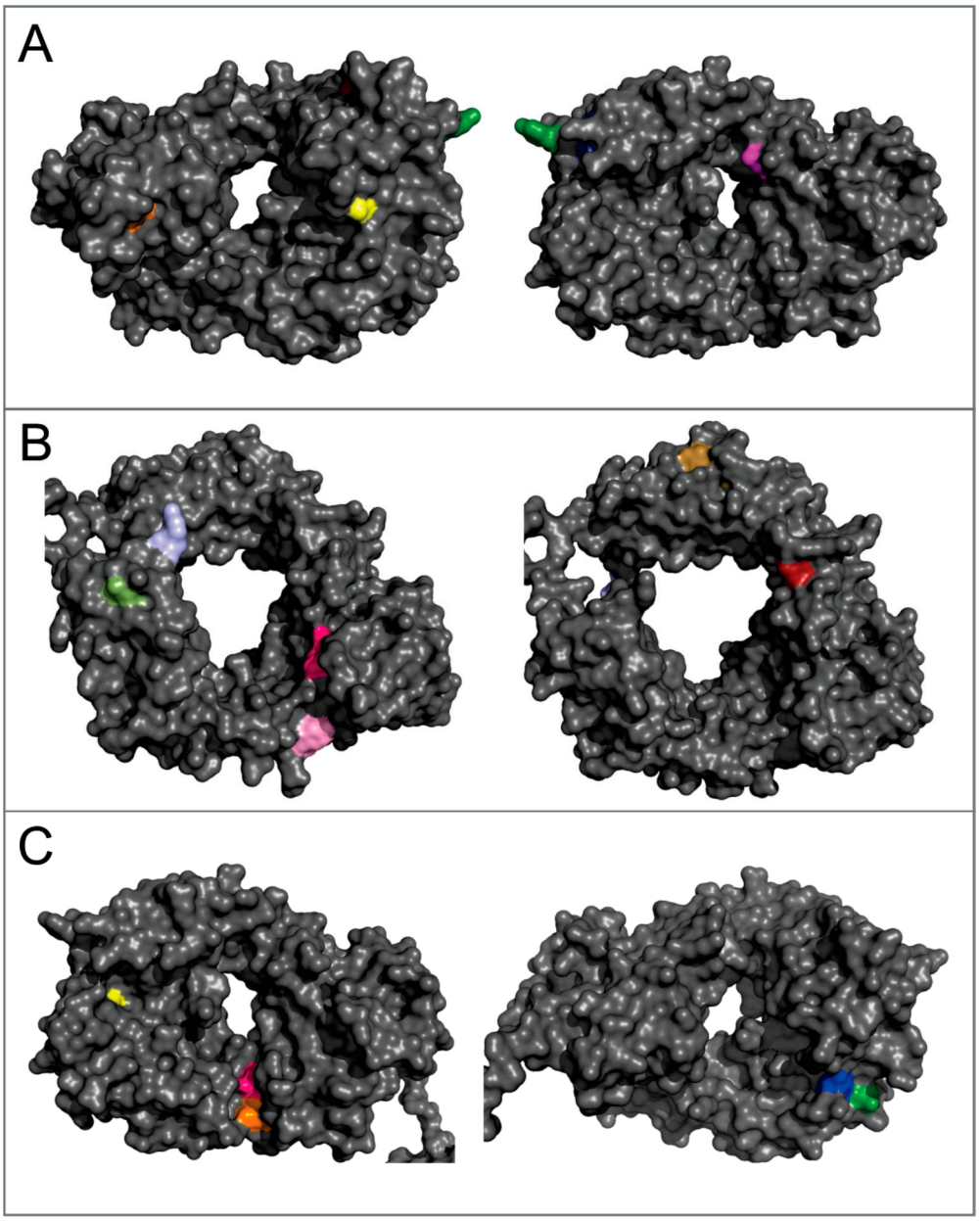

Figure 8. Homology models of mAb1 with the location of Tyr residues. (**A**) The heavy chain Fab region; (**B**) the heavy chain Fc region; and (**C**) the light chain. All Tyr residues are in color; the other residues are grey.

4. Materials and Methods

4.1. Reagents

The reagents used in this study included AAPH (EMD Chemicals, Gibbstown, NJ, USA), tris (2-carboxyethyl) phosphine (TCEP), trifluoroacetic acid (TFA), formic acid (Thermo Scientific, Waltham, MA, USA), DL-dithiothreitol (DTT), iodoacetic acid (IAA), L-Met, L-Trp, L-Tyr, pyridoxine (vitamin B6) (Sigma-Aldrich, St. Louis, MO, USA), trypsin (Roche, Indianapolis, IN, USA), water, acetonitrile, potassium phosphate monobasic, potassium phosphate dibasic (J.T. Baker, Phillipsburg, NJ, USA), and potassium chloride (Mallinckrodt Chemicals, Phillipsburg, NJ, USA).

4.2. Protein Production

MAb1 and mAb2 are humanized mAbs based on a human IgG1 framework containing heavy chain V_HIII and light chain V_KI subgroup sequences. MAb3 is a humanized mAb based on a human IgG2 framework containing heavy chain $V_{HI\beta}$ and light chain V_{LKI} subgroup sequences. MAb4 is a humanized mAb based on a human IgG4 framework. All mAbs are approximately 150 kDa in this study and were expressed in Chinese Hamster Ovary cells and purified through standard antibody purification procedures, including affinity chromatography, cation-exchange chromatography, anion-exchange chromatography, and final ultrafiltration and diafiltration steps. The purified mAbs thus obtained were further buffer exchanged into 20 mM sodium acetate buffer at pH 5.5 using 10,000 molecular weight cutoff (MWCO) Amicon Ultra-15 centrifugal filter devices (Millipore) and diluted to 20 mg/mL as the starting materials for the following studies in this work.

4.3. AAPH Stress of MAb1

Two milliliters of mAb1 at 10 mg/mL in 20 mM sodium acetate buffer at pH 5.5 was incubated with 1, 3, or 5 mM AAPH (final concentrations) for 24 h at 40 °C in 3 cc glass vials. The incubation was performed in chambers without illumination (in the dark). After incubation, all small molecule materials, including untreated AAPH, degraded AAPH, and other oxidants, were immediately removed from the antibody solution through buffer exchange using Zeba Spin desalting columns (Thermo Scientific), and the antibody was stored in 20 mM sodium acetate buffer at pH 5.5.

4.4. SEC Analysis

SEC provides quantitative information about the molecular size distribution of the protein. Size variants of the mAbs were separated using a TosoHaas TSK G3000SWXL column (7.8 × 300 mm) eluted isocratically with a mobile phase consisting of potassium phosphate and potassium chloride (pH 6.2). The separation was conducted at 25 °C with a flow rate of 0.5 mL/min. The detection wavelength was set at 280 nm.

Fractions of the entire peak of higher-order aggregate, dimer, and monomer species of mAb1 stressed by 5 mM AAPH were collected using the same column and chromatography conditions as mentioned above. The amount of mAb1 injected for fractionation was 0.5 mg. All collected fractions from SEC were concentrated to 10 mg/mL and buffer exchanged to 20 mM sodium acetate buffer at pH 5.5 using 10,000 MWCO Amicon Ultra-15 centrifugal filter devices.

4.5. SEC-MALS Analysis

An 18-angle Dawn enhanced optical system (EOS) light scattering detector with a 30 mW solid-state laser (λ = 690 nm) from Wyatt Technology was used for all SEC-MALS measurements. The sample temperature was maintained at 25 °C by a water-cooled Peltier temperature controller. The instrument was calibrated with 99.9% toluene (chromatography grade). For the SEC-MALS analysis, a detector gain setting of 100× was used for all photodiodes at fixed angles from 38° to 148°. Because the radius of gyration of mAb1 is <10 nm, 20 µL of a dilute solution (4 mg/mL) of mAb1 was used to normalize the voltage of the photodiodes relative to the 90° detector using a photodiode detector gain setting of 100× at the end of each experiment. During the experimental procedure, 10 µL of protein solution at 6 mg/mL was injected for each sample. Astra 5.3.4.20 Software (Wyatt Technology Corporation, Santa Barbara, CA, USA) was used to acquire and process the static light scattering data, with a dn/dc value of 0.185 mL/g applied to calculations with the appropriate extinction coefficient at UV 280 nm.

4.6. SDS-PAGE Analysis

The enriched monomer, dimer, and higher-order aggregates, along with an unoxidized control, were denatured in the presence or absence of a reducing agent, TCEP, and analyzed by SDS-PAGE. Non-reduced samples were denatured by heating in the SDS-

PAGE sample buffer at 60 °C for 10 min, while reduced samples were heated in the same buffer with the presence of TCEP. Each sample (3 μg) was loaded and separated on a 4–12% polyacrylamide gradient gel along with MW standards. The protein components were then visualized by Coomassie R-250 staining solution. The polyacrylamide gel, protein ladder, SDS-PAGE sample buffer, SDS-PAGE running buffer, Coomassie R-250 staining solution, and distaining solution were purchased from Invitrogen.

4.7. Tryptic Peptide Map

Control, higher-order aggregates, dimer, and monomer species were diluted to 0.5 mg/mL in 360 mM Tris, 2 mM EDTA, 40 mM DTT, 6 M guanidine hydrochloride buffer at pH 8.6. The diluted solution was incubated at 37 °C for 1 h to reduce all inter- and intra-chain disulfide bonds in mAb1. After the reduction, free thiol groups were protected through alkylation by adding freshly prepared IAA solution with a final IAA concentration of 90 mM. The alkylation reaction was completed in 15 min at room temperature with protection from light. The excess IAA was quenched by the addition of 1 M DTT solution to the final concentration of 50 mM. Immediately following the reduction and alkylation, samples were buffer exchanged to 25 mM Tris, 2 mM $CaCl_2$ buffer at pH 8.2 using Zeba Spin desalting columns. Trypsin was then added at a ratio of 1:45 (w:w) to the antibody solution, which was subsequently incubated at 37 °C for 5 h. After digestion was complete, 10% TFA was added to a final concentration of 0.3% to quench trypsin activities. Tryptic peptides were injected into an Agilent 1200 HPLC system for liquid chromatography (LC) separation and a Thermo Fisher Scientific LTQ Orbitrap XL mass spectrometer for mass analysis.

Details of the LC separation method were reported previously [41]. In brief, gradient elution was applied to a Jupiter C18 column (2.0 × 250 mm, 5 μm, 300 Å) from Phenomenex. The flow rate was 0.25 mL/min and the column temperature was maintained at 55 °C. The injection amount was 35 μg and the detection wavelength was set to 214 nm. The mass spectrometry data of LC eluents were collected by an LTQ Orbitrap XL mass spectrometer and analyzed using Xcalibur 2.0.7 (Thermo Fisher Scientific) [42].

4.8. Intrinsic Fluorescence Spectroscopy

Intrinsic fluorescence spectra of mAb1 were collected using a Horiba Jobin Yvon Fluoromax-4 spectrofluorometer with a temperature-controlled water bath. All protein solutions contained 0.3 mg/mL mAb1 in 20 mM sodium acetate buffer at pH 5.5. The emission spectrum was collected from 365 to 500 nm with the excitation wavelength of 325 nm at 25 °C. A blank spectrum of the formulation buffer was subtracted from each sample spectrum. The excitation and emission slit widths were both set at 5 nm and data were collected with 0.2 nm increments and 0.2 s integration time.

The bityrosine standard was synthesized by Hande Science. The purity of bityrosine standard was >93%, as determined by the HPLC analysis. The emission spectra of 5 and 10 μM bityrosine standard were collected at the same condition as the mAb1 samples.

4.9. Aggregation Inhibitor Screening

In the initial screening, MAb1 at 10 mg/mL in 20 mM sodium acetate buffer at pH 5.5 with 1 mM AAPH was incubated with 2 mM aggregation inhibitors (Met, Trp, Tyr, His, or pyridoxine) at 40 °C for 72 h. In the subsequent screening, mAb2, mAb3, and mAb4 at 10 mg/mL in the same buffer including 1 mM AAPH were incubated with 2 mM aggregation inhibitors (Trp, pyridoxine, or Tyr) at 40 °C for 72 h. In addition, mAbs in 20 mM sodium acetate buffer at pH 5.5 without or with 1 mM AAPH were also incubated at 40 °C for 72 h as negative and positive controls, respectively, in both screening studies. After incubation, AAPH and other excipients were immediately removed from mAb solutions using Zeba Spin desalting columns. The purified samples were in 20 mM sodium acetate buffer at pH 5.5 and injected into a SEC column for size analysis.

5. Conclusions

In summary, the study results showed that free radicals can cause substantial mAb oxidation and aggregation. Free radicals can be introduced into therapeutic protein formulations from light exposure, excipient raw materials, and so on. Trp, pyridoxine, Tyr, or its homologs, in combination with other anti-oxidant excipients, can be an effective approach to protect therapeutic proteins against both aggregation and oxidation under oxidative stresses.

Author Contributions: Conceptualization, K.Z., Y.J.W. and J.A.J.; methodology, K.Z.; data curation, K.Z., D.R., W.L., T.S. and J.K.Y.H.; writing—original draft preparation, K.Z.; writing—review and editing, K.Z., D.R., Y.J.W., W.L., T.S., J.K.Y.H. and J.A.J. All authors have read and agreed to the published version of the manuscript.

Funding: The authors declare no competing financial interest.

Institutional Review Board Statement: Not applicable.

Informed Consent Statement: Not applicable.

Acknowledgments: The authors would like to thank Eileen Y. Ivasauskas for editorial assistance, and Sreedhara Alavattam and Wei Liu for reviewing this manuscript.

Conflicts of Interest: The authors declare no conflict of interest.

Abbreviations

AAPH, 2,2′-azobis (2-amidinopropane) dihydrochloride; Cys, cysteine; EOS, enhanced optical system; HIS, histidine; DTT, DL-dithiothreitol; HPLC, high-performance liquid chromatography; IAA, iodoacetic acid; LC, liquid chromatography; mAb, monoclonal antibody; Met, methionine; MW, molecular weight; MWCO, molecular weight cutoff; NAC, N-acetyl cysteine; SDS-PAGE, sodium dodecyl sulfate polyacrylamide gel electrophoresis; SEC, size-exclusion chromatography; SEC-MALS, size-exclusion chromatography and multi-angle light scattering; *t*-BHP, *tert*-butyl hydroperoxide; TCEP, tris(2-carboxyethyl) phosphine; Trp, tryptophan; Tyr, tyrosine; UV, ultraviolet.

References

1. Roy, S.; Mason, B.D.; Schöneich, C.S.; Carpenter, J.F.; Boone, T.C.; Kerwin, B.A. Light-induced aggregation of type I soluble tumor necrosis factor receptor. *J. Pharm. Sci.* **2009**, *98*, 3182–3199. [CrossRef] [PubMed]
2. Ha, E.; Wang, W.; Wang, Y.J. Peroxide formation in polysorbate 80 and protein stability. *J. Pharm. Sci.* **2002**, *91*, 2252–2264. [CrossRef] [PubMed]
3. Kroon, D.J.; Baldwin-Ferro, A.; Lalan, P. Identification of sites of degradation in a therapeutic monoclonal antibody by peptide mapping. *Pharm. Res.* **1992**, *9*, 1386–1393. [CrossRef] [PubMed]
4. Hovorka, S.; Schöneich, C. Oxidative degradation of pharmaceuticals: Theory, mechanisms and inhibition. *J. Pharm. Sci.* **2001**, *90*, 253–269. [CrossRef]
5. Wecksler, A.T.; Yin, J.; Tao, P.L.; Kabakoff, B.; Sreedhara, A.; Deperalta, G. Photodisruption of the structurally conserved Cys-Cys-Trp triads leads to reduction-resistant scrambled intrachain disulfides in an IgG1 monoclonal antibody. *Mol. Pharm.* **2018**, *15*, 1598–1606. [CrossRef]
6. Li, S.; Schöneich, C.; Borchardt, R.T. Chemical instability of protein pharmaceuticals: Mechanisms of oxidation and strategies for stabilization. *Biotechnol. Bioeng.* **1995**, *48*, 490–500. [CrossRef] [PubMed]
7. Wei, Z.; Feng, J.; Lin, H.-Y.; Mullapudi, S.; Bishop, E.; Tous, G.I.; Casas-Finet, J.; Hakki, F.; Strouse, R.; Schenerman, M.A. Identification of a single tryptophan residue as critical for binding activity in a humanized monoclonal antibody against respiratory syncytial virus. *Anal. Chem.* **2007**, *79*, 2797–2805. [CrossRef]
8. Chumsae, C.; Gaza-Bulseco, G.; Sun, J.; Liu, H. Comparison of methionine oxidation in thermal stability and chemically stressed samples of a fully human monoclonal antibody. *J. Chromatogr. B* **2007**, *850*, 285–294. [CrossRef]
9. Ji, J.A.; Zhang, B.; Cheng, W.; Wang, Y.J. Methionine, tryptophan, and histidine oxidation in a model protein, PTH: Mechanisms and stabilization. *J. Pharm. Sci.* **2009**, *98*, 4485–4500. [CrossRef]
10. Keck, R.G. The use of t-butyl hydroperoxide as a probe for methionine oxidation in proteins. *Anal. Biochem.* **1996**, *236*, 56–62. [CrossRef]
11. Viner, R.I.; Krainev, A.G.; Williams, T.D.; Schöneich, C.; Bigelow, D.J. Identification of oxidation-sensitive peptides within the cytoplasmic domain of the sarcoplasmic reticulum Ca^{2+}-ATPase. *Biochemistry* **1997**, *36*, 7706–7716. [CrossRef]

12. Liu, D.; Ren, D.; Huang, H.; Dankberg, J.; Rosenfeld, R.; Cocco, M.J.; Li, L.; Brems, D.N.; Remmele, R.L. Structure and stability changes of human IgG1 Fc as a consequence of methionine oxidation. *Biochemistry* **2008**, *47*, 5088–5100. [CrossRef]
13. Boyd, D.; Kaschak, T.; Yan, B. HIC resolution of an IgG1 with an oxidized Trp in a complementarity determining region. *J. Chromatogr. B* **2011**, *879*, 955–960. [CrossRef] [PubMed]
14. Lu, H.S.; Fausset, P.R.; Narhi, L.O.; Horan, T.; Shinagawa, K.; Shimamoto, G.; Boone, T.C. Chemical modification and site-directed mutagenesis of methionine residues in recombinant human granulocyte colony-stimulating factor: Effect on stability and biological activity. *Arch. Biochem. Biophys.* **1999**, *362*, 1–11. [CrossRef] [PubMed]
15. Wang, W.; Vlasak, J.; Li, Y.; Pristatsky, P.; Fang, Y.; Pittman, T.; Roman, J.; Wang, Y.; Prueksaritanont, T.; Ionescu, R. Impact of methionine oxidation in human IgG1 Fc on serum half-life of monoclonal antibodies. *Mol. Immunol.* **2011**, *48*, 860–866. [CrossRef]
16. Nguyen, T.H.; Burnier, J.; Meng, W. The kinetics of relaxin oxidation by hydrogen peroxide. *Pharm. Res.* **1993**, *10*, 1563–1571. [CrossRef]
17. Hensel, M.; Steurer, R.; Fichtl, J.; Elger, C.; Wedekind, F.; Petzold, A.; Schlothauer, T.; Molhoj, M.; Reusch, D.; Bulau, P. Identification of potential sites for tryptophan oxidation in recombinant antibodies using tert-butylhydroperoxide and quantitative LC-MS. *PLoS ONE* **2011**, *6*, e17708. [CrossRef] [PubMed]
18. Liu, H.; Gaza-Bulseco, G.; Xiang, T.; Chumsae, C. Structural effect of deglycosylation and methionine oxidation on a recombinant monoclonal antibody. *Mol. Immunol.* **2008**, *45*, 701–708. [CrossRef] [PubMed]
19. Niki, E. Free radical initiators as source of water- or lipid-soluble peroxyl radicals. *Methods Enzymol.* **1990**, *186*, 100–108.
20. Werber, J.; Wang, Y.J.; Milligan, M.; Li, X.; Ji, J.A. Analysis of 2,2′-azobis (2-amidinopropane) dihydrochloride degradation and hydrolysis in aqueous solutions. *J. Pharm. Sci.* **2011**, *100*, 3307–3315. [CrossRef] [PubMed]
21. Steinmann, D.; Ji, J.A.; Wang, Y.J.; Schöneich, C. Oxidation of human growth hormone by oxygen-centered radicals: Formation of Leu-101 hydroperoxide and Tyr-103 oxidation products. *Mol. Pharm.* **2012**, *9*, 803–814. [CrossRef]
22. Yoshida, Y.; Itoh, N.; Saito, Y.; Hayakawa, M.; Niki, E. Application of water-soluble radical initiator, 2,2′-azobis[2-(2-imidazolin-2-yl)propane] dihydrochloride, to a study of oxidative stress. *Free Radic. Res.* **2004**, *38*, 375–384. [CrossRef]
23. Sluzky, V.; Tamada, J.A.; Klibanov, A.M.; Langer, R. Kinetics of insulin aggregation in aqueous solutions upon agitation in the presence of hydrophobic surfaces. *Proc. Natl. Acad. Sci. USA* **1991**, *88*, 9377–9381. [CrossRef]
24. Carpenter, J.F.; Kendrick, B.S.; Chang, B.S.; Manning, M.C.; Randolph, T.W. Inhibition of stress-induced aggregation of protein therapeutics. *Methods Enzymol.* **1999**, *309*, 236–255.
25. Ratanji, K.D.; Derrick, J.P.; Dearman, R.J.; Kimber, I. Immunogenicity of therapeutic proteins: Influence of aggregation. *J. Immunotoxicol.* **2014**, *11*, 99–109. [CrossRef]
26. Finley, E.L.; Dillon, J.; Crouch, R.K.; Schey, K.L. Identification of tryptophan oxidation products in bovine alpha-crystallin. *Protein Sci.* **1998**, *7*, 2391–2397. [CrossRef]
27. Kerwin, B.A. Polysorbates 20 and 80 used in the formulation of protein biotherapeutics: Structure and degradation pathways. *J. Pharm. Sci.* **2008**, *97*, 2924–2935. [CrossRef]
28. Zhao, F.; Ghezzo-Schöneich, E.; Aced, G.I.; Hong, J.; Milby, T.; Schöneich, C. Metal-catalyzed oxidation of histidine in human growth hormone. Mechanism, isotope effects, and inhibition by a mild denaturing alcohol. *J. Biol. Chem.* **1997**, *272*, 9019–9029. [CrossRef]
29. Matxain, J.M.; Padro, D.; Ristilä, M.; Strid, Å.; Eriksson, L.A. Evidence of High •OH Radical Quenching Efficiency by Vitamin B6. *J. Phys. Chem. B* **2009**, *113*, 9629–9632. [CrossRef] [PubMed]
30. Liu, J.L.; Lu, K.V.; Eris, T.; Katta, V.; Westcott, K.R.; Narhi, L.O.; Lu, H.S. In vitro methionine oxidation of recombinant human leptin. *Pharm. Res.* **1998**, *15*, 632–640. [CrossRef]
31. Chu, J.W.; Yin, J.; Brooks, B.R.; Wang, D.I.C.; Ricci, M.S.; Brems, D.N.; Trout, B.L. A comprehensive picture of non-site specific oxidation of methionine residues by peroxides in protein pharmaceuticals. *J. Pharm. Sci.* **2004**, *93*, 3096–3102. [CrossRef] [PubMed]
32. Simat, T.J.; Steinhart, H. Oxidation of free tryptophan and tryptophan residues in peptides and proteins. *J. Agric. Food. Chem.* **1998**, *46*, 490–498. [CrossRef]
33. Mozziconacci, O.; Arora, J.; Toth, R.T.; Joshi, S.B.; Zhou, S.; Volkin, D.B.; Schöneich, C. Site-specific hydrolysis reaction C-terminal of methionine in Met-His during metal-catalyzed oxidation of IgG-1. *Mol. Pharm.* **2016**, *13*, 1317–1328. [CrossRef]
34. Qi, P.; Volkin, D.B.; Zhao, H.; Nedved, M.L.; Hughes, R.; Bass, R.; Yi, S.C.; Panek, M.E.; Wang, D.; Dalmonte, P.; et al. Characterization of the photodegradation of a human IgG1 monoclonal antibody formulated as a high-concentration liquid dosage form. *J. Pharm. Sci.* **2009**, *98*, 3117–3130. [CrossRef]
35. Pigault, C.; Gerard, D. Influence of the location of tryptophan residues in proteins on their photosensitivity. *Photochem. Photobiol.* **1984**, *40*, 291–296. [CrossRef]
36. Bommana, R.; Chai, Q.; Schöneich, C.; Weiss, W.F.; Majumdar, R. Understanding the increased aggregation propensity of a light-exposed IgG1 monoclonal antibody using hydrogen exchange mass spectrometry, biophysical characterization, and structural analysis. *J. Pharm. Sci.* **2018**, *107*, 1498–1511. [CrossRef]
37. Lu, D.; Liu, Z. Dynamic redox environment-intensified disulfide bond shuffling for protein refolding in vitro: Molecular simulation and experimental validation. *J. Phys. Chem. B* **2008**, *112*, 15127–15133. [CrossRef]
38. DiMarco, T.; Giulivi, C. Current analytical methods for the detection of dityrosine, a biomarker of oxidative stress, in biological samples. *Mass Spectrom. Rev.* **2007**, *26*, 108–120. [CrossRef]

39. Wang, Y.; Mattice, W.L. Intramolecular vs intermolecular formation of bityrosine upon photoreaction of poly(l-tyrosine) in dilute aqueous solution. *Polym. Bull.* **1992**, *28*, 345–349. [CrossRef]
40. Grewal, P.; Mallaney, M.; Lau, K.; Sreedhara, A. Screening methods to identify indole derivatives that protect against reactive oxygen species induced tryptophan oxidation in proteins. *Mol. Pharm.* **2014**, *11*, 1259–1272.
41. Yang, Y.; Strahan, A.; Li, C.; Shen, A.; Liu, H.; Ouyang, J.; Katta, V.; Francissen, K.; Zhang, B. Detecting low level sequence variants in recombinant monoclonal antibodies. *MAbs* **2010**, *2*, 285–298. [CrossRef] [PubMed]
42. Ren, D.; Zhang, J.; Pritchett, R.; Liu, H.; Kyauk, J.; Luo, J.; Amanullah, A. Detection and identification of a serine to arginine sequence variant in a therapeutic monoclonal antibody. *J. Chromatogr. B* **2011**, *879*, 2877–2884. [CrossRef]

International Journal of
Molecular Sciences

MDPI

Article

Development of a New Highly Selective Monoclonal Antibody against Preferentially Expressed Antigen in Melanoma (PRAME) and Identification of the Target Epitope by Bio-Layer Interferometry

Jwala Priyadarsini Sivaccumar [1], Antonio Leonardi [2], Emanuela Iaccarino [1], Giusy Corvino [1], Luca Sanguigno [2], Angela Chambery [3], Rosita Russo [3], Mariangela Valletta [3], Debora Latino [1], Domenica Capasso [4], Nunzianna Doti [1], Menotti Ruvo [1,*] and Annamaria Sandomenico [1,*]

[1] Istituto di Biostrutture e Bioimmagini, CNR, 80134 Napoli, Italy; jwala.priyadarsini@gmail.com (J.P.S.); emanuela.iaccarino@gmail.com (E.I.); giusycorvino1986@gmail.com (G.C.); latinodebora@gmail.com (D.L.); nunzianna.doti@cnr.it (N.D.)
[2] Dipartimento di Medicina Molecolare e Biotecnologie Mediche, Università degli Studi di Napoli Federico II, 80142 Napoli, Italy; leonardi@unina.it (A.L.); lucasanguigno@libero.it (L.S.)
[3] Dipartimento di Scienze e Tecnologie Ambientali, Biologiche e Farmaceutiche (DISTABIF), Università L. Vanvitelli, 80100 Caserta, Italy; angela.chambery@unicampania.it (A.C.); rosita.russo@unicampania.it (R.R.); mariangela.valletta@unicampania.it (M.V.)
[4] Centro di Servizio di Ateneo per le Scienze e Tecnologie per la Vita (CESTEV), Università di Napoli Federico II, 80145 Napoli, Italy; domenica.capasso@unina.it
* Correspondence: menotti.ruvo@unina.it (M.R.); annamaria.sandomenico@cnr.it (A.S.)

Abstract: Background: Monoclonal antibodies (mAbs) against cancer biomarkers are key reagents in diagnosis and therapy. One such relevant biomarker is a preferentially expressed antigen in melanoma (PRAME) that is selectively expressed in many tumors. Knowing mAb's epitope is of utmost importance for understanding the potential activity and therapeutic prospective of the reagents. Methods: We generated a mAb against PRAME immunizing mice with PRAME fragment 161–415; the affinity of the antibody for the protein was evaluated by ELISA and SPR, and its ability to detect the protein in cells was probed by cytofluorimetry and Western blotting experiments. The antibody epitope was identified immobilizing the mAb on bio-layer interferometry (BLI) sensor chip, capturing protein fragments obtained following trypsin digestion and performing mass spectrometry analyses. Results: A mAb against PRAME with an affinity of 35 pM was obtained and characterized. Its epitope on PRAME was localized on residues 202–212, taking advantage of the low volumes and lack of fluidics underlying the BLI settings. Conclusions: The new anti-PRAME mAb recognizes the folded protein on the surface of cell membranes suggesting that the antibody's epitope is well exposed. BLI sensor chips can be used to identify antibody epitopes.

Keywords: PRAME; mAb; bio-layer interferometry; epitope identification

Citation: Sivaccumar, J.P.; Leonardi, A.; Iaccarino, E.; Corvino, G.; Sanguigno, L.; Chambery, A.; Russo, R.; Valletta, M.; Latino, D.; Capasso, D.; et al. Development of a New Highly Selective Monoclonal Antibody against Preferentially Expressed Antigen in Melanoma (PRAME) and Identification of the Target Epitope by Bio-Layer Interferometry. *Int. J. Mol. Sci.* **2021**, *22*, 3166. https://doi.org/10.3390/ijms22063166

Academic Editor: Donald J. Buchsbaum

Received: 28 February 2021
Accepted: 18 March 2021
Published: 20 March 2021

1. Introduction

Cancer is a disease with great molecular diversity and unpredictable nature. To combat its complexity and achieve improved treatment outcomes, modern oncology is shifting from empirical treatment strategies to biomarker-driven treatment models based upon the molecular profile of tumors from single individuals. The development of personalized cancer therapy is reliant on the identification and validation of specific biomarkers, which are associated, or even coincident, with the therapeutic targets whose activity is modulated by the administered drugs. In cancer, most drugs are monoclonal antibodies able to bind with high affinity and selectivity specific sites of the targets, thus preventing pathologically relevant interactions or blocking aberrant activities [1]. In this context, knowing the antibody's epitope on the target protein is of utmost importance to plan the antibody use

and to understand its therapeutic potential. One group of tumor-specific biomarkers called preferentially expressed antigen of melanoma (PRAME), also known as MAPE (melanoma antigen preferentially expressed in tumors), cancer-testis antigen 130 (CT130), and OIP4 (OPA-interacting protein 4) was initially identified in an autologous cytolytic T lymphocyte clone in a melanoma cell line [2]. Although PRAME belongs to the category of cancer-testis antigen, it is aberrantly reexpressed in many types of cancers, including metastatic melanoma, head and neck carcinoma, renal cell cancer, multiple myeloma, non-small cell lung carcinomas, neuroblastoma, chronic myeloid leukemia, acute leukemia, uveal melanoma, several sarcoma subtypes, and in triple-negative breast cancers. In most of them, its presence is associated with a poor prognosis [3]. High levels of PRAME expression are correlated with favorable outcomes following chemotherapy treatments of hematological malignancies, such as acute myeloid and lymphoblastic leukemia [4,5].

PRAME is a member of the leucine-rich repeat (LRR) family of proteins and physiologically acts mainly by inhibiting the retinoic acid-mediated differentiation, proliferation and apoptosis [6]. However, the precise molecular functions of PRAME and its role in oncogenesis are not well understood. Hence, far, by epitope-tagged immunoprecipitations and mass spectrometry, it has been established that PRAME facilitates the recruitment of cullin2 ubiquitin ligases to the EKC/KEOPS complex in the nucleus where it is involved in the transcriptional regulation of target genes [7–9]. Several studies have also shown that upregulation of PRAME expression in various types of malignancies is linked to hypomethylation of DNA promoters [10–14]. Furthermore, the upregulation of PRAME features cell stemness, invasion, and metastasis in triple-negative breast cancer by promoting the epithelial-to-mesenchymal transition (EMT) through the activation of ZEB1 and downregulation of *BMP7* and *TSPAN13* genes) [15]. By all these features, PRAME is emerging as an interesting biomarker and a potential therapeutic target for a number of diseases [3]. Several immunotherapeutic clinical trials targeted PRAME by means of PRAME peptides and adoptive T cell therapy with autologous pre-existing circulating PRAME-specific T cells or genetic engineering of high-affinity PRAME-specific TCR T cells [3,16].

Numerous evidence also indicates that PRAME is membrane-bound in several cancer cells and that antibodies targeting the extracellular region 310–331 show effectiveness to detect cancers and potentially treat them through targeted therapies [17]. On the other hand, a TCR mimicking a human antibody was developed to recognize a PRAME peptide (300–309) in complex with HLA-A2, enabling antibody-dependent cellular cytotoxicity (ADCC) [18]. Further, anti-PRAME TCR mimetics can enhance antibody-dependent phagocytosis on PRAME-positive cancer cells by synergistic treatments with CD47 blockade agents [19].

All these recent evidences support PRAME as a promising target for developing CAR-T-based immunotherapies using CARs that bind PRAME peptides bound to HLAs or the protein on cancer cells expressing it on their surface. They also support the use of antibodies and related drug conjugates, alone or in combination with immune checkpoint inhibitors, for the targeted therapy of PRAME-positive cancers.

The epitopes recognized by antibodies obtained by immunization with full-length folded proteins are often unknown and may request extensive investigations with overlapping synthetic peptides or mutational studies. Antibodies raised against small synthetic peptides have the advantage that the binding site is known a priori. However, they may display a relatively low affinity for the full-length parent proteins where the structure of the epitope may differ considerably from that of the original immunogen. In the case of PRAME, the epitope analysis of a panel of mAbs [20] and the development of a polyclonal antibody against the predicted extracellular PRAME 310–331 peptide [16] have been recently described. Capture experiments of protein fragments with antibody-immobilized sensor chips can also be performed in this instance using, for example, label-free devices that provide real-time evidence of the capture and of the release of the bound epitope [21,22]. Instruments

working in flow are well suited for these purposes; however, dilution of the sample and difficulties in collecting the bound fractions may represent an important limitation.

Here, we report the generation of a monoclonal antibody against the central protein domain of PRAME spanning residues 161 to 415. The selected murine monoclonal antibody, named 2D5, exhibits a very strong affinity for the protein (dissociation constant in the picomolar range), binds and efficiently recognizes the native PRAME protein in Western blotting and FACS analyses. The epitope of the antibody also has been identified by immunoaffinity capturing the trypsin digested protein fragments on a bio-layer interferometry sensor chip derivatized with the antibody, taking advantage of the small volume used in the experiments and the lack of fluidics.

2. Results

2.1. Proteins Expression and Purification

The human PRAME protein (UniProtKB—P78395) spanning residues 161–415 was expressed in *E. coli* as N-terminal His-tagged recombinant protein using the pET28a vector (*rh*PRAME, Figure S1). The recombinant protein was mostly recovered after repeated dialysis against PBS containing 0.5 M urea and 1 mM DTT with a purity higher than 90%, as demonstrated by SDS–PAGE analysis on 12% polyacrylamide gel. The protein was detected as a band at MW between 37 kDa and 25 kDa in agreement with the predicted molecular weight of about 33 kDa (Figure S2A,B). Lower concentrations of urea lead to precipitation of most protein; therefore, the final sample was stored in a final buffer containing the denaturing agent at 0.5 M. However, some diluted protein samples were recovered and characterized by gel filtration to assess that it was not aggregated and used to perform immunization of the animals for producing the monoclonal antibodies, the ELISA and the SPR assays. GF analysis of the pure protein showed that the fraction recovered after urea removal was monomeric and highly pure (See Figure S3A–C). The anti–PRAME 2D5 mAb was obtained >90% pure as assessed by 15% SDS–PAGE under reducing and nonreducing conditions (Figure S4).

2.2. Binding of 2D5 Anti-PRAME mAb to rhPRAME by ELISA and SPR

The selected and purified murine anti-PRAME 2D5 monoclonal antibody was tested for its capability to properly recognize the *rh*PRAME by ELISA (Enzyme linked Immunosorbet assay) and SPR (Surface Plasmon Resonance) direct binding assays. As shown in Figure 1, the 2D5 mAb recognized the coated *rh*PRAME protein in a dose-dependent and saturable manner. A rough estimation of the affinity obtained by fitting the data points with a non linear algorithm provided a K_D of 198 $\pm$ 34 pM. We also performed a preliminary comparison of the binding to *rh*PRAME between the new mAb and a commercially available polyclonal antibody (Abcam code ab89097). Data preliminarily showed that 2D5 bound to a greater extent the protein compared to the commercial product (Figure S5), although it must be noted that the commercial product was a polyclonal antibody, thus likely at a lower effective concentration generated against the full-length protein. To further characterize this interaction, we performed dose-dependent binding assays through SPR immobilizing the protein on a CM5 sensor chip. As shown in Figure 2, the 2D5 mAb bound very efficiently and dose-dependently the immobilized *rh*PRAME, exhibiting an apparent affinity constant (K_D) of 34.9 $\pm$ 5.0 pM. The strong affinity is mostly derived from the very slow dissociation rate ($k_d = 4.51 \times 10^{-5}$ s^{-1}). Binding to the immobilized protein was already nearly saturated using the antibody at 2.0 nM. Association and dissociation rate constants and related kinetics parameters for all binding experiments are reported in Table 1.

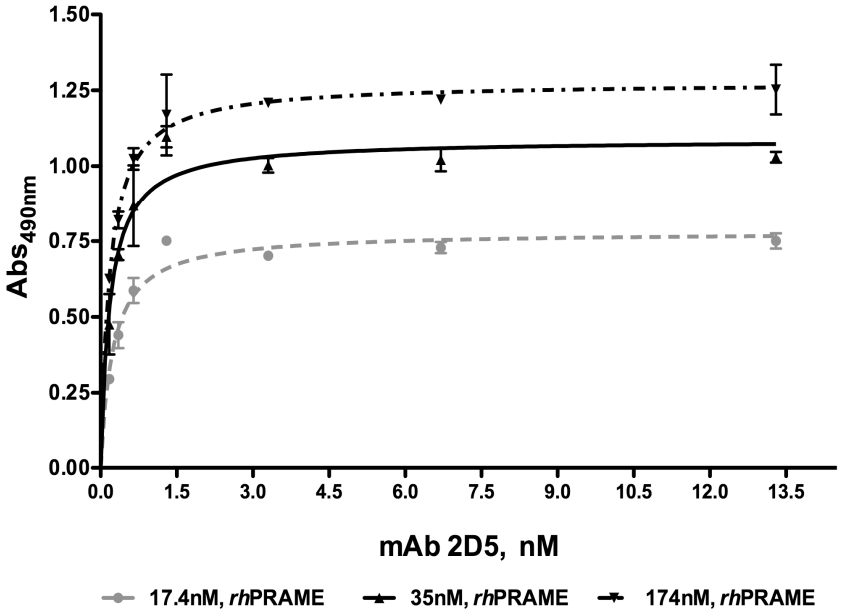

Figure 1. ELISA testing of the binding between the anti-preferentially expressed antigen in melanoma (PRAME) 2D5 mAb and *rh*PRAME) coated at the reported concentrations. A K_D of 0.19 ± 0.03 nM was roughly estimated as the average value of the least 3 independent experiments.

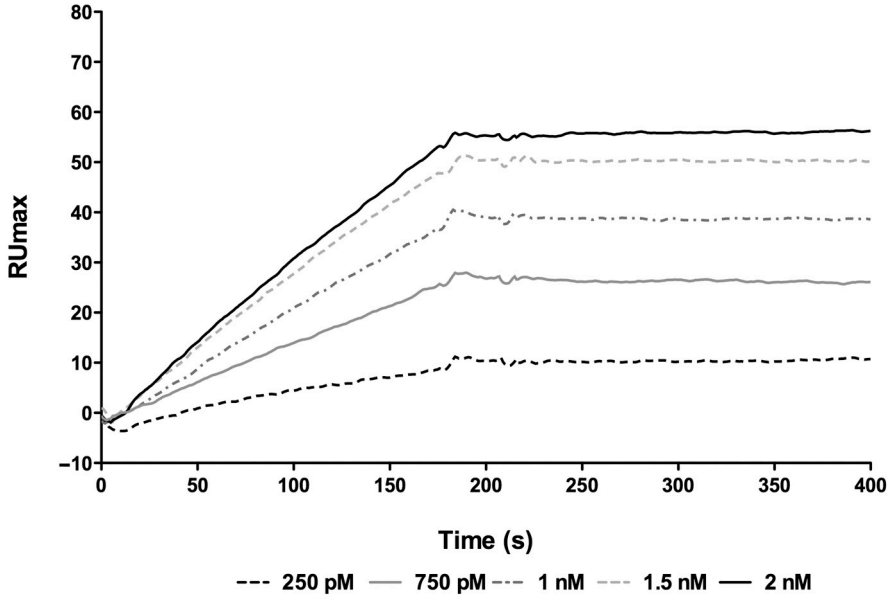

Figure 2. SPR dose–response assays between the immobilized *rh*PRAME and the anti-PRAME 2D5 mAb at various concentrations. The overlaid sensorgrams obtained at mAb concentrations between 250 pM and 2.0 nM are shown. All experiments were carried out at 25 °C at a constant flow rate of 20 µL/min using HBS-EP as a running buffer. Kinetic parameters are reported in Table 1.

Table 1. SPR kinetic rates and apparent affinity binding constants of anti-PRAME mAb 2D5 for *rh*PRAME.

nM	Ka (1/Ms)	Kd (1/s)	K_D (M)	SE (RI)
0.25	3.53×10^5	2.11×10^{-4}	5.97×10^{-10}	0.153
0.5	2.77×10^6	4.36×10^{-5}	1.57×10^{-11}	0.056
0.7	3.60×10^5	9.73×10^{-6}	2.71×10^{-11}	0.049
1	2.92×10^6	3.09×10^{-5}	1.06×10^{-11}	0.041
1.5	1.18×10^6	4.16×10^{-5}	3.51×10^{-11}	0.028
2	8.21×10^5	6.43×10^{-5}	7.83×10^{-11}	0.048
average			3.49×10^{-11} *	

* The average was calculated excluding the deviating kd values obtained at 0.25 nM and 0.7 nM.

2.3. Detection of Endogenous PRAME in Cell-Based Assays

The binding specificity of the anti-PRAME 2D5 mAb was assessed by its ability to detect the endogenous PRAME by Western blotting and FACS analysis in cancer cell lines expressing the protein. For this purpose, we used the L1236 and U2OS cancer cells, whereas the KG1 cell line, not expressing the protein, was selected as a negative control. As shown in Figure 3A,B, the 2D5 mAb was able to detect the endogenous PRAME protein by WB in both the L1236 (Figure 3A)- and U2OS (Figure 3B)-positive cell lines, while, as expected, no bands were detected in the PRAME-negative KG1 cells. We next performed a flow cytometry analysis on U2OS cells by combining cell surface and intracellular marker labeling. A commercial anti-PRAME antibody (Abcam, ab89097) and an IgG1 (isotype control) were used as positive and negative controls, respectively. The U2OS cells were harvested and incubated with either the commercial anti-PRAME antibody or the 2D5 mAb; following this step; cells were permeabilized and incubated again with the primary antibodies. As shown in Figure 4A, the cells treated with the 2D5 mAb displayed a significant shift of fluorescence intensity as compared to cells incubated with the isotype control. The same increase of fluorescence intensity was observed when the cells were treated with the commercial anti-PRAME antibody used at the same concentration. The data (Figure 4B) show that the binding signal was saturated at the lowest antibody concentrations (7.5 µg/mL).

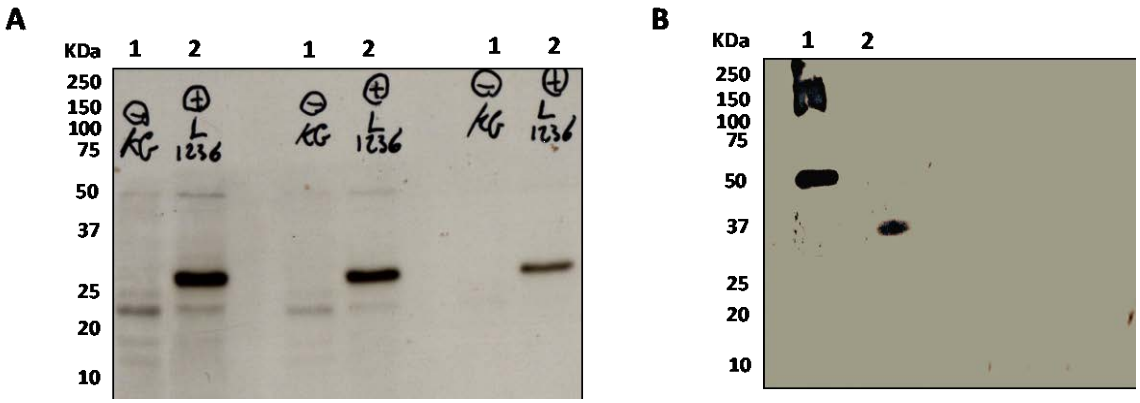

Figure 3. (**A**) Western blotting analysis of endogenous PRAME in L1236 (PRAME-positive) and KG1 (PRAME-negative) cell extracts using the mAb 2D5 at various concentrations. (**B**) Western blotting analysis of U2OS cell extracts using the mAb 2D5 at 5.0 µg/mL. In (**A**) M: markers; 1: KG1 cell extract probed with 2D5 at 5.0 µg/mL; 2: L1236 cell extract probed with 2D5 at 5.0 µg/mL; 3: KG1 cell extract probed with 2D5 at 2.0 µg/mL. 4: L1236 cell extract probed with 2D5 at 2.0 µg/mL; 5: KG1 cell extract probed with 2D5 at 1.0 µg/mL; 6: L1236 cell extract probed with 2D5 at 1.0 µg/mL. In (**B**) M: markers; 1: U20S (PRAME-positive) cell extract; 2: *rh*PRAME used as a positive control.

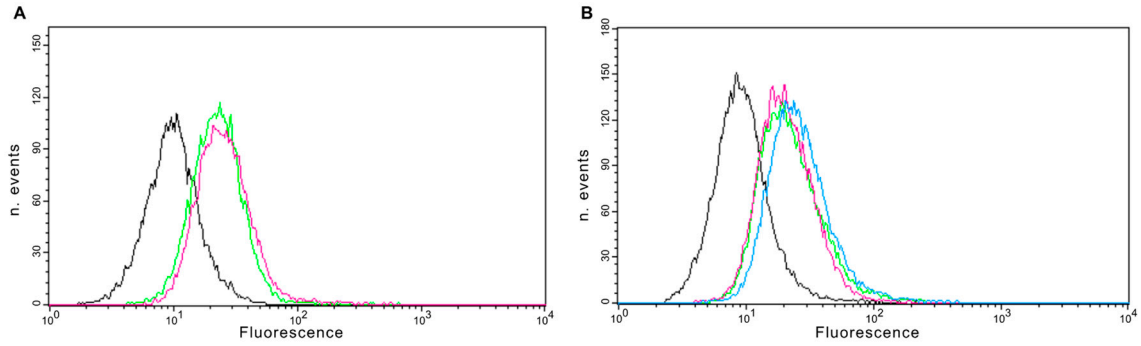

Figure 4. Flow cytometry analysis of U2OS cells using the 2D5 monoclonal antibody and the commercial antibody code ab89097, used as a positive control. (**A**) Cells at a density of 5×10^7 cells/mL were incubated with 15 μg/mL of the commercial anti-PRAME antibody (green curve) or 2D5 mAb (magenta curve). (**B**) Cells were incubated with 7.5 (magenta curve), 15 (green curve) or 30 μg/mL (blue curve) of anti-PRAME 2D5 mAb. Black curves represent the cells incubated with isotype control antibody. These pictures are representative of different independent experiments.

2.4. Identification of the mAb 2D5 Epitope on rhPRAME

To identify the protein epitope recognized by the anti-PRAME 2D5 mAb, an aliquot of the antibody was immobilized on the surface of the bio-layer interferometry (BLI) sensor chip (ForteBio, Fremont, CA, USA). The binding to *rh*PRAME was first assessed in preliminary experiments (Figure S6), exposing the sensor chip to a 1.0 μM solution of the intact protein, the same concentration as the digested protein. Remarkably all experiments were performed in a cuvette of only 4 μL total volume; therefore, only small amounts of material were used in these assays. Next, the sensor chip was exposed to the mixture of peptides obtained by treating the protein with trypsin. No binding was observed in this case due to the inability of the system to detect analytes with a molecular weight below around 7 kDa [23]. The bound fraction was eluted using a solution at pH 2.0 (0.1% TFA in H_2O, 4.0 μL) and collected in a plastic tube. The procedure was repeated 10 times, collecting the eluted fraction always in the same tube to accumulate the material for the mass spectrometry analysis. The final sample, concentrated under vacuum up to about 10 μL, was analyzed by MALDI-TOF mass spectrometry (MS). The starting mixture was analyzed in a parallel experiment, as described in the section of Methods. A peptide mapping of the protein by MALDI-TOF MS (Figure 5A, upper panel) showed a sequence coverage of 66%, which is rather extensive considering the non-optimal reducing and denaturing conditions (0.5 urea) used to retain the protein solubility during the digestion (Figure 5D). The MALDI-TOF analysis of the bound peptides (Figure 5A, lower panel and Figure 5C) showed that, besides several ion signals deriving from human keratin contaminants, a clear ion signal at *m/z* 1446.92 was uniquely detected in the sample. This signal corresponded to the monoisotopic ion of fragment 202–212 of PRAME (see arrow in Figure 5A, lower panel; (R)KKNVLRLCCKK(L), theoretical monoisotopic $[M + H]^+$ mass 1446.84 Da, $\Delta = -0.08$ Da). Worth of note, this peptide, containing four missed cleavage sites (see magnification in Figure 5E), was undetectable within the whole tryptic digest, a finding strongly suggestive of the highly selective enrichment deriving from the binding to the immobilized antibody.

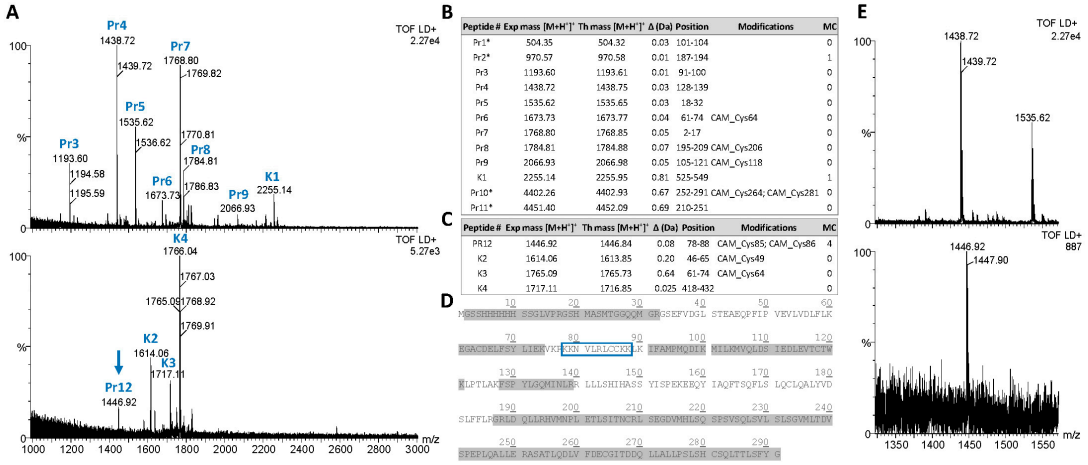

Figure 5. (**A**) Matrix-assisted laser desorption ionization time-of-flight (MALDI-TOF) spectra in the *m/z* range 1000–3000 of tryptic peptides (upper panel) and antibody-bound eluted peptides (lower panel) of human recombinant PRAME protein. (**B**) List of tryptic peptides from human recombinant PRAME protein (Pr) and human keratins (K) as identified by MALDI-TOF MS analyses on the digested protein. (**C**) List of tryptic peptides from the antibody-bound fraction eluted from the sensor tip as identified by MALDI-TOF MS analysis. Peptide's theoretical and experimental masses, along with mass errors, amino acid positions and modification and the number of trypsin missed-cleavage sites, are reported (*, peptide ions not shown in MALDI-TOF spectra). (**D**) Tryptic peptides identified by MALDI-TOF MS analysis and mapping on the PRAME protein region 161–415. Sequence regions corresponding to the mapped tryptic peptides are shaded gray. The His-tag-containing linker (His-Tag) at the protein N-terminus is bold and underlined. The protein region 202–212, corresponding to the peptide uniquely detected in the antibody-bound sample, is blue boxed. (**E**) Magnification of the *m/z* region containing the ion signal at *m/z* 1446.92, uniquely detected in the sample of antibody-bound peptides.

2.5. ELISA and BLI Binding between Biotin-PRAME Peptides and the Anti-PRAME 2D5 mAb

The synthetic peptide reproducing the potential epitope, spanning residues 202–212 of *rh*PRAME (See Table S1), was next used in ELISA binding assays with the anti-PRAME 2D5 mAb to assess its recognition by the mAb. As shown in Figure 6, biotin-PRAME (202–212) bound in a dose-dependent manner the anti-PRAME 2D5 mAb, exhibiting an affinity constant estimated to be 0.55 ± 0.10 μM, much lower compared to that displayed by the protein, which is estimated to be between of 33.4 (SPR) and 198 pM (ELISA). Given the much lower affinity compared to the recombinant protein antigen, we investigated the specificity of the binding by designing and testing, in the same assay, a set of mutated peptide variants. Peptide sequences are reported in Table S1 together with that of the parent molecule. The 3 new peptides are (i) mutant K203A-R207A-K211A where the basic residue K203, R207 and K211 were replaced by alanine; (ii) mutant V205A-L206A-L208A where the hydrophobic residue V205, L206 and L208 were changed to alanine and (iii) mutant C209S-C210S where the 2 cysteines were replaced with the structurally homologous residue serine. As can be seen again in Figure 6, while mutants V205A-L206A-L208A and C209S-C210S completely lost the ability to bind to the antibody, the peptide K203A-R207A-K211A where the basic residues were replaced with alanines retained part of the affinity with 2D5. These observations were fully confirmed in parallel assays performed by BLI using the same peptides (See Figure S7A–D). Data indeed showed that the mutated peptide K203A-R207A-K211A was the only able to retain some affinity for the antibody and that the wt peptide exhibited a KD (0.59 μM) similar to that measured by ELISA (Figure S8). This observation suggests that most contribution to binding is provided by the hydrophobic residues and by cysteines, while a minor role is played by the positively charged lysines and arginines. A possible role in the recognition played by covalent bonds formed through the reactive thiols of the cysteines side-chains is ruled out by the observation that mutant V205A-L206A-L208A is fully unable to bind the antibody. The data thus indicate that the antibody recognition is specific for this protein region, although the reduced binding strongly indicates that other protein sites are involved and contribute to achieving an

affinity in the pM range. The robust binding observed with the protein also opens the hypothesis that the real epitope might be conformational, thus strongly dependent on protein folding and structure, or it extends outside the N- or the C-terminus of the 202–212 fragment, including other residues removed by trypsin.

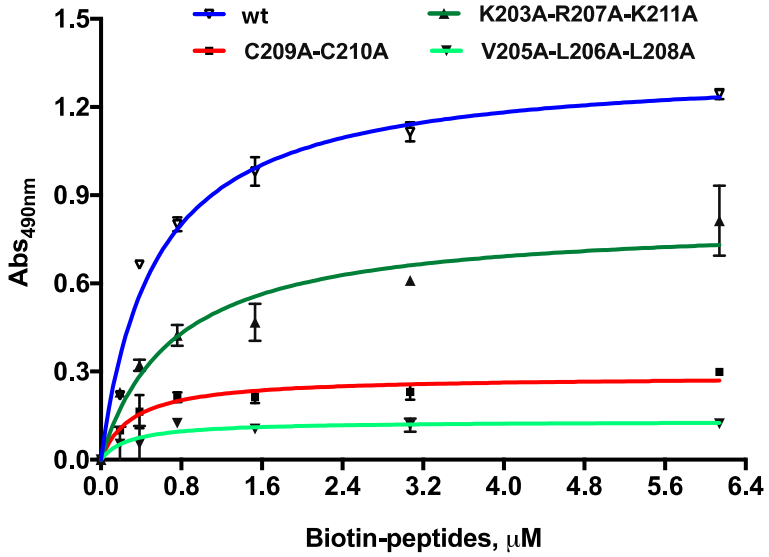

Figure 6. Dose–response ELISA binding of the biotin-PRAME (202–212) wild-type and mutanted peptides to the coated 2D5 mAb. For the wild type peptide, an affinity constant of 0.55 ± 0.10 μM was roughly estimated. The binding to the mutated variants under the same conditions are also reported.

3. Discussion

Although hundreds of thousands of different antibodies are commercially available against essentially any protein (see, for example, www.proteinatlas.org/about/antibodies (accessed on 14 November 2020)), many others are continuously developed to fulfill the need of ever more selective and sensitive reagents for both the detection of biomarkers and the modulation of therapeutically relevant biological activities. One critical prerequisite for the success of an antibody is the knowledge of its binding site on the target protein, information that is often missing also for many commercial products. The binding site can be identified by various approaches, including site-directed mutagenesis, through the use of synthetic peptides or by fragmenting the protein and isolating the binding fragment by various approaches.

Recently, an epitope analysis of a panel of mAbs targeting PRAME protein has been reported [20]. Here, we explored the used of BLI biosensors to capture a fragment of the PRAME protein recognized by a newly generated monoclonal antibody.

Unlike many other CTAs, PRAME belongs to the leucine-rich repeat (LRR) family of proteins. Its localization on cell membranes [24] makes it a suitable diagnostic cancer biomarker and a target appropriate for developing diagnostic, monoclonal antibodies. The precise functions of PRAME and its contribution to oncogenesis are so far poorly understood; therefore, inhibitors can be difficult to design and develop.

Beyond its involvement in DNA hypomethylation [10,15], one leading hypothesis for its antiapoptotic activity relies on its ability to repress, in a cancer-specific manner, the expression of the potent tumor suppressor TRAIL through the binding to RAR (retinoic acid receptor) and to EZH2 that epigenetically represses TRAIL gene expression [25,26]. However, one such mechanism occurs within the cell, and the binding sites are unknown; thus, inhibitors like monoclonal antibodies cannot be easily managed. No mechanisms associated with its cell-surface localization have been so far reported, thus given its selective expression on several cancer cells, including lymphoma cells [4,5], the use of antibodies against the outer protein regions can be envisaged for CAR-T-based immunotherapies

where no specific functions of the protein must be modulated. Recent evidence has indeed shed light on PRAME as a cell-surface cancer biomarker [17] and as a target for TCR mimic antibodies (TCRm) [18,19], opening the possibility for effective CAR-based T cell therapies. We found that our antibody binds to a region located on the protein second LRR domain. Basing on the ability of the 2D5 antibody to bind the protein in cytofluorimetry experiments and on the very hydrophilic nature of the composing residues, the region is likely well exposed on the outer protein surface. However, any further hypothesis is precluded by the lack of information on the protein structure. The huge difference in affinity exhibited by the isolated epitope compared to the full-length protein (around 550 nM compared to 35 pM, which is about 17,000-fold lower) also indicates that the antibody binds much better the epitope when it is embedded in the protein tridimensional structure where it likely adopts a more structured conformation. This observation strongly suggests the intriguing hypothesis that the antibody recognizes a specific protein conformation that is lost in the isolated peptide, thus leading to the highly reduced affinity. However, the ability of 2D5 to detect the protein in Western blotting suggests that the affinity for the unfolded protein is still sufficiently high for analytical applications and that also other protein residues contribute to the recognition. Given the properties exhibited by the antibody, including the high affinity (K_D = 33.4 pM) and the very slow dissociation rate (kd = 4.5 $\times$ 10^{-5} s^{-1}), we believe that 2D5 could be a candidate for the generation of scFv-based new CARs. In light of the possibility to target PRAME as an extracellular biomarker, investigating in deeper detail its cellular localization and its interactions with cell-membrane partners would be an interesting future goal. Radioimmunoconjugates and Ab-drug conjugates may also be explored in the context of targeting PRAME-positive cancer cells in an effort to provide effectiveness against cancer cells. Although additional functional studies are required, this new anti-PRAME 2D5 mAbs could be a useful reagent to explore the potential of this class of biotherapeutics in terms of pharmacological efficacy and off-target effects in many PRAME-positive tumors.

4. Materials and Methods

The cDNA of PRAME 161–415 and the corresponding pET28a plasmid were generated in the laboratory of Prof. Antonio Leonardi, University of Naples Federico II, Napoli. Reagents and buffers for protein expression and purification were from GE Healthcare (Milan, Italy) and Sigma-Aldrich/Merck-Millipore (Milan, Italy). Reagents for peptide synthesis were from GL Biochem (Shanghai, China), IRIS Biotech GmbH (Marktrewitz, Germany) and Sigma-Aldrich/Merck-Millipore (Milan, Italy). Reagents, sensor chips and the Biacore 3000 instrument for surface plasmon resonance analyses were from GE Healthcare (Milan, Italy). Reagents for ELISA were from Sigma-Aldrich/Merck-Millipore (Milan, Italy). The human osteosarcoma cell line (U2OS) was kindly provided by Prof. Alfredo Budillon (IRCCS-Fondazione Pascale, Naples, Italy). KG1 and L1236 cells were kindly provided by Dr. Antonello Pinto (IRCCS-Fondazione Pascale, Naples, Italy). α-cyano-4-hydroxycinnamic acid (4-CHCA) and tosyl-phenylalanyl-chloromethyl ketone (TPCK)-treated trypsin needed for MALDI-TOF analysis were from Sigma-Aldrich (Milan, Italy). Acetonitrile (Honeywell Riedel-de Haen), trifluoroacetic acid and LC–MS grade water (Honeywell Riedel-de Haen) used for the same purpose were from Fisher Scientific (Milan, Italy). Bio-layer interferometry (BLI) experiments were performed using a BLITZ instrument and ARG2 sensor chips (Alfatest, Milano, Italy). A commercial mouse anti-PRAME antibody was obtained from Abcam (code ab89097, Milan, Italy).

4.1. Expression and Purification of Recombinant PRAME Region 161–415

Expression of recombinant human PRAME region 161–415, hereafter *rh*PRAME, was performed in the *E. coli* strain BL21(DE3). Bacterial cells were transformed with the recombinant plasmid pET28a containing the gene corresponding to PRAME region 161–415 (cloning site BamH1/HindIII). The successfully transformed *E. coli* colonies were picked-up and grown at 37 °C in Luria–Bertani (LB) medium supplemented with kanamycin under

continuous shaking until the absorbance at 600 nm reached 0.5–0.6. The *rh*PRAME expression conditions were optimized, inducing expression with 1 mM IPTG and incubating the bacteria at 37 °C for 3 h culture to obtain inclusion bodies. *E. coli* cells were harvested by centrifugation at 14,000 rpm for 20 min at 4 °C. The pellet was re-suspended in 50 mM TRIS, 0.15 M NaCl, 1 mM EDTA, 1 mg/mL lysozyme pH 8.0 and kept on the rotor wheel for 30 min at 4 °C, then was further lysed by sonication. The protein was recovered from the inclusion bodies after centrifugation, washing with 20 mM Tris-HCL, pH 8.0, 100 mM NaCl, and final solubilization in a denaturing buffer containing 8 M urea at 4 °C overnight. Insoluble cell debris was again removed by centrifugation. The supernatant fraction was collected and loaded on Ni-NTA agarose resin. The resin was washed with 25 mM TRIS, 4 M urea, 250 mM NaCl, 1 mM DTT, 5 mM Imidazole, pH 7.4. The bound protein was eluted with the same buffer containing 500 mM Imidazole. Fractions containing the purified *rh*PRAME were pooled and dialyzed against the same buffer containing 2 M urea and 1 mM DTT (or 10 mM β mercaptoethanol) overnight at 4 °C. The recovered protein was again dialyzed against 500 mL of PBS buffer containing 1 M urea and 1 mM DTT (or 10 mM β mercaptoethanol) at 4 °C for 4 h and then against the same buffer, but containing only 0.5 M urea overnight at 4 °C since urea removal leads to abundant precipitation. Some protein was recovered and characterized by gel filtration (GF) to assess that it was not aggregated and used to perform immunization of the animals for producing the monoclonal antibodies, the ELISA and the SPR assays. Analytical GF separations were performed on a BIOSEP S-2000 30 × 7.8 mm ID column (Phenomenex, Castel Maggiore, Italy) using 25 mM phosphate buffer pH 7.5 containing 150 mM NaCl as running buffer. The flow rate was 1.0 mL/min; detection was performed at 280 nm. The peak collected from the column was analyzed by 15% SDS–PAGE and dot-blot using an anti-HIs antibody at 5.0 μg/mL. Protein purity was evaluated during the purification by 15% SDS–PAGE analysis staining with Coomassie brilliant blue.

4.2. Immunization of Mice and Generation and Purification of mAbs against rhPRAME

BALB/c mice were housed and handled according to the institutional guidelines (Project identification code 2013/0038120, approved by the Ethical Animal Care and Use Committee, University of Naples "Federico II". Date of approval 24 April 2013). Four 5-week old BALB/c mice (Jackson Lab) were immunized with 100 μg of highly purified *rh*PRAME, from which the urea was removed following extensive dialysis and recovery of the residual soluble protein. The protein was emulsified with Complete Freund's adjuvant. To obtain hybridomas secreting anti-PRAME antibodies, we operated as previously described [27–30]. Hybridoma supernatants were screened by ELISA for binding to *rh*PRAME, and those secreting antibodies with strong reactivity were re-cloned twice by limiting dilution and tested in dose-dependent ELISAs to confirm binding. Subcloned hybridomas were cultured in OPTI-MEM medium containing 10% FBS and adapted gradually to serum-free cell medium. The selected hybridoma was transferred to bioreactors (INTEGRA Biosciences AG, CH-7000 Chur, Switzerland) for large-scale antibody production. Monoclonal antibodies were purified by protein G affinity and size exclusion chromatography (not shown), as reported previously [27–30]. The mAb concentration was determined by Nanodrop 200 °C, and the purity and homogeneity were detected by 15% SDS–PAGE.

4.3. ELISA Binding Assays of 2D5 mAb to rhPRAME and to Biotin-PRAME Peptides

ELISA binding assays were performed as described previously [27–31]. For dose–response binding assays, *rh*PRAME was coated at three concentrations (17.4 nM, 35 nM and 174 nM) on microtiter ELISA plates in triplicate wells. The selected purified anti-PRAME 2D5 mAb was tested at increasing concentrations between 0.17 nM and 13.3 nM. An HRP-conjugated anti-mouse antibody (Bio-Rad, Milano, Italy) was used as the secondary antibody to detect the bound mAb. OPD was used as a chromogenic substrate. Comparative binding experiments between mAb 2D5 and a commercial mouse anti-PRAME antibody (code ab89097, Abcam, Milano, Italy) were performed coating the protein at

3 concentrations (0.5, 1.0 and 5.0 μg/mL) and using the two antibodies at 0.5 μg/mL. Detection of bound antibodies was performed using an HRP-conjugated anti-mouse antibody (Bio-Rad, Milano, Italy) at 1.0 μg/mL. For ELISA epitope binding experiment, the 2D5 mAb was coated at 6.7 nM and dose–response binding was tested using the N-terminally modified peptide PRAME (202–212), named biotin-PRAME (202–212) (See Table S1), at concentrations ranging between 46 nM and 6.14 μM. Streptavidin-HRP (Sigma-Aldrich, Milano, Italy) was used at the final concentration of 0.15 μg/mL diluted in PBS. Detection was achieved using an OPD tablet (Sigma-Aldrich, Milano, Italy), the peroxidase reaction was stopped with 50 μL/well of 2.5 M H_2SO_4, and the optical density was measured at 490 nm, using a multiwell plate reader (BioTek, Winooski, VT, USA). All experiments were performed 3 times and in triplicate. The binding of the mutated biotin-PRAME peptides (reported in Table S1) was evaluated in the same conditions. Data were fitted using GraphPad ver. 6.0 by applying a nonlinear regression analysis algorithm.

4.4. SPR-Based Affinity Measurements

All SPR analyses were performed on a Biacore 3000 instrument (GE Healthcare), using CM5 sensor chips with immobilized a highly purified (no urea was present) fraction of the recombinant protein. HBS-EP (10 mM HEPES, pH 7.4, 150 mM NaCl, 3 mM EDTA, 0.005% surfactant P20) was used as running buffer. The immobilization was carried out following the canonical amino coupling chemistry [32], operating at a flow rate of 5 μL/min, using the Wizard application. The chip surface was activated with a 50:50 (*v/v*) EDC/NHS mixture (containing 0.4 M EDC and 0.1 M NHS). *rh*PRAME was immobilized at 10 μg/mL in 10 mM NaAc, at pH 4.5. The remaining active ester groups were finally blocked with 1 M ethanolamine-HCl at pH 8.5. A reference channel was opportunely prepared to perform the same procedure without the ligand. The binding ability of the selected anti-PRAME 2D5 mAb was tested at increasing concentrations ranging between 0.25 nM and 2.0 nM. All analyses were carried at 25 °C, at a 20 μL/min constant flow rate, and injecting 60 μL volume of analyte solutions opportunely diluted at different concentrations. HBS-EP was used to prepare the antibody samples. NaOH at 5 mM was used to regenerate the chip surface after the binding with the antibody. For each individual injection, experimental sensorgrams were aligned, subtracted of blank signal and were then overlaid. All mathematical manipulations and fitting operations were performed using the BIA evaluation software, version 4.1 (GE Healthcare) and assuming a 1:1 Langmuir binding model. The final apparent K_D was determined by calculating the average of the values obtained in separate experiments at 0.5 nM, 1.0 nM, 1.5 nM and 2.0 nM where the kd (koff) and ka (kon) were not grossly different.

4.5. Western Blot Analyses of Endogenous PRAME in Extracts of Cell Expressing and not Expressing the Protein

Western blotting analyses were performed using standard procedures. Cells were grown as previously reported [33–35]. Cell extracts from KG1 (PRAME-negative cells) and L1236 cells (PRAME-positive) were prepared as previously described [28,35]. Proteins were separated on a 15% SDS–PAGE gel and transferred to a polyvinylidene difluoride membrane (Millipore, USA). After blocking with 5% NFDM, the membrane was incubated with the anti-PRAME 2D5 mAb at 1.0, 2.0 and 5.0 μg/mL overnight at 4 °C. Similarly, Western blotting analyses were performed on U20S cells (PRAME-positive using *rh*PRAME as a positive control. Hybridization was set up using the 2D5 mAb at 5.0 μg/mL. Detection was performed using an ECL substrate kit (Pierce, Thermo Fisher, Waltham, MA, USA) according to the manufacturing procedures. Images were acquired using the ChemiDoc imaging system (Bio-Rad).

4.6. Flow Cytometry Analysis

The human osteosarcoma cell line (U2OS) was grown in DMEM supplemented with 10% fetal bovine serum (FBS), 2 mM L-glutamine, 100 U/mL penicillin, 100 μg/mL streptomycin (EuroClone, Milano, Italy) and was maintained in humidified air containing

5% CO_2 at 37 °C. Adherent cells at about 70% confluence were detached using 0.25% trypsin, 2 mM EDTA (EuroClone, Milano, Italy), centrifuged and suspended in PBS1x. For surface receptor labeling, cell aliquots (5×10^5 cells) were treated in the same manner with the commercial mouse anti-PRAME antibody (code ab89097, Abcam, Milano, Italy), the anti-PRAME 2D5 mAb or a mouse IgG isotype control antibody (Cell signaling Technologies, Boston, MA, USA), at the different concentrations. For intracellular staining, cells were fixed and permeabilized using an intrastain kit (Dako, Glostrup, Denmark), according to the manufacturer's instructions and incubated again with the primary antibodies. After washing, cells were treated with a FITC-conjugated secondary antibody (Jackson ImmunoResearch Laboratories Inc, Baltimore, USA) and diluted according to the manufacturer's recommendations. Labeled cells were washed and analyzed using a flow cytometer equipped with a 488 nm argon laser (FACScan, Becton Dickinson, CA, USA). A total of 20,000 events for the sample were collected, and values of fluorescence intensity were obtained from the histogram statistic of CellQuest software. All FACS analyses were performed at least 3 times.

4.7. Bio Layer Interferometry-Based Epitope Capture Assay

The anti-PRAME 2D5 mAb was immobilized on an ARG2 BLI sensor tips as previously reported following the EDC/NHS method [36]. The antibody was diluted at a concentration of 5.0 µg/mL in sodium acetate buffer 10 mM, pH 5.0 (4.0 µL) and exposed to the preactivated sensor chip for 3 min. The surface was deactivated with ethanolamine 0.5 M pH 8.0 and extensively washed with PBS1x buffer (4.0 µL). One single dose experiment was carried out to assess the binding of the protein on the new sensor chip in the presence of urea. The binding of *rh*PRAME was tested at 1.0 µM, the concentration of the digested protein used in the capture experiment. Capture experiments were performed using the fragment mixture obtained following digestion with trypsin (see below) at the final concentration of 1.0 µM. The experiment was repeated 10 times, accumulating the eluted fraction in a single pooled fraction. For each run, the tryptic peptide mixture (4.0 µL) was exposed to the Anti-PRAME 2D5 mAb derivatized sensor chip for 3 min. After washing the chip with PBS for 1 min, the captured peptides were eluted with 4 µL of 0.1% TFA in H_2O. The pooled fraction containing the eluted peptides was lyophilized and reconstituted in 30 µL of water/acetonitrile (70:30, *v/v*, containing 0.1% TFA) and analyzed by MALDI-TOF MS. See Scheme 1.

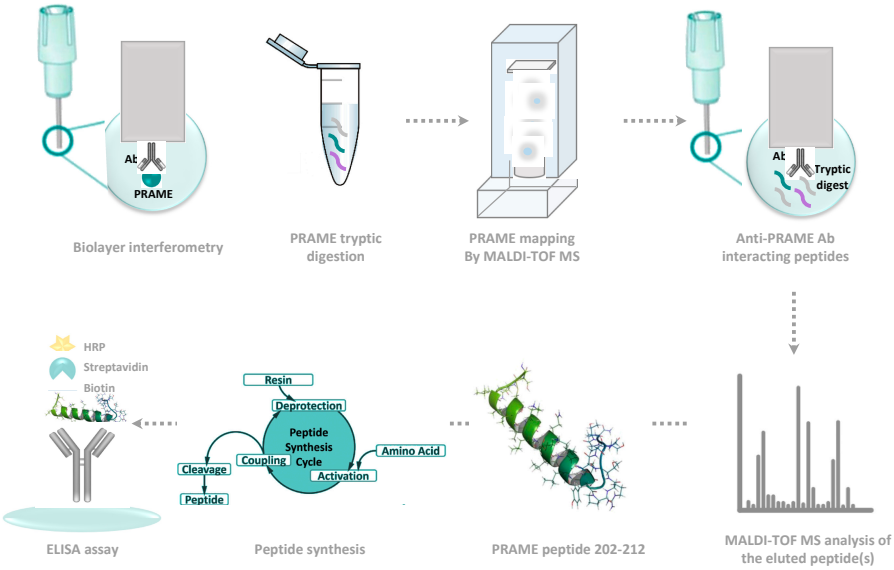

Scheme 1. Schematic representation of the approach followed to identify the epitope of mAb 2D5.

The binding of the biotinylated PRAME peptides (See Table S1) to the 2D5 antibody was similarly performed using SA BLI sensor chips. Peptides were immobilized at 20 μg/mL in PBS running buffer by 3 min exposure (contact time) of the solution to the sensor tips. Bound nonspecific material was washed by short washing (10 sec pulses) with NaOH 5 mM. The chips were extensively equilibrated with PBS. An SA sensor chip functionalized with biocytin was used as a negative control to test the monoclonal antibody specificity. Dose–response binding experiments with the soluble mAb were performed in the concentration range between 0.5 and 7.5 μM (volume 4 μL) in PBS buffer. Each individual assay was completed performing the following steps: (i) exposure to running buffer to acquire the initial baseline (baseline, exposure time 30 s); (ii) exposure to antibody solutions (association, volume 4.0 μL, exposure time 120 s); (iii) exposure to running buffer (dissociation, exposure time 120 s); (iv) exposure to 5 mM NaOH (regeneration, exposure time 10 s). The shaker speed was set to 2000 rpm according to the manufacturer's instructions. Data were exported from the BLItz Pro 1.2 software and re-plotted with GraphPad Prism, version 5.00, GraphPad software (San Diego, CA, USA). Plateau values of binding as reflected by changes in optical thickness (nm) at 140 s were used to calculate the affinity constant (KD) by applying a nonlinear curve fitting and one binding site hyperbola as a model (GraphPad Prism).

4.8. Tryptic Digestion and MS Analysis

*rh*PRAME (5.0 μg) in around 150 μL of 25 mM Tris-HCl buffer, pH 8.2 (around 1.0 μM), containing 0.5 M urea, 40 mM NaCl and 0.3 mM DTT was further added of DTT up to 10 mM and left for 1 h at 55 °C. The protein was next alkylated with 7.5 mM IAM (iodoacetamide) by incubating the solution for 30 min at room temperature in the dark. The enzymatic hydrolysis was performed by adding TPCK-treated trypsin (4.0 ng/μL) at an enzyme/substrate (E/S) ratio of 1:50 (*w/w*) and by incubating the sample at 37 °C for 16 h. The peptide mixture was analyzed by matrix-assisted laser desorption ionization time-of-flight (MALDI-TOF) mass spectrometry to identify the protein fragment generated, as previously reported [37]. Briefly, 1.0 μL of samples were mixed with 1.0 μL of saturated α-cyano-4-hydroxycinnamic acid matrix solution at 10 mg/mL in acetonitrile/water (1:1, *v/v*), containing 0.1% TFA. A droplet of the resulting mixture (1.0 μL) was placed on the MALDI-TOF micro MX (Waters, Manchester, UK) target plate and dried at room temperature. Once the liquid was completely evaporated, samples were loaded into the mass spectrometer and analyzed. In reflectron mode, the instrument was externally calibrated using a tryptic alcohol dehydrogenase digest (Waters, Milan, Italy). For linear mode analysis, a 4-point external calibration was applied using an appropriate mixture (10 pmol/μL) of ProteoMass ACTH Fragment, insulin, cytochrome C and horse Mb as calibration standard (Sigma-Aldrich, Milan, Italy). All spectra were processed and analyzed by using the Mass Lynx 4.1 software. The tryptic peptides captured by the mAb 2D5 and eluted from the sensor chip were similarly analyzed.

4.9. Peptide Synthesis

The synthetic biotin-PRAME (202–212) peptide (Bio-βAla-KKNVLRLCCKK, Table S1) and the mutated variants (See Table S1), amidated at the C-terminus, were prepared by the Fmoc/tBu methodology as reported elsewhere [38,39] and purified by RP-HPLC. Identity was assessed by LC–MS analyses. The peptides were biotinylated on the N-terminus using biotin-N-hydroxysuccinimide (biotin-NHS, Sigma-Aldrich, Milan, Italy) dissolved in dimethylformamide (DMF) containing 5% di-iso-propyl-ethylamine [39]. After assembly, the peptides were cleaved from the Rink-amide resin and purified by RP-HPLC, as previously reported [36]. The final products were identified by ESI-TOF LC–MS analyses using an Agilent 1290 Infinity LC System coupled to an Agilent 6230 TOF mass spectrometer. The experimental MWs were in agreement with the theoretical values (See Table S1).

5. Conclusions

We generated a new anti-PRAME monoclonal antibody by immunizing mice with a recombinant fragment of the human protein encompassing residues 161–415. One high-affinity antibody named 2D5 (K_D = 35 pM) was isolated and used in a number of assays to detect the full-length protein by cytofluorimetry on the surface of cell membranes and by Western blotting in cell extracts. Using an approach based on the immobilization of the antibody on BLI sensor chips and immunoaffinity capture of PRAME peptides obtained after trypsin digestion, we also identified a unique protein fragment (region 202–212) that is able to bind the antibody. By using this fast, inexpensive and novel method, the protein region involved in antibody recognition was, therefore, rapidly delineated, also taking advantage of the small volume (4 μL) of the sensor cuvette and of the lack of fluidics of the label-free system, which enables accumulation of the eluted material following repeated binding-elution cycles. Given the high affinity and the ability to recognize the protein on the surface of cell membranes, the antibody has the potential to become a good template for developing T cell-based immunotherapies.

Supplementary Materials: Supplementary materials can be found at https://www.mdpi.com/1422-0067/22/6/3166/s1.

Author Contributions: Conceptualization, M.R., A.L., A.S., A.C.; methodology, J.P.S., A.S., L.S., G.C., D.C., E.I., R.R., M.V., D.L., N.D.; investigation, J.P.S., A.S, L.S., G.C., D.C., E.I., R.R., M.V., D.L., N.D.; writing—original draft preparation, J.P.S., A.S.; writing—review and editing, M.R., A.S.; supervision, M.R., A.L., A.S.; funding acquisition, A.L., M.R.; review-editing, M.R., A.S.; data curation, A.S. All authors have read and agreed to the published version of the manuscript.

Funding: Authors acknowledge the support from the "Research Project on CAR-T cells for hematological malignancies and solid tumors" granted from Ministero della Salute. Support was also received from Regione Campania for the projects: (i) "Development of novel therapeutic approaches for treatment-resistant neoplastic diseases (SATIN)"; (ii) "Fighting Cancer resistance: Multidisciplinary integrated Platform for a Technologically Innovative Approach to Oncotherapies (Campania Oncotherapies)"; (iii) NANOCAN, NANOfotonica per la lotta al CANcro.

Institutional Review Board Statement: Not applicable.

Informed Consent Statement: Not applicable.

Data Availability Statement: Not applicable.

Acknowledgments: Authors also wish to thank Maurizio Amendola for the technical support for mass spectrometry and Leopoldo Zona for NMR analyses.

Conflicts of Interest: The authors declare no conflict of interest.

Abbreviations

PRAME	Preferentially expressed antigen in melanoma
EMT	Epithelial-to-mesenchymal transition
TCR	T cell receptor
FACS	Fluorescence assisted cell-sorting
SPR	Surface plasmon resonance
ELISA	Enzyme-linked immunosorbent assays
K_D	Thermodynamic dissociation constant
K_d	Kinetic dissociation constant
MALDI-TOF	Matrix Assisted Laser Desorption Ionization Time of Flight

References

1. Sivaccumar, J.; Sandomenico, A.; Vitagliano, L.; Ruvo, M. Monoclonal antibodies: A prospective and retrospective view. *Curr. Med. Chem.* **2021**, *28*, 435–471. [CrossRef]
2. Ikeda, H.; Lethe, B.; Lehmann, F.; van Baren, N.; Baurain, J.F.; de Smet, C.; Chambost, H.; Vitale, M.; Moretta, A.; Boon, T.; et al. Characterization of an antigen that is recognized on a melanoma showing partial HLA loss by CTL expressing an NK inhibitory receptor. *Immunity* **1997**, *6*, 199–208. [CrossRef]
3. Al-Khadairi, G.; Decock, J. Cancer Testis Antigens and Immunotherapy: Where Do We Stand in the Targeting of PRAME? *Cancers* **2019**, *11*, 984. [CrossRef] [PubMed]
4. Abdelmalak, C.A.; Yahya, R.S.; Elghannam, D.M.; El-Khadragy, A.E.; Abd El Messih, H.M. PRAME gene expression in childhood acute lymphoblastic leukemia: Impact on prognosis. *Clin. Lab.* **2014**, *60*, 55–61. [CrossRef] [PubMed]
5. Zhang, Y.H.; Lu, A.D.; Yang, L.; Li, L.D.; Chen, W.M.; Long, L.Y.; Zhang, L.P.; Qin, Y.Z. PRAME overexpression predicted good outcome in pediatric B-cell acute lymphoblastic leukemia patients receiving chemotherapy. *Leuk. Res.* **2017**, *52*, 43–49. [CrossRef]
6. Wadelin, F.; Fulton, J.; McEwan, P.A.; Spriggs, K.A.; Emsley, J.; Heery, D.M. Leucine-rich repeat protein PRAME: Expression, potential functions and clinical implications for leukaemia. *Mol. Cancer* **2010**, *9*, 226. [CrossRef] [PubMed]
7. Wadelin, F.R.; Fulton, J.; Collins, H.M.; Tertipis, N.; Bottley, A.; Spriggs, K.A.; Falcone, F.H.; Heery, D.M. PRAME is a golgi-targeted protein that associates with the Elongin BC complex and is upregulated by interferon-gamma and bacterial PAMPs. *PLoS ONE* **2013**, *8*, e58052. [CrossRef] [PubMed]
8. Costessi, A.; Mahrour, N.; Sharma, V.; Stunnenberg, R.; Stoel, M.A.; Tijchon, E.; Conaway, J.W.; Conaway, R.C.; Stunnenberg, H.G. The human EKC/KEOPS complex is recruited to Cullin2 ubiquitin ligases by the human tumour antigen PRAME. *PLoS ONE* **2012**, *7*, e42822. [CrossRef]
9. Costessi, A.; Mahrour, N.; Tijchon, E.; Stunnenberg, R.; Stoel, M.A.; Jansen, P.W.; Sela, D.; Martin-Brown, S.; Washburn, M.P.; Florens, L.; et al. The tumour antigen PRAME is a subunit of a Cul2 ubiquitin ligase and associates with active NFY promoters. *EMBO J.* **2011**, *30*, 3786–3798. [CrossRef]
10. Schenk, T.; Stengel, S.; Goellner, S.; Steinbach, D.; Saluz, H.P. Hypomethylation of PRAME is responsible for its aberrant overexpression in human malignancies. *Genes Chromosomes Cancer* **2007**, *46*, 796–804. [CrossRef]
11. Ortmann, C.A.; Eisele, L.; Nuckel, H.; Klein-Hitpass, L.; Fuhrer, A.; Duhrsen, U.; Zeschnigk, M. Aberrant hypomethylation of the cancer-testis antigen PRAME correlates with PRAME expression in acute myeloid leukemia. *Ann. Hematol.* **2008**, *87*, 809–818. [CrossRef]
12. Gutierrez-Cosio, S.; de la Rica, L.; Ballestar, E.; Santamaria, C.; Sanchez-Abarca, L.I.; Caballero-Velazquez, T.; Blanco, B.; Calderon, C.; Herrero-Sanchez, C.; Carrancio, S.; et al. Epigenetic regulation of PRAME in acute myeloid leukemia is different compared to CD34+ cells from healthy donors: Effect of 5-AZA treatment. *Leuk. Res.* **2012**, *36*, 895–899. [CrossRef]
13. Siebenkas, C.; Chiappinelli, K.B.; Guzzetta, A.A.; Sharma, A.; Jeschke, J.; Vatapalli, R.; Baylin, S.B.; Ahuja, N. Inhibiting DNA methylation activates cancer testis antigens and expression of the antigen processing and presentation machinery in colon and ovarian cancer cells. *PLoS ONE* **2017**, *12*, e0179501. [CrossRef]
14. Lee, Y.K.; Park, U.H.; Kim, E.J.; Hwang, J.T.; Jeong, J.C.; Um, S.J. Tumor antigen PRAME is up-regulated by MZF1 in cooperation with DNA hypomethylation in melanoma cells. *Cancer Lett.* **2017**, *403*, 144–151. [CrossRef] [PubMed]
15. Al-Khadairi, G.; Naik, A.; Thomas, R.; Al-Sulaiti, B.; Rizly, S.; Decock, J. PRAME promotes epithelial-to-mesenchymal transition in triple negative breast cancer. *J. Transl. Med.* **2019**, *17*, 9. [CrossRef]
16. Orlando, D.; Miele, E.; De Angelis, B.; Guercio, M.; Boffa, I.; Sinibaldi, M.; Po, A.; Caruana, I.; Abballe, L.; Carai, A.; et al. Adoptive Immunotherapy Using PRAME-Specific T Cells in Medulloblastoma. *Cancer Res.* **2018**, *78*, 3337–3349. [CrossRef] [PubMed]
17. Pankov, D.; Sjostrom, L.; Kalidindi, T.; Lee, S.G.; Sjostrom, K.; Gardner, R.; McDevitt, M.R.; O'Reilly, R.; Thorek, D.L.J.; Larson, S.M.; et al. In vivo immuno-targeting of an extracellular epitope of membrane bound preferentially expressed antigen in melanoma (PRAME). *Oncotarget* **2017**, *8*, 65917–65931. [CrossRef] [PubMed]
18. Chang, A.Y.; Dao, T.; Gejman, R.S.; Jarvis, C.A.; Scott, A.; Dubrovsky, L.; Mathias, M.D.; Korontsvit, T.; Zakhaleva, V.; Curcio, M.; et al. A therapeutic T cell receptor mimic antibody targets tumor-associated PRAME peptide/HLA-I antigens. *J. Clin. Investig.* **2017**, *127*, 2705–2718. [CrossRef]
19. Mathias, M.D.; Sockolosky, J.T.; Chang, A.Y.; Tan, K.S.; Liu, C.; Garcia, K.C.; Scheinberg, D.A. CD47 blockade enhances therapeutic activity of TCR mimic antibodies to ultra-low density cancer epitopes. *Leukemia* **2017**, *31*, 2254–2257. [CrossRef]
20. Misyurin, V.A.; Finashutina, Y.P.; Turba, A.A.; Larina, M.V.; Solopova, O.N.; Lyzhko, N.A.; Kesaeva, L.A.; Kasatkina, N.N.; Aliev, T.K.; Misyurin, A.V.; et al. Epitope Analysis of Murine and Chimeric Monoclonal Antibodies Recognizing the Cancer Testis Antigen PRAME. *Dokl. Biochem. Biophys.* **2020**, *492*, 135–138. [CrossRef]
21. Terral, G.; Champion, T.; Debaene, F.; Colas, O.; Bourguet, M.; Wagner-Rousset, E.; Corvaia, N.; Beck, A.; Cianferani, S. Epitope characterization of anti-JAM-A antibodies using orthogonal mass spectrometry and surface plasmon resonance approaches. *MAbs* **2017**, *9*, 1317–1326. [CrossRef] [PubMed]
22. Wiegand, P.; Lupu, L.; Huttmann, N.; Wack, J.; Rawer, S.; Przybylski, M.; Schmitz, K. Epitope Identification and Affinity Determination of an Inhibiting Human Antibody to Interleukin IL8 (CXCL8) by SPR- Biosensor-Mass Spectrometry Combination. *J. Am. Soc. Mass Spectrom.* **2020**, *31*, 109–116. [CrossRef]
23. Cusano, A.M.; Aliberti, A.; Cusano, A.; Ruvo, M. Detection of small DNA fragments by biolayer interferometry. *Anal. Biochem.* **2020**, *607*, 113898. [CrossRef]

24. Proto-Siqueira, R.; Figueiredo-Pontes, L.L.; Panepucci, R.A.; Garcia, A.B.; Rizzatti, E.G.; Nascimento, F.M.; Ishikawa, H.C.; Larson, R.E.; Falcao, R.P.; Simpson, A.J.; et al. PRAME is a membrane and cytoplasmic protein aberrantly expressed in chronic lymphocytic leukemia and mantle cell lymphoma. *Leuk. Res.* **2006**, *30*, 1333–1339. [CrossRef]
25. De Carvalho, D.D.; Mello, B.P.; Pereira, W.O.; Amarante-Mendes, G.P. PRAME/EZH2-mediated regulation of TRAIL: A new target for cancer therapy. *Curr. Mol. Med.* **2013**, *13*, 296–304. [CrossRef]
26. De Carvalho, D.D.; Binato, R.; Pereira, W.O.; Leroy, J.M.; Colassanti, M.D.; Proto-Siqueira, R.; Bueno-Da-Silva, A.E.; Zago, M.A.; Zanichelli, M.A.; Abdelhay, E.; et al. BCR-ABL-mediated upregulation of PRAME is responsible for knocking down TRAIL in CML patients. *Oncogene* **2011**, *30*, 223–233. [CrossRef]
27. Foca, G.; Iaccarino, E.; Foca, A.; Sanguigno, L.; Untiveros, G.; Cuevas-Nunez, M.; Strizzi, L.; Leonardi, A.; Ruvo, M.; Sandomenico, A. Development of conformational antibodies targeting Cripto-1 with neutralizing effects in vitro. *Biochimie* **2019**, *158*, 246–256. [CrossRef]
28. Sandomenico, A.; Leonardi, A.; Berisio, R.; Sanguigno, L.; Foca, G.; Foca, A.; Ruggiero, A.; Doti, N.; Muscariello, L.; Barone, D.; et al. Generation and Characterization of Monoclonal Antibodies against a Cyclic Variant of Hepatitis C Virus E2 Epitope 412-422. *J. Virol.* **2016**, *90*, 3745–3759. [CrossRef]
29. Sandomenico, A.; Foca, A.; Sanguigno, L.; Caporale, A.; Foca, G.; Pignalosa, A.; Corvino, G.; Caragnano, A.; Beltrami, A.P.; Antoniali, G.; et al. Monoclonal antibodies against pools of mono- and polyacetylated peptides selectively recognize acetylated lysines within the context of the original antigen. *MAbs* **2016**, *8*, 1575–1589. [CrossRef]
30. Foca, A.; Sanguigno, L.; Foca, G.; Strizzi, L.; Iannitti, R.; Palumbo, R.; Hendrix, M.J.; Leonardi, A.; Ruvo, M.; Sandomenico, A. New Anti-Nodal Monoclonal Antibodies Targeting the Nodal Pre-Helix Loop Involved in Cripto-1 Binding. *Int. J. Mol. Sci.* **2015**, *16*, 21342–21362. [CrossRef]
31. Viparelli, F.; Cassese, A.; Doti, N.; Paturzo, F.; Marasco, D.; Dathan, N.A.; Monti, S.M.; Basile, G.; Ungaro, P.; Sabatella, M.; et al. Targeting of PED/PEA-15 molecular interaction with phospholipase D1 enhances insulin sensitivity in skeletal muscle cells. *J. Biol. Chem.* **2008**, *283*, 21769–21778. [CrossRef]
32. Johnsson, B.; Lofas, S.; Lindquist, G. Immobilization of proteins to a carboxymethyldextran-modified gold surface for biospecific interaction analysis in surface plasmon resonance sensors. *Anal. Biochem.* **1991**, *198*, 268–277. [CrossRef]
33. Tan, P.; Zou, C.; Yong, B.; Han, J.; Zhang, L.; Su, Q.; Yin, J.; Wang, J.; Huang, G.; Peng, T.; et al. Expression and prognostic relevance of PRAME in primary osteosarcoma. *Biochem. Biophys. Res. Commun.* **2012**, *419*, 801–808. [CrossRef]
34. Lavorgna, A.; De Filippi, R.; Formisano, S.; Leonardi, A. TNF receptor-associated factor 1 is a positive regulator of the NF-kappaB alternative pathway. *Mol. Immunol.* **2009**, *46*, 3278–3282. [CrossRef]
35. Schwering, I.; Brauninger, A.; Distler, V.; Jesdinsky, J.; Diehl, V.; Hansmann, M.L.; Rajewsky, K.; Kuppers, R. Profiling of Hodgkin's lymphoma cell line L1236 and germinal center B cells: Identification of Hodgkin's lymphoma-specific genes. *Mol. Med.* **2003**, *9*, 85–95. [CrossRef]
36. Iaccarino, E.; Calvanese, L.; Untiveros, G.; Falcigno, L.; D'Auria, G.; Latino, D.; Sivaccumar, J.P.; Strizzi, L.; Ruvo, M.; Sandomenico, A. Structure-based design of small bicyclic peptide inhibitors of Cripto-1 activity. *Biochem. J.* **2020**, *477*, 1391–1407. [CrossRef] [PubMed]
37. Russo, R.; Rega, C.; Chambery, A. Rapid detection of water buffalo ricotta adulteration or contamination by matrix-assisted laser desorption/ionisation time-of-flight mass spectrometry. *Rapid Commun. Mass Spectrom.* **2016**, *30*, 497–503. [CrossRef] [PubMed]
38. Verdoliva, A.; Ruvo, M.; Cassani, G.; Fassina, G. Topological mimicry of cross-reacting enantiomeric peptide antigens. *J. Biol. Chem.* **1995**, *270*, 30422–30427. [CrossRef] [PubMed]
39. Caporale, A.; Doti, N.; Monti, A.; Sandomenico, A.; Ruvo, M. Automatic procedures for the synthesis of difficult peptides using oxyma as activating reagent: A comparative study on the use of bases and on different deprotection and agitation conditions. *Peptides* **2018**, *102*, 38–46. [CrossRef] [PubMed]

MDPI
St. Alban-Anlage 66
4052 Basel
Switzerland
Tel. +41 61 683 77 34
Fax +41 61 302 89 18
www.mdpi.com

International Journal of Molecular Sciences Editorial Office
E-mail: ijms@mdpi.com
www.mdpi.com/journal/ijms

MDPI
St. Alban-Anlage 66
4052 Basel
Switzerland

Tel: +41 61 683 77 34
Fax: +41 61 302 89 18

www.mdpi.com

ISBN 978-3-0365-3164-9